Cooling and Crystallization of Komatiite Flows

by Mark Shore

A thesis submitted to the School of Graduate Studies in partial fulfillment of the requirements for the degree of Ph.D. in Earth Sciences

Ottawa-Carleton Geoscience Centre
University of Ottawa
Ottawa, Ontario, Canada

ISBN 0-612-16465-9

UNIVERSITÉ D'OTTAWA
UNIVERSITY OF OTTAWA

Abstract

Despite their ~2710 Ma age, thin komatiite lava flows in Munro township, NE Ontario have sufficiently well-preserved primary structures, textures, mineralogy, and whole-rock geochemistry to constrain the physical processes of cooling and crystal growth. Seawater convection drove a cooling and fracturing front through the upper surface and was the dominant mechanism of heat loss, leading to pronounced textural asymmetry within flows. Large plate-like crystals of olivine in the upper layers of flows grew by constrained crystallization arising from strong thermal gradients and the high lattice thermal conductivity and near-infrared transparency of olivine (3–5 times greater than that of the surrounding melt). Such crystals exhibit a very strong preferred orientation with the *a* crystallographic axis perpendicular to flow surfaces. Major and minor-element zoning within olivine crystals is closely modeled by fractional crystallization from the bulk liquid, and whole-rock geochemical variations within flows by crystal fractionation of highly magnesian olivine. The high chromium content of olivine is of mineralogical and technological interest, and is due to two substitutional mechanisms: $^{[6]}Cr^{3+} + {}^{[4]}Al^{3+} \rightleftharpoons {}^{[6]}Mg^{2+} + {}^{[4]}Si^{4+}$ and $2\ {}^{[6]}Cr^{3+} + {}^{[6]}\square \rightleftharpoons 3\ {}^{[6]}Mg^{2+}$. Dendritic chromian spinel crystals nucleated heteroepitaxially on olivine substrates; the crystallographic relationship between the phases is $[111]_{sp} \parallel [100]_{ol}$, $[1\bar{1}0]_{sp} \parallel [001]_{ol}$, and $[2\bar{1}1]_{sp} \parallel [010]_{ol}$. The Cr-spinel crystals have features typical of metallic, ionic, and organic crystal dendrites, but rarely found in minerals. Immobility of Mg and Si and a systematic loss of Ca in these altered rocks is due to a serpentinization reaction buffered by the desilication of glass or fine-grained plagioclase in the groundmass. Serpentinization occurred under conditions of low confining pressure, caused up to 30% expansion of the basal portions of flows, and predated tectonism at ~2700 Ma.

Acknowledgements

A thesis, although it has a single author, is rarely (if ever) written without help, advice, or encouragement from others. The Natural Sciences and Engineering Research Council provided financial support in the form of a scholarship to me and research grants to my supervisor. An Ontario Graduate Scholarship in my first year at the University was also appreciated.

Over the course of my studies my understanding of geology and mineralogy was greatly increased through courses, seminars, and day-to-day contact with the faculty, staff, and students of the Ottawa-Carleton Geoscience Centre. I particularly thank Professors André Lalonde and Keith Benn for informative discussions of mineralogy and structural geology, respectively. A large part of the credit for the geochemical data presented in this thesis must go to Ron Hartree, geochemical analyst of the Department. For three years he shared both his office and his knowledge of XRF spectroscopy with me, and encouraged me to develop and modify his analytical procedures for my own uses.

I thank my supervisor, Professor Anthony Fowler, for his guidance and friendship. Tony gave me time and a free rein to explore a great many ideas and methods. Not all of these succeeded—and a couple were expensive failures—but I greatly appreciate the confidence that Tony showed in me during our years of work.

Finally, and most of all, I thank Christiana Cavazzoni, my wife, who for years has put up with my prolonged absences in the field, or in books, or in front of computer screens. Neither graduate students nor geologists make easy husbands, and the combination of the two must at times be maddening. Christiana's love and support enabled me to carry out my research, and it is to her that I dedicate this thesis.

Table of Contents

1 Introduction and aims of thesis

1.1 Ages, locations, and characteristics of komatiites

1.1.1 Definition of komatiite

A komatiite is an ultramafic volcanic rock, or more rigorously a volcanic rock that contains more than 18 wt.% MgO on a volatile-free and cumulus olivine-free basis (Arndt and Nisbet, 1982). The name is derived from the Komati River of South Africa, which flows near the komatiite type section (Viljoen and Viljoen, 1969). Lavas with high MgO contents due to mechanical concentration of cognate or xenocrystic olivine crystals (e.g., picrites, ankaramites, basanites, boninites, etc.) are not komatiites. Related intrusive or sub-volcanic rocks may be prefaced with appropriate adjectives (e.g., komatiite dike, komatiite-related dunite sill). Spatially and genetically associated lavas containing between 12 and 18 wt.% MgO are known as komatiitic basalts. The placement of the division at 18% reflects an apparent compositional gap (an analogous gap in SiO_2 content exists in certain felsic volcanic suites) in komatiitic rocks from southern African, western Australia, and the Superior Province of Canada (Nisbet et al., 1982; Binns et al., 1982; Jensen and Pyke, 1982). Most known komatiites are of mid to late Archean age (3.4 to 2.7 Ga), although rare occurrences are as young as the late Cretaceous. Sadly, komatiites appear to be extinct (Arndt, 1994).

The most notable geochemical characteristics of komatiites are their high concentrations of mantle-compatible elements (MgO 20–30 wt.%; Ni 1000–2000 µg/g, Cr 2000–3000 µg/g, and Co 75–150 µg/g; combined PGE 10–20 ng/g) and low to very low concentrations of mantle-incompatible elements (K 500–1000 µg/g, P 50–100 µg/g, Rb 1–2 µg/g, and Ba 20–50 µg/g; lanthanide elements 1 to 10 times chondritic abundance; Th <150 ng/g, U <50 ng/g). Mineralogically, komatiites are olivine-rich rocks, with lesser amounts of augite, pigeonite, altered glass, minor plagioclase, and accessory chromian spinel. A distinctive characteristic of many komatiite flows is the presence of blade- or plate-like olivine crystals set in a much finer-grained groundmass. This is known as spinifex texture, and varies from millimeter-size randomly oriented skeletal olivine crystals to decimeter-long sheaves of subparallel plate-like olivine crystals (see Arndt (1994) for a more complete definition). Many komatiite flows are internally layered with a spinifex-textured upper portion and fine-grained cumulus-textured lower portion. These are respectively known as the A and B layers, and are illustrated in Fig. **1.1**, together with

the textures and nomenclatures of the various internal subdivisions (see also Arndt et al., 1977; Donaldson, 1982).

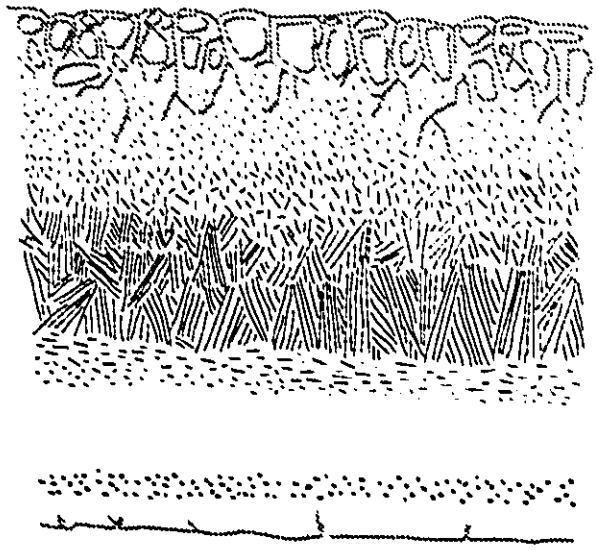

Fig. 1.1 Diagram of a spinifex-textured komatiite flow with typical subdivisions. Not all komatiite flows are internally layered, and of those that are, only some show full development of all subdivisions. The layers are described as follows:
A_1: brecciated flowtop/microspinifex;
A_2: randomly oriented spinifex;
A_3: coarse oriented spinifex;
B_1: aligned skeletal olivine;
B_2: smooth-weathering cumulate;
B_3: "knobby" cumulate;
B_4: smooth-weathering cumulate and basal chill.
Diagram is based upon 1 to 2 m thick flows but similar structures are found in thinner (<0.5 m) and thicker (>10 m) flows.

Komatiites were the hottest lavas known to have erupted on Earth. Their elevated liquidus temperatures (up to ~1560 °C) and depolymerized melt structures would have given komatiites viscosities as low as 0.1 to 0.2 Pa s, about 100 times lower than typical near-liquidus basalts (Nisbet et al., 1993). Komatiites in the strict sense are predominantly restricted to the Archean or early Proterozoic eras. Rare komatiitic basalts and other highly magnesian lavas are present in some Phanerozoic volcanic sequences, and some of these may be related to komatiites.

Komatiites have been intensively studied for various reasons. Apart from their white-hot temperatures, they were the most fluid terrestrial lavas erupted, contain fascinating crystal textures, hold significant information about the Archean mantle and tectonic processes, and host a significant number of economic nickel deposits. This thesis is concerned with a number of currently unresolved questions about cooling and crystal growth within komatiite flows.

1.1.2 Field locations

The Abitibi greenstone belt in the Superior Province of the Canadian shield is one of the largest and best-known in the world (Fig. **1.2**). The metavolcanic rocks of the Abitibi range in composition from komatiite flows to leucite-bearing ultrapotassic tuffs. Near the town of Kirkland Lake, Ontario, outcrops of these compositionally extreme rocks are found within a few km of each other. In the central portion of the Abitibi belt, metamorphic grade and strain are equally variable. Metamorphosed komatiites span a wide range of recrystallization, strain, and chemical alteration and include fuchsite and ankerite-bearing schists, coarsely recrystallized massive actinolite rocks, serpentine–chlorite–actinolite–magnetite rocks with good preservation of mesoscopic primary textures, and rare flows with exceptional preservation of primary mineralogy and microscopic-scale textures. All komatiites have been altered to some degree, and rather than using the cumbersome term metakomatiite, the term komatiite is used throughout this thesis. For my purposes I required the least-altered, least-deformed, best-exposed komatiites available. Long summer days conducting geophysical surveys in the Abitibi had taught me to slog long distances in perfectly straight lines while carrying heavy equipment through hot, humid, insect-infested swamps that even moose avoid. Consequently, to obtain the best komatiites I was capable of revisiting the most remote bogs in the Abitibi: unfortunately for the hungry black flies and deer flies this was not necessary.

I examined a number of komatiite and komatiitic basalt occurrences in the Abitibi, including flows in the Val d'Or area, Lamotte township ("Spinifex Ridge" and the site of the former Marbridge mine), Roquemaure township, Boston Township, Dundonald township (the site of the former Alexo mine and Falconbridge's "Beach" Ni prospect), southwestern Munro township (Falconbridge's "Mickel zone" Ni prospect), and various other areas around Kirkland Lake, west of Matachewan, east of Foleyet, and in the Pontiac subprovince south of Rouyn-Noranda. With the exception of Alexo, where metamorphism is highly variable and where fresh komatiites with relict olivine can be found, in none of these lavas did the exposure or preservation, either mineralogical or textural, begin to approach that of the flows that outcrop at Pyke Hill in north-central Munro Township.

Pyke Hill—an informal name—is a small glacially scoured hill covered by sparse stands of jack pine in Munro Township, 50 km north of Kirkland Lake, Ontario (Photos **1.1** and **1.2**). It lies 20 km east-northeast of the town of Matheson, along a gravel road

leading north of Highway 101 (Fig. **1.3**). The well-preserved and well-exposed komatiite flows on this hill (Figs. **1.4** and **1.5**) were first mapped by Satterly in 1950 (Satterly, 1951), and subsequently described as ultramafic lavas in a classic paper by Pyke et al. (1973). The flows are part of the Stoughton-Roquemaure (Jensen and Langford, 1985) or Kidd-Munro (Jackson and Fyon, 1991) group of mafic-ultramafic volcanic rocks and related intrusives, which comprise a narrow to moderately wide (5–20 km), laterally extensive (~100 km) portion of the Abitibi greenstone belt (MERQ-OGS, 1983). As noted, the Pyke Hill flows are exceptionally fresh; in fact, on the basis of descriptions of other localities in the literature, these flows appear to be the best preserved in the northern hemisphere. For this reason I made Pyke Hill the primary area of study. I also analyzed a small number of samples from other areas, in part to compare analytical results from the University of Ottawa Geochemistry lab to those of Arndt and Barnes, who studied the Alexo flow in considerable detail (Arndt, 1986a; Barnes et al., 1983; Barnes, 1985).

1.1.3 Early work in the Abitibi

Nickel deposits in the Timmins area were exploited on a small scale soon after gold exploration began around 1900. In addition, a number of ultramafic bodies were prospected for industrial minerals such as talc and asbestos, including a thick serpentinized dunite sill in Munro Township that was mined for asbestos from 1950–57. Most if not all of these deposits are hosted in komatiites or komatiite-related rocks. However, the rocks were mapped as intrusive peridotites and their textures and compositions drew little scientific attention. J. Satterly of the Ontario Department of Mines specifically noted the unusual textures of certain flows he observed while mapping Munro township in 1950 (Satterly, 1951). Other ODM geologists who mapped spinifex-textured rocks as lava flows include Bruce (1926), Berry (1940), Prest (1950), and Abraham (1953). Of these, Berry's description of the texture is the most accurate, and he was the only one to include a photograph of the texture in outcrop.

Although many field geologists before 1970 had mapped komatiites as lava flows, few had carried out chemical analyses of these rocks, and they appear to have been generally considered as simply metabasalts with unusual textures. The prevailing opinion among academic geologists was that ultramafic lavas did not exist, largely because Bowen (1922) had correctly pointed out the very high liquidus temperatures of ultramafic lavas, the fact that such temperatures were never observed in present-day lavas, and the equivocal nature of most proposed ultramafic lavas (largely picrites). A lack of

geochemical analyses, coupled with petrographic study of samples that lacked relict olivine or recognizable olivine pseudomorphs led ODM geologists to (half-heartedly) conclude that spinifex texture was caused by contact metamorphism of basalt flows by picritic sills intruded along flow contacts (e.g., Satterly, 1951).

Viljoen and Viljoen (1969), working in South Africa and methodically combining field mapping, geochemical analyses, and petrography, first recognized the significance of spinifex-textured ultramafic lavas. As the Viljoens examined the spinifex-textured lavas of the Komati formation, Naldrett and Mason (1967) were studying a related group of rocks near the Alexo mine site in Dundonald township. Although they considered the rocks to be ultramafic sills, Naldrett and Mason noted the possibility that they could be lavas of unusual composition. Following the proposal of the Viljoens that komatiites formed a distinctive group of volcanic rocks, Pyke et al. (1973) studied the Munro township flows in detail. Their classic paper, together with works by Viljoen and Viljoen, formed much of the basis for the future study and nomenclature of komatiite flows.

1.1.4 Modern work in the Abitibi

Pyke Hill komatiites have been sampled for a number of specialized geochemical studies, e.g., oxygen isotopes (Beaty and Taylor, 1982), Re–Os, Rb–Sr, and Sm–Nd isotopic systems (Walker et al., 1988), and Au and platinum group element abundances (Crockett and MacRae, 1986). Although detailed sampling was carried out at the location by Naldrett and colleagues, only partial analyses were published (Arndt et al., 1977). In terms of detailed study of individual flows in the Abitibi, Arndt worked primarily with komatiites and komatiitic basalts in northern Munro township (Arndt, 1975; Arndt et al., 1977) and in Dundonald township (Arndt, 1986a), and Barnes on flows at Alexo and in the Timmins area (Barnes et al., 1983; Barnes, 1985). Both authors' work at Alexo was somewhat hampered by middling quality of the exposure and (more critically) complex folding and faulting of the flow, as well as intrusion by the Dundonald sill. In addition, only one of seventeen analyses in Arndt (1986a) is from the B-layer. Work by Lajoie and Gélinas (1978) and Gélinas et al. (1977) on "Spinifex Ridge" in Lamotte township, Quebec, was hindered by the highly altered nature of the lavas (no primary mineralogy is preserved in these serpentine-chlorite-actinolite-magnetite rocks) and the authors' contestable interpretations of a number of structures (e.g., cross-bedding, within-flow brecciation, and multiple layering of size-graded crystals within B-layers). Such features have not been reported in other komatiites, and in my opinion some are of tectonic origin.

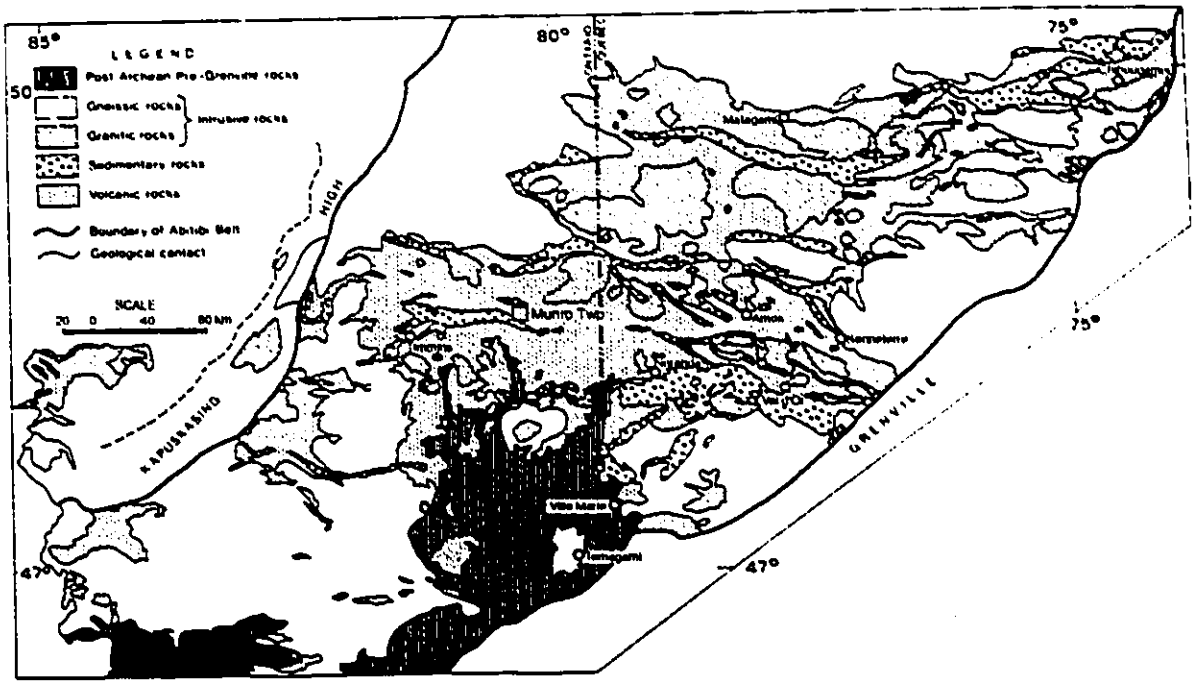

Fig. 1.2 Map of the Abitibi subprovince, 1:5 000 000 scale (after Jensen and Langford, 1985). Munro Township is indicated by the outlined square.

Fig. 1.3 Map of Munro Twp., redrawn from Ontario Ministry of Natural Resources 1: 100 000 scale forestry map. Not all trails are shown, and not all roads/trails are driveable. The visitor may wish to check the availability of up-to-date 1:20 000 scale maps at the local offices of the MNR. For a detailed, if dated, geological map see Satterly (1951). An open-file geological report by R. Johnstone may be available through the Ministry of Northern Development and Mines.

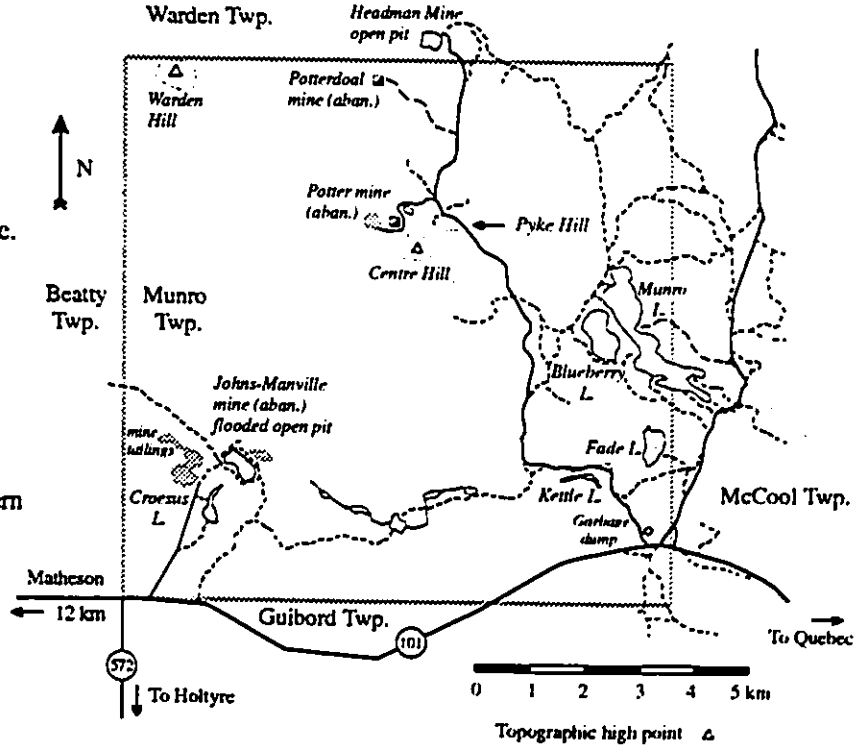

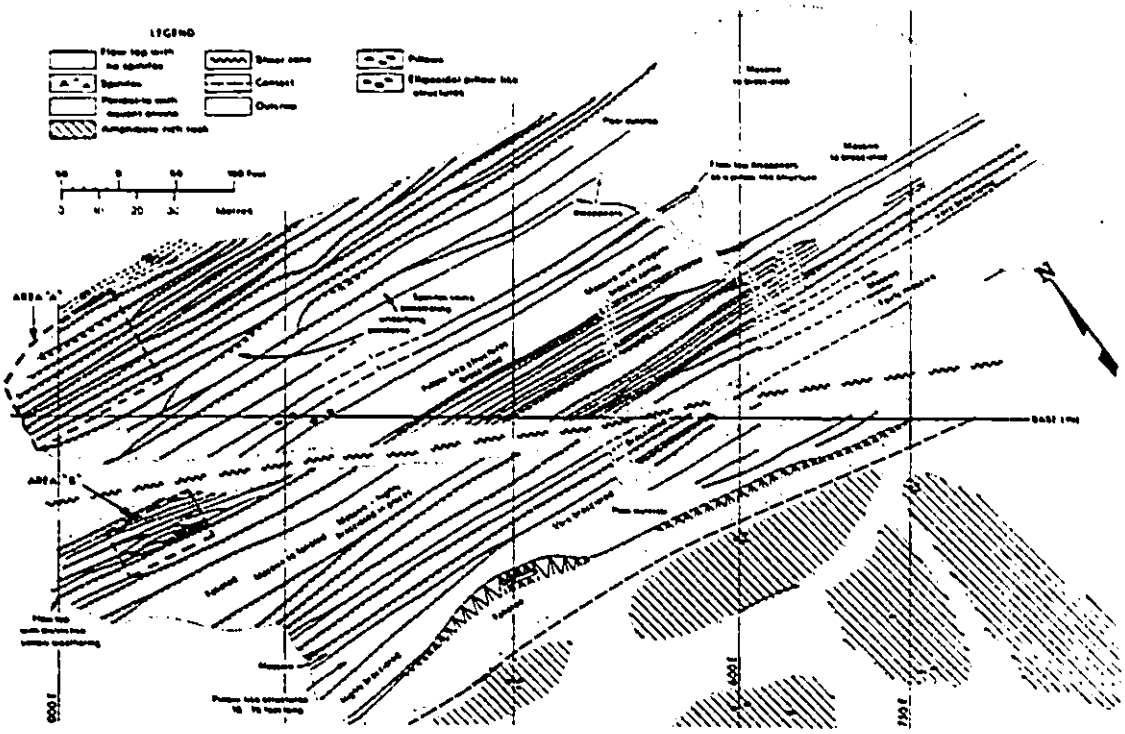

Fig. 1.4 Detailed geology of Pyke Hill, from Pyke et al. (1973). The western edge of the hill is the best exposed (possibly due to the acidic sulfide-rich tailings from the former Potter mine) and for this reason the areas A and B are the most frequently visited and studied parts of the exposure.

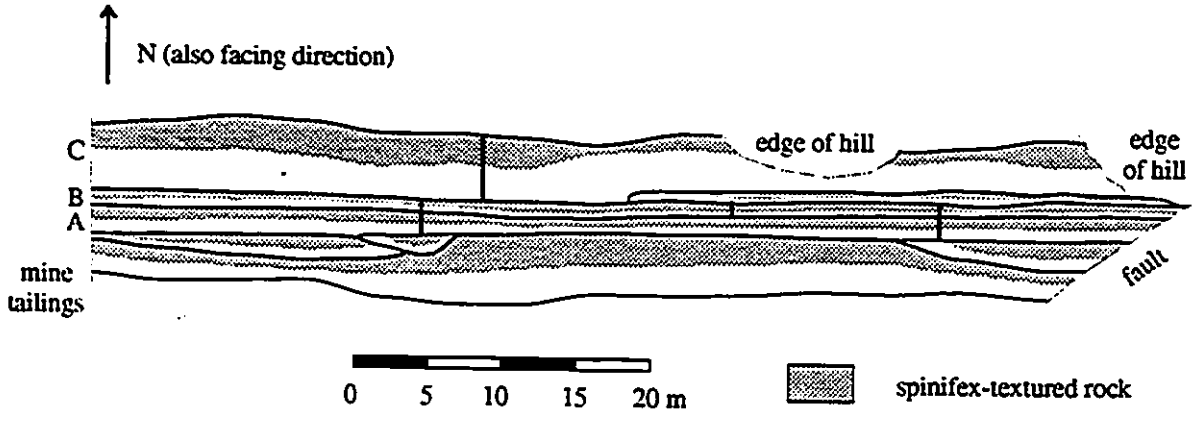

Fig. 1.5. Map of the spinifex-textured flows examined in greatest detail (N edge of area A of Fig. 1.4). Oriented samples for thin sections and geochemical analysis were taken across flows A, B, and C (thick vertical lines; see Appendix 7). Note, particularly for the three middle flows, the low thickness to width ratio (the length of these flows is unknown).

Photo 1.1 Looking eastwards towards Pyke Hill. The hill is covered by rather sparse stands of jack pine, but very little soil or weathering is present (weathered rinds are normally 1–2 mm thick, a stark contrast to the >30 m depths common in Western Australia). The light brown to red sands visible in the foreground are sulfide-bearing tailings from the Potter mine, a Cu-Zn mine which operated briefly in the 1960s. The tailings are oxidizing and give off noticeable amounts of SO_2; whatever may be said about the superb preservation and exposure of the komatiites, Pyke Hill stinks.

Photo 1.2 View looking west from the NW crest of Pyke Hill. Although several low hills are visible to the right (Warden Hill is in the far distance) the characteristic flatness of the Abitibi landscape is apparent. Green tones did not reproduce well, but the vegetation consists largely of black spruce, with lesser amounts of jack pine, birch, poplar, and tamarack. Bogs and marshes are quite common. The ~35 meter high timber headframe of the Potter mine is visible in the left middle distance.

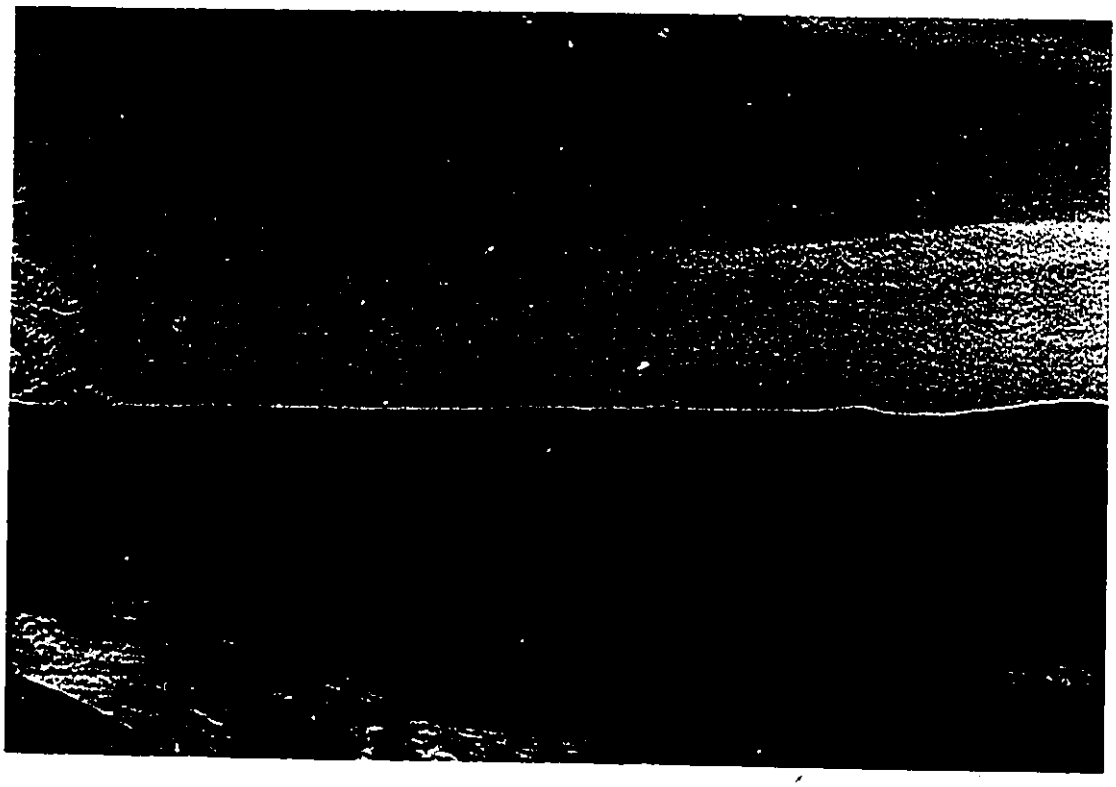

1.1.5 Work in Australia, southern Africa, and elsewhere

Outside of Canada, research into komatiites has been dominated by the study of occurrences in Zimbabwe, South Africa, and Western Australia. For example, Bickle, Nisbet, and colleagues have closely studied komatiites of the Belingwe belt, Zimbabwe, which include the freshest komatiites known (Nisbet et al., 1987). They have considered a broad range of topics including the petrogenesis of komatiites (Nisbet et al., 1993), the tectonic setting of greenstone belts (Bickle et al., 1994), as well as detailed descriptions of komatiite stratigraphy (Nisbet et al., 1977) and individual flows (Renner et al., 1994). In Australia, much of the research on komatiites has concentrated on geochemical or economic aspects of Ni mineralization. This is due in part to deep Tertiary weathering which generally restricts mapping and sampling to drill core or underground mine exposures. However, because rocks associated with ore deposits are studied with more than passing interest such work has been done in great detail, including ambitious integrated geochemical–volcanological–mineralogical models of komatiite eruption, flow, and crystallization (Lesher and Arndt, 1995; Hill et al., 1995). In the context of research on Australian komatiites the detailed petrographic work of Thomson (1989a, 1989b) on texturally well-preserved greenschist-facies komatiites from Kambalda is something of an exception.

Komatiites in smaller, more remote, or less-known greenstone belts have also been studied: e.g., the Cape Smith foldbelt of northern Quebec (Hynes and Francis, 1982), the Ottawa Islands in Hudson Bay (Arndt, 1982), the Baltic Shield (Barnes and Often, 1990), Brazil (Rivalenti et al., 1989), etc., but with the exception of Arndt (1982), these are generally geochemical studies of highly altered and strained rocks, and not useful for this particular study. The late Cretaceous komatiites of Gorgona Island, Colombia are an exception, fresh, undeformed, and located *in situ* on an oceanic island or fragment of an oceanic plateau (Echeverria and Aitken, 1986; Storey et al., 1991). However, a complete petrological study of these rocks has not yet appeared in the literature.

1.1.6 Brief discussion of komatiite petrogenesis

Because of their very high temperatures and high concentration of mantle-compatible elements, komatiites are considered to have formed as high-percentage partial melts of the mantle. Over the last two decades, the consensus has changed from favoring very high (>50%) degrees of partial melting at moderate depths (~50–100 km) to lower

degree partial melts that form at greater depths (150–300 km) (Herzberg, 1992). Their source may be thermal plumes formed at the core–mantle boundary and thus not representative of the Archean upper mantle (Nisbet et al., 1993; Arndt, 1994). Because of the low concentrations of incompatible elements in komatiites, the rock left behind after the extraction of a komatiite melt, at least at shallower depths (~200 km) would be a highly magnesian, ultradepleted dunite or harzburgite. Such mantle would be both buoyant and refractory, and is interpreted to underlie many Archean shields (e.g., Cox et al., 1987; Herzberg, 1993).

The overall impression given by geochemical studies is that komatiites form a relatively homogeneous group of rocks, perhaps more so than present-day mid-ocean ridge basalts. One would be hard-pressed to distinguish a typical late Archean komatiite flow from northeastern Ontario from a similar Australian or Zimbabwean flow on the basis of texture, mineralogy, chemistry, or age. Certain middle Archean (~3.5 Ga) komatiites from the Kaapvaal, Zimbabwean, and Pilbara cratons are notable for their relatively low Al_2O_3 content and heavy rare earth element (HREE) depletion with respect to the light rare earth elements (LREE). Such rocks have been termed "Al-depleted" komatiites (Nesbitt et al., 1979). [One might question why a primary chemical feature is called a depletion; Arndt (1994) suggested instead that the terms "Barberton-type" and "Munro-type" komatiites be used.] The lower Al content is considered a primary feature caused by partial melting at depths where HREE-compatible majorite garnet—or perhaps more accurately a solid solution of pyrope ($^{[8]}Mg_3{}^{[6]}Al_2{}^{[4]}Si_3O_{12}$), almandine ($^{[8]}Fe_3{}^{[6]}Al_2{}^{[4]}Si_3O_{12}$), and majorite ($^{[8]}(Mg,Fe)_3{}^{[6]}(Mg,Fe,Al,Si)^{[4]}Si_3O_{12}$)—is a residual phase. Certain authors have proposed that relatively small variations in the abundances of high-field strength elements in 2.7 Ga komatiites are of petrogenetic significance (e.g., Xie and Kerrich, 1994). However this thesis is not primarily concerned with either the tectonic setting or petrogenesis of komatiites, but rather the processes of crystallization and differentiation that occurred after a komatiite lava was erupted.

1.2 Textural and crystallization studies

1.2.1 Previous studies of komatiite cooling and crystallization

Donaldson has studied olivine crystal growth in detail (e.g., Donaldson, 1974, 1976, 1982). Much of his work was concerned with olivine crystal growth, habit, and chemical zoning in harrisite and lunar basalts, and so does not directly treat komatiites. However, some of the picritic compositions he investigated are reasonably close analogs to komatiites. Mineral compositions and phase relationships have been studied in detail, both at low and high pressures (e.g., Green et al., 1975; Arndt, 1976, 1977; Kinzler and Grove, 1985; Agee and Walker, 1990).

Huppert, Sparks, and their colleagues treated the subject of cooling and crystal growth in komatiites in a number of influential studies strongly based on fluid mechanics (Huppert et al., 1984; Huppert and Sparks, 1985a, 1985b, 1989; Turner et al., 1986). Their investigations into the potential physical consequences of the high temperatures and low viscosities of molten komatiites are highly innovative and could explain enigmatic features associated with many Ni-sulfide mineral deposits. However, it must be pointed out that they have developed detailed mathematical models for what is a poorly constrained physical problem. Certain textural features that should be common in komatiites if they generally behaved as theorized are actually rather rare. Contact relationships and trough-like structures in certain komatiite flows have been interpreted by Huppert and Sparks (and others) as primary features caused by thermal erosion. Such contacts can be equivocal in folded, faulted, and pervasively altered metavolcanic rocks (e.g., Cowden, 1988). Even if some of these features are primary, different interpretations are still possible: e.g., modern subaerial or submarine lavas commonly flow down pre-existing valleys or topographic lows.

The theoretically driven approach to understanding komatiite behavior tends to neglect more typical exposures as well as the general compositional uniformity of komatiites world-wide. Field evidence suggests that komatiites generally behaved as highly fluid basalts, rather than assimilating substrates in a "voracious" manner (the term is from Nesbitt, 1986). Evidence for more "normal" behavior includes komatiite flows that formed molds of underlying stromatolites (Byerly et al. 1986), the common preservation of lower chilled or glassy flow margins (Pyke et al., 1973; my work), and the extremely depleted incompatible trace element patterns typical of komatiites that would be sensitive to even

small amounts of crustal assimilation (e.g., Jochum et al., 1991; Shirey and Barnes, 1994). However, very detailed sampling programs of komatiites in the proximity of Australian Ni deposits has shown subtle but unequivocal evidence of some degree of assimilation of crustal or substrate material (McNaughton et al., 1988; Lesher and Arndt, 1995). In addition there is strong reason to believe that typical komatiites would contain only about 200–400 μg/g S (Section **3.2.4**). Economically mineralized flows contain far more than this amount, a gain that cannot be attributed to hydrothermal alteration.

1.2.2 Open areas of research

Few experimental studies of olivine growth in komatiites that include growth rates and habits have been conducted—Fleet (1975a) and Donaldson (1982) being notable exceptions—and a comprehensive study of the chemical composition of komatiitic olivines has not yet been carried out. One study of Cr-spinel composition and morphology has been carried out (Zhou and Kerrich, 1992); however several conclusions regarding the growth of such crystals can be disputed (see Section **4.2**). A satisfactory explanation for the dendritic morphology of Cr-spinel and augite several meters from cooling contacts, or the extremely fine-grained nature of plagioclase, where present, has not yet been offered. The processes leading to within-flow fractionation can be studied in greater detail, as can the low-grade hydrothermal alteration of well-preserved lava flows.

1.2.3 Problems with certain accepted ideas

Theoretical studies of komatiite substrate melting and assimilation, or turbulent within-flow convection (e.g., Huppert et al., 1984) have probably overemphasized the role of these processes in typical flows (Marsh, 1988, 1989; Davaille and Jaupart, 1993b). A number of related experiments are potentially flawed by quantitative or qualitative behavioral differences of analog materials (Section **5.3.2**). In komatiites, unequivocal evidence of melting and assimilation is rare, and in many flows no such evidence is found. Certain physical models involve geologically unlikely, or at least unusual, scenarios. A fundamental weakness of all quantitative thermal models is that the cooling effects of seawater under high pressure have been neglected. Whereas the conductive cooling of a thin, laterally extensive sheet of stagnant lava is a reasonably well-constrained Stefan-type problem, the effect of the convection of water and steam through a fractured flowtop, and continuing flow of lava beneath a solid crust can serve to make numerical modeling of

cooling little more than guesswork. If the basic physical premises of a numerical model are faulty, its mathematical rigor is clearly of little use.

Some recent work on komatiite petrogenesis is specialized or even speculative, e.g., the analysis of progressively less-abundant elements, the role of majorite garnet in variability of the concentration of REE and high field-strength elements, the potential of olivine flotation in a world-wide komatiitic mantle ocean, or the origin of komatiites at convective instabilities at the core–mantle boundary. Large experimental errors in earlier phase diagrams of peridotite at high pressures and temperatures recently noted by Zhang and Herzberg (1994) may act as a warning against overly ambitious modeling.

1.3 Objectives and original contributions of thesis

This thesis has as its aim the investigation of the cooling and crystallization of komatiite flows, and the relation of heat transfer to the morphology of crystals and within-flow chemical differentiation. As is not untypical in the Earth sciences, this has required study across a range of disciplines, comprising igneous petrology, mineralogy, physical volcanology, structural geology, crystal growth, and mechanisms of heat transfer. The techniques used include optical and scanning electron microscopy, X-ray fluorescence spectroscopy, electron microprobe analysis, and detailed field mapping. One advantage of such an approach is clear: by studying everything from cooling fractures in a flowtop to the crystal chemistry of Cr in olivine one obtains a broad view of the problems at hand, and becomes attuned to potential errors and inconsistencies in previous work. (The disadvantage is that one cannot become an expert in everything, so certain topics are treated shallowly or in passing.)

In this thesis I make several contributions to original knowledge. The geochemical analyses of the major, minor, and more-abundant trace elements of the Pyke Hill komatiites that I obtained are of extremely high quality, and rank among the best in the literature. The chemical variations I have measured within individual flows are consistent with the careful studies of other researchers (e.g., Arndt, 1986a), but by combining Pearce element ratio analysis with highly precise data I arrive at some unexpected but robust conclusions. I use both routine and high-precision electron microprobe data and crystal chemical considerations to explain the high concentration of Cr in komatiite olivines; again, the group of high-precision analyses are probably the best available in the literature.

I compare the zoning of olivine and the within-flow differentiation to what would be expected due to fractional crystallization of olivine.

Although highly competent petrologists have studied the textures of komatiites for decades (and I concur with many of their conclusions), I present significant new interpretations of the growth and chemistry of olivine and Cr-spinel. In addition, I point out the potential importance of such features as asymmetric alteration of flow margins (indicative of syn-volcanic hydration and contact metamorphism), and the presence of ~0.1 vol.% of ~100 μm diameter amygdules (indicative of both low $H_2O + CO_2$ contents and high confining pressures, i.e., >500 m water depth). I develop a comprehensive model of the serpentinization process, including explanations for the immobility of Mg and Si, the leaching of Ca, Na, K and Sr, and the occurrence of uniaxial expansion of up to ~25% that predated Kenoran deformation at 2700 Ma.

With respect to more theoretical considerations, I point out that detailed thermal models of previous researchers are seriously flawed in neglecting the propagation of a fracturing/cooling hydrothermal front. I propose that constrained crystallization, caused by large thermal gradients and the high lattice and radiant thermal conductivity of olivine was in large part responsible for the formation of spinifex texture. This millimeter to decimeter-scale texture so characteristic of komatiites likely arose through small temperature differences on the μm-scale of the leading tips of growing olivine crystals.

2 Physical volcanology of komatiites

2.1 Morphology and structures of flows

2.1.1 General characteristics of komatiite flows

Typical features of many komatiite flows include internal layering and the development of spinifex texture (discussed at more length in Section **3.1.1**). A complete list of research papers on aspects of komatiite flow morphology would be lengthy; important ones include Viljoen and Viljoen (1969), Pyke et al. (1973), Arndt (1975), Arndt et al. (1977), Donaldson (1982), Barnes et al. (1983), Barnes (1985), Arndt (1986a), and Thompson (1989a). A typical spinifex-textured komatiite may be divided into an upper spinifex-textured A-layer and a lower massive or cumulus-textured B-layer. Additional subdivisions are shown in Fig. **1.1** (after Pyke et al., 1973; Arndt et al., 1977). Komatiites also occur as massive, highly jointed flows, and as transitional combinations of the two forms.

Many of the flow morphologies found in komatiite flows elsewhere in the world are found at Pyke Hill. These include spinifex-textured flows containing the full range of internal subdivisions (i.e., layers A_1 through B_4), flows with thin spinifex-textured tops on much thicker massive bases, and massive, strongly fractured lava tubes. Some of the latter contain what appear to be drainage cavities near their centers (Photo **2.1**). Features that are not well developed or exposed at Pyke Hill include polyhedrally jointed massive flows, pillows, and tuffs. Polyhedrally jointed flows are found elsewhere in Munro Township and throughout the Abitibi (Photos **2.2** and **2.3**; see also Arndt et al., 1977). Well-formed pillows are uncommon in komatiites, but have been described in Zimbabwe and northern Norway (Nisbet et al., 1977; Barnes and Often, 1990). Pillowed komatiitic basalts are more common and are found, for example, in Roquemaure Township, Quebec, ~30 km east of Munro Township (Photo **2.4**). Pillow selvages in such lavas are commonly quite narrow; this is probably due to the rapid crystallization of highly magnesian liquids which thus form only thin glassy rinds (Section **4.2.5**). Komatiitic tuffs and other pyroclastic rocks are also quite rare, but have been reported at Steep Rock Lake, Ontario (Wilks and Nisbet, 1988), Norway (Barnes and Often, 1990), Ruth Well, Western Australia (Nisbet and Chinner, 1981), and Gorgona Island off the west coast of Colombia (Echeverria and Aitken, 1986). Reasons for the rarity of such features are discussed in Section **2.1.4**.

2.1.2 Shape and size of komatiite flows

Obviously no direct observations have been made of the eruption and flow of a komatiite. [For that matter, none have yet been made of an active eruption of any lava type on the ocean floor, although some flows have been examined within several days of their eruption (Haymon et al., 1993).] Because Archean lavas are variably exposed, metamorphosed, faulted, and deformed, and cannot be dated by high-resolution chronological methods such as U–Th decay-series disequilibria, magnetostratigraphy, or biostratigraphy, information must be obtained indirectly. Such features as the geographic extent of similar rock types (e.g., formations and groups, used less rigorously than in Phanerozoic sequences), flow thickness, flow morphology, vesicularity, thickness of chilled margins, facing directions, associated sedimentary or volcanic rocks, inferred tectonic setting, etc., all acquire more importance than they do in younger rocks.

Komatiite flows at Pyke Hill typically form wide, thin flows (Pyke et al., 1973; Arndt et al., 1977). Some flows are 1.2–1.5 m thick, and a minimum of 75 m wide (both the eastern and western ends disappear under cover). One flow with a fully exposed cross-section is 40 m wide, but has a maximum thickness of only 70 cm. I have found no directional indicators such as feeder dikes, branching lava tubes, budding pillows, or vesicle trains, nor do I know of any reported in the literature. For this reason the original direction of lava flow cannot be determined. At Pyke Hill, lava tubes and the terminal margins of spinifex-textured flows are symmetrical in cross-section. Flow may therefore have been approximately perpendicular to the plane of the exposed section (i.e., originally from the north or south, before the flows were folded into an east-west trending syncline). Several flows between 1–1.5 m thick, including those used as the type examples of komatiite layering (Pyke et al., 1973), have lengths of at least 100 m (the flows are covered by tailings to the west, and cut off by the north edge of the hill to the east). The lateral edges of individual flows range from rounded margins consisting of fractured rock in massive lava tubes and spinifex-textured flows (Photos **2.5** and **2.6**) to one sharply terminated flow with angles of ~30° (Photos **2.7** to **2.9**). The latter flow has a fully exposed width of 40 m, and a maximum thickness of 75 cm. The acute angle of repose is presumably due to an extremely fluid lava rapidly spreading and inflating beneath a cooled plastic skin. Even in the most fluid pahoehoe basalt, subaerial lava toes have considerably blunter, more-rounded terminations than this particular subaqueous komatiite. [Dr. N.T. Arndt has offered another explanation: that pressure due to the overlying flow could have collapsed the underlying flow margin while it was still plastic and partially molten.]

Estimates have been made of the width and lateral extent of komatiite flows in South Africa (Viljoen and Viljoen, 1969), Zimbabwe (Renner et al., 1994), and Western Australia (Hill et al., 1995). Areas in excess of several hundred square kilometers have been proposed for certain flows or flow units of modest (~10 m) thickness.

2.1.3 Jointing of komatiites

Massive flows (i.e., flows lacking spinifex texture) typically exhibit a characteristic polyhedral jointing pattern (see Photos **2.3** and **2.4**) sometimes termed "polysuturing". Such joints are primary and caused by thermal contraction during the crystallization and cooling of the lava body. The great majority of fractures are confined within individual flows and terminate at the upper or lower flow margin; fractures are also most numerous at the flowtop. The distribution and orientation of fractures in a massive komatiite lava tube at Pyke Hill is shown in Fig. **2.1**. This diagram—actually a very large-scale map— is of key importance in the modeling of the cooling of subaqueous komatiite flows. The fractures have a preferred orientation perpendicular to the margins of the tube that is quite different from the orientation of the few conjugate joints formed during north-south tectonic shortening. Spinifex-textured flows are also fractured and veined. Although it is more difficult to see fractures on the rough surface of spinifex-textured layers, in actuality they are somewhat less abundant than in massive flows. A consideration of the density of the crystalline rock (calculated as a mixture of olivine with a density of 3.35 g cm^{-3} and nonvesicular crystalline basalt with a density of ~3.0 g cm^{-3}) and the liquid (density of 2.75 g cm^{-3}) shows that a molten komatiite will contract by ~10–15 vol.% as it crystallizes and cools to ambient temperature. The most important shrinkage from the standpoint of fracturing and subsequent hydrothermal cooling occurs from 1000 °C to ~0 °C, where the solid rock would have contracted by ~3 vol.% (mineral expansivity data of Saxena and Shen, 1992). Flows are relatively thin and have a free upper surface, so vertical contraction is easily accommodated. However, bulk rocks have low tensile strengths and readily fracture under the large horizontal stresses induced by cooling.

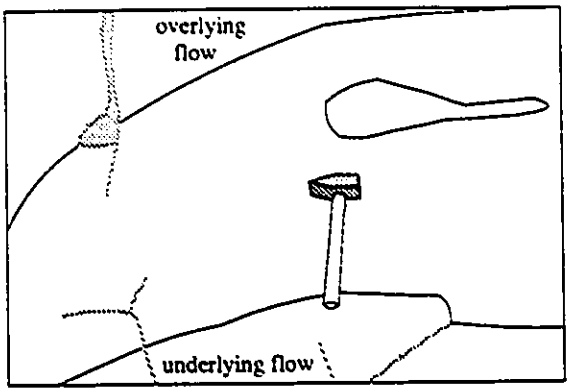

Photo 2.1 Photograph of part of a massive lava tube at Pyke Hill (area B of Fig. 1.4). The outcrop is a rounded dome, and there is no higher ground from which to get a picture of the entire tube. The profile of the tube resembles a flattened semicircle; the top of the underlying spinifex-textured flow is quite flat, but appears irregular because of the camera angle and ground curvature. The structure above the hammer head appears to be a drainage cavity that was subsequently refilled. Such structures are fairly common in basalts. Hammer is 38 cm long.

Photo 2.2 Massive, polyhedrally jointed komatiite flow in the Pontiac subprovince, 2 km E of Lake Opasatica, near Rollet (40 km SSW of Rouyn-Noranda along Hwy. 101). The flow consists of individual blocks of 20–40 cm size that are not displaced with respect to their neighbours. The flow is approximately upright,with the base of the hammer resting on the top surface of an underlying flow. The fractured blocks are smaller in size (5-10 cm) at the top of the flows. Hammer is 30 cm long.

Photo 2.3 Detail of polyhedral joints of flow shown in Photo 2.2. Serpentine has filled most of the joints, leaving the flow a tough, monolithic mass. Presumably the flow was a tightly-packed assemblage of individual blocks in the period shortly after it erupted and cooled. Syn- or post-volcanic ingress of water and expansion during serpentinization then knit (or sutured) the blocks together.

Photo 2.4 Komatiitic basalt pillows in SW Rocquemaure Township, Quebec (30 km east of Munro Township). Optical microscopy shows that the lava consists of ~40 vol.% serpentinized skeletal olivine in a chlorite-rich groundmass. The narrowness of the pillow selvages is likely due to the difficulty of quenching Mg-rich silicate liquids to glass. The lens cap has a diameter of 55 mm.

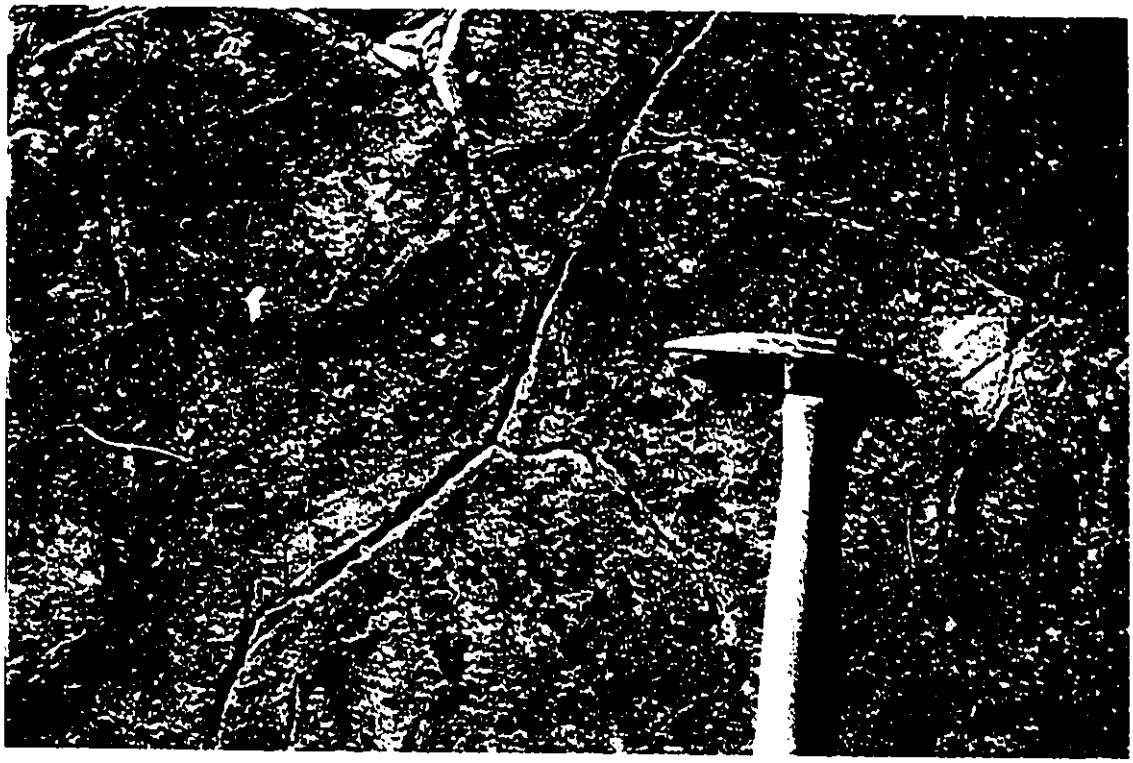

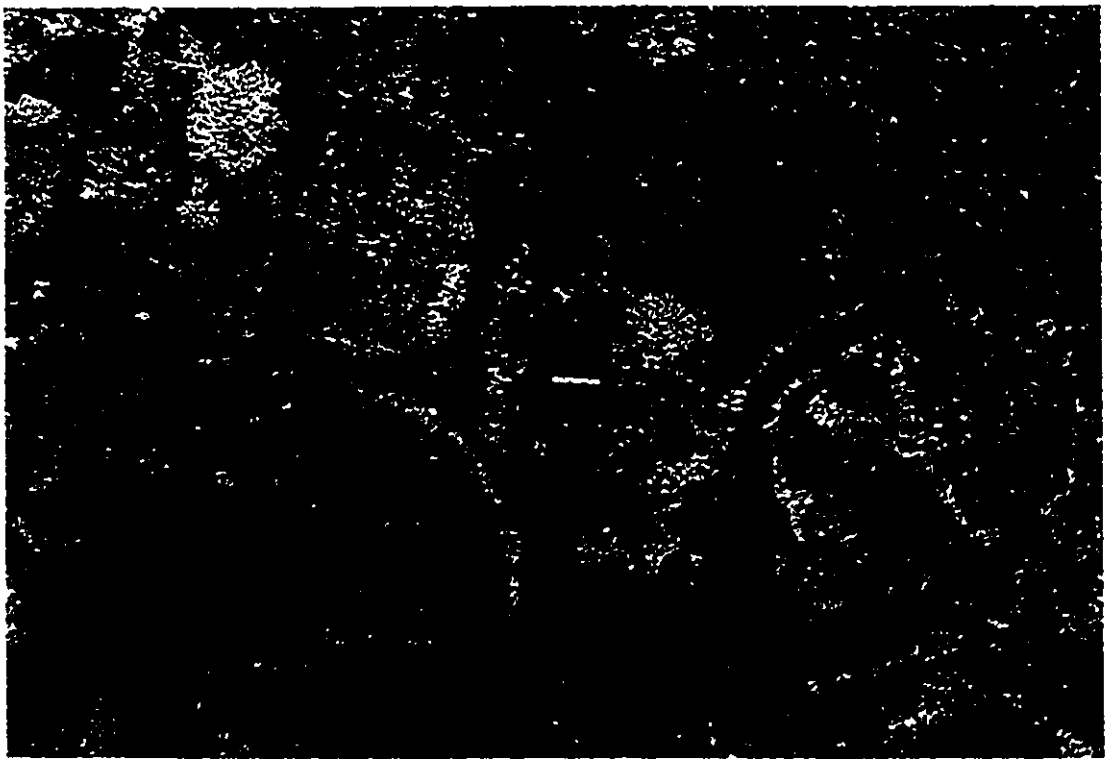

Photo 2.5 Margin of massive-textured lava tube at Pyke Hill (Area B of Fig. 1.4) Note the high standing angle of the terminal margin, and the presence of what appear to be multiple lobes (possibly breakouts of molten lava) separated by serpentine-filled fractures. The fractures, both in the lava tube and the overlying flow, are similar to those mapped in Fig. 2.1. Lens cap is 55 mm in diameter.

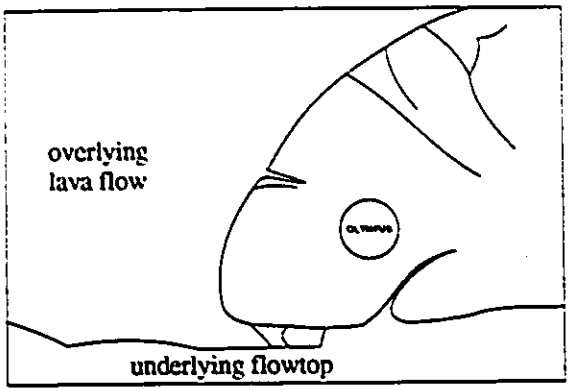

Photo 2.6 Blunt termination of spinifex-textured flow from Pyke Hill (area A of Fig. 1.4). Spinifex texture is not visible in photograph, but begins about 30 cm behind lens cap. The flow margin is highly brecciated, and could have acted as a levee damming the molten lava behind it. Compare to Photos 2.7 to 2.9. Looking east, facing direction is to the left. Lens cap is 55 mm in diameter.

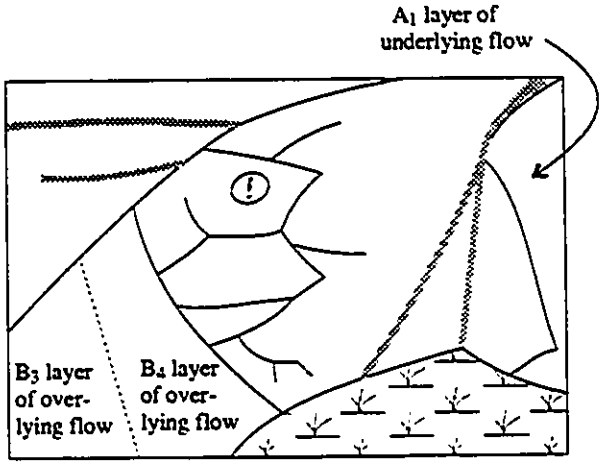

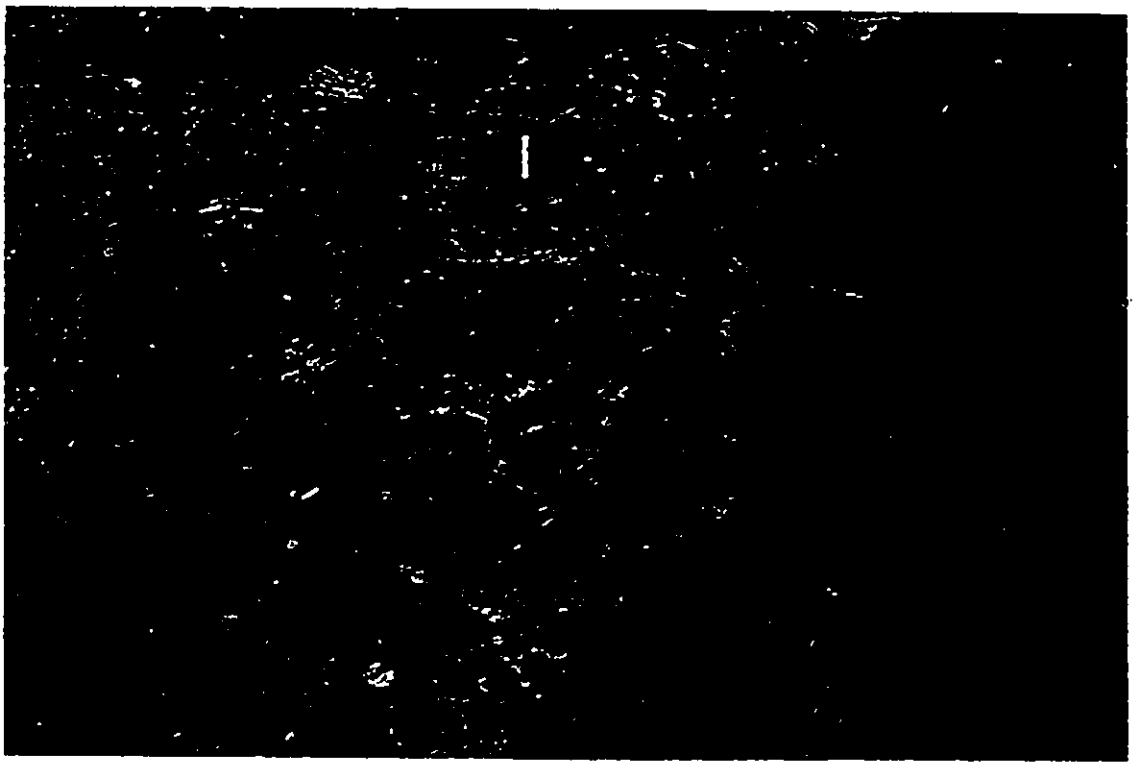

Photo 2.7 Termination of a thin spinifex-textured lava flow at Pyke Hill, looking west. This particular flow is exposed over its entire 40 m E-W width, but is never more than ~70 cm thick. The thin flow appears orange because it was stripped of vegetation and then scrubbed with bleach to remove lichen. It overlies the spinifex-textured flowtop of a thicker flow to the left, and is in turn overlain by the cumulate layer of another thick flow to the right. Note that the margin of the flow is not brecciated or rubbly, but simply pinches out at a ~30° angle to the paleohorizontal (see Photos **2.8** and **2.9**). Although the frame of the photograph is tilted slightly, the 75–80° northward dip of the lavas is evident in comparison to the horizon. Hammer is 38 cm long.

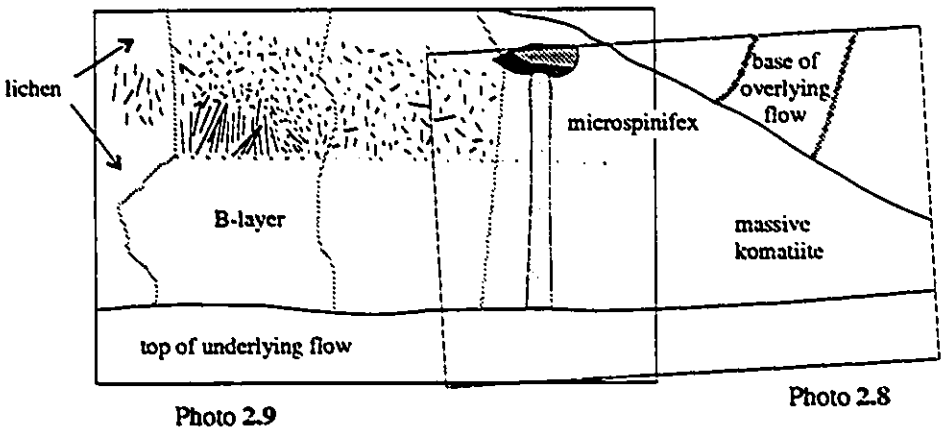

Photos 2.8 and 2.9 Close-up photographs of the flow pictured in Photo 2.7. Note the abrupt development of layering and spinifex texture less than 70 cm from the margin of a flow that is ~50 cm thick. The acute angle (~30°) the flow surface made with the paleohorizontal and the presence of microspinifex texture (rapidly transitional to coarse spinifex texture) indicate that the lava was fluid and largely aphyric. Compare to Photos 2.5 and 2.6. Hammer is 38 cm long.

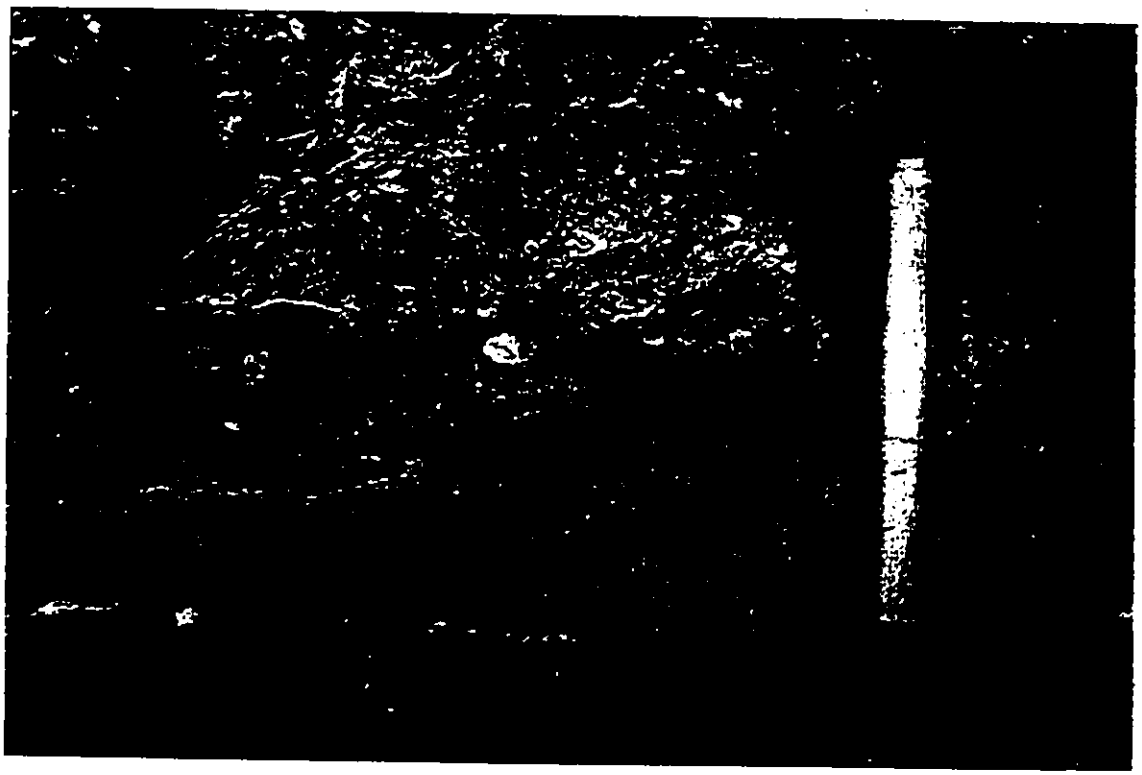

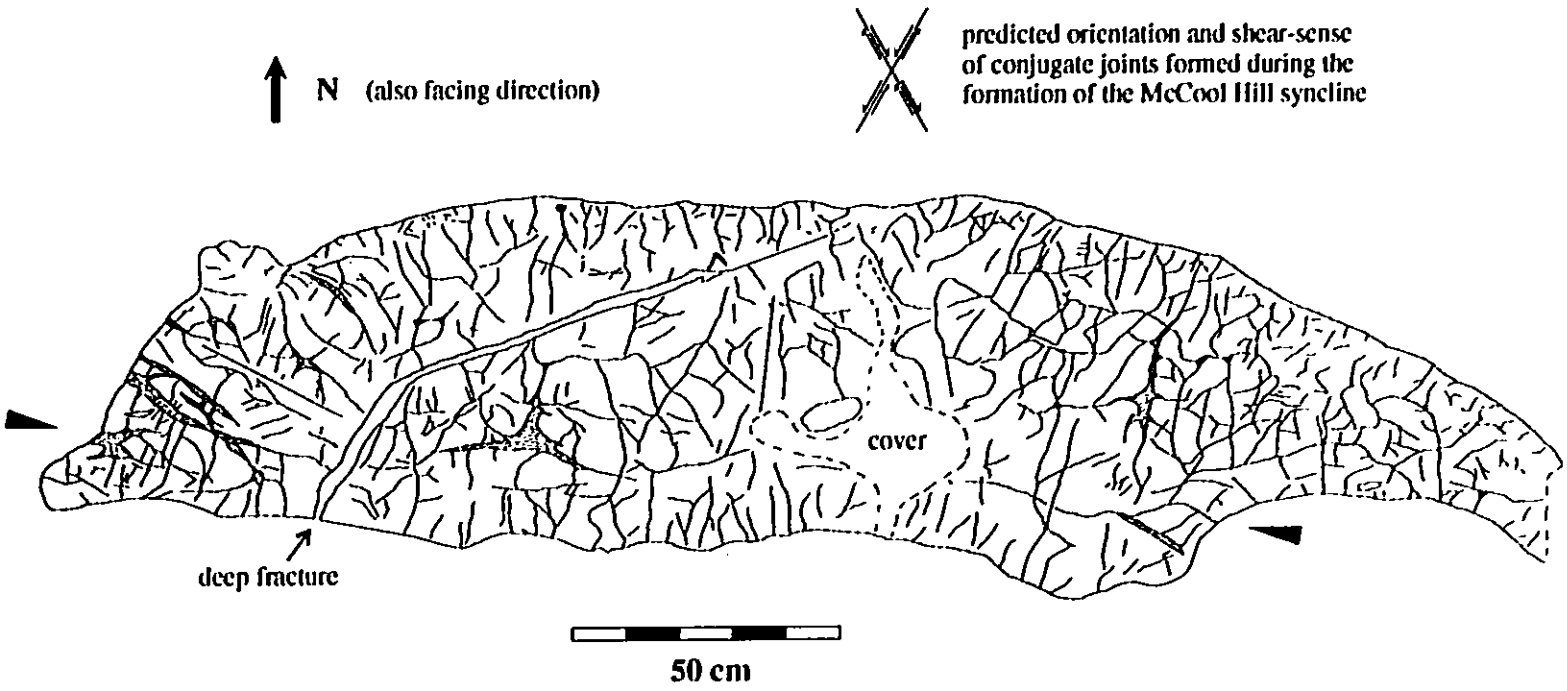

Fig. 2.1 Map of fractures in a massive komatiite lava tube from Pyke Hill (Area B of Fig. 1.4). Fracture widths are not shown except for the thickest serpentine or chlorite-filled veins (stippled fill), but range from ~2 cm to <10 μm. A rough estimate of the median width of the fractures is ~0.5 mm. The map was redrawn from a montage of 20 photographs of the outcrop. The irregular level of the base may indicate two closely timed surges of lava (pointers indicate the possible top of the first surge); a small lava bud occurs to the upper left.

Any fractures formed in the crust of a hot lava flow would allow the entry of cold seawater, further accelerating the cooling. This would lead to a self-propagating cooling/cracking front moving downwards through the flow (Section **5.2.2**). Such fracturing is not unique to komatiites; similar joints have been described in a number of basalt flows. The major distinction is that the volumetric increase and growth of secondary minerals during the serpentinization of komatiitic lavas leads to the suturing of adjacent blocks.

2.1.4 Amygdules, vesicles, and inferred depths of eruption

Introduction

Most known komatiite flows appear to have been subaqueous. Evidence for this includes their interlayering with pillow basalt, chert, or pelite, very low degrees of vesicularity, brecciated glassy flowtops, and the rare presence of hyaloclastites or komatiite pillows. The characteristic depth of eruption of komatiites, if there was one, is unknown. Komatiites interlayered with stromatolites in South Africa (Byerly et al., 1986), and others associated with cross-bedded quartz arenites in the Three Mile Lake greenstone belt, Ontario (Dr. J.A. Donaldson, personal communication), are likely to have erupted in or near shallow water. Characteristic features of Phanerozoic subaerial basalts, such as oxidized upper margins or the development of soils between flows, are rare or absent in Archean lavas because the atmosphere was less oxygenated and land flora and fauna had not developed at that time. However, vesiculation caused by the exsolution of dissolved gas under low confining pressure would occur regardless of the age of the lava. See Aubele et al. (1988) for a detailed discussion of the processes and characteristics of vesiculation in basalt flows.

Amygdules in Pyke Hill and other komatiites

Indirect evidence suggests that many komatiites were erupted into deep water. The Pyke Hill lavas contain up to ~0.2 vol.% of talc-filled amygdules within B_1 and B_2 layers. Most of these are sub-spherical and have uniform diameters of ~100 μm. The size of these amygdules is comparable to that of vesicles found in mid-ocean ridge basalt (MORB), typically between 5 and 200 μm in diameter. The amygdules have many points of similarity to unfilled vesicles in modern subaerial basalts (Photos **2.10** and **2.11**). Their walls are typically lined with very small oxide grains. Clinopyroxene crystals with former

melt adhering to their tips protrude slightly through the vesicle walls, and some vesicles appear to have been trapped beneath overlying olivine crystals. In certain uncommon cases, the upper portion of an amygdule forms an embayment in an overlying olivine crystal; the gas-filled vesicle presumably prevented growth or actively assisted in olivine dissolution via Marangoni-type convection (e.g., Donaldson and Henderson, 1988).

Renner et al. (1994) noted vesicles (amygdules, presumably?) in fresh komatiites from Zimbabwe that were of similar size and abundance to those in the Pyke Hill flows. Other komatiite flows in the Abitibi contain larger amygdules or vesicles. About 6 km south of Pyke Hill, altered komatiite flows in Guibord Township contain chlorite-filled amygdules up to 1 cm in diameter. The primary nature of these is made clear by the clustering of Cr-spinel crystals 10–20 μm in size at one end of individual amygdules. In a thin section I made of a sample from this flow, a consistent orientation is found in all eight amygdules that contain such crystals. Presumably the Cr-spinel grains collected on the molten interior surface of a vesicle through surface tension effects, and slid to its base. [This is probably one of the least useful field methods of determining facing directions ever proposed, so I will not insist that it be named after me.] Arndt (1986a) also described amygdules and vesicles filled with residual melt from the Alexo area. I also visited the Boston Creek komatiite in Boston Township 20 km SSE of Kirkland Lake. This 60–90 meter-thick komatiitic basalt flow contains well-developed clinopyroxene spinifex textures. The flow is interlayered with pillow basalts, and overlain by a finely banded chert (Photo **2.12**). The uppermost layer of the flow is highly vesicular, and contains trains of mm-sized vesicles (Photo **2.13**). The Boston Creek flow contrasts sharply with the brecciated, unsedimented, and vesicle-free flowtops typical of the Pyke Hill komatiite flows; the latter appear to have been erupted at greater depths, and/or had a lower volatile content.

Volatile content and eruption depth of komatiites

The significance of the very low vesicularity of the Pyke Hill komatiites is that the lavas must have been both volatile-poor and erupted at considerable depths. To illustrate, 0.1 wt.% of H_2O (a very low water content) exsolved from 1 cm^3 of lava at 1000 °C would occupy ~16 cm^3 at atmospheric pressure. Even at a water depth of 100 m, the gas would still occupy ~1.5 cm^3, corresponding to 60% vesicularity if no vapor escaped. Komatiites do not contain hydrous primary minerals and so the water content of the cooling liquid would have continued to increase until exsolution occurred. This should

have caused a significant degree of vesicularity in at least some interior portions of a flow (Aubele et al., 1988). [The solubility of volatiles increases with confining pressure, but not enough to significantly alter this conclusion.]

The argument that komatiites are weakly vesiculated because they were anhydrous (i.e., << 0.1 wt.% H_2O) is geochemically untenable. Hydrogen has a number of unique properties, but during partial melting it behaves as a relatively abundant, moderately incompatible trace element. Even such depleted rocks as normal MORB (N-MORB) typically contain 0.3–0.7 wt.% H_2O in fresh glass (Johnson et al., 1994), and assuming broad similarities between N-MORB and komatiites one might expect 0.1–0.2 wt.% H_2O in the latter. Recent measurements of the H_2O content of glass inclusions in komatiite olivines by McDonough and Danyushevsky (1995) support this estimate (~0.19 wt.% H_2O in undifferentiated melt).

A more reasonable hypothesis for the lack of vesicularity, if shallow water depth is assumed, is that komatiites lost most of their dissolved volatiles before cooling. This process would have been facilitated by the very low viscosity of molten komatiite. Such degassing has been observed in Hawaiian lavas erupted from Kilauea Volcano (Dixon et al., 1991), but it should be noted that even strongly degassed subaerial basalts commonly have scoriaceous or vesicular interior zones (e.g., Aubele et al., 1988). In addition, degassing in basalts is most complete in lavas that experience fire-fountaining and subsequent long periods of flow at low pressure. Realistically, these can only occur in subaerially erupted lavas. Because there is strong evidence that the Pyke Hill lavas were subaqueous, I favor a combination of high confining pressures and low concentration of volatiles to explain their sparse vesicularity. [Hyaloclastic komatiites that occur at Pyke Hill and Alexo did not require high volatile contents, simply water–hot rock interaction.]

Uncommon rocks such as komatiitic tuffs may have been erupted at unusually shallow depths. Others, such as the flows interlayered with stromatolites, may have degassed prior to solidification in shallow water. Most komatiites, however, appear to have been erupted into deep water (e.g., ~500 m or greater). The degree of vesicularity of a lava is only a qualitative measure of depth, and certainly does not permit a distinction between depths characteristic of a mid-ocean ridge, back-arc spreading center, seamount, or oceanic plateau (or even a deep continental rift). However, for the important purpose of estimating the heat transfer between seawater and hot rock, an order-of-magnitude estimate of depth is sufficient.

Photo 2.10 Photomicrograph of talc-filled amygdule in the B_2 layer of a 1.2 m thick Pyke Hill komatiite flow. Note the generally circular (spherical) shape of the wall, the fine layer of oxide crystals that collected on the inner surface, and the rounded tip of the augite crystal protruding into the amygdule. Field of view is 200 μm.

Photo 2.11 Vesicle of subaerial basalt flow erupted from Kilauea Iki in 1991. [The vesicle is filled with epoxy from the sectioning process.] Although the vesicles in this basalt can be much larger (up to 5 mm) and more irregular than the amygdules in komatiites, certain similarities exist., such as the coalescence of smaller vesicles and protrusion of augite (highly dendritic, in this case). Groundmass is nearly opaque, due both to a high content of submicroscopic Fe-Ti oxides and the fact that this section is 150 μm thick. Field of view is 200 μm.

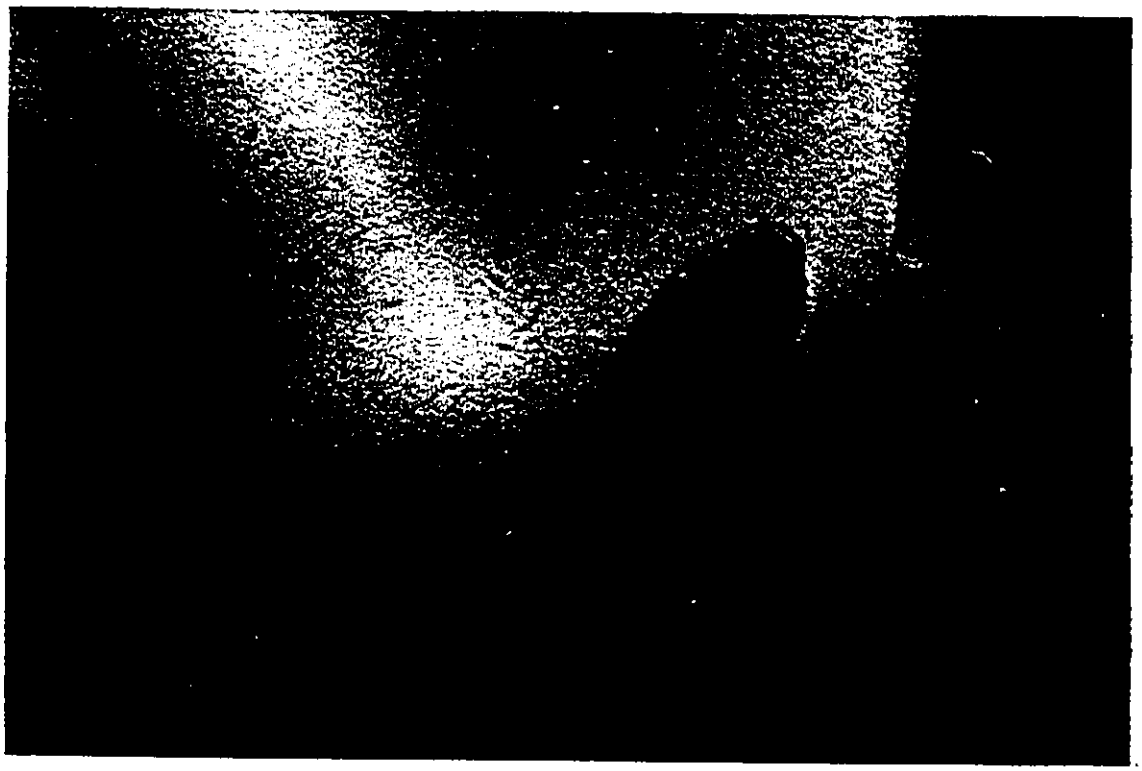

Photo 2.12 Top of Boston Creek komatiitic basalt flow, 3 km east of the small settlement of Boston Creek. The rocks are, from right to left: dense rock with medium-grained clinopyroxene spinifex texture (not visible in photograph); dark green aphanitic vesicular rock; lighter green (presumably more altered) aphanitic vesicular rock; a massive, reddish-brown weathering aphanitic rock (possibly an exhalite); a finely laminated grey chert; and an overlying basalt flow (barely visible). The hammer is 38 cm long.

Photo 2.13 Detail of the Boston Creek komatiitic basalt flowtop. The photograph is oriented with paleovertical upright. The green color did not reproduce well, but the dark spots are vesicles, which are aligned in trains. Such structures are rarely reported in komatiites. The lens cap is 55 mm in diameter.

2.2 Lava viscosity and flow morphology

2.2.1 Significance of viscosity

The most important factor controlling lava flow morphology is viscosity. Viscosity determines factors ranging from the rate of release of dissolved volatiles and thus in part the explosivity of a magma, the effusion rate during eruption, and the physical forms that lava will assume during eruptions (e.g., compare basaltic sheet flows to rhyolite domes). For a lava of a given composition and restricted viscosity range, an important dimensionless parameter is the ratio of the spreading rate under gravity to the solidification rate of the crust (Griffiths and Fink, 1992). Lavas that spread rapidly with respect to the rate at which they cool and solidify will tend to form thin, laterally extensive flows. Conversely, lavas that cool rapidly with respect to their spreading rates will form lava tubes or pillows.

2.2.2 Methods of calculating melt viscosities

To my knowledge no direct measurements of komatiitic liquid viscosities have been made. However the empirical method used by Shaw (1972) to calculate the viscosity of a silicate melt works well for relatively depolymerized liquids such as basalt and molten diopside. [Shaw developed an Arrhenian relationship of the form $\eta = \exp\left(m\left(T^{-1} + c_0\right) + c_1\right)$, where η is viscosity, T is absolute temperature, c_0 and c_1 are constants (for silicate melts), and m is a compositionally dependent parameter.] The calculated and measured viscosities of two liquids are shown in Table 2.1 and Fig. 2.2 (viscosities were measured with a precision of $\pm 10\%$ using rotating-cup viscometers). Huppert and Sparks (1985a) noted that Shaw's equation underestimates the viscosity of molten MgO–SiO_2 mixtures (given in Urbain et al., 1982) and recommended that the molar coefficient for Mg in the Shaw equation be changed. However, the effect of composition on viscosity is rather more complicated than modeled by Shaw or Huppert and Sparks. For example, at a given temperature the viscosity of molten $MgSiO_3$ is greater than that of $CaSiO_3$, but the viscosity of molten $MgAl_2Si_2O_8$ is less than that of $CaAl_2Si_2O_8$ (Urbain et al., 1982).

Table 2.1 Measured and predicted viscosity of two molten silicates

Halemaumau olivine tholeiite[1]			Diopside[2]		
Temperature (°C)	Measured η (Pa s)	Calculated η (Pa s)	Temperature (°C)	Measured η (Pa s)	Calculated η (Pa s)
1186	33.7	28.2	1402	1.16	1.14
1215	22.3	20.9	1540	0.399	0.462
1233	17.3	17.5	1672	0.198	0.221
1252	13.6	14.5	1781	0.123	0.129
1267	11.6	12.6	1857	0.091	0.091
1318	6.50	7.86	1931	0.070	0.067
1364	4.23	5.28	2039	0.051	0.044
1411	2.72	3.60			
1507	1.28	1.75			
1604	0.657	0.912			

[1] Shaw (1972).

[2] Urbain et al. (1982).

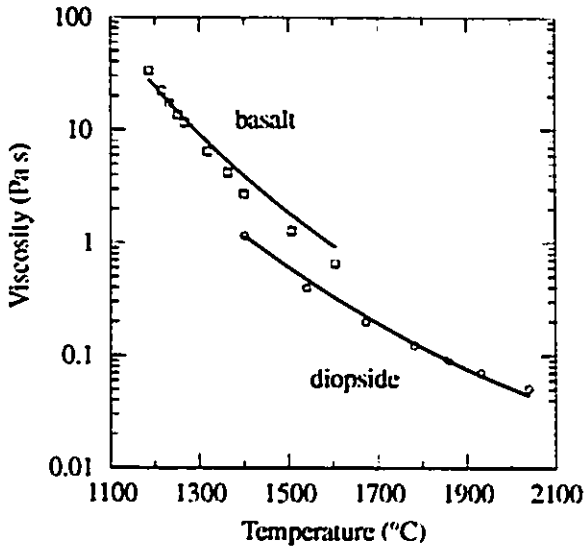

Fig. 2.2 Measured viscosities of basaltic and diopsidic liquids (data from Table 2.1). The viscosities calculated using the method of Shaw (1972) are plotted as solid curves.

In a multicomponent melt, in particular an aluminum and alkali-bearing one, the effect on viscosity of any one component can depend upon the particulars of the melt structure. For example, Al acts as a network modifier (i.e., depolymerizing agent) in alkali-free melts, but as a network former (i.e., polymerizing agent) in alkali-bearing ones. In the 5-component mixture of MgO, FeO, CaO, Al_2O_3, and SiO_2 that constitutes approximately 98 wt.% of a komatiite, it is likely that MgO, FeO, and CaO will have rather similar effects on viscosity. Among the minor constituents, only Na_2O and H_2O could have any appreciable effect on viscosity; however, due to their low concentration and the intrinsically depolymerized nature of a komatiite melt, their overall effect would be quite minor. For these reasons, I see little point in modifying Shaw's empirical equation for an improved fit to a few 2- or 3-component melts. A more accurate method for predicting molten silicate viscosity would require a detailed model based upon the structural chemistry of polymerized silicate liquids. This will not be attempted here.

2.2.3 *Viscosity and flow of komatiite lavas*

Using Shaw's method, the calculated viscosity of a fully molten komatiite lava containing 28 wt.% MgO and at a temperature of 1560 °C is 0.09 Pa-s. [Molten komatiite and room-temperature olive oil have identical viscosities, although other properties of the fluids differ significantly.] By comparison, field and laboratory measurements of typical near-liquidus basalts indicate viscosities of 20–50 Pa-s. Because silicate liquids crystallize as they cool, the effect of suspended crystals upon viscosity must also be considered. The empirical Einstein-Roscoe relationship for a liquid–solid suspension is $\eta = \eta_0(1-R\phi)^{-2.5}$, with η the effective viscosity of the suspension, η_0 the viscosity of the pure liquid, ϕ the volume fraction of particles, and R a factor dependent upon the shape and range of size of the particles, usually taken as 1.67 (McBirney and Murase, 1984). The very low viscosity of komatiitic liquid increases sharply with cooling and crystallization. The calculated viscosity of a crystal-free liquid and a crystal-bearing lava with progressive fractional crystallization of olivine is shown in Fig. **2.3** (see also Section **4.1.1**; Appendix **2**).

Simplistically, the low viscosity of komatiites should lead to thin, laterally extensive flow units, as is commonly observed. As flowing lavas cooled, the composition of the melt would have changed and the volume of suspended olivine crystals increased. The viscosity of the lavas would have increased and their flow structures become similar to those of basalts (e.g. pillows, lava tubes, shelves, drainage cavities, etc.) In fact, at ~1200 °C most basalts are fluid and largely crystal-free, but a komatiite would be a

viscous crystal-liquid mush. However, the height, surface area, and morphology of lava flows do not depend solely on viscosity, but are also functions of extrusion rate, topography, cooling rates (e.g., subaqueous vs. subaerial eruption), and volatile content (e.g., Griffiths and Fink, 1992). The range of flow shapes observed at Pyke Hill (and many other komatiite locales) is consistent with gravity flow of lavas of varying degrees of crystallinity down gentle slopes (<5°; possibly <1°). Given the relatively low viscosities of even partially crystallized komatiites, it is unlikely that much more than rubble or a thin brecciated crust would be left in place on steeper slopes (e.g., Tribble, 1991).

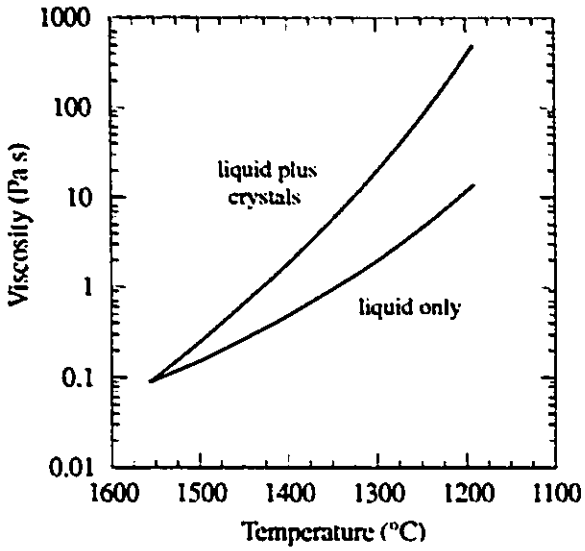

Fig. 2.3 Calculated viscosity of a komatiitic liquid (MgO=27.5 wt.%) with progressive fractional crystallization of olivine. The olivine and liquid compositions and temperature were calculated using iterative steps of 0.5 mol% olivine. The viscosity with and without suspended olivine crystals is calculated using the method of Shaw (1972). The large variation of viscosityover the range of olivine crystallization is evident. Because basaltic liquids have viscosities in the range 10–100 Pa s, cooled, partially crystallized komatiite lavas might have flow structures similar similar to those of basalt. Details of the calculations are noted in Appendix 2. [At 1200 °C the crystal-bearing komatiite lava contains ~40 vol.% olivine.] (Note: 1 Pa s = 10 poise.)

This creates some difficulties, because our primary source of information about the behavior of molten subaqueous lavas consists of observations of Kilauean basalts that, after flowing ~10 km to the sea, typically in closed lava tubes, spill down the steep (~30°) submarine flank of Hawaii (Moore, 1975; Tribble, 1991). Because of their steep slopes and limited effusion rates such lavas invariably form pillows or very narrow sheet flows. For this reason, and because such areas are hazardous, with downslope avalanches of hot debris, numerous hydrogen-oxygen explosions, and sharp blocks of vesicular lava that sink from the ocean surface (features vividly shown in underwater films of active flows), the detailed study of the cooling of a single tube or pillow is impractical. These lavas are

typically observed by scuba divers at 5–30 m depths, a fraction of the ~2.5 km depth of modern mid-ocean ridges. Because of the shallow water depth, steep topographic slope, and restricted nature of the observations, these lava flows are imperfect analogs of deep-water eruptions. Relevant observations of lavas erupted at mid-ocean ridges are discussed in Section 5.2.2.

2.2.4 *Physical and textural effects of lava flow*

A number of researchers have suggested that the development of spinifex texture would be inhibited in steadily flowing lava, and point to spinifex-free komatiite pillows, lava tubes, and massive flows; I would also add spinifex-textured flows with anomalously thin A-layers (i.e., A/B $<<1$). In such flows lava may have continued to flow beneath a rigid crust during cooling. The loosely packed, solid to somewhat skeletal equant olivine crystals found in massive flows are consistent with crystal growth in well-mixed silicate liquids; in such situations compositional and thermal gradients would have been minimized by flow of the liquid and the growth of equant crystals is favored (Baronnet, 1984; Tiller 1991a, 1991b).

The development of spinifex texture appears to be favored under many other circumstances, from the mm-size capsules of experimental petrologists to the cores of lava flows tens of meters thick. In the flow with the acute margin (shown in Photos 2.7 to 2.9) it is important to note that spinifex texture developed less than 0.5 m from the terminal margin of the flow. Thus the suggestion (e.g., Thomson, 1989a) that the development of spinifex texture required a flow to be dammed behind a breccia wall or lava levee is not correct. The less restrictive condition that spinifex textures formed during stagnation of komatiite flows (e.g., Arndt et al., 1977; Arndt, 1986a) cannot be determined by field studies alone.

Arndt et al. (1979) and Hill et al. (1995) held that the thickness, areal extent, flow morphology, and general paucity of interflow sediments indicated that typical komatiite lavas erupted in large volumes and spread rapidly. This is consistent with studies of basalt morphology (e.g., Baragar, 1984; Walker, 1992), observations of active Hawaiian flows (Hon et al., 1994), and theoretical analysis and experimental modeling of gravity currents in a solidifying material (Huppert et al., 1985a; Griffiths and Fink, 1992). However, simply because a solidified komatiite flow is tens of meters thick, hundreds of meters wide, and possibly tens of kilometers long does not mean that it ever existed as a fully-molten body

of that size. The careful observations of Hon et al. (1994) in particular, show that growth of basalt flows can be a slow, long-lived, and migratory process in which molten lava, under hydrostatic pressure and enclosed in a thin plastic layer of glass, inflates the center and elevates the surface of a largely solidified flow. Remarkably, Arndt (1982) envisaged that same process as having occurred in certain well-exposed Proterozoic komatiitic basalt flows in the Ottawa Islands, Hudson Bay. The implications of such lava transport mechanisms are obvious: Reynolds numbers of flows calculated using estimated lava thicknesses and viscosities and unknown paleoslopes and effusion rates may be little more than educated guesses.

This brings up the contentious point of whether the behavior of komatiite lavas was qualitatively different from that of other silicate lavas. Huppert et al. (1984, and numerous subsequent articles) suggested that komatiites, due to their low viscosities and high temperatures, flowed turbulently and could thermally and chemically assimilate their less-refractory wallrocks or substrates. Although the core idea is sound, many komatiites (including those at Pyke Hill) show no evidence of such behavior. Post-eruptive thermal assimilation would appear to require somewhat special circumstances, such as channeled flow of long duration above significantly less-refractory substrates. Certain economically mineralized flows or others with anomalous trace element content do show evidence of assimilation of other rocks. Certainly I know of no viable alternate theory to explain high magmatic concentrations of isotopically variable S in komatiite-hosted nickel deposits (e.g., Naldrett, 1989; C.M. Lesher, unpublished data, 1994), "contaminated" komatiites with anomalous REE concentrations and Nd isotopic ratios (Arndt and Jenner, 1986; Lesher and Arndt, 1995), or ocellar komatiites containing "xenomelts" of underlying sedimentary rocks (McNaughton et al., 1988). Such assimilation need not necessarily be post-eruptive, but could have occurred during contact with less-refractory wall rocks in dike, sill, or magma chamber walls. See Section **5.2.3** for further discussion.

3 Petrology of flows

3.1 Characteristic textures of komatiite flows

3.1.1 Spinifex texture

Even highly altered or deformed komatiites can preserve relict spinifex texture that is easily recognizable in the field. However, microscopic textures and primary minerals are obliterated in such rocks. Because altered komatiites are far more common than fresh ones, the origin and significance of spinifex texture were misinterpreted for several decades. Recognition of komatiites as a distinctive rock type coincided with a surge of interest in Archean geology and in textural features of magmatic rocks (sparked in large part by lunar rocks), and with the development of improved microanalytical techniques. The unusual morphology of the olivine, Cr-spinel, and clinopyroxene crystals in komatiite flows has attracted attention since well-preserved komatiites were first investigated nearly 30 years ago (e.g., Viljoen and Viljoen, 1969; Pyke et al., 1973). [In the subsequent sections I commonly use the terms skeletal, dendritic and spherulitic. Skeletal crystals have complex habits, with external faces of low Miller-index that are commonly discontinuous and multiply repeated, and that enclose large volumes of melt (relative to the size of the crystals). Skeletal crystals typically have hollow cores. A dendrite is a single crystal possessing an open, multiply-branching habit with crystallographic orientation maintained between different branches. A spherulite is a curving to radiating array of branches or fibers that commonly fan out from a common point; the fibers are typically elongated along identical crystallographic axes, the orientations of which gradually diverge.]

Macroscopic appearance of komatiite flows

As noted in Chapter 1, spinifex texture consists of skeletal to plate-like olivine crystals in a groundmass of dendritic or spherulitic clinopyroxene, dendritic Cr-spinel, and altered glass or intergrown plagioclase and pigeonite. Branching, coarsely acicular augite crystals in komatiitic basalts can form a somewhat analogous texture, but I will not discuss this. Olivine would have comprised about ~30–40 vol.% of an unaltered spinifex-textured komatiite, but because even the freshest Pyke Hill flows are partially serpentinized, olivine typically forms only 5–10% of the mode.

Spinifex texture occurs on a millimeter to meter-scale and is easily visible to the naked eye; in fact Arndt (1994) suggested that the term spinifex be reserved solely for such mesoscopic scales. I will show in Chapter 5 that the processes of heat flow and olivine crystallization that led to the formation of spinifex texture probably occurred on a much smaller scale. Others have proposed that different processes, such as double-diffusive convection (i.e., opposed thermal and compositional density gradients), are vital to the origin of spinifex texture (e.g., Turner et al., 1986). Regardless, a proper investigation of spinifex texture must begin with the basic mechanisms of crystal growth from silicate liquids (which I promptly defer until Chapter 5).

No detailed experimental studies of crystal habits and growth rates as a function of undercooling have been carried out for komatiites themselves. Instead, natural or synthetic terrestrial and lunar mafic volcanic rocks have been used as analogs. This is reasonable because many of the crystal habits of olivine in Mg-rich basalts or picrites resemble those found in komatiites. Clinopyroxene crystallizes from komatiitic liquids only after a significant degree (~45 wt.%) of olivine has formed. At that point the temperature, melt composition, and liquidus phases (olivine and Cr-spinel) are similar to those of magnesian basalts, and experimental results from such melts are likely applicable to komatiites. In support of this, a number of terrestrial and lunar basalts contain skeletal, dendritic, or spherulitic clinopyroxene closely resembling that found in komatiites. The predominant difference between such rocks and basalts containing more equant clinopyroxene and plagioclase crystals may lie in the degree and duration of superheating and concentration of crystal nuclei (Lofgren, 1983; Arndt, 1994).

The internal layering of spinifex-textured komatiite flows was reviewed by Donaldson (1982). Other detailed studies include Pyke et al. (1973), Arndt et al. (1977, 1979), Arndt, (1986a), Thomson, (1989a, 1989b), and Renner et al. (1994). I summarize the observations, beginning from the topmost layer. [For brevity I refer to the original magmatic phases, not the present altered assemblage.] The A_1 layer is a flowtop breccia consisting of cm-size, rounded blocks and globules of chilled lava, commonly containing equant phenocrysts of olivine (many with dendritic overgrowths) set in a groundmass of skeletal olivine and glass. Over a distance of 5–15 cm, with a progressive decrease in the concentration of fractures and an increase in the grain size of the skeletal olivine, it grades into the A_2 layer. This layer consists of randomly oriented, plate-like skeletal olivine crystals (typically 0.2–2 cm in maximum length) set in a groundmass of dendritic to spherulitic augite, Cr-spinel, and glass. Over a distance of 10–50 cm, with progressive

increase in the size and parallelism of olivine crystals, the A_2 layer grades into the A_3 layer. This layer consists of large (20 cm to >100 cm in size) sheaves of hundreds or thousands of subparallel olivine crystals with pronounced plate-like habits. The sheaves are generally oriented approximately perpendicular to the upper surface of the flow. In many flows the A_3 layer terminates abruptly against the B_1 layer, which contains a mixture of finer-grained plate-like and equant olivine crystals, commonly aligned parallel to the upper surface of the flow. With a sharply gradational decrease in the concentration of the plate-like crystals, the B_1 layer grades into the B_2 layer, which consists of loosely packed olivine crystals (0.3–1.0 mm in size) in a fine-grained groundmass of augite, pigeonite, and minor glass and Cr-spinel. Underlying this, a 10–20 cm thick layer (the B_3 layer) containing subspherical clots of crystals that stand out in relief on weathered surfaces (knobby weathering) is commonly present in the Pyke Hill flows. About 10 cm above the flow base, a sharp transition back to smooth-weathering surfaces marks the top of the B_4 layer, which typically has a very fine-grained or glassy basal layer somewhat similar to the upper chill but thinner. Typical komatiite textures and structures are shown in Photos **3.1** to **3.4**.

Photo 3.1 Characteristic development of internal subdivisions in a Pyke Hill komatiite flow. On the right edge are the A_2/A_3 layers (randomly oriented and coarse oriented spinifex), which make an unusually abrupt transition to the highly jointed A_1 layer. To the left (stratigraphically above) of the A_1 layer and flowtop is the ~10 cm thick B_4 layer (basal cumulate) of a subsequent flow. The lens cap lies on the B_3 layer (knobby cumulate) of that flow. Outcrop surface is orange because it was scrubbed with bleach; note the blue-black color of the broken rock. Lens cap is 55 mm in diameter.

Photo 3.2 This 1.5 m thick Pyke Hill flow exhibits a sharp undulatory contact between the A_3 and B_1 (aligned skeletal olivine) layers. The B_1 layer is unusually thick in this section of the flow; its sharply gradational contact with the underlying B_2 layer is clearly visible. Less visible but of potential importance to hydrothermal cooling are the fine fractures and serpentine-filled veinlets that cut the rock. The coin is 27 mm in diameter (the loon is properly oriented with respect to paleohorizontal).

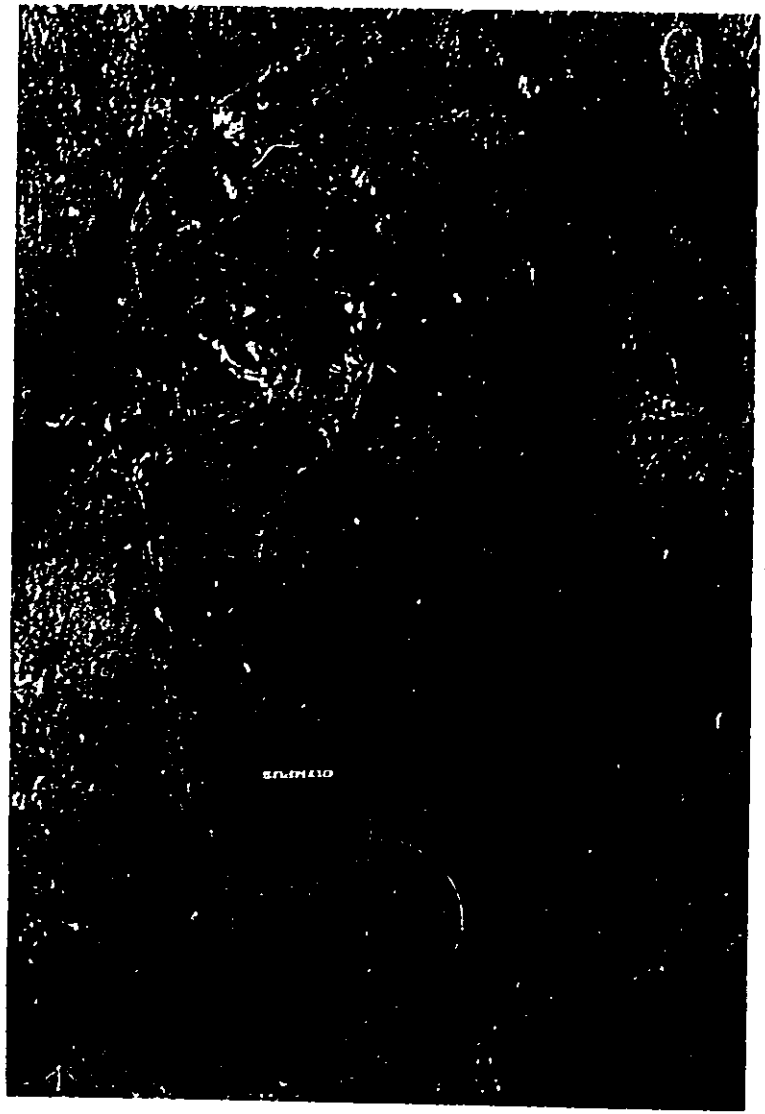

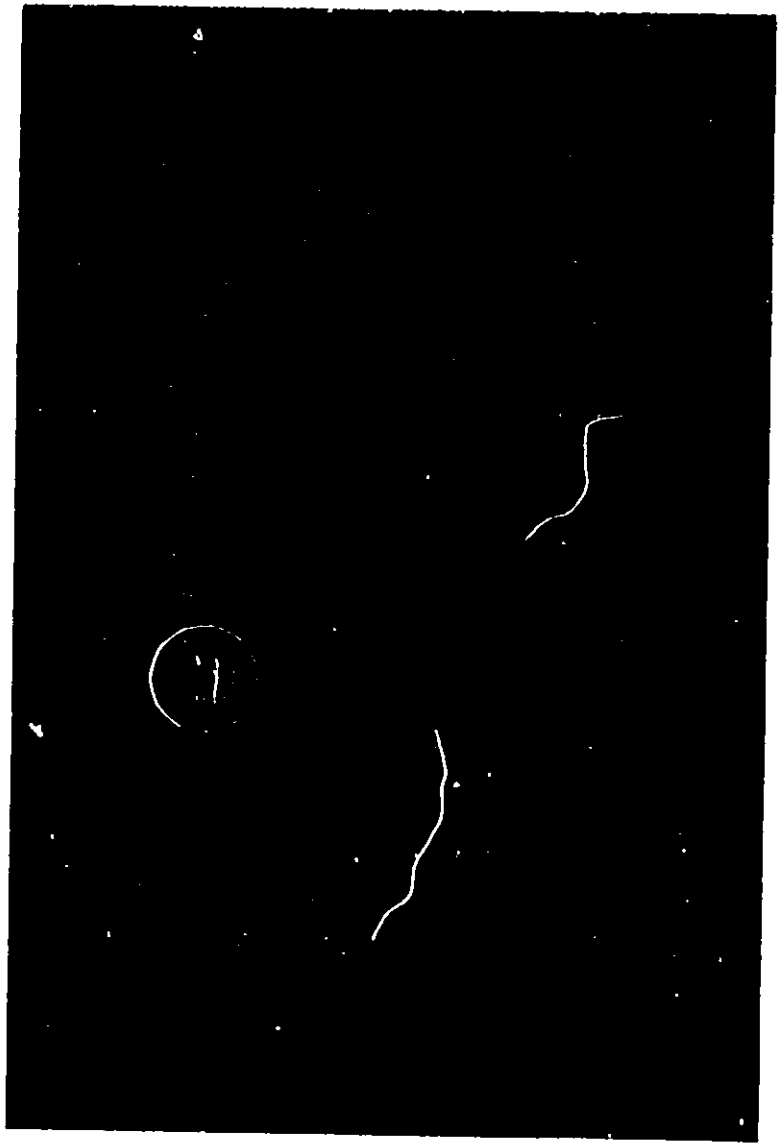

Photo 3.3 Detailed photograph of the A_3/B_1 contact of a 1.2 m thick flow at Pyke Hill. The finely ribbed appearance of the A_3 layer is due to differential weathering of partially serpentinized olivine and mostly unaltered augite-rich groundmass. The A_3/B_1 contact was undulatory at this spot; the waterline on the coin is parallel to the upper and lower flow surfaces. This texture is strongly indicative of flow-induced alignment of crystals late in the cooling and crystallization of the lava.

Photo 3.4 A spinifex-textured "vein" (or more precisely, a small sill) intruding the B-layer of a thick flow at Pyke Hill. One 4 cm thick spinifex-textured dike that I sampled contained a miniature version of the layering found within flows, with a 5 mm thick layer of equant olivine crystals overlain by plate-like olivine crystals. The illustrated sill, however, seems to consist entirely of spinifex-textured material. The B-layer rock must have been relatively cool to undergo brittle fracture; thus a komatiitic magma intruding the fracture may have been strongly cooled by conduction through both the upper and lower surfaces. The asymmetric structure of most komatiite flows may arise both from the greater cooling of the upper surface, and the gravity settling of equant olivine crystals interfering with the growth of oriented crystals below. The magma was presumably poor in olivine phenocrysts when it intruded the fracture. Because of the uniqueness and prominence of this sill (near the most-visited area of Pyke Hill) I did not sample it.

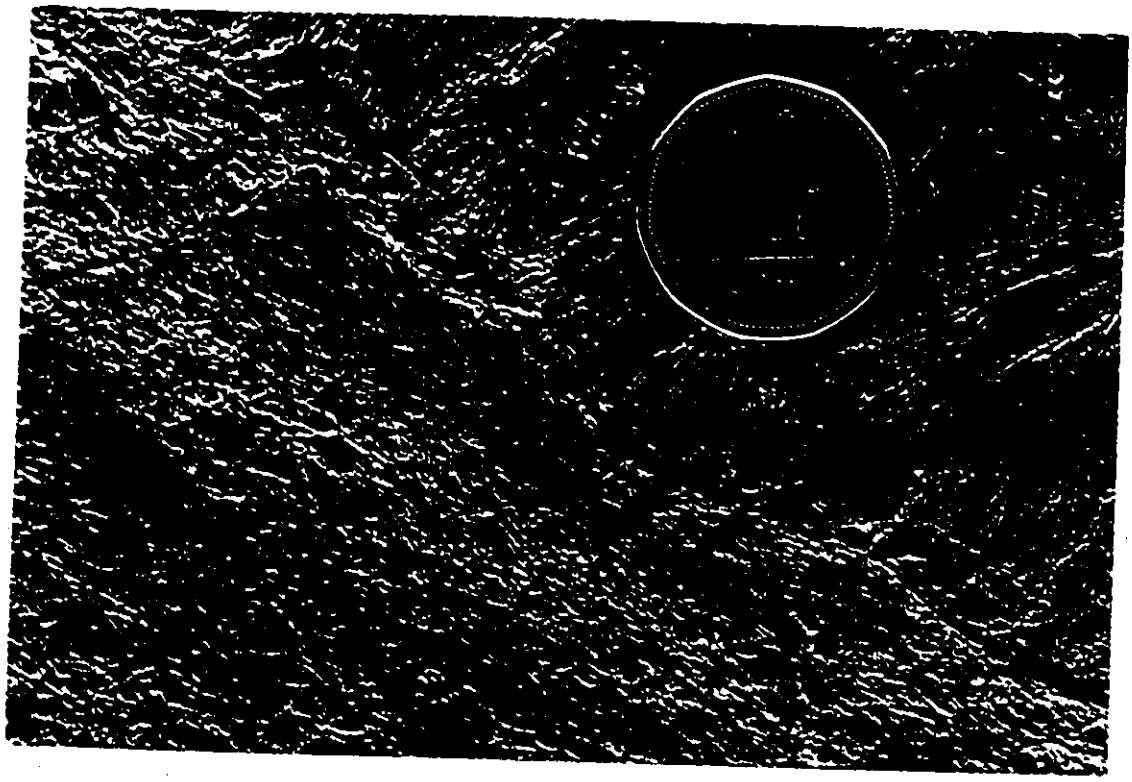

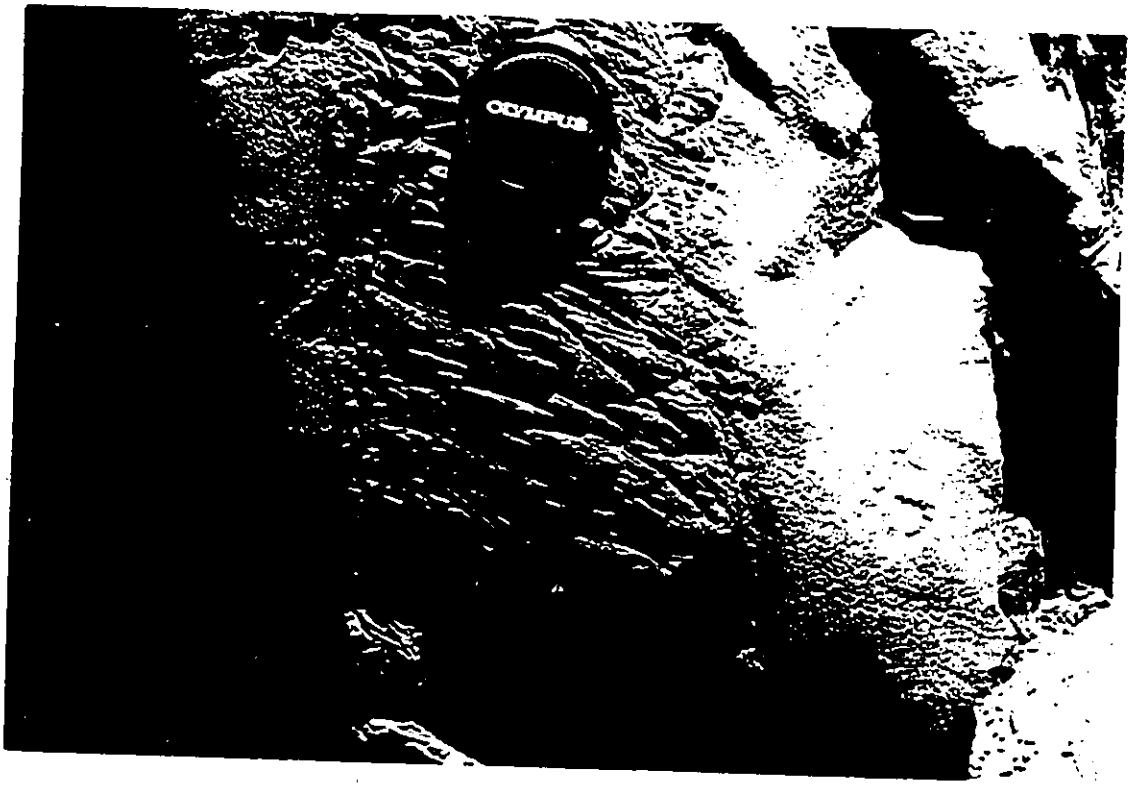
OLYMPUS

3.1.2 Olivine crystal habits

Introduction

The crystal habit of olivine in spinifex-textured komatiites, particularly within A_3 layers, is strongly non-equidimensional, with crystal dimensions much greater parallel to the *a* and *c* crystallographic axes than parallel to *b*. [Throughout this work I follow the mineralogical rather than the crystallographic convention for olivine: i.e., space group *Pbnm* with $a = 4.75$ Å, $b = 10.19$ Å, and $c = 5.98$ Å, instead of space group *Pnma* with $a = 10.19$ Å, $b = 5.98$ Å, and $c = 4.75$ Å.] Occasionally the incorrect term "acicular" (i.e., needle-like) is used to describe the habit of these crystals; the correct terms are tabular or plate-like. Although the largest such crystals I have observed are ~600–800 μm thick ($\| b$) and 5–10 cm long ($\| a$ or c), dimensions 2 to 3 times greater have been reported (Donaldson, 1982). Reports of much larger olivines may be due to a failure to distinguish between closely spaced *en échelon* crystals.

Researchers have studied the habit and growth rate of olivine from mafic liquids in varying detail (e.g., Drever and Johnson 1957; Green et al., 1975; Donaldson, 1976; Donaldson 1979; Kirkpatrick et al., 1981). A broad conclusion of these studies is that olivine, due to its simple close-packed structure of $M^{2+}O_6$ octahedra and non-polymerized SiO_4 tetrahedra (Fig. 3.1), grows more rapidly at a given undercooling than do more structurally and chemically complex silicates. Fleet (1975a) suggested that the relatively sluggish growth of olivine parallel to the *b*-axis was caused by protosite geometry; i.e., whereas constituent cations (e.g., Mg^{2+}) or anions (SiO_4^{4-}) can be added one-by-one to {021} or {110} faces, during growth on {010} the formation of alternate M2 protosites requires the correct orientation of three independent SiO_4 tetrahedra (Fig. 3.2). This is potentially a rate-limiting step during rapid growth of olivine from Mg-rich silicate melts and hence growth parallel to *b* is suppressed. [This hypothesis is, however, difficult to test; perhaps a molecular dynamics simulation of olivine crystallization could be attempted.] In contrast, olivine grown more slowly (i.e., at smaller undercoolings) adopts an equant habit that minimizes surface energy, implying interface-controlled growth. To quote directly from the comprehensive experimental study of Donaldson (1976) on the crystal habit of olivine: "The larger the olivine content of the melt, the slower the cooling rate at which a particular olivine shape grows." This can be understood in terms of the interplay between temperature, olivine solubility, chemical diffusivity, and the crystal–melt interface. Magnesium-rich melts have high concentrations of olivine constituent elements and

relatively high chemical diffusivities, which minimize the growth-limiting effects of chemical diffusion. Such melts are weakly polymerized, a factor that could reduce the average crystal–melt interfacial energy and thus permit the formation of crystals with large surface areas.

With the exception of two unusual crystal morphologies ("swallow-tail" and "radiating spherulitic"), all of the olivine crystal habits in Donaldson's classification system (Donaldson, 1976, 1982) are found in komatiites. In the A_3 layer, several habits can be found within a single thin section. Highly disequilibrium textures such as feather olivine can be found alongside relatively thick, plate-like, generally non-skeletal olivine crystals. Rather than using terms such as master and secondary blades (e.g., Thomson, 1989a), I will simply note that olivine crystals in close proximity may have grown at different times and rates. In such cases the larger, thicker crystals presumably began growing before the smaller crystals.

Dendritic and skeletal olivine crystals

Chilled margins commonly contain large equant olivine crystals set among much finer-grained skeletal olivine in glass (Photo 3.5). Serpentine or chlorite pseudomorphs after dendritic olivine crystals can be found within the outermost ~1 mm of well-preserved glassy chill margins (Photo 3.6). The olivine presumably grew by branching along favorable crystallographic directions but because of complete serpentinization these directions cannot be determined. The olivine dendrite axes are quite straight, in contrast to the highly curved augite dendrites elsewhere in the flows. Within ~1–2 cm of a flowtop, still in the A_1 layer, olivine crystals achieve lengths of 100–200 μm. Although such crystals typically have hollow cores and rounded interior embayments, their exterior faces are well-formed and sharply planar.

From the study of well-preserved olivine crystals in various orientations, it appears that {021} and {120} were the most rapidly growing faces. The common occurrence of isolated U and H-shaped crystal sections (Fig. 3.3; Photo 3.7) indicates that growth on {021} faces was faster in the [100] direction than towards [001], and that growth on {120} faces was faster in the [100] direction than towards [100] (Fig. 3.4). In larger olivine crystals from A_3 layers, well-formed 20–50 μm {041} faces occur at $\{021\}\wedge\{0\bar{2}1\}$ or $(010)\wedge\{021\}$ intersections (Fig. 3.5). It is possible that these {041} tips only formed during the final stages of olivine growth. However, if they were present throughout olivine

growth then the re-entrant formed by the intersection of the {021} and {041} faces would have acted as an edge lowering the kinetic barrier for the nucleation of new 2D growth layers. The effect on growth rates might be comparable to that of a screw dislocation or twin planes (e.g., Baronnet, 1984; Tiller, 1991a).

Renner et al. (1994) pointed out significant textural differences between the upper and lower chilled margins of certain extremely fresh komatiite flows near Zvishavane, Zimbabwe. [All of their observations apply equally to the Pyke Hill lavas.] The upper chill is brecciated and consists of a once-glassy groundmass that is now serpentinized (even in these otherwise fresh flows), and contains olivine microlites that are noticeably more skeletal and less numerous than those of the lower chill. Olivine phenocrysts also tend to have fine skeletal overgrowths in the upper chill, but this feature is much less common in the lower chill. Renner et al. suggest that these differences could have originated if the lavas were subaerial and the flowtop (in air) cooled more slowly than the base (against underlying rock). They suggest (p. 396): "Thus the faster cooling rates in the lower chills would have led to homogeneous nucleation of numerous small equant microlites, whereas the slightly lower cooling rates experienced by the upper chills led to the growth of less numerous skeletal hopper crystals." However, I think this interpretation is most likely incorrect, for the following reasons:

(1) The Pyke Hill lavas, which almost certainly were subaqueous flows, have identical textures. [I include the presence of brecciation, as well as sparse small vesicles or amygdules that I consider to signify eruption in deep water; see Section **2.1.4.**]

(2) In silicates the presence of a glassy groundmass is more characteristic of fast cooling rates than slow ones; the same applies for the presence of skeletal mineral overgrowths.

(3) Had the lowest part of the basal chill cooled more quickly, an upwards transition to textures resembling those of the flowtop would be expected.

(4) The cooling of the outermost few millimeters of subaerial basalts occurs largely through radiation and is quite rapid, probably exceeding the cooling rates at the base. Thus glassy flowtops are common in subaerial Hawaiian lava flows; glassy flow bases are less widely reported. This would be especially true of much hotter komatiites, which also have very thin (1–2 mm, compared to the 1–2 cm of typical basalts) glassy rinds due to the rapidity of olivine nucleation and growth in ultramafic liquids.

All of the observed features are consistent with more *rapid* crystallization of the upper chill, most likely due to quenching in deep water.

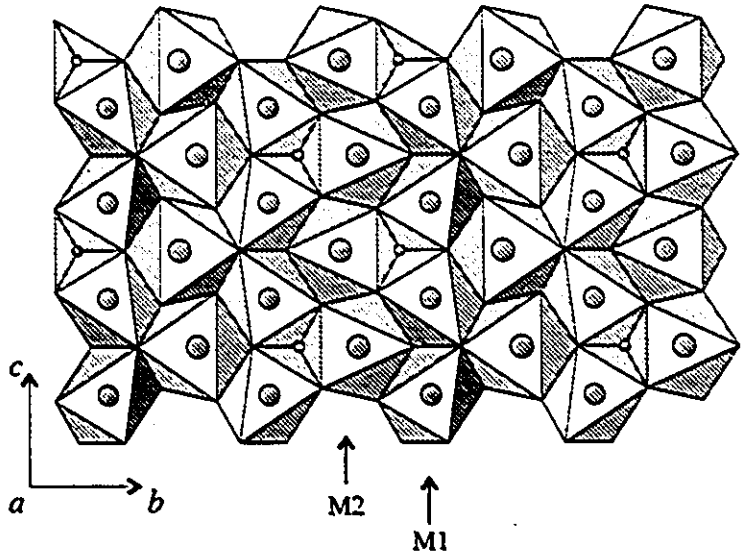

Fig. 3.1 Cystal structure of olivine, shown in pseudo-3D aspect. The mineral consists of edge-sharing chains of M1 and M2 octahedra. The SiO_2 tetrahedra are not linked to each other. The olivine structure resembles a distorted form of hexagonal close-packing. Its comparatively simple structure helps account for the rapidity of its growth in ultramafic liquids. Data used to make this figure are taken from Brown (1982).

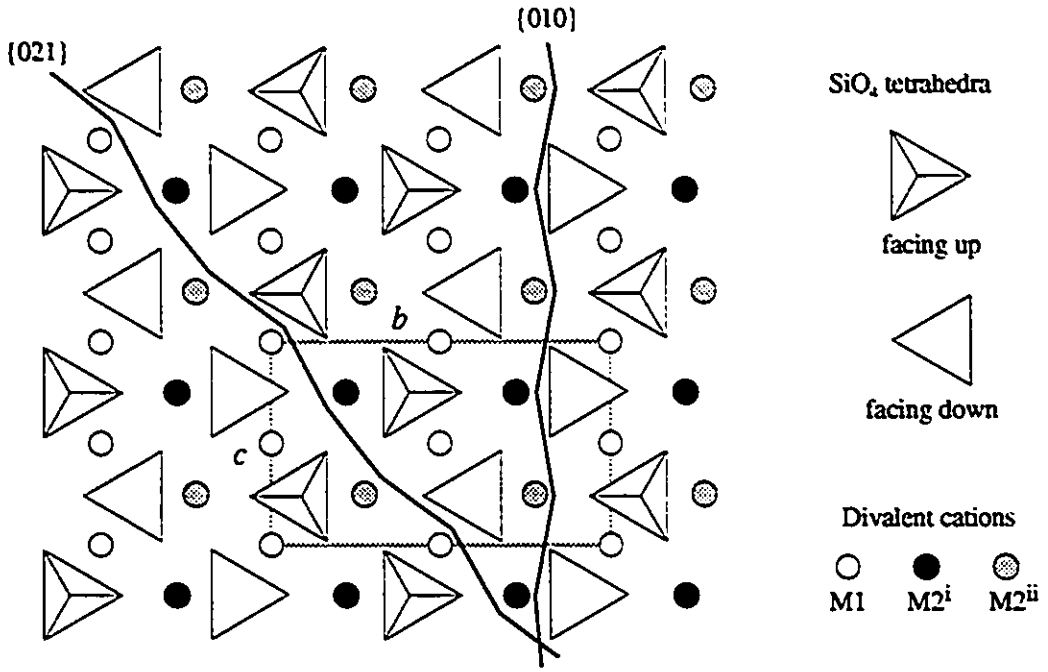

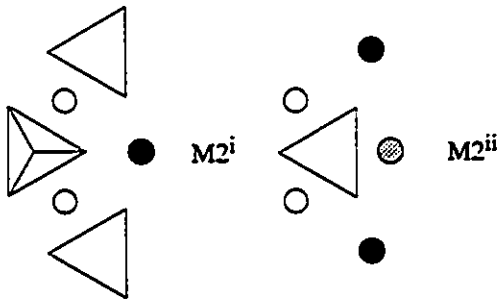

Fig. 3.2 Above: Olivine structure and unit cell projected on (100). Two common crystal forms, {021} and {010}, are illustrated along with their interrupted bonds (after Fleet, 1975a). Left: Although all fully-formed M2 sites are identical, the two M2 protosites $M2^{i}$ and $M2^{ii}$ are not equivalent during growth. The $M2^{i}$ site requires the proper orientation of three individual silica tetrahedra, and may be a rate-limiting step during the rapid growth of olivine, thus accounting for the plate-like habit (thin parallel to *b*) of rapidly grown crystals.

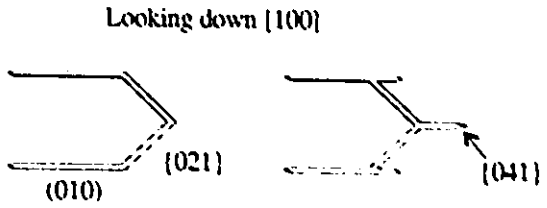

Fig 3.3 Skeletal U and H-shaped olivine crystals. In thin section these commonly appear as a row of seemingly unconnected crystals extending from the (021)∧(02$\bar{1}$) edge of a larger crystal. Compare to Photos 3.7 and 4.5.

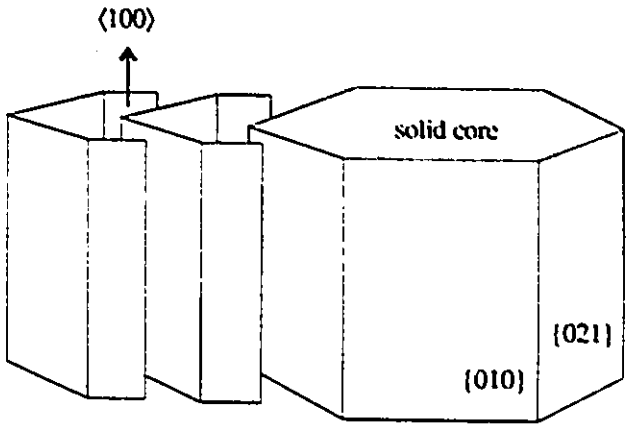

Fig. 3.4 Three-dimensional view of the above. Although this is rarely seen in thin section, skeletal extensions must be linked to the main body of a crystal. Presumably this type of growth is due to a preferred direction of growth within the {010} or {021} plane, for example towards ⟨100⟩.

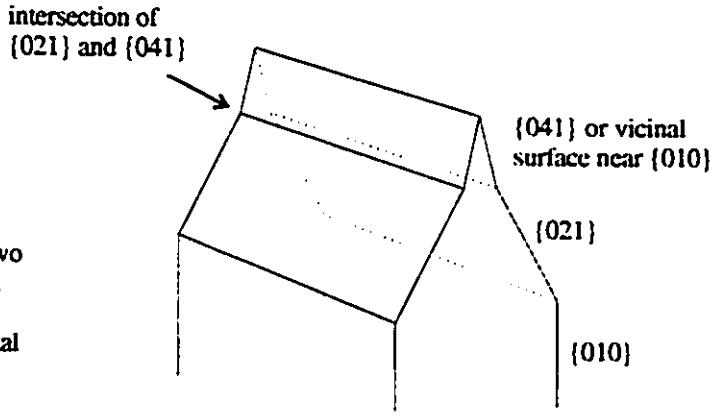

Fig. 3.5 Edges (or re-entrants) formed by the intersection of {021} planes with {041} planes or other surfaces could have acted as long-lived loci of easy nucleation for new two dimensional growth layers on both surfaces. A photomicrograph of this specific feature was not included; however compare to crystal in lower left corner of Photo 4.5.

Photo 3.5 Lower chilled margin of a thin spinifex-textured komatiite flow from Pyke Hill. Large equant olivine phenocrysts are set in a groundmass of skeletal olivine, clustered microphenocrysts of olivine, and reddish-brown altered glass. The clustering of olivine microphenocrysts is discussed by Renner et al. (1994); similar behavior is found in many minerals and presumably arises through surface energy effects. Note the strong but localized alteration (serpentinization of olivine and formation of magnetite) associated with fractures. Plane-polarized light; field of view is 2 mm.

Photo 3.6 Detail of the lowermost glassy chilled basal margin of the same flow. A glassy layer ~0.8 mm thick formed upon contact with the underlying flowtop. The photomicrograph shows acicular microlites of (serpentinized) olivine with multiple dendritic extensions, set in an orange-brown groundmass of altered glass. The uneven coloration of the glass is due to Fe and Cr-rich solute rejected by the growing olivine and (possibly) submicroscopic Cr-spinel that nucleated on olivine fibers. Similar textures involving clinopyroxene or plagioclase and Fe-Ti oxides are found in many basalts. Plane-polarized light; field of view is 200 μm.

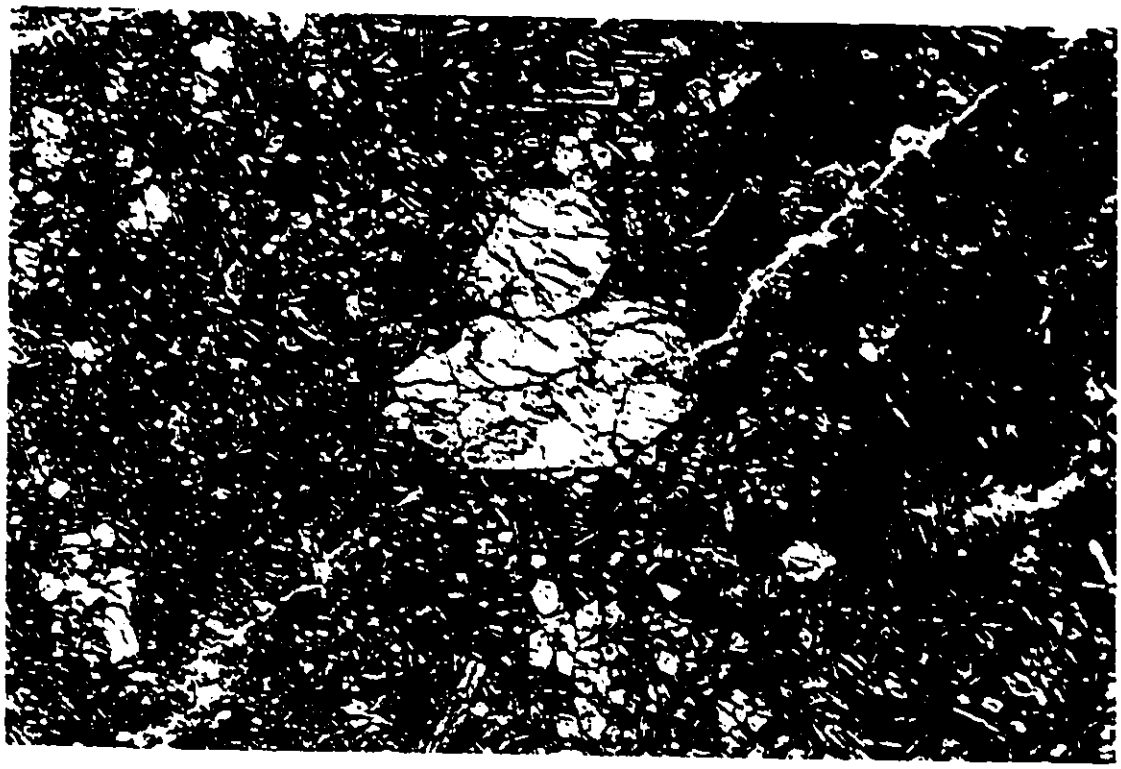

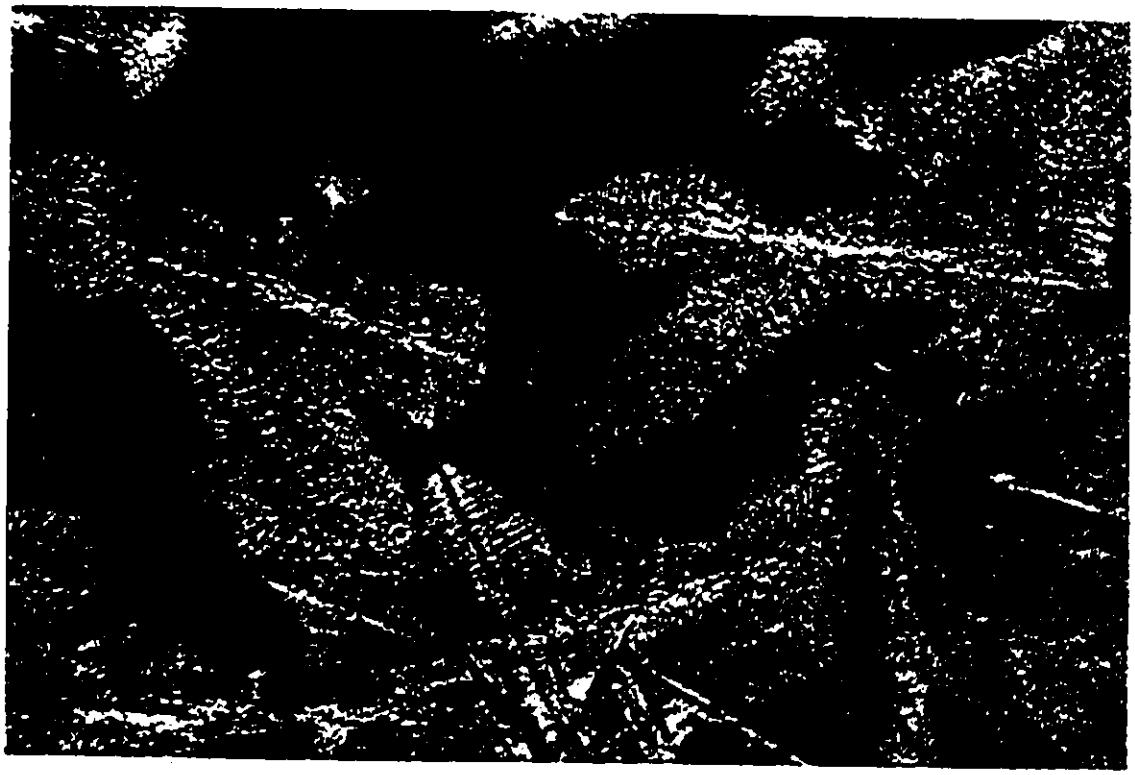

Photo 3.7 Serpentinized skeletal olivine showing U and H-shaped cross sections (see Fig. 3.3). The dark dendritic crystals are Cr-spinel and the groundmass consists of skeletal augite and chlorite. The bleaching of the groundmass adjacent to olivine (or conversely the darkening away from olivine) is a common feature in these komatiites. Plane-polarized light; field of view is 500 μm.

Photo 3.8 "Feather" olivine from the A_3 layer of a 1.5 m thick Pyke Hill flow. All vestiges of the original olivine are gone, but submicroscopic (<200–300 nm) crystals of Cr-spinel that nucleated on the olivine fibers remain as markers. Near top edge of photograph, larger dendrites of Cr-spinel that nucleated on a thin plate-like olivine crystal are visible. Plane-polarized light; 2 mm field of view.

"Feather" olivine crystals

Very small Cr-spinel crystals typically line the margins of olivine crystals (see Section **4.2.3**), and in certain completely altered olivines are the only means of determining the shape and size of the original crystal. Scattered throughout the A_2 and A_3 layers of the studied flows, with a surface concentration of 2–5 crystals per ~10 cm^2 polished section, are nearly opaque patches of reddish-brown groundmass. Upon careful examination, it is seen that these consist of μm to sub-μm Cr-spinel grains that trace out the edges of highly branching "feather" olivines (Photo **3.8**) The terminology is that of Donaldson (1976), who found that feather-textured olivine developed only by very rapid cooling (400–1400 K hr^{-1}) of basaltic liquids. This crystal habit has not been previously described in komatiites. The difficulty of examining partially serpentinized olivine crystals in a microcrystalline dark groundmass, as compared to experimental charges with pristine olivine in transparent glass, is emphasized by the fact that Donaldson stated that feather-textured olivines are not found in komatiites (Donaldson, 1982). Actually, between one to five such crystals are typically visible in each polished section from the A_2 and A_3 layers of thin Pyke Hill flows, and apart from their alteration look identical to the feather olivines grown by Donaldson (1976). In komatiites they occur in the groundmass between plate-like olivine crystals, and probably formed at relatively low temperatures (but before augite crystallization) in strongly undercooled, partially differentiated patches of melt.

Equant olivine

Many olivine crystals in komatiites (phenocrysts in chilled margins, and crystals in B-layers or in massive flows) have equant habits similar to those of typical basalts (e.g., Photos **3.5**, **3.10**). Thus, spinifex texture is not caused by compositional or growth-rate factors alone. Miniature analogs to layered komatiite flows have been observed in many high-temperature crystallization experiments on ultramafic compositions. The silicate charges in such experiments commonly have a layer of equant, granular olivine at the base of the capsule or crucible, overlain by skeletal olivine that grew during the quenching of the charge (e.g., Green et al., 1975; Agee and Walker, 1988; Zhang and Herzberg, 1994). The skeletal habit of such crystals is readily understood, because the cooling rates during quenching are on the order of 10–50 K s^{-1}. Such cooling rates far exceed any possible in the interior of even very thin komatiite flows (e.g., Donaldson, 1982). The fast growth rates of skeletal olivine that are possible in quenched komatiite liquids (e.g., ~10 μm s^{-1}, Green et al., 1975) indicate that olivine growth—at least parallel to the *a* and *c*

crystallographic axes—is unlikely to be limited by chemical diffusion or surface kinetics in the interior of spinifex-textured komatiite flows. Some typical crystal habits of olivine from the interior of komatiite flows are illustrated in Photos **3.9** to **3.12**.

Preferred orientation of plate-like olivine in A_3 layers

After this thesis had been submitted for examination, I received a preprint of a work (Chai et al., 1996) demonstrating that the thermal diffusivity of olivine is strongly anisotropic (Section **5.1.2**). This fact, coupled with the optical anisotropy of olivine (Section **5.1.4**) and my own model of constrained cooling (Section **5.1.5**), indicated that a preferred crystallographic orientation of olivine should exist in the coarse oriented sheaves of A_3 spinifex-textured layers. Using 10 samples from 4 different Pyke Hill flows I prepared 14 oriented thin sections from sheaves that were perpendicular (± 30°) to upper flow surfaces (paleohorizontal). By measuring the orientation of Cr-spinel dendrites (such crystals epitaxially overgrow olivine; Section **4.2.3**) it was possible to determine which olivine crystallographic axis, *a* or *c*, grew perpendicular to the flow surface (and thus presumably parallel to the maximum thermal gradient). In all 14 samples of known orientation, the *a* axis was perpendicular to the flow surface.

Photo 3.9 Skeletal, largely serpentinized olivine crystals from the A_2 layer 15 cm below the top of a 1.2 m thick flow from Pyke Hill. [This photomicrograph of a thick section was underexposed in order to emphasize the habit of the olivine crystals rather than groundmass crystals.] Compare to Photo **3.10**. Plane-polarized light. 2 mm field of view.

Photo 3.10 B_2 cumulate from a thin flow immediately overlying that of Photo **3.9**. Partially serpentinized equant olivine crystals form a touching framework; groundmass is a very fine-grained mixture of augite and altered glass. A colorless, talc-filled amygdule approximately 100 μm in diameter is visible in the upper right corner. The long axes of the olivine grains are of similar length to those shown in Photo **3.9**, but the crystal habits are otherwise quite different. Two somewhat skeletal crystals are visible along the right edge of the frame. Plane-polarized light, 2 mm field of view.

Photo 3.11 Looking down the *a* crystallographic axis of two parallel plate-like olivine crystals in an oriented thick section. The *c* axis runs parallel to the long edge of the photograph and the *b* axis parallel to the short edge. The crystallographic directions were determined by optical methods (quartz wedge) in sections cut perpendicular to olivine crystallographic axes (see Section 4.2.3). Small grains of relict olivine are present, but the crystals have largely been altered to serpentine, chlorite, and magnetite. The lower crystal appears to curve slightly; upon close examination it is seen that the crystallographic orientation does not change, but that the crystal tip migrated via a series of small steps. Note, for example, the shingled appearance of the lower crystal. Plane-polarized light; 2 mm field of view.

Photo 3.12 Detail of the upper olivine crystal in Photo 3.11. The crystal surface is a highly complex mix of protrusions and reentrants. Internal surfaces tend not to show crystal faces, whereas external surfaces show well developed {010} and {021} forms. Plane-polarized light, 500 μm field of view.

3.1.3 Chromian spinel crystal habits

The growth and crystal habit of Cr-spinel are closely linked phenomena, and are discussed in detail in Section **4.2.**

3.1.4 Augite crystal habits

Augite did not crystallize within the uppermost 10–20 mm of a flow, which instead contained a Ca- and Al-rich basaltic glass (now devitrified). Augite is abundant throughout the rest of the flow, forming up to ~30 vol.% of rocks from the A_2 and A_3 layers. Before describing the crystal habits of augite, I note an important series of crystal-growth experiments performed by Lofgren (1983). Using finely powdered crystalline basalts as starting material, he demonstrated that some nuclei of plagioclase and clinopyroxene could survive superheating of several degrees for many hours. Upon subsequent cooling, these residual nuclei exerted a profound influence upon the texture of the charge and crystal habits of the constituent minerals. When erupted, typical present-day basalts are at or near multiple saturation in olivine, clinopyroxene, and plagioclase, and contain phenocrysts, microphenocrysts, or microlites of one or more of those minerals; few if any modern basalts are completely aphyric.

Most spinifex-textured komatiites contain 2–10 vol.% of olivine phenocrysts in their chilled margins, indicating that they were not erupted as truly superheated liquids. [However, see Arndt (1994) for a discussion of the possible role of superheating in the textures and mineralogy of komatiitic basalts.] At low pressures, there is an extended temperature range over which only olivine crystallizes in komatiites (Fig. **3.6**). An aphyric komatiite magma at 1560 °C and an olivine-rich one at 1400 °C would both be strongly superheated with respect to Cr-spinel, augite, and plagioclase. The potential effect on the nucleation and growth of Cr-spinel is discussed in Section **4.2.3.**

The superheating of a typical komatiite magma means that the growth of augite crystals could not be "seeded" by pre-existing nuclei. Based on general observations of crystal growth and specific observations of augite crystals that grow away from olivine {010} faces (Photos **3.13** and **3.14**), it is reasonable to assume that olivine played some role in the nucleation of augite. However, to judge by the lack of crystallographic orientation between the two minerals, the role of olivine was a minor one (e.g., it may have acted as a local heat sink) and it was not a substrate for epitaxial growth of augite.

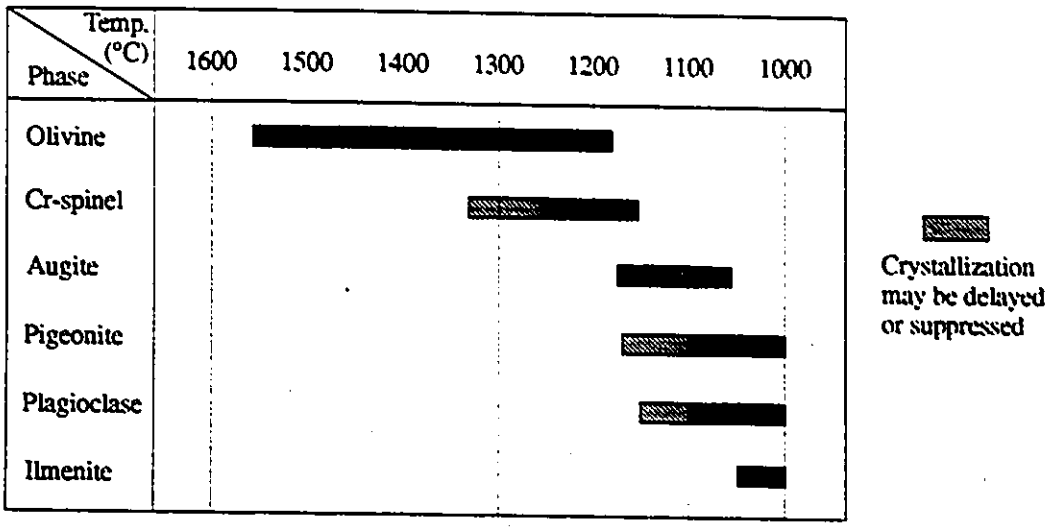

Fig. 3.6 Illustrative diagram of crystalline phases vs. lava temperature for a komatiite with ~27.5 wt.% MgO. Sources: my own petrographic, textural, and microprobe analyses combined with fractional crystallization calculations; experimental data from Arndt (1976) and Kinzler and Groves (1985).

Dendritic augite crystals in the A-layer have much more complex shapes than do most olivines. Many augite crystals are strongly curved, indicating highly imperfect crystals or growth along non-crystallographic axes, and are thus better described as spherulites. Fleet (1975b) and Fleet and MacRae (1975) describe the orientation and habit of augite crystals in A-layer komatiites. Although its crystal habit is rather striking, the formation of augite is of less importance than that of olivine. Growth of olivine determined the macroscopic and mesoscopic textures of spinifex-textured komatiites well before growth of augite began. In addition, whole-rock geochemical data indicate that little or no fractionation of augite occurred within the 1 m and 6 m-thick komatiite flows studied (Section 3.2.3). I found no textural or mineralogical evidence of an augite-forming (or pigeonite-forming) olivine–liquid reaction in any of the Pyke Hill komatiites that I examined.

Augite crystals in the lower portions of the B-layers are much more equant than their counterparts in the A-layer. Although elongated along the *c*-axis and with hollow cores, B-layer augite crystals lack the branching and curving dendritic arms so typical of A-layer ones. The B-layer crystals are also less aluminous than the dendritic A-layer crystals, suggesting they grew more slowly.

3.1.5 Pigeonite and plagioclase habits

Some experimental studies (Kinzler and Grove, 1985; Ginibre, 1995; Parman et al., 1996) of komatiites and basaltic komatiites indicate that pigeonite is the first silicate mineral to crystallize after olivine. However, augite is by far the most abundant pyroxene within the Pyke Hill flows. [The experimental studies noted above have shown that rapid cooling can suppress pigeonite growth.]

Small (50–100 μm), equant crystals of pigeonite (identified optically) are present within the B-layer of Pyke Hill flows. These occur both pure or mantled by a layer of augite. In other komatiite flows (Barnes, 1985; Renner et al., 1994) pigeonite is also mantled by augite, and commonly serpentinized.

Plagioclase is uncommon in the Pyke Hill flows, and is only found near the centers of thicker flows. Even in the 5 to 6 meter thick flow studied, plagioclase crystals are only ~2 μm thick by ~20 μm long. Throughout most of the thick flow, and all of the thin flows, plagioclase cannot be detected optically. Where it can be detected (either by reflected light microscopy or by backscattered electron imaging on the SEM) plagioclase forms very fine dendritic intergrowths with pigeonite. It is difficult to determine if growth of one mineral—whether plagioclase or pigeonite—dominated, or whether a cooperative division of elements (i.e., Ca, Na, and Al into plagioclase and Mg, Fe, and Mn into pigeonite) occurred between the two minerals to permit more rapid crystal growth.

Photo 3.13 Relatively coarse dendrites and skeletal crystals of augite in the A_3 layer of a thin flow from Pyke Hill. There is little evidence of any preferred orientation between the augite and olivine crystals. Plane-polarized light; field of view is 2 mm.

Photo 3.14 Reflected light photomicrograph of a Pyke Hill komatiite sectioned nearly parallel to (010) of a plate-like olivine crystal. The crystal is seen at right edge of photo and underlies most of the field of view at a depth of ~5–25 μm. Most of the field of view is filled with the groundmass immediately adjacent to the olivine (010) surface. Small bright cruciform crystals are dendrites of Cr-spinel; their orientation is clearly controlled by the underlying olivine (see Section **4.2.3**). The augite dendrites, on the other hand, show little or no evidence of systematic orientation. Reflected light; field of view is 500 μm.

3.2 Geochemistry of the flows

3.2.1 Sampling and analytical techniques

Sampling of komatiites

Pyke Hill is an internationally known site regularly visited by geologists. Differential weathering of the exposed komatiite following the retreat of a continental ice sheet in the late Pleistocene has brought out fine details not visible on freshly broken rock. Outcrop surfaces are typically smooth and flat, and the komatiite is mechanically tough. Pounding these uniquely exposed and accessible outcrops into rubble in order to take samples is rather inconsiderate, and using a portable diamond drill leaves small but unsightly holes. Despite this, it was necessary to obtain samples at selected points across certain flows, so I attempted to minimize the impact of sampling. To collect samples from the two 1.0–1.5 meter thick flows studied I used a hammer to collect oriented blocks of ~0.2 to 1 kg from ledges located in a less-visited area of the hill. For the 5–6 meter thick flow studied, I collected both blocks and short, 25 mm diameter diamond drill cores, also from an inconspicuous area. [See Fig. 1.5 and Appendix 7 for detailed sample locations.] The distance above the flow base to the point where a sample was taken was determined by tape-measure; because the thick flow had an irregular, steeply sloping surface, the measurement accuracy for that flow is only ± 10 cm.

Analytical methods (whole rocks)

I performed all analyses using a Philips PW2400 X-ray fluorescence (XRF) spectrometer in the University of Ottawa Geochemistry Laboratory. Analytical procedures were developed by Mr. Ron Hartree and subsequently modified by the two of us; full details are presented in Appendix 4. I present a summary here. A mixture of 1.3000 g of rock powder and 4.0750 g of lithium borate flux is fused to form a homogeneous glass disk. The disk is analyzed in vacuum, with the Kα or Lα X-ray photoemission peak and background count-rates measured for each element. On-line instrumental control and data reduction consisting of background subtraction, stripping of overlapping peaks, and correction for matrix effects and spectrometer drift is carried out by means of Philips software (modified by us) running on a PC. I optimized the nonlinear background corrections in the spectral region of the Nb to Rb Kα peaks for komatiitic compositions. Major, minor, and trace-element analytical precision is excellent; for certain trace elements

precision approaches 1–2 μg/g. A subset of samples was also analyzed as unfused pressed-powder pellets; the analytical precision for Rb, Sr, Y, and Zr was ~0.3 μg/g.

Requirement for high accuracy

Broadly speaking, over the last few decades more effort has been expended by geochemists on the analysis of progressively less-abundant trace or ultratrace elements than on the improved analysis of major, minor, and relatively abundant (i.e., 10–1000 μg/g) trace elements. [Reasons for this are beyond the scope of this study.] Accurate analytical data for both major and trace elements are required in order to constrain both magmatic differentiation and subsequent alteration in komatiites, and if possible to distinguish between the two processes. If an abundant element such as Ca shows evidence of mobility in these rocks, then little may be gained by analyzing less-abundant elements of equal or greater mobility (such as K, Sr, Rb, or Ba). Conversely, if an olivine-incompatible element such as Ti shows immobile behavior then there is little point in analyzing Nb, Hf, Ta, Th, or the lanthanide elements. [I refer specifically (and only) to the study of post-eruptive differentiation of komatiites, and in particular to the use of Pearce element ratio diagrams. The accurate analysis of many trace elements is obviously required for petrogenetic studies.]

3.2.2 Pearce element ratio diagrams

The construction of Pearce element ratio (PER) diagrams requires at least one element (*M*) that is strongly incompatible (i.e., $D_{MO}^{\alpha/L} \leq 0.01$; see Section **4.1.1**) during differentiation, immobile during alteration, and that can be accurately analyzed (Pearce, 1987; Ernst et al., 1988). When a given rock is altered, various elements are gained or lost and an overall change of mass and/or volume may occur. These processes affect the concentration of elements that have not been added to or taken from the rock, so that a rigorous definition of "immobile element" is not simple. [Similar problems in multi-component diffusion are resolved using center-of-mass coordinate systems, but this is not practical for altered rocks.] Importantly, the relative ratios (in weight or cation fractions) of immobile elements are not affected by alteration. An element that meets the above conditions (termed a "conserved element") is used as the denominator in cation ratios that are constrained by the composition and stoichiometry of any fractionated minerals.

Consider a plot of (Mg+Fe)/Th vs. Si/Th in a suite of rocks related through crystal fractionation. [Where facilities for its sensitive analysis are available, Th can be a nearly ideal conserved element in mafic and intermediate rocks.] Such a plot would have a slope of 2.0, ~1.0, ~0.5, and 0.0 for fractionation of pure olivine, orthopyroxene, clinopyroxene, and feldspar, respectively. By using combinations of plots or more complex numerators and denominators, the crystallization sequence of a closed magmatic system can be determined. Whether a group of rocks originated in an open system or is unrelated may be determined by other methods, e.g., by examining the correlation between two or more conserved elements.

In komatiites that have experienced olivine fractionation, either Al or Ti could be used as a conserved element, as both are incompatible in olivine and essentially immobile under conditions of low-grade hydrothermal metamorphism. I chose to use Al because the first three samples I crushed were contaminated by a small amount of Ti, P, and Zr-rich dust lurking beneath a jaw crusher. I replaced two by sampling adjacent parts of the original blocks but the third (MS93-01) was a short drill core and could not be replaced.

The great utility of PER analysis is that it avoids the "closure problem" that arises in the geochemical analysis of major elements. Much has been written about this, but it suffices to say that because the total weight fraction of a rock is constrained to equal 100 wt.%, major element concentrations cannot vary independently of each other. Many articles on this subject are surprisingly tedious, but two noteworthy short comments are those of Vines (1987) and Pearce (1987). I will focus on specific arguments to show that PER analysis can reveal subtleties of the fractionation and alteration of komatiite lavas.

The variation of geochemical data in a simple system such as these komatiite lava flows can arise from various sources:

- mechanical accumulation of pre-existing olivine phenocrysts;
- fractional crystallization of olivine from the melt to a solidifying upper crust or lower cumulate pile (olivine can be added to or lost from a given part of a flow);
- open-system behavior (i.e., new lava continued to flow beneath the crust during cooling, mixing with or replacing the differentiated melt);
- possibly, melting and assimilation of underlying rocks;
- post-emplacement alteration and metamorphism;
- analytical error.

Distinguishing between these different effects is usually difficult, but it can be done in well-preserved rocks, given accurate and precise chemical analyses.

In komatiites, the variation of different oxides is commonly studied using MgO (in wt.%) as the independent variable, much as SiO_2 is used in Harker diagrams (e.g., Arndt, 1986a, 1994). Geochemical data taken across relatively fresh flows scatter near a line (more generally, a surface) in compositional space that contains the point (curve) representing the liquid and the point (curve) representing the mean fractionated olivine. The rationale behind the "olivine control line" is intuitively clear, and it works reasonably well. However, it has flaws, and can be improved upon.

I present my argument graphically, using an arbitrary pair of immobile elements, A and B. Every analysis is subject to error bounded by the precision of the measurement technique. [Matrix corrections in XRF spectroscopy can induce correlation of errors between elements, but this effect is minor in fused samples and will be ignored.] The meaning of the vertical and horizontal error bars on a typical x-y scatterplot is clear. Note, however, that element concentrations are given in wt.%, i.e., grams of analyte per 100 grams of sample. Although neither element A nor B has been added to or lost from the system, other elements may have been, and thus both concentrations can change, i.e., $[A]_{initial} = \frac{A}{A+B+(C)}$ and $[A]_{final} = \frac{A}{A+B+(C+\Delta C)}$, where C is the sum of the other elements present in the sample. Each data point is shifted towards or away from the origin (0,0) by an amount that may vary from sample to sample (Fig. 3.7). Recalculating the analyses to 100 wt.% on an anhydrous basis reduces but *does not eliminate* this problem, except in the unlikely case that alteration solely involved the addition of water. Such shifts are present but not noticeable in plots of two conserved oxides (e.g., Al_2O_3 vs. TiO_2), because these form linear arrays that pass through the origin.

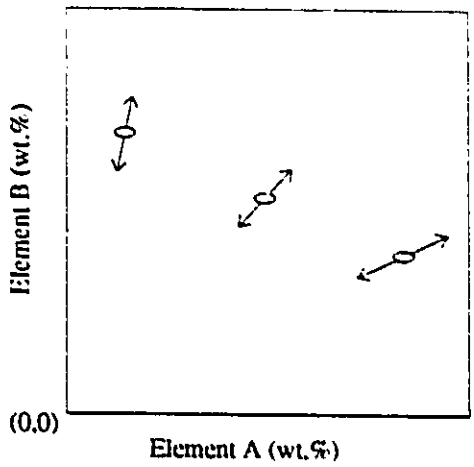

Fig. 3.7 The concentration of immobile elements (here shown for two elements related by a hypothetical magmatic fractionation trend) can be changed by gain or loss of other elements during alteration. The relative change can greatly exceed analytical precision (indicated by the size of the elliptical symbols), and will generally vary between different samples.

3.2.3 Geochemistry of the Pyke Hill flows

Introduction

The Pyke Hill flows, as previously documented (Pyke et al., 1973; Arndt et al., 1977) are typical Munro-type late Archean komatiites. Complete analyses are presented in Appendix 6; the more significant results are discussed below. Compositionally, the Pyke Hill lavas are quite similar to komatiites of comparable age from Zimbabwe and Western Australia. They are also very fresh, as komatiites go, and contain relict olivine, fresh clinopyroxene and Cr-spinel, and beautifully preserved textures down to the microscopic scale. However, the bulk of the olivine is serpentinized, all glass is altered to submicroscopic clays, and the fine-grained groundmass is permeated by veins and microfractures. In places, metamorphic tremolite has formed, as well as minor phases such as andradite and heazlewoodite (Ni_3S_2). My analyses show that Mg, Al, Si, Ti, P, Cr, Co, Ni, Y, and Zr were immobile during the alteration of the flows. Elements that show evidence of mobility include Na, K, Ca, Mn, Fe, Zn, Rb, Sr, and Ba. Alteration and element mobility is discussed further in Sections 3.2.4 and 4.4.4.

Within-flow differentiation of komatiite lavas

The primary geochemical variations within the Pyke Hill flows are consistent, within the limits of analytical accuracy, with the fractionation solely of olivine. This result is similar to those of other studies of within-flow variations (e.g., Arndt, 1986a; Nisbet et al., 1987). Arndt (1994) has discussed the advantages that the variable gain or loss of olivine, a mineral with a stoichiometric composition that is readily calculated from the co-existing melt, brings to the study of altered komatiites. In short, if an element shows variations that are inconsistent with olivine fractionation (i.e., if data points do not plot near the "olivine control line"), then either another mineral also crystallized, or the flow has been altered. (Other less likely possibilities will not be discussed here.) The analytical data unequivocally show that Pyke Hill lavas are geochemically altered; more interestingly, it is possible to look beyond this alteration to determine the precise composition of the olivine that fractionated within the flows.

Linear regression analysis of the PER data for whole-rock geochemical analyses from the three closely spaced flows studied shows that the only mineral that fractionated was olivine. More specifically, it was olivine of composition Fo $93.7 \pm 1.0(2\sigma)$, or equivalently mg# $= 94.6 \pm 1.0(2\sigma)$. [The mg# of olivine = 100[Mg]/([Mg]+[Fe]), where [Mg] and [Fe] are the molar concentrations of those elements in olivine, whereas the forsterite content Fo = 100[Mg]/$\sum$[M1 + M2 cations]). The inferred composition of the olivine is given in Table **3.1** (for more details see the captions to Figs. **3.8** to **3.16**). Moreover the estimated concentrations of Mg, Cr and Ni are virtually identical to those determined by electron microprobe analyses of magnesian olivine phenocrysts within the flows, and that of Co is consistent with experimentally determined distribution coefficients for that element (e.g., Beattie et al., 1991). Variable loss of Mn occurred, possibly due to hydrothermal alteration; the most affected samples were omitted from the regression analysis. The loss of Ca from the lavas was so pronounced that PER regression could not be used to determine the Ca content of the fractionated olivine.

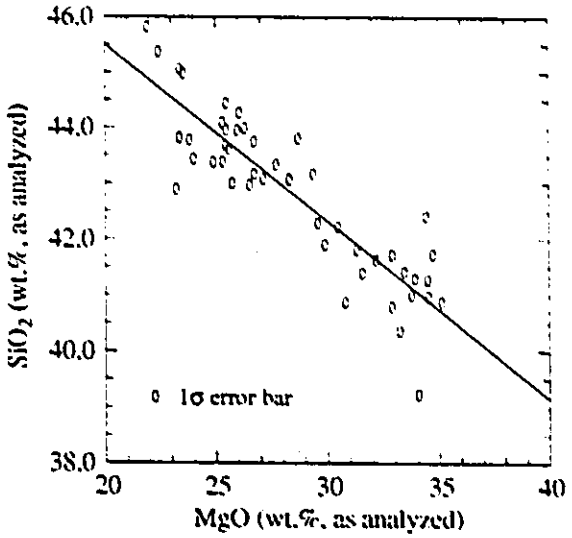

Fig. 3.8 Simple x-y plot of SiO_2 vs. MgO as measured in 45 reasonably fresh whole-rock samples from three adjoining komatiite flows from Pyke Hill. Three additional samples (two flowtop breccias and one aphanitic basal chill) were not included due to their greater alteration. The best-fit line calculated by least-squares regression is $SiO_2 = 51.84 - 0.3172$ MgO ($r^2 = 0.780$). To reduce clutter, the symbols are scaled to the size of the 1σ rather than the 2σ errors. The scatter clearly exceeds that due to analytical error, and is caused by variable amounts of hydration and gain or loss of other elements (see text).

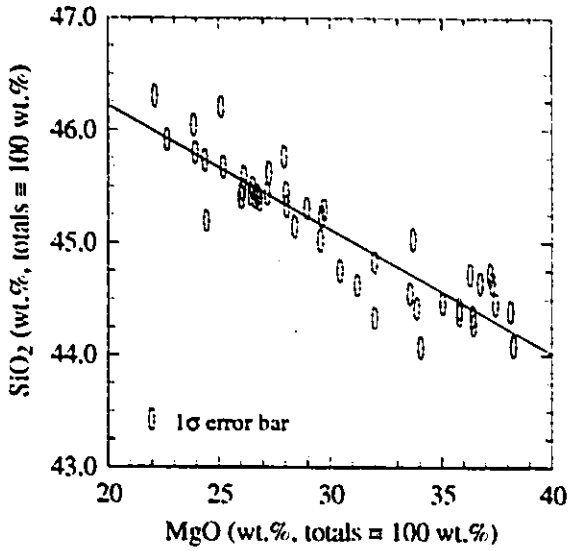

Fig. 3.9 Simple x-y plot of SiO_2 vs. MgO (same analyses as in Fig. 3.8, but recalculated so that the totals equal 100 wt.%, anhydrous). Scatter has been reduced from Fig. 3.7 but not eliminated. The best-fit line is $SiO_2 = 48.43 - 0.1106$ MgO ($r^2 = 0.819$). The calculated SiO_2 at 52.4 wt.% MgO (i.e., the MgO concentration of Fo_{94}) is 42.6 wt.%, a rather poor match to the ideal concentration of 41.6 wt.%. Thus the best-fit line is not a very good olivine-control line. This diagram is a typical example of the way within-flow chemical variations are examined in komatiites. The symbols are scaled to the size of the 1σ analytical error. The ordinate scale has been expanded from that of Fig. 3.8.

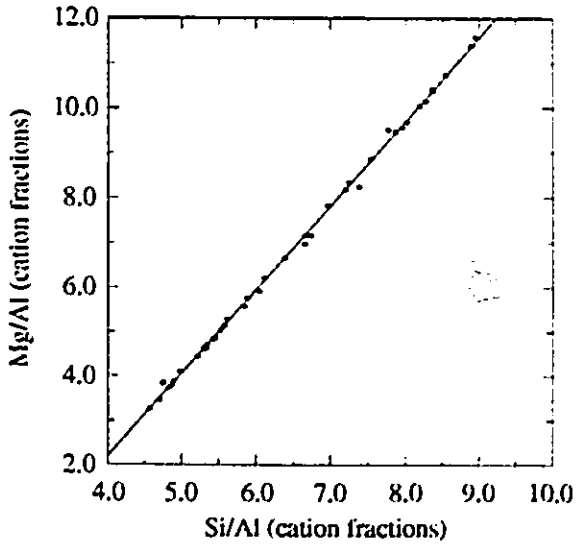

Fig. 3.10 Pearce element ratio (PER) diagram of Mg/Al vs. Si/Al (same analyses as in Fig. 3.8). The great improvement of the fit is discussed in the main body of the text. The 2σ analytical error, ± 0.0044 for (Si/Al) and ± 0.0047 for (Mg/Al), is much smaller than the size of the symbols. The line of best fit is (Mg/Al) = 1.8747(Si/Al) – 5.300 ($r^2 = 0.999$, standard error (s.e.) of slope = 0.0101). This within-flow variation is caused by fractionation of olivine with a mean composition of $Fo_{93.7 \pm 1.0}$ (2σ error). This is indistinguishable from the olivine phenocrysts in chilled margins ($Fo_{93.4 \pm 0.3(2\sigma)}$) measured by electron microprobe.

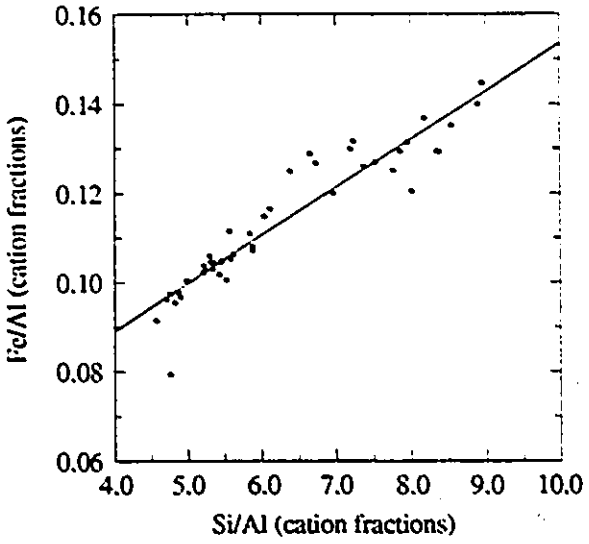

Fig. 3.11 PER diagram for Fe (same analyses as in Fig. 3.8). Analytical error is much smaller than the size of the symbols. Samples have gained or lost up to ~10% of their original Fe, with some suggestion of greater loss in the B-layer rocks. However, the data do not show any marked systematic scatter about the best-fit line (Fe/Al) = 0.1074(Si/Al) + 0.4616 (r^2 = 0.884, s.e. of slope = 0.0059), which corresponds to $Fa_{5.4 \pm 0.5(2\sigma)}$. This is indistinguishable from the $Fa_{5.6 \pm 0.4(2\sigma)}$ of olivine phenocrysts in chilled margins (measured by electron microprobe); thus Fe appears to have been mobile on a local scale only.

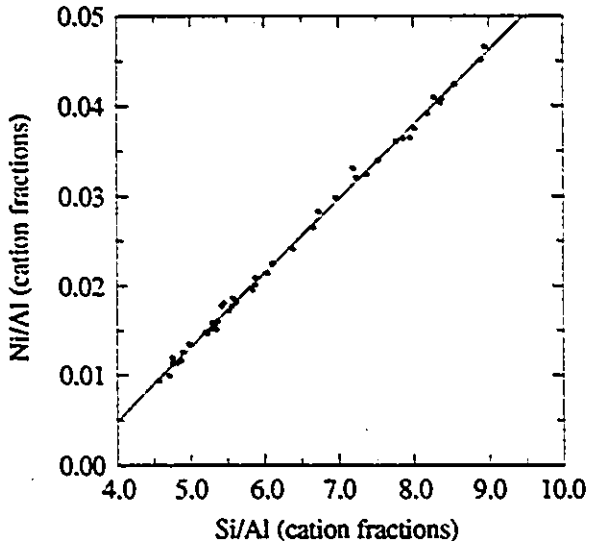

Fig. 3.12 PER diagram for Ni (same analyses as in Fig. 3.8). Analytical error is smaller than the size of the symbols. The best-fit line is (Ni/Al) = 0.00827(Si/Al) – 0.0282 (r^2 = 0.997, s.e. of slope = 0.00063). This corresponds to an olivine containing 0.426 ± 0.01(2σ) wt.% NiO (3350 µg/g Ni), which compares well to the 0.403 ± 0.005(2σ) wt.% measured in olivine phenocrysts by the electron microprobe.

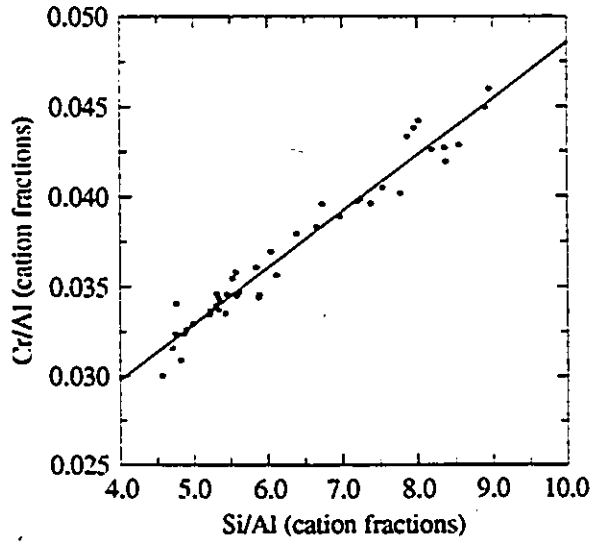

Fig. 3.13 PER diagram for Cr (same analyses as Fig. 3.8). Analytical error is smaller than the size of the symbols. The best-fit line is (Cr/Al) = 0.00313(Si/Al) + 0.0173 (r^2 = 0.956, s.e. of slope = 0.00010). This corresponds to an olivine containing 0.16 ± 0.01(2σ) wt.% Cr_2O_3 (1100 µg/g Cr), which compares well to the 0.14 ± 0.02(2σ) wt.% measured in olivine phenocrysts by the electron microprobe.

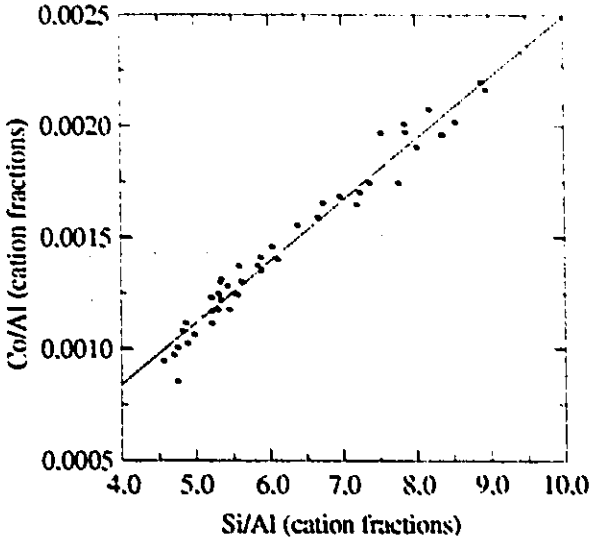

Fig. 3.14 PER diagram for Co (same analyses as in Fig. 3.8). Analytical error is difficult to specify; the 2σ precision of replicate Co analyses is ±3 μg/g, but two-thirds of these rocks were coarsely ground in a tungsten carbide shatterbox, which typically added 5–10 μg/g Co to each sample. Because the level of Co contamination is more-or-less independent of sample composition, it has a minimal effect on the slope of the best-fit line, the equation of which is (Co/Al) = 0.000276(Si/Al) – 0.00264 (r^2 = 0.966), equivalent to ~110 μg/g Co in olivine.

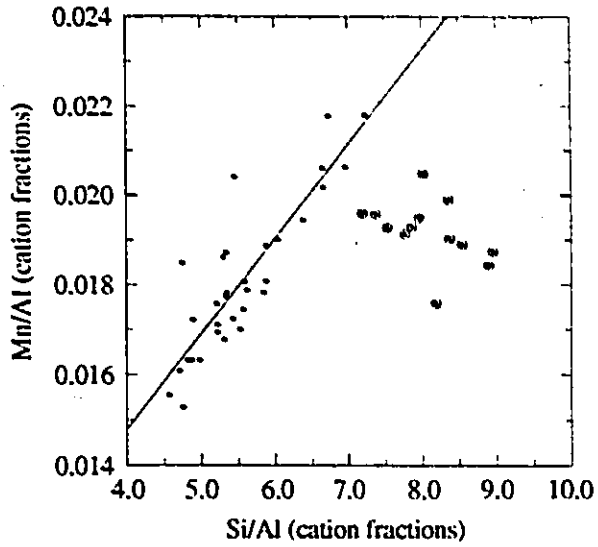

Fig. 3.15 PER diagram for Mn (same analyses as in Fig. 3.8). Analytical error is smaller than the size of the symbols. Manganese has clearly been mobile in these flows, particularly in the more-serpentinized B-layer samples. Omitting those analyses (shown by a dot within a circle) from the regression, the best-fit line is (Mn/Al) = 0.00212(Si/Al) + 0.00633 (r^2 = 0.739, s.e. of slope = 0.00023). This corresponds to an olivine containing 0.10 ± 0.02(2σ) wt.% MnO (~800 μg/g Mn), which is indistinguishable from the 0.092 ± 0.01(2σ) wt.% measured in olivine phenocrysts by the electron microprobe. Up to ~30% of the original Mn was lost from the most altered samples; two or three samples appear to have gained ~10% Mn relative to their original content.

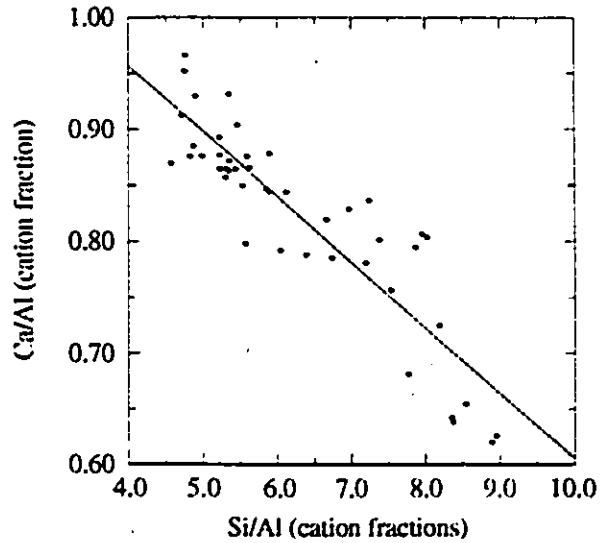

Fig. 3.16 PER diagram for Ca (same analyses as in Fig. 3.8). Analytical error is much smaller than the size of the symbols. A negative slope on a PER diagram cannot be explained by crystal fractionation. On the basis of the Ca-content of olivine phenocrysts, the predicted slope would be +0.0055. The best-fit line is actually (Ca/Al) = –0.0585(Si/Al) + 1.1905 (r^2 = 0.791). The loss of Ca is roughly proportional to the amount of serpentine in each rock (see Section 4.4.2 for discussion of this point).

Table 3.1 Composition of fractionated olivine derived via PER analysis

Element	Atoms per atom of Si	Calculated olivine composition	Olivine phenocrysts[1]
Mg	1.8747	52.2(3) wt.%	51.9(1) wt.%
Fe	0.1074	5.3(3)	5.5(1)
Ni	0.0083	0.426(5)	0.403(3)
Ca	0.0055[2]	not determined	0.214(3)
Cr	0.0031	0.16(1)	0.137(7)
Mn	0.0021[3]	0.10(1)[3]	0.091(5)
Co	0.0003	0.014(1)	not analyzed
ΣM	2.0014	—	—

[1] Mean of 4 high-precision analyses (see Appendices 3 and 5).

[2] From microprobe analysis. [3] Selected analyses (see Fig. 3.15).

Fractionation of olivine

As described in Section **4.1.1** and Appendix **2**, it is relatively simple to model the fractional crystallization of olivine and therefore the changing composition of the melt. In my calculations I have assumed that olivine–melt system is closed, with a fixed composition estimated from several relatively unaltered, undifferentiated samples. Open behavior of the olivine–melt system (i.e., if liquid was added, lost, or mixed during crystallization) would have had little effect on most compositional ratios in olivine (e.g., MnO wt.% vs. FeO wt.%), but could significantly change the shape of the zoning profiles of the crystals (e.g., FeO vs. distance from crystal core). In a closed system, the bulk composition of a layered flow must be that of the original magma (liquid plus or minus olivine). Complicating factors arise in determining the original composition and correcting for varying degrees of alteration and expansion of the flow, but these can be accounted for. An open system would contain an overall excess or shortage of olivine (possibly plus or minus Cr-spinel). This could arise through the flow of undifferentiated lava continuing within the core of a flow and supplying olivine constituents to a crystallizing crust or cumulate layer, or depositing suspended olivine phenocrysts. Arndt (1986a) and Barnes (1985) present evidence of open-system behavior in other komatiite flows from the Abitibi greenstone belt.

The tightly constrained, highly magnesian composition of the fractionated olivine is useful, because it indicates that the olivine crystallized from a melt that had not undergone a high degree of differentiation. Unfortunately, in liquids as Mg-rich as komatiites, the mg# of the equilibrium olivine changes very gradually during the initial stages of fractional crystallization. My modeling shows (Fig. **4.1**) that the mean composition of the crystallized olivine would decrease by 1% Fo only after 25 mol% (~22 wt.%) of olivine had crystallized. Thus even a tightly constrained mean olivine composition is not much better at determining the amount of within-flow differentiation than is a simple mass-balance calculation. For example, using the MgO content of the initial magma ($MgO_{init} \equiv 27.5$ wt.%), the fractionated olivine ($MgO_{ol} \equiv 52$ wt.%), and a differentiated lava ($MgO_{diff} \equiv 22$ wt.%), $MgO_{init} = c \times MgO_{oliv} + (1-c) \times MgO_{diff}$, where c is the weight fraction of olivine. Therefore $c = \frac{MgO_{init} - MgO_{diff}}{MgO_{ol} - MgO_{diff}} = 0.19$, so approximately 19 wt.% olivine was removed from the most differentiated lava.

The two methods are somewhat complementary: using PER regression one can accurately determine the mean composition of the olivine fractionated over the entire flow, whereas using mass-balance calculations the olivine gained or lost from any individual sample can be calculated. For the latter method the composition of the initial magma must be determined, which is not trivial (see Arndt, 1986a; Nisbet et al., 1993). In principle one can calculate the amount of olivine lost or gained across a vertical section of a flow by taking closely spaced samples. However, when this is done in thick spinifex-textured flows one commonly finds that the amount of cumulus olivine in the B-layer exceeds that lost from the overlying A-layer (e.g., Barnes et al., 1983; this work, Fig. **3.17**). The flows therefore acted as open systems that gained olivine from through-flowing lava, and that also locally underwent some degree of differentiation via the loss of olivine.

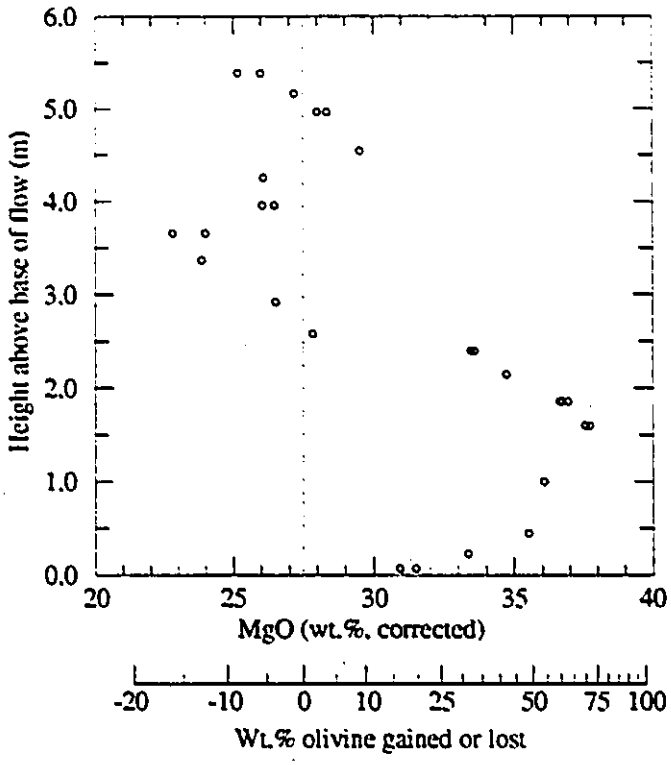

Fig 3.17 Plot of wt.% MgO content of samples vs. their height above the base of a 5.3 m thick flow from Pyke Hill. MgO has been "corrected" by recalculating analytical totals to 100 wt.% (anhydrous) after adjusting for leaching of Na, Ca, and Mn (see text) by making $Na_2O = 0.09\ Al_2O_3$, $CaO = 1.00\ Al_2O_3$, and $MnO = 0.016\ Fe_2O_3T$. An additional abscissa scale has been calculated assuming that the original magma contained 27.5 wt.% MgO (as determined from the least-altered near-flowtop sample, and olivine-melt equilibrium). This scale represents the wt.% olivine (relative to the mass of the original magma) that must be gained or lost to account for the whole-rock composition. Although some differential vertical expansion has occurred (Section 4.4.3) and the height above the base does not directly correlate to the original mass-proportions of the flow, more olivine accumulated in the B-layer than was lost from the overlying A-layer (which shows both gain and loss of olivine).

Absence of Cr-spinel and clinopyroxene fractionation

Chromian spinel is a high-temperature phase in most basalts, where it occurs as small (sub-mm) octahedral or subhedral crystals, commonly included within larger olivine crystals. Such crystals appear to have adhered to the olivine surface and been subsequently enclosed by the more rapidly growing olivine (Photo 4.3). Due to these factors, Cr-spinel and olivine commonly fractionate together in basalts. However, in komatiites the situation is quite different. Chromium is contained in solid solution within olivine at high temperatures, and Cr-spinel nucleates epitaxially upon olivine as the temperature falls (these points are discussed in detail in Sections 4.1.2 and 4.2.3). Apart from one massive lava tube containing equant Cr-spinel crystals and slightly enriched in Cr, olivine was the sole phase that fractionated Cr in the Pyke Hill flows studied (see also Arndt, 1986a).

In principle, fractionation of clinopyroxene could occur during the crystallization of thick komatiite flows (such fractionation unequivocally occurs in thick komatiitic basalt flows). Because augite contains ~20 wt.% CaO, variations of Ca/Al or Ca/Ti would be a sensitive test of augite fractionation in unaltered rocks. However Ca was mobile in the Pyke Hill komatiites and thus cannot be used for this purpose. An alternative could be

variations in whole-rock Ti/Al, since these elements are unlikely to have identical augite–melt partition coefficients. In fact, the ratio of TiO_2 to Al_2O_3 (in wt.%) in the studied flows is 0.0460(6), whereas in 41 microprobe analyses of augite (Appendix 5) it averages 0.11(3). However, the difference is small, and coupled with the low concentration of these elements in augite the whole-rock Ti/Al is an insufficiently sensitive test of augite fractionation.

3.2.4 Alteration and mobility of elements

Introduction

Alteration—predominantly serpentinization in the Pyke Hill flows—has removed Fe, Mn, Ca, Na, K, Sr, Rb, Ba, and S from the B-layer of thick flows to varying degrees. In certain samples (both A and B-layers) the concentration of geochemically mobile incompatible elements such as K and Rb may have increased from the original magmatic levels. Such alteration occurs even in mineralogically and texturally well-preserved samples, and is a common feature of other komatiites (e.g., Barnes et al., 1983; Arndt, 1986a; Nisbet et al., 1987). A mineralogical explanation for this is given in Section **4.4.4**. The elements Al, P, Ti, Cr, Ni, and Zr are generally considered immobile in low-grade metavolcanic rocks, and this is confirmed by the chemical analyses of the studied flows.

Magnesium and silicon

The elements Mg and Si are rarely considered to be immobile in submarine basaltic rocks. Cation exchange with seawater containing high levels of Mg^{2+} and the formation of secondary chlorite commonly causes large increases in the MgO content of altered modern lavas (Thompson, 1991). Loss or gain of substantial amounts of Si can also occur, particularly during greenschist facies alteration. In the suite of samples collected from Pyke Hill, however, the gain or loss of either element was negligible. The magnitude of the scatter about the best-fit line on the PER regression of Mg/Al vs. Si/Al (Fig. **3.10**) indicates that the mean gain or loss of both elements combined is <0.5% (relative to their original concentration). The combined analytical uncertainty of the ratios is ~0.2% (1σ). The immobile behavior of Mg and Si will be considered a demonstrated fact for the study of within-flow olivine fractionation; the reasons these elements were immobile are discussed in Section **4.4**.

Alkali and alkaline-earth elements

The alkali elements Na, K, and Rb, as well as Sr and Ca, show variations that cannot be caused by olivine fractionation. Similar variations are observed in other komatiite flows (Arndt, 1986a, 1994). For example, a plot of Al_2O_3 vs. TiO_2 (Fig. **3.18**) extrapolates through the origin (based on olivine analyses, it should actually pass through the point ~0.10 wt.% Al_2O_3 and ~0.003 wt.% TiO_2). However a plot of CaO vs. TiO_2 has a negative y-intercept; similarly, a Pearce element ratio diagram of Ca/Al vs. Si/Al has a negative slope (Fig. **3.16**). This is not caused by crystal fractionation, but by the removal of Ca and the alkalis from the komatiite groundmass during the serpentinization of olivine. The subject is discussed at length in Section **4.4.2**.

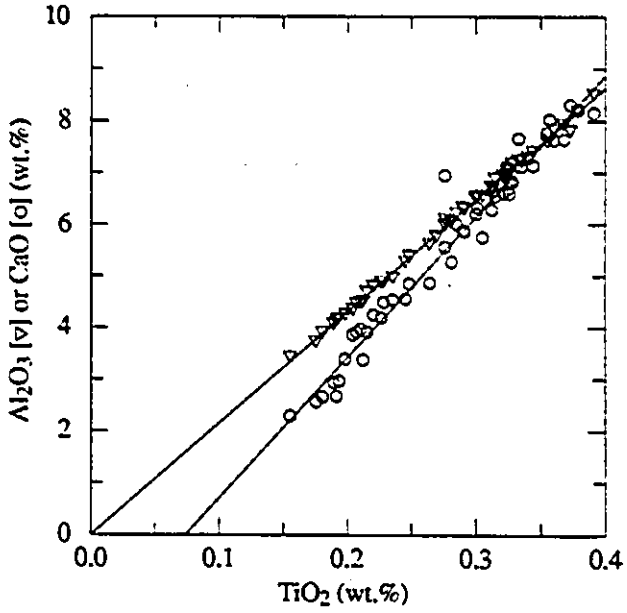

Fig. 3.18 Plot of Al_2O_3 and CaO vs. TiO_2 for 50 whole-rock analyses of komatiite samples from three spinifex textured flows and one massive lava tube. The data have not been recalculated to 100 wt.%, and 2σ analytical error is smaller than the size of the symbols used. The best-fit line for Al is $Al_2O_3 = 21.50(TiO_2) + 0.02$ ($r^2 = 0.998$), readily explainable because Al and Ti are both incompatible in olivine and immobile during low-grade alteration. The best-fit line for Ca is $CaO = 27.17(TiO_2) - 2.02$ ($r^2 = 0.963$). This is more complicated, since the negative y-intercept cannot be explained by crystal fractionation, and yet the close correlation with TiO_2 seems inconsistent with alteration. See Section 4.4.2.

Manganese

In komatiite olivines the concentration of Mn is closely correlated to that of Fe (e.g., Fig. **4.2**). This is to be expected under reducing magmatic conditions, since Fe^{2+} and Mn^{2+} have very similar olivine–melt partition coefficients (Beattie et al., 1991; Appendix **2**). However this relationship is less constant in the whole-rock data, which indicate that Mn is lower than expected in the B-layers of the studied flows. A simple explanation for

this observation is that Mn was preferentially removed from these layers during serpentinization. Under typical hydrothermal conditions, some of the Fe^{2+} and Mn^{2+} removed in solution from olivine would oxidize to Fe^{3+} and Mn^{3+} (and/or Mn^{4+}). Whereas Fe^{3+} typically forms highly insoluble compounds that precipitate very close to the site of alteration, Mn ions can remain in solution and be removed. The composition of secondary magnetite also shows this effect (≥99 wt.% Fe_3O_4, ~0.1 wt.% MnO). At the present time, Mn mobility is illustrated by hydrothermal plumes at mid-ocean ridges, in which dissolved Mn/Fe is much greater than Mn/Fe of the source basalts (e.g., Sansone et al., 1991; Mandernack and Tebo, 1993), or the MnO_2-rich nodules abundant on certain areas of the ocean floor.

Phosphorus

Phosphorus is an element that may have been of biochemical importance to early life forms (E.G. Nisbet, personal communication). Also, as a high field strength element it is occasionally considered an immobile element. This practice is not recommended, as the easy solubility of apatite in weak acids or the relatively high level of phosphorus in modern seawater—high enough to allow some organisms to form phosphate-based shells—shows. There are very few precise analyses of phosphorus in komatiites in the literature, so I report them here as a matter of interest. In the Pyke Hill lavas, P_2O_5 falls on olivine control lines, implying it was immobile. The concentration of P_2O_5 in the least differentiated samples is ~0.018 wt.% (~80 µg/g P). Certain more metamorphosed komatiites from elsewhere in the Abitibi that I analyzed contain P at or below detection level (~10 µg/g P), implying its mobility during more extensive alteration.

Sulfur

I analyzed a limited number of samples in the form of pressed pellets, which permitted the reliable determination of sulfur. In the Pyke Hill flows S concentrations lie close to an olivine control line, with a mean of ~300 µg/g (for analytical totals recalculated to 100 wt.%, anhydrous). If this concentration is close to the original magmatic level, then the komatiites would have been highly undersaturated in S. Similar concentrations of sulfur in Pyke Hill lavas were reported by Crockett and MacRae (1986). The concentration of S in these unmineralized flows is considerably less than the 1500–3000 µg/g solubility of S in komatiitic melts (e.g., Naldrett, 1989), and far less than the 1–30 wt.% S content of mineralized komatiites. Because it behaves as a moderately

incompatible element during partial melting of the mantle, a low concentration of S in unmineralized komatiites is consistent with their depleted nature. By comparison, the concentration of S in N-MORB and primitive Hawaiian basalts is typically 800–1200 μg/g (Mathez, 1976; Clague et al., 1995). Recent ion microprobe measurements have found S contents of 350–540 μg/g in glass inclusions in olivine crystals in a komatiite from Zimbabwe (McDonough and Danyushevsky, 1995). These correspond to S contents of ~200–250 μg/g in the bulk liquid, quite similar to my own estimate from whole-rock geochemistry. Sulfur plays an essential role in the formation of komatiite-hosted Ni deposits; the much-debated hypothesis of substrate assimilation is briefly discussed in Section **5.2.3.**

Chlorine

I analyzed the same group of pressed-pellet samples for Cl. The concentration of Cl (analytical totals recalculated to 100 wt.%, anhydrous) varied between 170 and 660 μg/g, with a mean of 330 μg/g. The concentrations were not controlled by olivine fractionation, nor did they correspond closely to the loss on ignition (LOI, which in these rocks is predominantly a measure of H_2O content) of a given sample. There is a weak increase in Cl towards the top surface of the flow that could have been caused by hot rock reacting with HCl formed during synvolcanic hydrothermal cooling (as currently witnessed in Kilauean flows), but this is purely speculative.

Summary

In the Pyke Hill komatiites, elements that are commonly assumed to be remain immobile during low-grade metamorphism (Al, P, Ti, Cr, Ni, Y, Zr) have behaved accordingly. Certain elements that are typically considered mobile during such alteration have either been immobile (Mg, Si) or show evidence of only a limited degree of local mobility (Fe, possibly S). Other elements in the lavas show clear evidence of systematic loss (Ca, Mn), or non-systematic loss or gain (Na, K, Sr, Rb).

The data indicate to a high level of precision that olivine was the only mineral that fractionated within the flows, and that its composition was essentially identical to that of the olivine phenocrysts found within the upper and lower chilled margins.

4 Mineralogy

4.1 Olivine

4.1.1 Introduction to olivine chemistry

Little variation exists in the compositional range of olivine from komatiites throughout the world. This is in sharp contrast to, for example, clinopyroxene in basalts, and is due to the restrictive crystal chemistry of olivine and the similar bulk chemistry and crystallization sequence of most komatiitic lavas. Because Mg and Fe comprise 99% of the M-site cations in olivine from komatiites, it is common practice (e.g., Nisbet et al., 1993) to use the mg# as a substitute for the forsterite content. For olivines in komatiites, mg# ≡ Fo + 0.9. Olivine in komatiites can be more magnesian (up to $Fo_{93.7}$, mg# = 94.6) than that of most peridotites, and considerably more magnesian than that of typical basalts. The Ni content, while high, is comparable to that of peridotites and some basalts. The Cr content is unusually high, and because it involves a number of interesting phenomena will be discussed at length below. Most of the compositional peculiarities of these olivines derive from the unusually hot and Mg, Ni, and Cr-rich nature of komatiite lavas.

Modeling olivine zoning

Olivine crystals are commonly strongly zoned in komatiite flows that have experienced only very low-grade metamorphic conditions. This zoning is a primary magmatic feature that can be closely modeled by fractional crystallization from the melt (e.g., Arndt, 1986a; Renner et al., 1994). Two quite different approaches to calculating the composition of the crystallizing olivine can be taken. One method is to calculate the equilibrium composition thermodynamically, taking into account temperature, liquid composition, latent heat of crystallization, entropy of mixing, non-ideal site occupancy, etc. (e.g., Hirschmann and Ghiorso, 1994). I have chosen to use experimentally determined exchange partition coefficients, a method that is simpler but of comparable or greater accuracy for minor elements in olivine. [As defined by Beattie et al. (1993b), the *molar partition coefficient* of a component *MO* (where *M* is an arbitrary cation) between phases α and β (or *L*, if a melt) is $D^{\alpha/\beta}_{M^*} = C^{\alpha}_{MO^*}/C^{\beta}_{MO^*}$, where $C^{\alpha}_{MO^*}$ is the mole fraction of component MO in phase α. The *exchange partition coefficient*, where the partition coefficient of one element is normalized by the value of the partition coefficient for

another element is defined as $K_{D\,M/N}^{\alpha/L} = D_M^{\alpha/L} / D_N^{\alpha/L}$.] Using olivine stoichiometry, an estimate of the original melt composition, and exchange partition coefficients slightly modified from Beattie et al. (1991, 1993a), I have calculated the compositions of olivine and residual liquid formed by fractional crystallization (see Appendix 2 for details and a sample calculation).

The mg# of olivine at any point is a function of the amount of olivine that has already crystallized from melt of a given initial composition (Fig. **4.1**). This allows the changing composition—and hence temperature, density, and viscosity—of the melt to be calculated. Olivine crystal zoning patterns provide an independent check of the modeling. If the assumptions of perfect fractional crystallization from a closed system and negligible solid-state diffusion are correct, then the Fe/Mg zoning (plotted against distance from the crystal midplane) in non-skeletal olivine crystals should resemble Fig. **4.1** or Fig. **4.11**; similar profiles have been measured in olivine from A_3 layers (Arndt 1986a; Renner et al.,1994). [Certain of my own analyses are also consistent with this pattern, but the analyzed points are too few and widely spaced to be definitive.] The growth of a small crystal from a much larger volume of melt, or appreciable solid-state diffusion could lead to significantly different zoning patterns (e.g., Arndt, 1986a).

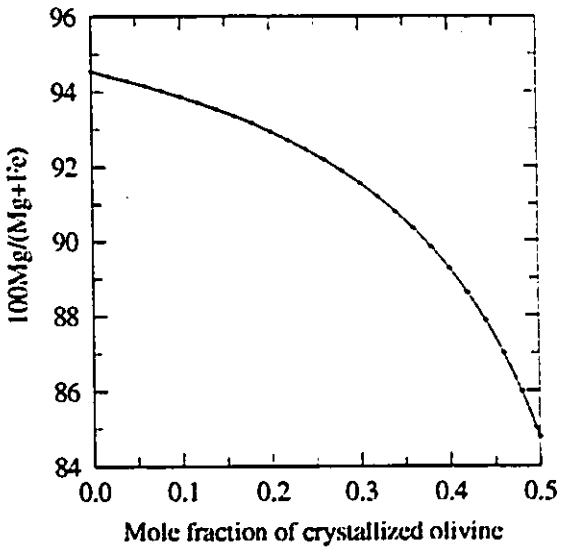

Fig. 4.1 Plot of calculated 100Mg/(Mg+Fe) vs. molar fraction of olivine crystallized from a batch of Pyke Hill komatiitic melt (Appendix 2). I have assumed perfect fractional crystallization, i.e., that ionic diffusion is negligible in the crystal but is very high in the liquid (or the liquid is mechanically well-mixed). The iteratively calculated Mg/(Mg+Fe) of the olivine is closely approximated ($r^2 = 0.999$) by the function 100Mg/(Mg+Fe) = $94.55 - 11.07\,F + 39.23\,F^2 - 98.91\,F^3$, where F is the mole fraction of olivine crystallized. Profiles similar to this have been measured by Arndt (1986a), Renner et al. (1994), and others in skeletal or plate-like olivine crystals. Points are only shown every 2 mol.%, although the iteration used 0.5 mol.% steps. For the mean compositions of melt and olivine, 50 mol.% olivine ≡ 45 wt.%.

Using (slightly modified) exchange partition coefficients from Beattie et al. (1991), I was able to closely match the concentrations of MnO, NiO, and CaO in the zoned olivines (Figs. **4.2–4.4**). Few data are available for the partitioning coefficients of Cr in olivine, so I chose coefficients to match the observed zoning (Fig. **4.5**, see also Section **4.1.2**). The data of Figs **4.6** and **4.7** are used to help determine the substitution mechanism of Cr in olivine (Section **4.1.2**)

A number of researchers (e.g., Arndt, 1986; Besson, 1988; Renner et al., 1994) have carried out microprobe traverses of olivine crystals from A and B-layers of flows. The most complete measurements of single-crystal zoning appear to be those of Besson (1988), but they have been published only in extremely abbreviated form. Accurate determinations of Mg and Fe in olivine are necessary because Fe increases only very gradually with crystallization of the first 15 mol% of olivine. In addition, the original $Fe^{2+}/(Fe^{2+}+Fe^{3+})$ of the melt must be estimated, the differentiation processes determined (i.e., the ratio of fractional crystallization, equilibrium crystallization, and open-system behavior), and the preservation of the zoning assessed (i.e., the extent of solid-state diffusion during subsolidus cooling). In this work the $Fe^{2+}/(Fe^{2+}+Fe^{3+})$ of the melt is derived from the composition of the most magnesian olivines in the chilled margins (mg# = 94.6) and from the best estimate of the original total iron content of the melt (~11.3 wt.% Fe_2O_3 total). The oxygen fugacity calculated from the estimated ferrous-ferric ratio and the bulk lava composition (Kress and Carmichael, 1991) is similar to that of present-day mid-ocean ridge basalts, about 2 (± 1) $\log_{10}$ units below the fayalite-quartz-magnetite (FMQ) oxygen buffer. Details of the calculations are contained in Appendix **2**.

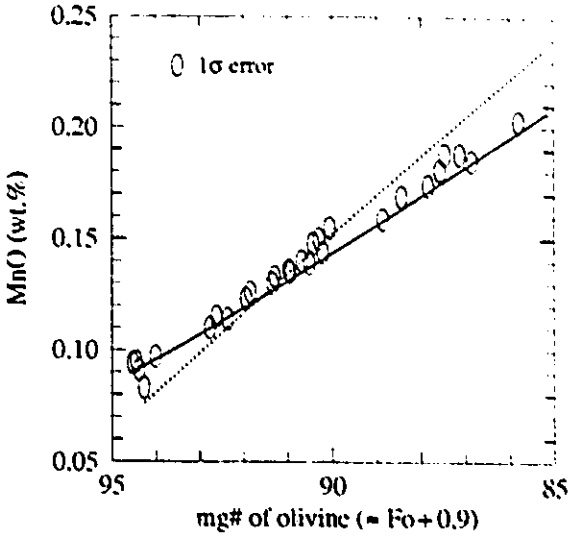

Fig. 4.2 MnO vs. olivine mg# in a group of 28 high-precision electron microprobe analyses covering nearly the entire compositional range of olivine from the Pyke Hill komatiites. The similar olivine-melt partitioning behavior of Mn^{2+} and Fe^{2+} is evident. The solid line was calculated assuming perfect fractional crystallization from the melt (see Section 4.1.1 for details); the dashed line uses the distribution coefficients of Beattie et al. (1991). The symbols are scaled to the size of the 1σ analytical error (±0.005 wt.% MnO; ±0.0013 Mg/(Mg+Fe)). Compare the simple behavior observed here with that of Cr, which has slightly improved analytical precision but much greater scatter (Fig. 4.5).

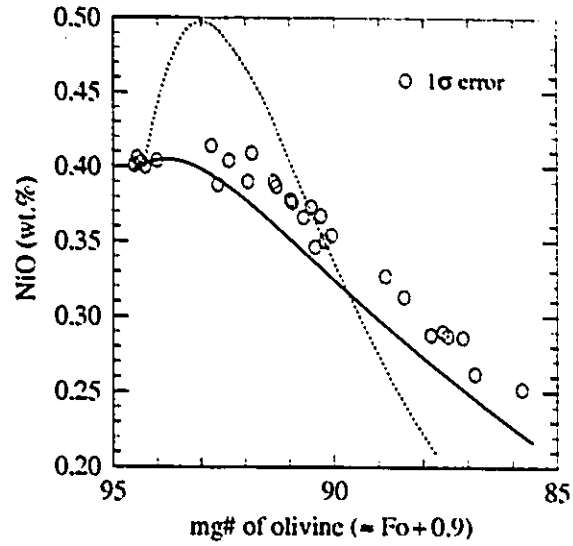

Fig. 4.3 NiO vs. mg# for the same group of 28 analyses as Fig. 4.2. The partition coefficient of Ni is low (~2.0) in the most Mg-rich komatiitic liquid, but increases as the liquid differentiates. For this reason NiO is nearly constant for mg# = 94.5 to 91.5, despite the crystallization of ~30 wt.% olivine (if perfect fractional crystallization occurred). The dashed line is calculated using the exchange coefficients of Beattie et al. (1991). Despite adjusting the Ni-Mg exchange coefficient to achieve a better fit to the observed NiO zoning pattern, the best fit I derived is consistently ~0.03 wt.% below the measured NiO in more Fe-rich olivines. Although small, this is considerably larger than the analytical uncertaintyof ±0.004(1σ) wt.% NiO (see Section 4.1.3).

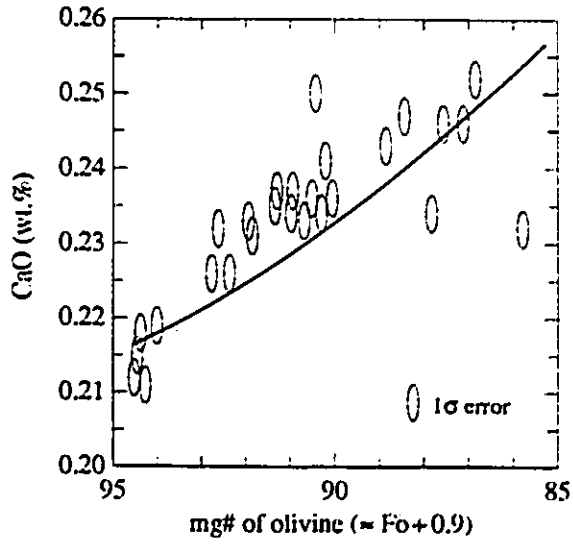

Fig. 4.4 CaO vs. mg# for the same group of 28 analyses as Fig. 4.2. CaO shows a weak, rather erratic variation with increasing Fe. Because one spectrometer on the microprobe would otherwise have been idle, the Ca peak and two background points were counted for 200 and 100 seconds each, reducing the 1σ error to ±0.0025 wt.% CaO. The curved line is the zoning calculated assuming perfect fractional crystallization. The relative increase with respect to the CaO concentration of chilled margin phenocrysts is +15%, much less than the +80% increase in the CaO concentration in the melt caused by ~45 wt.% olivine crystallization. The curve calculated using the exhange coefficients of Beattie et al. is a very poor fit to the observed zoning, and is not plotted (see Section 4.1.5).

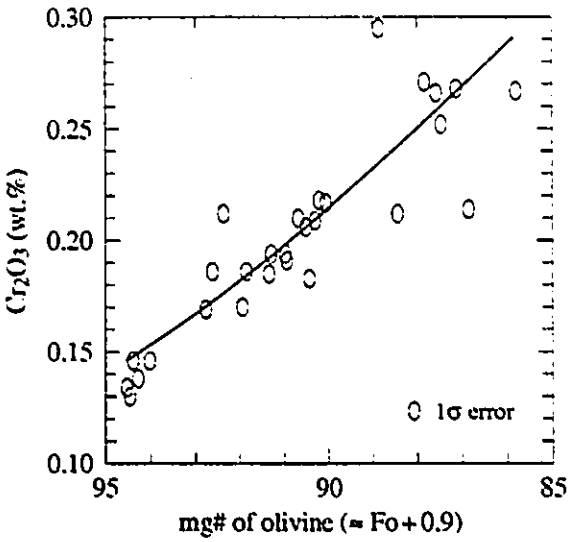

Fig. 4.5 Cr_2O_3 vs. mg# for the same 28 analyses as Fig. 4.2. The partitioning behavior of Cr is similar to that of Fe or Mn, but with much more scatter that is not due to analytical error (1σ precision is ±0.004 wt.% Cr_2O_3). The curved line is the zoning calculated for fractional crystallization with an empirical distribution coefficient (see Section 4.1.1). The various factors governing the entry of Cr into olivine are discussed at length in Section 4.1.2.

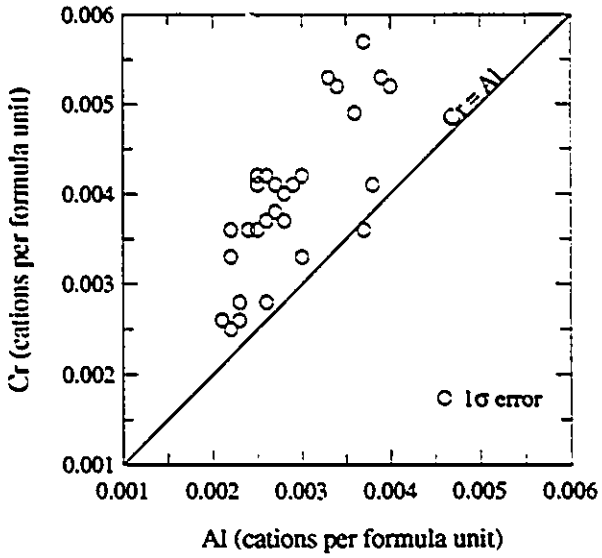

Fig. 4.6 High-precision analyses show that on a molar basis Cr is typically present in excess of Al. Because the Na-content of these olivines is negligible (<0.008 wt.% Na_2O), this excess implies either the presence of Cr^{2+} or a coupled substitution involving a vacancy in an olivine M-site (see Section 4.1.2 for discussion). The margins of olivine crystals in A_3 layers have the highest concentration of excess Cr, and olivine phenocrysts the lowest.

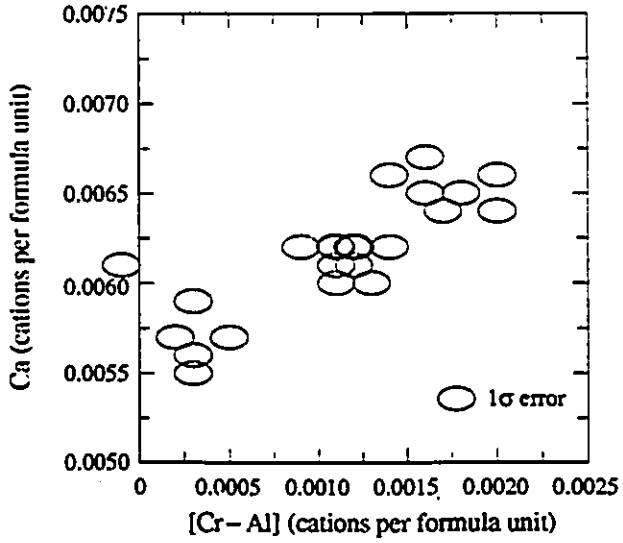

Fig. 4.7 Although close to the limits of analytical precision, there is a correlation between the concentration of Ca and that of excess Cr. This could be due to the small partial molar volume of several of the potential substitution mechanisms for Cr in olivine, which could favor the incorporation of the large Ca^{2+} cation. See Section 4.1.2 for details. All analyses are plotted, but several points in the central group are superimposed.

4.1.2 Chromium content of olivine

Introduction

Chromium is present in concentrations of 1000–2200 μg/g in komatiite olivines, a factor 10–20 times greater than olivine in typical terrestrial basalts, and 20–30 times that of olivine in spinel lherzolites. Only some lunar and meteoritic olivines, and a small percentage of olivine inclusions in diamond contain as much Cr. Donaldson (1982) considered five possible explanations for the high concentration of Cr in komatiitic olivine:

(a) delayed crystallization of Cr-spinel;
(b) rapid growth of olivine leading to disequilibrium partitioning behavior of Cr;
(c) high temperature and MgO in melt increasing the Cr partition coefficient;
(d) high concentration (2000–3000 μg/g) of Cr in komatiite melt;
(e) low f_{O_2} leading to increased Cr^{2+} in melt, with $D^{ol/L}_{Cr(III)} > D^{ol/L}_{Cr(II)}$.

Donaldson dismissed (b), since olivine crystals of different habit, grain size, distance from cooling contacts, and growth rate all have high Cr contents (however systematic variations exist; see below). Explanation (e) may be ruled out since olivines from komatiite experimental charges held at the relatively oxidizing Ni-NiO buffer also have high Cr. In addition, certain experiments show that the partition coefficient of Cr^{2+} is similar to that of Cr^{3+}, at least at low concentrations (see below). Donaldson dismissed explanation (a) on weaker grounds, namely that some komatiitic olivine crystals have inclusions of Cr-spinel. In fact, textural and compositional evidence (presented below) show that Cr supersaturation in the melt probably did occur due to delayed nucleation of Cr-spinel. Explanation (c) has not been supported by subsequent experiments and in fact is contrary to the behavior of Ni, another element with strong octahedral site preference that leads to its early partitioning from high-temperature melt into olivine. For explanation (d) to be correct, $D^{ol/L}_{CrO_*}$ must be higher than is commonly thought. The very low Cr content of olivine that crystallized concomitantly with Cr-spinel (i.e., in most basalts), or underwent prolonged diffusive exchange with orthopyroxene, diopside, Cr-spinel, or garnet (i.e., in peridotites) may be misleading, and in fact several recent experiments show that $D^{ol/L}_{CrO_*}$ is actually similar to $D^{ol/L}_{FeO_*}$ (see below).

Crystal chemistry of Cr

The crystal chemistry of Cr in olivine is complex, in part because it can enter in the +2, +3, or +4 valence state (Scheetz and White, 1972; Rager et al., 1991). Because it is a promising material for a tunable near-IR laser, considerable work has been done in recent years to grow and characterize Cr-doped forsterite. Optical spectra show the presence of all three valence states in certain such crystals grown in Ar (because of traces of O_2 and H_2O such atmospheres are typically oxidizing, with $-6 \leq \log_{10} f_{O_2} \leq -5$). Multiple valences, including electrochemically unstable combinations such as Cr^{2+} and Cr^{4+}, are presumably stabilized in different crystal sites. A simpler example of this phenomenon occurs at low f_{O_2} in the Fe–O system, where wüstite ($Fe_{1-x}O$, or $Fe^{2+}_{1-3x}Fe^{3+}_{2x}O$) or magnetite ($Fe^{2+}Fe^{3+}_2O_4$) is in equilibrium with oxygen-saturated metallic iron (Fe^0).

Certain Cr ions (Cr^{2+}, Cr^{3+}, and Cr^{4+}) gain high crystal field stabilization energies (CFSE) in octahedral sites, which favors the crystallization of particular minerals and suppresses that of others. This is one reason for the stability and widespread occurrence of chromite and the rarity of Cr^{2+}-bearing minerals. Few studies have specifically examined the partitioning of Cr into olivine, but in a number of others the distribution coefficient can be determined from the Cr content of coexisting olivine and glass, or less accurately from the Cr content of olivine and the initial sample (e.g., Green et al., 1975; Akella et al., 1976; Huebner et al., 1976; Schreiber and Haskin, 1976; Arndt, 1976; Murck and Campbell, 1986; Agee and Walker, 1990). Unfortunately, the earlier studies are hampered by relatively low-quality microprobe analyses, and the usefulness of some of the newer studies is limited by incomplete (e.g., Al or Na are omitted) or relatively low precision (e.g., energy dispersive detector) analyses. I have examined data from two recent studies (Murck and Campbell, 1986; Agee and Walker, 1990). These comprise 41 usable olivine–glass pairs that define a $K_{D\,Cr/Mg}^{ol/L}$ of 0.20–0.26 over a wide range of temperature, pressure, and oxygen fugacity. This value is reasonably close to the exchange partition coefficient of 0.21 that I have estimated for zoned komatiitic olivines crystallizing before Cr-spinel (see below). The consistency of the Cr distribution coefficient over large changes in f_{O_2} would appear to indicate that $D_{Cr(III)O^{\bullet}}^{ol/L} \approx D_{Cr(III)O^{\bullet\bullet}}^{ol/L}$.

Effect of ionic radius on olivine–melt partitioning of elements

Assuming that Cr in olivine is present in near-equilibrium concentrations, it is necessary to determine how it is accommodated in the mineral structure. The composition and crystal structure of olivine are relatively inflexible: Si is always very close to 1 atom per formula unit (a.p.f.u.); Na, Al and Ti are generally $<<0.01$ a.p.f.u.; and Ca in non-calcic olivines (i.e., excluding $Ca(Mg, Fe, Mn)SiO_3$) rarely exceeds ~0.01 a.p.f.u.

The importance of the charge and effective ionic radius of M-site cations was shown by Beattie (1994), who modeled the effect of lattice strain energy upon olivine–liquid partition coefficients. The unit cell volume (V) of many olivines is controlled by the mean radius of the M-site cation. This is shown in Fig. **4.8**, in which V is plotted against the mean of the cubed cation radius (R); i.e.:

$$R = \sum_{i=1}^{n} X_i \cdot (r_i)^3$$

where X_i is the mole fraction and r_i the ionic radius of the ith element in the M1 or M2 site. Table **4.1** summarizes the effective ionic radii and crystal field stabilization energies of cations capable of significant substitution ($D_{MO_x}^{oil/L} > 0.01$) in olivine.

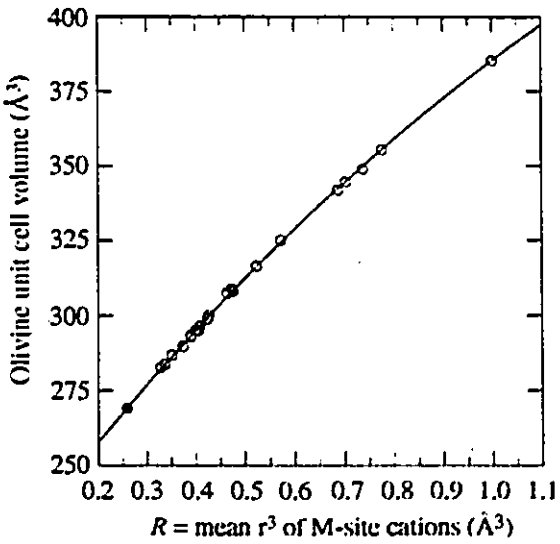

Fig. 4.8 Olivine unit-cell volume is a smooth function of the mean cubed radius of the M1 and M2 site cations (R). Here cell volumes of 18 silicate olivines containing divalent cations (Mg, Ca, Cr, Mn, Fe, Co, Ni, and Zn), plus LiSc, $Li_{0.5}Sc_{0.5}Mg$, and LiIn olivines and laihunite ($Fe_3Si_4O_8$) have a best-fit equation of $V(Å^3) = -45.0\ R^2 + 213.3\ R + 217.1$ (r^2=0.9996). Extrapolation to a hypothetical $MgCr_2Si_4O_8$ laihunite-type mineral gives a unit-cell volume of 269.2 Å³ (filled symbol). Symbols are larger than the relative uncertainty of cation radii (± 0.005 Å). The relative uncertainty of R is much larger than that of a typical unit-cell volume measurement (± 0.1–0.2 Å³). Data from Brown (1982), Deer et al., (1982), and others.

Table 4.1 Nominal radii of ions in tetrahedral or octahedral coordination with oxygen

Ion	radius (pm)	CFSE (kJ/mol)	Ion	radius (pm)	CFSE (kJ/mol)	Ion	radius (pm)	CFSE (kJ/mol)
$^{[4]}Si^{4+}$	26	0	$^{[6]}Al^{3+}$	53.5	0	$^{[6]}Co^{2+}$	74.5	-90
$^{[4]}Al^{3+}$	39	0	$^{[6]}Ti^{4+}$	60.5	0	$^{[6]}Li^{+}$	76	0
$^{[4]}Cr^{4+}$	41	-110	$^{[6]}Cr^{3+}$	61.5	-250	$^{[6]}Fe^{2+}$	78	-50
$^{[4]}Ti^{4+}$	42	0	$^{[6]}Fe^{3+}$	64.5	-0	$^{[6]}Cr^{2+}$	80	-95
$^{[4]}Cr^{3+}$	45*	-70	$^{[6]}Ni^{2+}$	69	-120	$^{[6]}Mn^{2+}$	83	-0
$^{[4]}Fe^{3+}$	49	-0	$^{[6]}Mg^{2+}$	72	0	$^{[6]}Ca^{2+}$	100	0
			$^{[6]}Zn^{2+}$	74	0	$^{[6]}Na^{+}$	102	0

Radii data from Shannon (1976), Smyth and Bish (1988), and Burns (1993). Where applicable, the ionic radius of the high-spin state is given. *Estimated value.

Substitutional mechanisms of Cr in olivine

The entry of significant amounts of Cr into olivine in komatiites can be explained by a number of (not necessarily exclusive) substitution mechanisms. I have ranked six of these in descending order of likelihood in Table 4.2.

Table 4.2 Potential substitution mechanisms for Cr in olivine

Substitution	Substitution mechanism
(1)	$^{[6]}Cr^{3+} + {}^{[4]}Al^{3+} \rightleftharpoons {}^{[6]}Mg^{2+} + {}^{[4]}Si^{4+}$
(2)	$2\ {}^{[6]}Cr^{3+} + {}^{[6]}\square \rightleftharpoons 3\ {}^{[6]}Mg^{2+}$ ($^{[6]}\square$ = octahedral site vacancy)
(3)	$^{[6]}Cr^{2+} \rightleftharpoons {}^{[6]}Mg^{2+}$
(4)	$^{[6]}Cr^{3+} + {}^{[6]}Na^{+} \rightleftharpoons 2\ {}^{[6]}Mg^{2+}$
(5)	$^{[4]}Cr^{4+} \rightleftharpoons {}^{[4]}Si^{4+}$
(6)	$^{[6]}Cr^{3+} + {}^{[4]}Cr^{3+} \rightleftharpoons {}^{[6]}Mg^{2+} + {}^{[4]}Si^{4+}$

•Mechanism (1): $^{[6]}Cr^{3+} + {}^{[4]}Al^{3+} \rightleftharpoons {}^{[6]}Mg^{2+} + {}^{[4]}Si^{4+}$

Cr^{3+} gains a large CFSE in octahedral coordination, facilitating its entry into olivine M1 or M2 sites (Burns, 1993). Because of its small size and large CFSE, $^{[6]}Cr^{3+}$ should, by analogy with $^{[6]}Ni^{2+}$, preferentially occupy the M1 site (Burns, 1993). One study of synthetic Cr-doped forsterite found Cr occupying both M1 and M2 sites in approximately 3:2 ratio (Bershov et al., 1983). However the Czochralski-grown crystals in that study were formed at high temperatures (~1900 °C) and cooled rapidly. A "quenched-in" disordered distribution of Cr may have been preserved if the energy difference between M1 and M2 sites is small.

The replacement of $^{[4]}Si^{4+}$ by the larger $^{[4]}Al^{3+}$ (~13 pm greater nominal radius) ion would lead to distortion of adjacent M1 and M2 octahedral sites. The low concentration of Al in olivines indicate that this distortion is not favored by the olivine structure (Deer et al., 1982; Agee and Walker, 1990; Beattie, 1994). Because the effective radius of $^{[6]}Cr^{3+}$ is ~11 pm smaller than $^{[6]}Mg^{2+}$, both elastic strain and electrostatic potential energy would be minimized if $^{[4]}Al^{3+}$ and $^{[6]}Cr^{3+}$ occupied adjacent T and M sites. Bershov et al. (1983) presented experimental evidence for such nearest-neighbour pairing in Czochralski-grown forsterite crystals. This substitutional mechanism was favored by Colson et al. (1989) for the substitution of Cr^{3+} in olivine and by Beattie (1994) for the general substitution of trivalent ions in olivine. In his energy calculations Beattie implicitly assumed that the M^{3+} and Al^{3+} ions are closely spaced.

Crystallization at high temperatures would favor the entry of Cr^{3+} and Al into olivine. At lower temperatures the $MgCrAlO_4$ component will be less soluble in olivine, which accounts for the simultaneous crystallization of Cr-spinel and Cr-poor olivine in common basaltic melts. Slow cooling or prolonged metamorphic heating of Cr-rich olivine would permit the exsolution of Cr-spinel that is observed in some dunites and komatiitic olivine adcumulates (e.g., Arai, 1978). A balanced reaction without oxidation or exsolution of orthopyroxene or silica is:

$$((Mg,Fe^{2+})_{2-x}Cr_x^{3+})Si_{1-x}Al_xO_4 \rightarrow (1-x)(Mg,Fe^{2+})_2SiO_4 + x(Mg,Fe^{2+})Cr^{3+}AlO_4$$

(Cr-bearing olivine) (Cr-free olivine) (spinel)

•Mechanism (2): $2\ ^{[6]}Cr^{3+} + {}^{[6]}\square \rightleftharpoons 3\ ^{[6]}Mg^{2+}$ ($^{[6]}\square$ = vacancy in octahedral site)

Olivines containing transition elements such as Fe are not strictly stoichiometric because small deficiencies or surpluses of metal or oxygen can be accommodated by vacancies, interstitial substitutions, or multiple metal valences. Oxidized olivine containing significant amounts of Fe^{3+} is common in altered rocks; the endmember mineral is laihunite ($Fe^{2+}Fe^{3+}_2Si_2O_8$), which has a structure similar to olivine but with M2 sites occupied by Fe^{3+} and half of the M1 sites vacant due to the substitution $2\ ^{[6]}Fe^{3+} + {}^{[6]}\square \rightleftharpoons 3\ ^{[6]}Fe^{2+}$ (Deer et al., 1982). The common occurrence of "ferriolivine" domains in naturally or artificially oxidized olivine (e.g., Khisina et al., 1995) indicates that its energy of formation is not particularly high. In synthetic Fo_{80} the equilibrium concentration of M-site vacancies is between 0.001% and 0.01% at temperatures and f_{O_2} relevant to komatiite crystallization (Nakamura and Schmalzried, 1983). This mechanism was also suggested by Colson et al. (1989) for Sc^{3+} and Yb^{3+}-bearing olivines (with M^{3+} > Al). The ionic radii of $^{[6]}Sc^{3+}$ and $^{[6]}Yb^{3+}$ are considerably larger than that of $^{[6]}Cr^{3+}$ (74.5, 86.8, and 61.5 pm, respectively), so a substitution of these elements that minimizes expansion (e.g., involves a vacancy) would be favored in olivine over one that increases it (e.g., involves $^{[4]}Al \rightleftharpoons {}^{[4]}Si$).

Assuming that the M–O bonding of olivine is predominantly ionic, the substitutions of Cr^{3+} and $\square^0$ for Mg^{2+} can be treated respectively as point charges of $+e$ and $-2e$ in the crystal lattice (Greenwood, 1968). The minimum electrostatic potential energy configuration will occur when a linear $Cr^{3+} - \square - Cr^{3+}$ array occupies adjacent M sites. Five distinct orientations are possible in olivine (spacings in Fo_{90} from Brown, 1982):

- M1–M1: 2.997 Å along [001];
- M1–M2: 3.210 Å along [011], 3.585 Å along [122], 3.650 Å along $[1\bar{2}1]$;
- M2–M2: 3.869 Å along [101].

The electrostatic potential energy (U) of these substitutions can be estimated by calculating the interaction of the point charges:

$$U = \frac{1}{4\pi\varepsilon_0 K}\left(\frac{+e(-2e)}{d_{Cr(1)-V}} + \frac{+e(-2e)}{d_{Cr(2)-V}} + \frac{+e(+e)}{d_{Cr(1)-Cr(2)}}\right)$$

where ε_0 is the permittivity of free space (8.854×10^{-12} F m^{-1}), e the elementary charge unit (1.602×10^{-19} C), K the bulk dielectric constant of forsterite (~7), and d_{i-j} the distance between point charges i and j. These simplified calculations neglect lattice strain

and nearest neighbor effects such as O^{2-}–O^{2-} repulsion around the vacancy. More rigorous calculations of defect energies in olivine (Hirsch and Shankland, 1993; Wright and Catlow, 1994) do not treat this type of "grown-in" nonstoichiometric defect; however their data indicate that the free energy of the $3\,Fe^{2+} \rightleftharpoons 2\,Fe^{3+} + \square^{0}$ substitution would be on the order of ~6 eV. This would be lowered by the CFSE of Cr^{3+} and the electrostatic potential energy of the defect array, but raised by the configurational entropy of the clustered ions. Regardless of the details, it is clear that clustering of the vacancy and Cr^{3+} ions is strongly favored and that the free energy of the all-M1 occupancy is –0.16 eV (~15 kJ/mol) lower than any other configuration (Table **4.3**). At closest separation, the electrostatic energy per Cr^{3+} ion is –1.2 eV (≈–117 kJ/mol). Because the hypothesized cluster is an electric quadrupole—with an electric field falling off as the fourth power of distance—it would interact only weakly with other clusters.

Table 4.3 Electrostatic potential energy of colinear $Cr^{3+} - \square^{0} - Cr^{3+}$ arrays in olivine

Occupied sites: Site spacing	0–1–2	0–1–3	0–1–4	0–2–4	0–2–5	0–2–6	0–3–6
2.997 Å	–2.41 eV	–1.83	–1.66	–1.21	–1.01	–0.92	–0.81
3.210 Å	–2.25	–1.71	–1.55	–1.12	–0.94	–0.86	–0.75
3.585 Å	–2.01	–1.53	–1.39	–1.01	–0.85	–0.77	–0.67
3.650 Å	–1.98	–1.51	–1.37	–0.99	–0.83	–0.75	–0.66
3.869 Å	–1.87	–1.42	–1.29	–0.93	–0.78	–0.71	–0.63

Assuming that mechanism (2) applied to Cr-bearing olivine, Arai (1978) suggested that the large $^{[6]}Ca^{2+}$ ion might be preferentially incorporated into M2 sites near Cr-occupied M1 sites due to the slight expansion of the former allowed by the vacancy and the small $^{[6]}Cr^{3+}$ ions. This is discussed in Section **4.1.4**.

•Mechanism (3): $^{[6]}Cr^{2+} \rightleftharpoons {}^{[6]}Mg^{2+}$

This substitution has been proposed for certain lunar and meteoritic olivines and experimentally demonstrated up to 25 mol% Cr (Scheetz and White, 1972; Li et al., 1995). At the f_{O_2} of komatiite magmas (calculated from olivine and whole-rock compositions), approximately equal amounts of Cr^{2+} and Cr^{3+} should be present in the melt (Roeder and Reynolds, 1991). The octahedral CFSE of Cr^{2+} is 90–100 kJ/mol, but

the ion is large (~80 pm radius) and due to the Jahn-Teller effect has a strong preference for axially elongated octahedral sites approaching square-planar geometry (Burns, 1993). In consequence, pure Cr_2SiO_4 does not have the olivine structure (Scheetz and White, 1972; Dollase et al., 1994). Provided that the total energy (CFSE, electrostatic potential energy, lattice strain energy) of the Cr^{3+} ion is lower than that of the Cr^{2+} ion then the former will be more compatible in olivine. Thus the partition coefficient of Cr^{3+} in olivine may be—anomalously—greater than that of Cr^{2+}, at least in Al-bearing melts and at low concentrations (e.g., Murck and Campbell, 1986; Agee and Walker, 1990). Synthetic olivine grown from Al-free constituents will have only mechanisms (2) and (3) available for the incorporation of Cr. Therefore the Cr^{2+}/Cr^{3+} in olivine at a given f_{O_2} may differ significantly between Al-free and Al-bearing melts.

Several criteria indicate that molten komatiites contained Fe^{3+}: the calculated Fe^{3+}/Fe^{2+} was 0.05–0.10 from estimated f_{O_2} values, a similar ratio can be derived from olivine–melt Fe contents, and Fe^{3+} is present in primary Cr-spinel (Zhou and Kerrich, 1992; my own microprobe analyses and a Mössbauer spectrum, acquired through the courtesy of Dr. A. E. Lalonde). However, this does not rule out Cr^{2+} as a melt species. The high concentration of Fe in the melt would have buffered $[Cr^{2+}]/[Cr^{3+}]$ by electron exchange between species, i.e., $Cr^{2+} + Fe^{3+} \rightleftharpoons Cr^{3+} + Fe^{2+}$ (c.f. Huebner et al., 1976). I make the not unreasonable assumption that the equilibrium constant of this redox reaction is lower in 1600–1700 K silicate melts than in 300 K aqueous solutions, where it is very large ($K \approx 10^{25}$); Roeder and Reynolds (1991) made the same assumption implicitly. As Cr^{3+} was removed from the melt into olivine or Cr-spinel, some of the remaining Cr^{2+} ions would have donated an electron (i.e., oxidized) to maintain $[Cr^{2+}]/[Cr^{3+}]$ near the equilibrium value.

•Mechanism (4): $^{[6]}Cr^{3+} + {}^{[6]}Na^{+} \rightleftharpoons 2\ {}^{[6]}Mg^{2+}$

The closest natural equivalent to this substitution would be the pyroxenes diopside ($CaMgSi_2O_6$) and kosmochlor ($NaCrSi_2O_6$). However, Na^+ has an excessively large ionic radius for the olivine M2 site and is monovalent, so the Na content of natural olivines is always very low. Of the alkali elements, only Li^+ is suitably sized (76 pm) for olivine. The continuous series Mg_2SiO_4–$LiScSiO_4$ has been synthesized (Ito, 1977), which suggests that a partial Mg_2SiO_4–$LiCrSiO_4$ series could exist. Forsterite with up to 1.25 wt.% Cr_2O_3, charge-balanced by an equimolar amount of Li, has been synthesized (Ito, 1977).

However, it is doubtful that complete solution exists: under similar conditions used to synthesize $LiScSiO_4$, a stoichiometric mixture of Li_2CO_3, Cr_2O_3, and SiO_2 reacts to form a mixture of $LiCrO_2$ and $LiCrSi_2O_6$ instead of $LiCrSiO_4$ (my experiments). In any event, the low concentration of Li in komatiite olivine (~1 µg/g; Richard et al., 1996) means that the substitution $^{[6]}Cr^{3+} + {}^{[6]}Li^{+} \rightleftharpoons 2\ {}^{[6]}Mg^{2+}$ will be insignificant.

•Mechanism (5): $^{[4]}Cr^{4+} \rightleftharpoons {}^{[4]}Si^{4+}$

This is an uncommon valence state of Cr, but occurs in some Cr-doped (100–300 µg/g Cr) forsterite crystals synthesized in air or oxygen (Rager et al., 1991). The radius of $^{[4]}Cr^{4+}$ is close to that of $^{[4]}Al^{3+}$, an ion known to substitute for $^{[4]}Si^{4+}$ in some silicates. The CFSE of $^{[4]}Cr^{4+}$ (~110 kJ/mol) would not directly aid this substitution in forsterite because any Cr^{4+} in the melt is also likely to occur in tetrahedral coordination; however it could promote the reduction of tetrahedrally coordinated Cr^{6+} (CFSE = 0) to Cr^{4+}. The latter ion has not been reported in minerals, as the $(CrO_4)^{2-}$ anion is favored under low-temperature oxidizing conditions, and Cr^{3+} under most other terrestrial conditions. At the f_{O_2} relevant to the crystallization of komatiites Cr^{4+} is unlikely to be an important species and therefore will not be discussed further.

•Mechanism (6): $^{[6]}Cr^{3+} + {}^{[4]}Cr^{3+} \rightleftharpoons {}^{[6]}Mg^{2+} + {}^{[4]}Si^{4+}$

Tschermak's substitution ($^{[6]}Al^{3+} + {}^{[4]}Al^{3+} \rightleftharpoons {}^{[6]}M^{2+} + {}^{[4]}Si^{4+}$) is important in pyroxenes and amphiboles crystallized at high pressures. However mechanism (6) is highly unlikely because the octahedral to tetrahedral site preference energy of Cr^{3+} in oxides exceeds 150 kJ/mol (Burns, 1993). The $^{[4]}Cr^{3+}$ ion is also significantly larger than $^{[4]}Si^{4+}$. This substitution will not be discussed further.

Chromium substitution in Pyke Hill olivines

To assess which of the above substitutional mechanisms apply to komatiite olivine requires the accurate analysis of several elements (Na, Al, and Cr) that are present in low concentrations and not typically analyzed in olivine. [At present there is no feasible method to measure the concentration of vacancies in these crystals.] Sample preparation and analytical procedures are critical: e.g., the Al content of olivine is generally quite low ($<<1\%\ Al_2O_3$), but erroneous electron microprobe analyses can be caused by surfaces contaminated with alumina polishing compounds, or secondary fluorescence of nearby

Al-rich minerals. Therefore I carried out special, high-precision microprobe analyses of selected olivine crystals (details in Appendix 3).

Both routine and high-precision analyses of olivine show that Cr concentration varies in a seemingly erratic fashion. The trend defined by chilled margin phenocrysts (Cr ≡ 1000 μg/g) and plate-like olivines in A_3 layers (Cr up to 2500 μg/g) can be approximated by assuming that $K_{D\,Cr/Mg}^{ol/L} = 0.21$. This is very close to the values that can be determined from the experimental data of Murck and Campbell (1986) and Agee and Walker (1990). The highest levels of Cr in olivine may be due to delayed nucleation of Cr-spinel in the rapidly cooled spinifex-textured layers; in the more slowly cooled B-layer, Cr-spinel presumably nucleated and grew at a higher temperature, lowering the concentration of Cr in the melt and by consequence in co-crystallizing olivine.

The high-precision data clearly show that there is insufficient Na in the olivines for mechanism (4) to be of any significance (Na_2O averages 0.004 wt.%, which is below the 3σ lower limit of detection of 0.008 wt.%). Sufficient Al is present (0.075–0.136 wt.% Al_2O_3) to charge-balance from 50 to 100% of the Cr via substitution mechanism (1) if the Al occupies tetrahedral sites (Fig. 4.6).

The direct detection of $^{[4]}Al$ in these olivine crystal would be difficult as there are only 2–4 Al atoms per 1000 Si atoms. This concentration is well below the resolution of nuclear magnetic resonance or single-crystal XRD structural refinement. It might be possible to determine Al site occupancy using X-ray absorption near edge structure (XANES) spectroscopy, but only after a substantial amount of preparatory work.

In olivine phenocrysts from chilled margins and in the cores of olivine from spinifex-textured layers Cr ≡ Al; excess Cr is generally restricted to the margins of the latter crystals. Increased substitution of Cr^{2+} into these crystals seems unlikely because the melt should have become more oxidized with falling temperature and the transfer of Fe^{2+} from the melt into olivine. Instead I suggest that mechanism (2) becomes important, particularly in the margins of strongly zoned crystals. Accounting for Cr^{3+} not charge-balanced by $^{[4]}Al$ requires vacancies in up to 0.15% of normally filled octahedral sites. This is more than an order of magnitude higher than the concentration expected in pure $(Mg_{0.8}Fe_{0.2})_2SiO_4$, but could be explained by a combination of $^{[6]}Cr^{3+}$ CFSE, compressive stress in the crystal margins, and possibly the relatively fast crystal growth rate. Unlike laihunite, the M-site vacancies in Cr-substituted olivine are probably disordered because

the maximum 0.15% is equivalent to just one vacancy per 80 unit cells. As noted above the electrostatic potential energy would be minimized by a linear array of Cr^{3+} – □ – Cr^{3+} ions along neighbouring M1 or M2 sites.

The possible role of strain in Cr-bearing zoned olivine crystals

Olivine unit-cell dimensions increase with FeO content. In olivine of composition Fo_{90}, the fractional change in lattice parameters for a 1% increase in fayalite content is +170 ppm for *a*, +280 ppm for *b*, and +190 ppm for *c* (Schwab and Küstner, 1977). A dislocation-free olivine crystal that showed normal zonation of Fe/Mg would have an interior in tension and an outer layer in compression. Olivine crystals in spinifex-textured layers are typically zoned from Fo_{92} to Fo_{84}. Such crystals have a pronounced plate-like habit (much thinner parallel to *b*), and the internal strain is probably anisotropic. In analogy to compositionally zoned semiconductor single crystals (e.g., Wagner et al., 1989), the unit cell of olivine is likely be tetragonally distorted, with shortening along *a* and *c* and compensatory expansion along *b*. The bulk strain in such crystals would be ~0.1%; given that olivine at 1300 °C has a compressibility of $\sim 1\times10^{-6}$ bar^{-1} and a Poisson's ratio of 0.24 (Isaak et al., 1989), this implies internal stresses of 1–2 kbar.

The compressive stress in zoned olivine crystals could be lowered by the creation of misfit dislocations, vacancies, or the preferential incorporation of small cations into M sites. The unit cell volumes of different olivines is a smooth function of the effective radii of the M-site cations (Brown, 1982; Fig. 4.8). Substitution mechanism (2) will reduce the unit cell volume because the radius of $^{[6]}Cr^{3+}$ is smaller than that of $^{[6]}Mg^{2+}$. The effective radius of a vacancy is less clear. Beattie (1994) assumed a minimum M-site radius of ~58 pm based on the tangential contact of six O^{2-} ions (radii of 140 pm), and I use this value for the vacancy. The unit-cell volume of a hypothetical "laihunite-type" chromian olivine is estimated by assuming that it has the same dependency upon the M-site cation radius as do other olivines (Table 4.4). [Endmember $MgCr_2Si_2O_8$ is thermodynamically unstable; an assemblage of eskolaite, enstatite, and tridymite (Cr_2O_3 + $MgSiO_3$ + SiO_2) or magnesiochromite and tridymite ($MgCr_2O_4$ + SiO_2) forms in its place (Li et al., 1995). We are interested in the partial molar volume of a "Cr-laihunite" component present in minor amounts (i.e., <1%).] Due to its very small unit-cell volume (269.2 Å^3), the substitution $2\ ^{[6]}Cr^{3+} + {}^{[6]}\square^{0} \rightleftharpoons 3\ ^{[6]}Mg^{2+}$ would reduce the lattice strain energy within the margins of the zoned crystals and thus be energetically favored. A

similar argument has been made (Tiller, 1991b, p. 391) for the cooperative substitution of O and C in silicon (molecular volumes: Si ≡ 20 Å^3; SiO_2 ≡ 45.5 Å^3; SiC ≡ 10 Å^3).

Table 4.4 Volume change of olivine and laihunite-type minerals

Mineral pairs	Substituting cations & radii	Replaced cations & radii	Unit-cell volume(Å^3)
Fayalite → laihunite	2 $^{[6]}Fe^{3+}$ + $^{[6]}\square$ 64.5 and ~58 pm	3 $^{[6]}Fe^{2+}$ 78 pm	307.54 → 283.9
Forsterite → $MgCr_2Si_2O_8$[1]	2 $^{[6]}Cr^{3+}$ + $^{[6]}\square$ 61.5 and ~58 pm	3 $^{[6]}Mg^{2+}$ 72 pm	289.94 → 269.2[1]
Fo_{92} → Fo_{86}	0.06 Fe^{2+} 78 pm	0.06 Mg^{2+} 72 pm	291.45 → 292.58

Data from Schwab and Küstner (1977) and Deer et al. (1982).

[1] Estimated volume of hypothetical endmember compound.

Other manifestations of intracrystalline strain

Many different heteroepitaxially grown semiconductor crystals (e.g., $In_{1-x}Ga_xAs$ grown on InP) contain regularly spaced lattice-controlled arrays of misfit dislocations separating regions of greater crystallographic perfection (Wagner et al., 1989). This phenomenon occurs when the epitaxial phase grows under compression because its lattice parameters are larger than those of the substrate, and is termed "cross-hatching". A similar effect could account for the unusual shape of certain relict olivine grains. Whereas relict olivine in partially serpentinized equant crystals in chilled margins or the B-layer has irregular, rounded boundaries, relict olivine in the A_3 layer tends to form semi-regular rectangular parallelepipeds with dimensions 50–150 μm ($\| a$) by 20–50 μm ($\| b$) by 30–100 μm ($\| c$) (Photos **4.1** and **4.2**). Serpentinization appears to have acted as a natural etching process that preferentially altered dislocation-rich domains of the olivine crystals. The preferred orientation of the patterns is not explained by the weak {100} and {010} cleavages found in olivine. In addition, the Pyke Hill komatiites are undergone so little strain that the much better {110} cleavage of clinopyroxene is rarely visible.

Photo 4.1 View looking down the *b* axis of a plate-like olivine crystal from the A_3 layer of a Pyke Hill flow. The *a* axis is parallel to the long edge of the photomicrograph. The crystal is distinctly divided into rectangular domains of unaltered olivine separated by serpentine and magnetite. I hypothesize that this could be due to concentrations of misfit dislocations that form during the growth of compositionally-zoned single crystals (see text). For an alternative possibility, see below. Plane-polarized light, 2 mm field of view.

Photo 4.2 View of a partially serpentinized plate-like crystal (same flow as Photo **4.1**) with *b* approximately parallel to the short edge of the photomicrograph. Fracturing and alteration may have started at stress concentrations such as near the base of terraces or reentrants. [One possible source of stress is the expansion created during serpentinization, which involves some circular reasoning.] The film was underexposed; the olivine is actually water-clear in thin section. Plane-polarized light; 500 μm field of view.

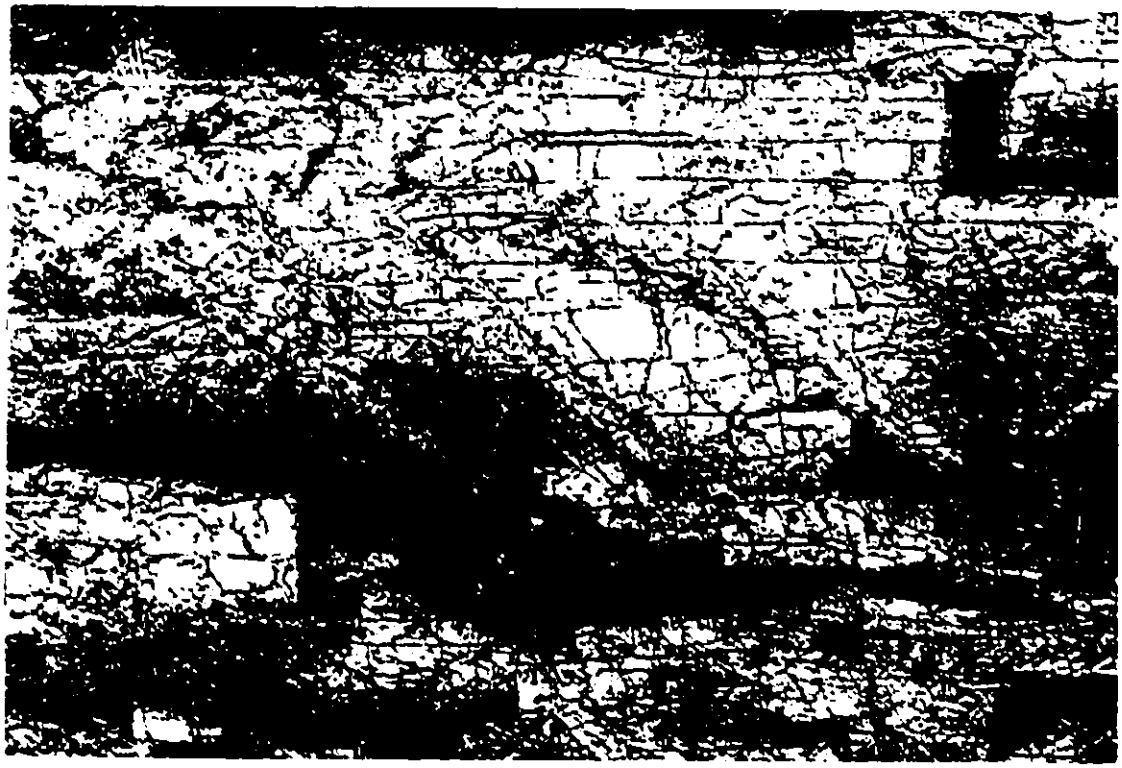

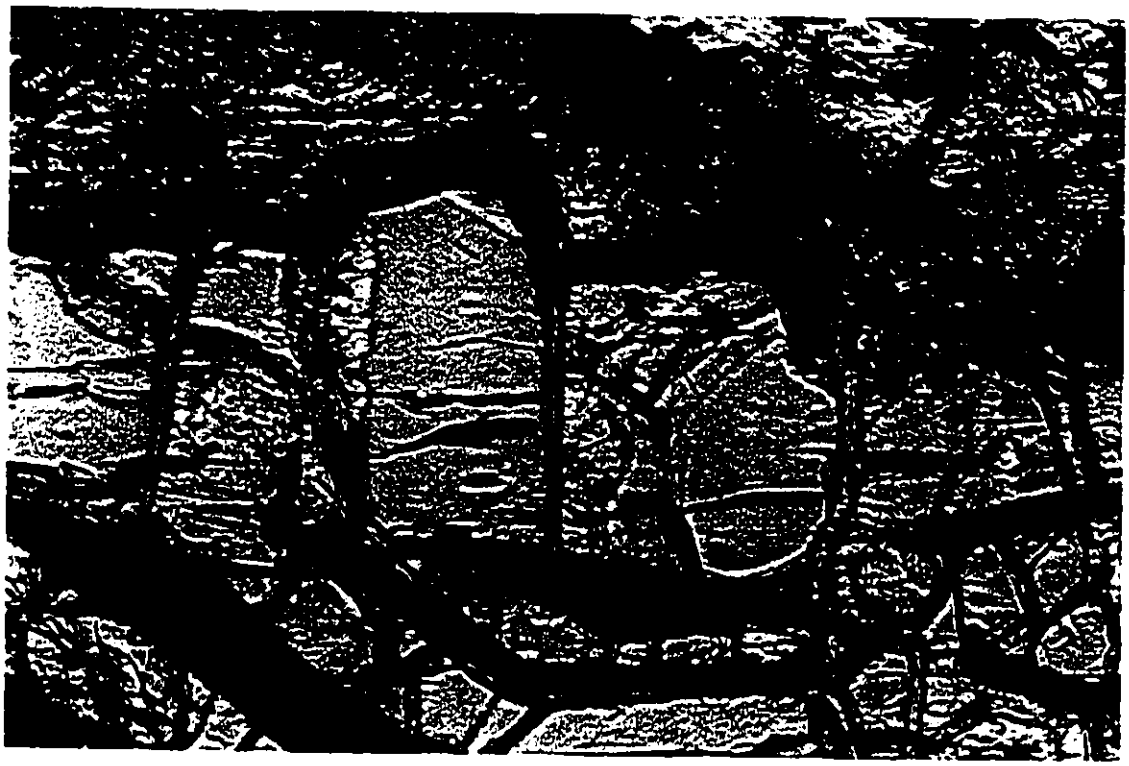

Direct measurement of Cr valence state

The valence state(s) of Cr could be determined with optical spectroscopic data but the olivine grains available from the Pyke Hill flows are somewhat small for this method. The molar absorption coefficient of Cr^{3+} in olivine is similar to that of other silicates, i.e., roughly 20 cm^{-1} mol^{-1} at ~480 nm (Rager et al. 1991; Taran et al., 1994). However the largest unaltered fragments in doubly-polished thick sections are only ~300 µm by 300 µm by 100 µm thick, and Ni^{2+} absorption bands would partly overlap those of Cr^{3+} (Burns, 1993). In addition, any Cr^{2+} absorption bands present would be obscured by the edges of Fe^{2+} bands (Burns et al., 1973). No Cr isotope exhibits the Mössbauer effect, so that method cannot be used to determine Cr valence states. Measurement of the wavelength shift of the Cr Lα and Lβ X-ray peak caused by changes in valence and oxygen coordination is not feasible because the Cr L photoemissions are extremely weak and are located on the shoulders of the oxygen Kα peak. Electron paramagnetic resonance can detect Cr^{3+}, Cr^{4+}, and Cr^{5+}, but not Cr^{2+}, requires inconveniently large samples, and would be complicated by the high concentration of Fe^{2+} in natural olivine. X-ray absorption near-edge structure (XANES) spectroscopy using synchrotron radiation could resolve the problem (Sutton et al., 1993). Steve Sutton (at the University of Chicago) and Sasa Bajt (at Brookhaven National Laboratory) carried out four XANES analyses of unaltered portions of olivine phenocrysts ($Fo_{94.5}$) that I extracted from a polished thick section of a chilled margin. The XANES analyses indicated that little or no Cr^{2+} was present.

Conclusion

On the basis of high-precision microprobe analyses, XANES spectroscopy, and crystal chemical considerations, between 60 to 100% of the Cr in komatiitic olivine is accommodated by the coupled substitution $^{[6]}Cr^{3+} + {}^{[4]}Al^{3+} \rightleftharpoons {}^{[6]}Mg^{2+} + {}^{[4]}Si^{4+}$ (see Fig. **4.6**). Chromium in excess of charge-balancing Al (mainly in the outer margins of plate-like olivine in spinifex-textured komatiites) is probably accommodated by the substitution $2\ {}^{[6]}Cr^{3+} + {}^{[6]}\square \rightleftharpoons 3\ {}^{[6]}Mg^{2+}$. An alternative explanation, that Cr^{2+} is present in some crystals, is not definitively ruled out but seems less likely.

4.1.3 Nickel content of Pyke Hill olivine

The calculated Ni concentrations in olivine, based on the exchange coefficients of Beattie et al. (1991), do not match the measured ones. *Ad hoc* changes to these

coefficients, while improving the fit, still fail to reproduce the observed Ni concentration within analytical error (Fig. 4.3). The partitioning of Ni depends strongly upon melt composition and structure. For example, liebenbergite (nickel olivine) has a lower melting point than forsterite, and in the binary Ni_2SiO_4–Mg_2SiO_4 system, $D_{Ni}^{ol\text{-}melt} < 1$. In liquids that contain less olivine this relationship is reversed. Burns (1993) suggested this could be due to a progressive decrease of octahedral sites in the melt; while this appears to be true, recent studies of synthetic silicate glasses have shown that Ni^{2+} may occur as $^{[4]}Ni^{2+}$ and $^{[5]}Ni^{2+}$, not $^{[6]}Ni^{2+}$ (Galoisy and Calas, 1993). Komatiites are hotter, more magnesian, and less polymerized than most experimentally investigated compositions, and near the liquidus they show nearly equal partitioning of Mg and Ni into olivine, with $D_{Mg}^{ol\text{-}melt} \equiv 1.70$ and $D_{Ni}^{ol\text{-}melt} \equiv 2.00$ (this work; Arndt, 1976; Arndt, 1986a). However it is in olivine crystallized from more differentiated liquids that the calculated Ni deviates most from the observed Ni content. This anomalous behavior could have been caused by factors other than the high temperature and Mg-content of the melt, e.g.:

•open-system crystallization, where the olivine grows from a larger volume of melt than has been assumed in the fractional crystallization model;

•Ni–S complexing, where some of the Ni is bound in sulfide liquid and unavailable for silicate formation;

•the presence of a high proportion of octahedral sites in the melt due to its low alkali content (e.g., Takahashi, 1978);

•kinetic effects such as growth rates that are fast with respect to the rate of Ni diffusion to the crystal surface.

Certain experiments using komatiitic compositions have also shown anomalously low Ni in olivine over a wide range of temperatures, but much of this can be attributed to experimental artifacts. Samples in Pt crucibles (e.g., Agee and Walker, 1990) may have lost Ni to the crucible, and samples in graphite crucibles (Green et al., 1975) or suspended in highly-reducing gas mixtures (Arndt, 1976) may have had reduced NiO activities (e.g., Dingwell et al., 1994).

4.1.4 Calcium content of Pyke Hill olivines

The concentration of Ca in the Pyke Hill olivines is considerably lower than that calculated using the coefficients of Beattie et al. (1991): i.e., 0.21–0.25 wt.% CaO vs. a predicted 0.18–0.45 wt.% for Fo_{94}–Fo_{84}. The data of Renner et al. (1994) for olivines

from komatiites of the Reliance Formation, Zimbabwe, show a simple increase from ~0.22–0.30 wt.% CaO for $Fo_{93.5}$–$Fo_{84.0}$ (WDS data from their Fig. 13(c), not Table 4, which seems to contain lower precision EDS analyses). In both cases the increase of Ca towards the crystal margins is less than would be expected from fractional crystallization. Part of the discrepancy arises from the experimental data underlying the determination of the exchange partition coefficient $K_{D\,Ca/Mg}^{ol/L}$ of Beattie et al. (1991). The line of best fit for $D_{CaO^*}^{ol-L}$ vs. $D_{MgO^*}^{ol-L}$ shows considerable scatter ($r^2 = 0.52$). Considering only basaltic compositions ($D_{Mg}^{ol-liq} \leq 8$), r^2 of the fit is worse, on the order of 0.1–0.2. [As a test, I analyzed glass and olivine from the margin of a recent Kilauean basalt flow, and found that Ca was similarly overpredicted.]

The difference between the measured and predicted Ca in komatiite olivine is therefore probably not significant in terms of magmatic processes. This is unfortunate, because anomalously low Ca concentrations in A_3 layer olivines could be related to compressive stress induced by compositional zoning. In addition, as noted above, Arai (1978) suggested a positive correlation could exist between the concentration of Ca and vacant M sites due to the small effective volume of the latter. Although there is a positive correlation between the concentrations of Ca and of (Cr – Al) in the olivines examined (Fig. 4.7), this may simply be due to increased Ca in the melt caused by fractional crystallization.

4.1.5 Olivine as a "geospeedometer"

The use of cation zoning as an potential indicator of rock cooling rates or crystal growth times was proposed by Onorato et al. (1978) for lunar olivines, and noted by Arndt for komatiite olivines (1986a). On the basis of preserved zoning patterns of major and minor elements in olivine it appears the crystallization process can be modeled closely by fractional crystallization. Post-crystallization processes are more difficult to constrain. The core of a crystal will undergo a certain degree of diffusive re-equilibration with the growing margin, but the rate of cooling and of olivine growth in komatiite flows is not known independently. The Fe–Mg interdiffusion rate in olivine depends on a number of factors, which obviously includes temperature, but also factors such as bulk composition (lower with increasing Mg), crystallographic orientation (lower along *a* and *b* than along *c*), oxygen fugacity (increasing $\propto (f_{O_2})^{1/6}$), and possibly dislocation density (all reviewed in Morioka and Nagasawa, 1991). To add to the difficulty, Chakraborty and Meissner (1995)

recently stated that previously measured Fe–Mg interdiffusion coefficients overestimate the true values by as much as two orders of magnitude. In my calculations I used a value for Fe–Mg diffusivity of 10^{-15} m^2 s^{-1}, as given by Morioka and Nagasawa (1991) for diffusion parallel to *b* in Fo_{90} at 1200 °C. This value is clearly subject to revision.

Given the uncertainties in the physical parameters, an overly detailed model of cation diffusion in olivine is rather pointless at present. As an approximation I have calculated the Mg–Fe zoning of an olivine crystal grown by perfect fractional crystallization from a primary melt (Fig **4.9**), and modeled the one-dimensional relaxation of the zoning using a discrete finite-difference method and assuming a 600 μm-thick plate-like crystal (the one-dimensional approximation is clearly appropriate for such crystals). If the olivine acted as a closed system, i.e., if minimal Fe–Mg exchange occurred between olivine and the groundmass, then the time to cool from ~1300 °C to ~1000 °C within the A_3 zone of a thick flow could not have exceeded one or two days without leaving a distinctive zoning pattern (Fig. **4.10**). Such a pattern is not observed. If significant Fe–Mg exchange occurred between olivine and the groundmass, then the zoning profile would be only slightly changed from the as-grown profile (Fig. **4.11**).

The cooling rate indicated by the preserved zoning in olivine (Arndt, 1986a; Renner et al., 1994; my observations) is marginally consistent with the experimental data of Kinzler and Grove (1985), who found that plagioclase failed to crystallize when linear cooling rates exceeded 3 °C per hour (i.e., flows that contain dendritic plagioclase would have required two days or longer to cool from 1150 °C to 1000 °C). Unfortunately Kinzler and Grove did not provide any illustrations or textural descriptions of the experimental phases, including crystal size, so a direct comparison with the groundmass of natural flows is not possible. [A cooling rate of 3 °C per hour requires a heat flow of ~5 kW m^{-2}, which can be maintained by conductive cooling through an unfractured 50 cm thick upper crust. Actual rates were probably considerably higher; see Section **5.2.2.**]

A more robust conclusion can be drawn from the observation that Mg/(Mg+Fe) of olivine in the Pyke Hill komatiites varies from 0.946 to 0.84, that of augite from 0.83 to 0.62, and very-fine grained groundmass pigeonite as low as ~0.50 (analyses in Appendix 5). Such disequilibrium between fine-grained primary silicates is a strong indication that post crystallization solid-state diffusion was minor in extent. This in turn indicates that the flows must have cooled rapidly.

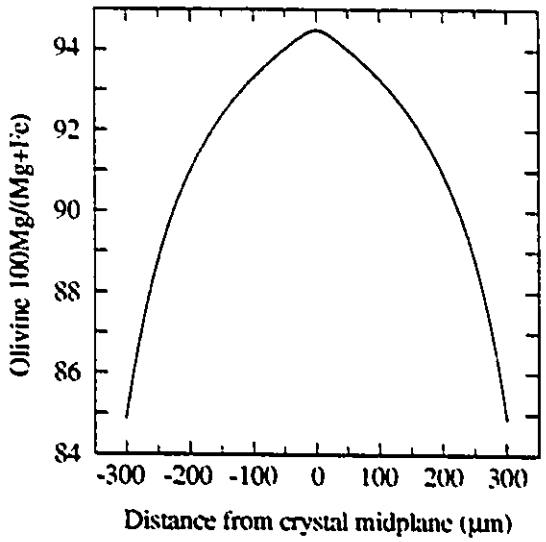

Fig 4.9 Calculated zoning profile of olivine formed by perfect fractional crystallization of a komatiite melt; olivine crystallizes up to ~Fo_{84}, (or 100Mg(Mg+Fe) = 85) at which point pyroxene becomes the liquidus phase. This is actually a bicubic spline fit to the compositions derived via an iterative method, but the difference ($\Delta Fo < 0.1$) is not noticeable on this scale. Similar but not identical profiles have been reported in olivines from spinifex-textured komatiites from Alexo and Zvishavane (Arndt, 1986a; Renner et al., 1994). The crystal thickness was chosen to be typical of those in A_3 layers of the Pyke Hill lavas.

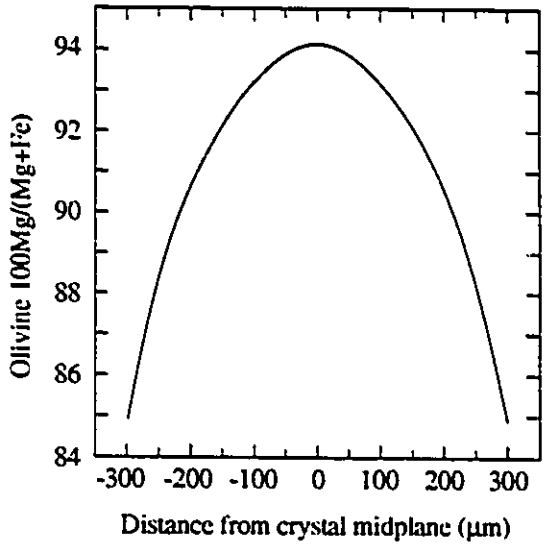

Fig. 4.10 Relaxation of profile shown in Fig. 4.9 via diffusion (60 hours at 1200 °C) assuming that the groundmass acts as a buffer with 100Mg/(Mg+Fe) = 85. The profile was calculated by an explicit finite-difference method, assuming diffusion only along the *b* crystallographic axis, a reasonable simplification for a plate-like olivine crystal elongated parallel to *a* and *c*. Apart from slightly decreased Mg in the core of the olivine ($\Delta Fo \leq 0.6$), there is little change from the as-grown profile. Even this minor change may have been exaggerated if Mg-Fe interdiffusion coefficients have been overestimated. See Section 4.1.5 for discussion.

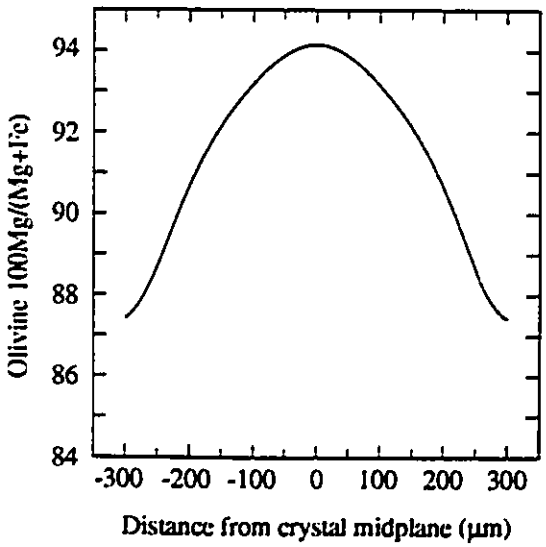

Fig. 4.11 Relaxation of profile shown in Fig. 4.9 via diffusion (60 hours at 1200 °C), but assuming that the olivine crystal is a closed system (i.e., the groundmass does not act as a source or sink of Mg or Fe). To my knowledge such bell-shaped profiles have not been reported in komatiite olivine crystals.

4.2 Chromian spinel

4.2.1 Introduction and chemical composition

In komatiites the crystal habit of chromian spinel (Cr-spinel) ranges from equant octahedral crystals to open dendrites with very small solid cores. Because the dendritic Cr-spinel crystals form such a striking contrast to the octahedral crystals typical of basalts and layered mafic intrusions (Photos **4.3** and **4.4**), I will discuss these at length below. However, even the equant crystals are somewhat unusual: I examined several hundred such crystals liberated (after 2700 Ma of confinement) by HF dissolution of the silicate groundmass. Many of these possessed hopper habits; i.e., they had stepped concentric pits in the shape of rounded equilateral triangles near the center of the {111} faces. Such habits are not found in Cr-spinel from basaltic rocks.

I did not take a particular interest in the chemical composition of the Cr-spinels, and so made only 33 EDS microprobe analyses (Appendix 5) with no claim to high precision. However, Zhou and Kerrich (1992) undertook a systematic study of Cr-spinel composition in the same exceptionally well-preserved Zimbabwean komatiite flows studied by Renner et al. (1994). The major element ratios of the Cr-spinels I analyzed span a range similar to those measured by Zhou and Kerrich, and are summarized as follows:

$Cr/(Cr+Al+Fe^{3+})$: 0.42–0.69, mean = 0.63;
$Al/(Cr+Al+Fe^{3+})$: 0.23–0.42, mean = 0.29;
$Fe^{3+}/(Cr+Al+Fe^{3+})$: 0.05–0.16, mean = 0.08;
$Mg/(Mg+Fe^{2+})$: 0.12–0.76, mean = 0.58;
$Fe^{2+}/(Mg+Fe^{2+})$: 0.24–0.88, mean = 0.42.

Photo 4.3 Olivine crystals containing small Cr-spinel crystals. In this glassy basalt (collected by A.D. Fowler in 1991 from a freshly erupted flow at Kilaeau Iki, Hawaii), equant euhedral to subhedral Cr-spinel crystals are found in all stages of incorporation into olivine, from adhering to the outer surface of olivine crystals to completely enclosed within them. In this photomicrograph an intermediate stage is visible for several of the Cr-spinel crystals (some out of focus due to the 150 μm thickness of the section), in which a narrow glass-filled tube leads from the Cr-spinel to the exterior of the olivine crystal. These tubes gradually neck down and close off, but traces of their former presence must remain as highly imperfect crystallographic layers, dislocation arrays, sets of microfractures, or even submicroscopic tubes. Plane-polarized light; field of view is 2 mm.

Photo 4.4 Both the crystal habit of Cr-spinel and its crystallographic relationship with olivine are much different in komatiite than in basalt. In this A_2 layer komatiite from Pyke Hill a well-developed open dendrite grew away from the serpentinized lattice olivine at middle left. To my knowledge, these spectacular dendrites have few if any equivalents among other igneous minerals. Plane-polarized light; field of view is 500 μm.

The cores of unaltered Cr-spinel crystals tend to be highest in Mg and Cr; Fe^{2+} and Fe^{3+} increase towards the margins (see also Zhou and Kerrich, 1992). Dendrite arms with small cross sections are particularly high in Fe; their relatively large surface areas would have facilitated diffusive equilibration with the groundmass. Crystals in more-altered samples or close to serpentinized olivines are commonly overgrown by a discontinuous narrow (0–5 μm thick), ragged coating of magnetite.

The very low metamorphic grade of the Pyke Hill flows was essential to the study of the Cr-spinel dendrites. The crystals can be studied in exceptional detail due to the well-preserved microtextures of the groundmass, which allowed the observation of characteristic features of dendritic growth that have not previously been described in minerals from igneous rocks. In addition, the presence of relict olivine enabled me to measure the crystallographic orientation between Cr-spinel dendrites and their olivine substrates in spinifex-textured rocks, a feature that can be explained by the heteroepitaxial nucleation of Cr-spinel upon olivine.

4.2.2 Morphology of Cr-spinel crystals

Chromian spinel dendrites have morphological characteristics similar to dendrites of ice and certain salts, organic molecules, and metallic alloys. These features are readily explainable by basic theories of terrace–ledge–kink crystal growth (Tiller, 1991a, 1991b). Perhaps because of the slow growth rates of geological systems, such features are less typical of minerals, although dendritic magnetite crystals are relatively common in rapidly chilled basalts (Haggerty, 1991) and gabbroic dikes (R. Kretz, personal communication). Müller et al. (1988) have described dendritic magnetite and wüstite in fayalite-bearing slags, and I have observed dendritic spinels—probably of $(Zn,Fe^{2+})(Al,Fe^{3+})_2O_4$ composition—in an Fe-, Zn-, and Pb-rich slag that also contained skeletal fayalite. Similar crystal habits are found in certain specimens of galena, silver, and gold. Most of the above mineral occurrences are difficult to study in detail because both mineral and groundmass are opaque, or nearly so. The komatiite groundmass is translucent, facilitating the study of crystallographic orientation and other fine details of the Cr-spinel dendrites. Because these skeletal, branching crystals are best studied in three dimensions, optical microscopy has significant advantages over the SEM.

To observe the shape of the dendrite tips, dendrites terminating within the 30–100 μm thickness of the polished section must be examined with transmitted light. Real tips

must not be confused with sharply angular terminations of dendrite arms visible in reflected light or by SEM; most of these are simply square or octahedral crystal sections truncated by the polished surface. The true shapes of dendrite tips vary from well-developed octahedral forms in certain short dendrite arms to paraboloids with very small radii of curvature (~100–200 nm) in the longest dendrite arms.

In randomly oriented thin sections Cr-spinel dendrites appear to have from one to as many as six elongated main axes (Photo **4.5**). Careful examination of crystallographically oriented thick sections using high magnification, convergent light, and serial focusing shows that the dendrites are elongated along three orthogonal axes (i.e., emanating from the six octahedral apices). Although dendrite cross-sections are circular close to the leading tip, they are square (~1.5–3 μm across) along most of their length (Photo **4.6**). Many dendrites can be followed along their axes back to octahedral cores. The orientation of the dendrite arms with respect to the Cr-spinel core (the {111} form) shows that their axes correspond to the ⟨100⟩ zone axes of the crystal. The orientation of the face-centered cubic Cr-spinel dendrites (space group $Fd\bar{3}m$) is identical to dendrites of fcc metals, which almost invariably favor ⟨100⟩ as growth directions (Tiller, 1991b).

The explanation for the preferred growth of cubic dendrites proposed by Tiller (1991a, pp. 93–99; 1991b, pp. 296–300) is directly applicable to the Cr-spinel dendrites, or for that matter any of the earlier-mentioned minerals. In this interpretation, the paraboloidal tip of a dendrite advances by layer growth of the four {111} facets about 200–1000 nm behind the tip (Fig. **4.12**). Instabilities of the planar crystal–melt interface several μm behind the dendrite tip lead to roughening, branching, and growth along the four ⟨100⟩ axes perpendicular to the main axis (Photo **4.8**). New branches are typically spaced 1–2 μm apart in most of the Cr-spinel crystals that I examined. Crystallographic orientation between the arms of the Cr-spinel dendrite is strictly preserved, and curved dendrites are very rare. Branches up to fourth order may be observed on some crystals in the A_3 layer of thin flows (Photo **4.7**).

Photo 4.5 Cr-spinel crystals nucleated heteroepitaxially on this U-shaped skeletal olivine (view is looking down the *a* crystallographic axis of olivine). Note the remarkable regularity of the size and spacing of the dendrites. Plane-polarized light; field of view is 500 μm.

Photo 4.6 Regularly spaced Cr-spinel dendrite arms that have branched off from a larger arm below the surface of the section. Note that the smaller arms (with square cross sections) can coalesce to form larger square cross sections, enclosing residual patches of melt. [Consideration of the 3D geometry of the inclusions suggests that these will rarely be preserved as pristine melt (the hydrothermally altered nature of the inclusions measured by Zhou and Kerrich (1992) should have alerted the authors to this possibility).] Reflected light; field of view is 100 μm.

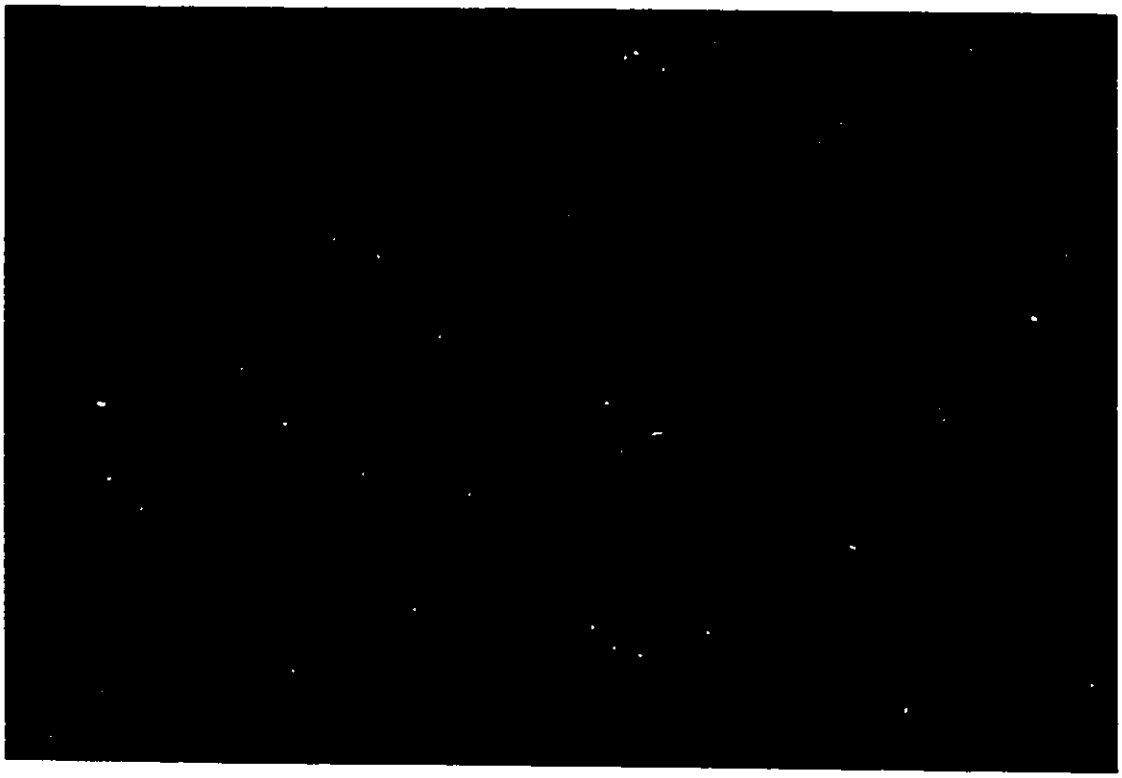

Photo 4.7 Detailed photomicrograph of a Cr-spinel dendrite. Growth was initiated from the lower right. Branches as high as fourth order are visible, as is the asymmetrical development of the second, third, and fourth order arms that is caused by shielding of one branch (or removal of most Cr from the melt in the vicinity of the branch) by a neighbouring one that grew first. Plane-polarized light; field of view is 200 μm.

Photo 4.8 Leading tip of a Cr-spinel dendrite that shows classic features of such growth including a paraboloidal tip (with a radius of <0.5 μm), low-amplitude side-branches that eventually form their own arms, and the alternating length of the branches caused by competition with neighbouring branches. Plane-polarized light, field of view is 100 μm.

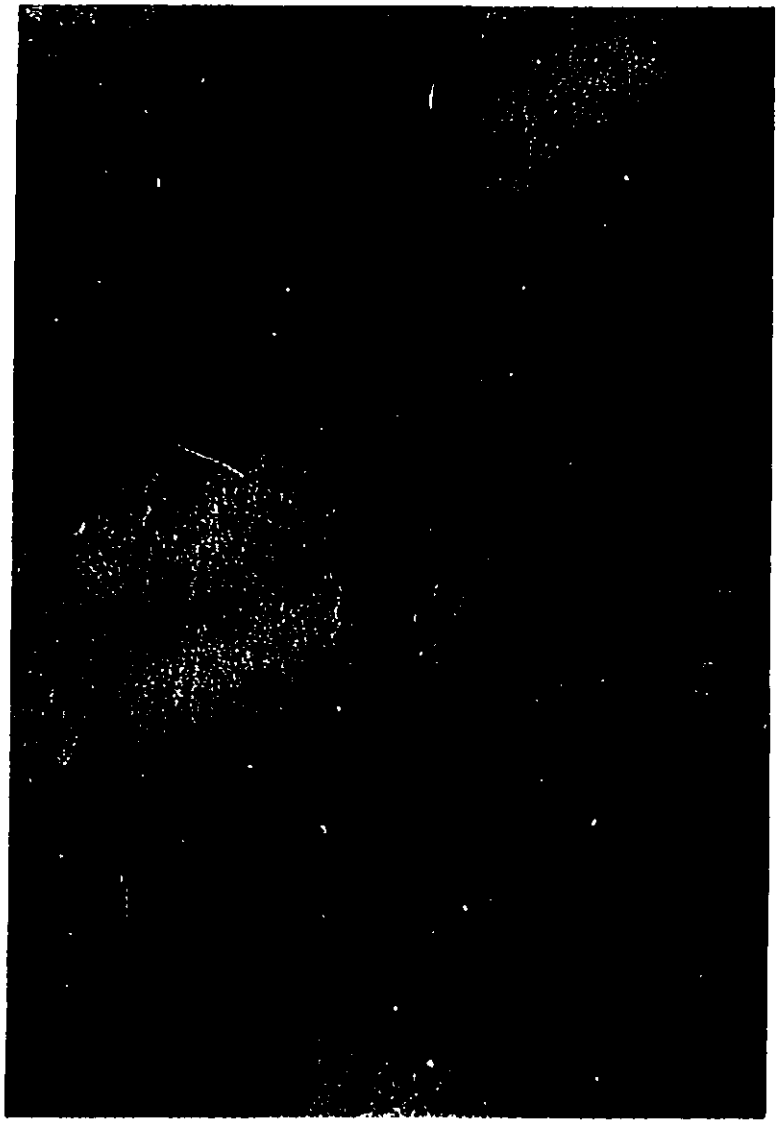

Second and third-order arms tend to alternate in length (Photo **4.8**), which is readily explained by shielding due to competition between neighbouring branches for the limited supply of Cr ions in the melt. Ideally, every second branch would stop growing at a certain distance, then every fourth branch after a longer distance, and so on; in real dendrites the symmetry is less perfect. Significantly, second and third-order arms branch only when well clear of their neighbors, otherwise forming long, smooth arms of square cross-section. Where present, third-order branches commonly show asymmetrical development, with longer ones found on the second-order arm that is closer to the core and that presumably formed earlier (Photo **4.7**).

4.2.3 Heteroepitaxial growth of Cr-spinel on olivine

Introduction

Heteroepitaxy is defined as the growth of one crystal on another of different composition, the two crystals maintaining a systematic crystallographic orientation relative to each other. Such growth is advantageous because it takes place at a smaller degree of supersaturation than is required for homogeneous nucleation from a vapor, melt, or solution. Heteroepitaxy occurs most readily if integral multiples of the lattice spacings of low Miller-index planes of the epitaxial and substrate crystals match within ~10 percent (Kern, 1989). A match between at least two nonparallel crystallographic planes is required in each crystal. The ideal case of a substrate having lattice parameters identical to those of the heteroeptiaxial phase does not occur in mineral growth, although it can be accomplished under specific combinations of temperature and composition in synthetic solid-solution crystals. More typically, strain due to lattice mismatch will grow with increasing area and thickness of the second phase, leading to dislocations, buckling, or misoriented subdomains within the epitaxial layers (e.g., Wagner et al., 1989). In epitaxially grown semiconductor wafers, lattice mismatch can even cause thin substrates to bend (Holloway, 1994).

Crystallographic relationship between Cr-spinel and olivine

Numerous researchers have noted that Cr-spinel crystals are concentrated at the margins of plate-like olivine crystals (e.g., Arndt, 1986a; Thomson, 1989a). A partial explanation is that these crystallized in a rejected-solute boundary layer that was richer in olivine-incompatible elements (including Cr) than the bulk melt (Arndt, 1986a). However, the crystallographic orientation of the Cr-spinel dendrites shows that more than a chemical

concentration gradient was involved. Both Thomson (1989a) and Besson and Vannier (1994) noted that a crystallographic relationship existed between olivine and Cr-spinel, but did not determine what the relationship was. [Because the Kambalda samples studied by Thomson lacked relict olivine, this would not have been possible.]

The lattice spacings of selected crystallographic planes in both olivine and Cr-spinel are listed in Table 4.5. Because of the close coincidence of lattice spacings, many combinations of these planes could be suitable for epitaxial growth of Cr-spinel crystals. The relative crystallographic orientation of the two minerals could be unambiguously measured from electron diffraction patterns using transmission electron microscopy. The crystallographic orientation of the olivine substrate could also be measured with an optical microscope equipped with a universal stage, but this technique is time-consuming and would not work for Cr-spinel, which is isotropic. I used another method, taking advantage of the fact that komatiites containing sheaves of partially serpentinized, plate-like olivine crystals commonly fracture along olivine–groundmass contacts. This exposes the {010} surfaces of the olivine crystals, which are striated due to the trace of {021} or {110} faces. The striations are visible to the naked eye, thus making it a simple matter to cut sections oriented perpendicular to the *a*, *b*, and *c* axes of the group of subparallel olivine crystals.

Table 4.5 Cr-spinel and olivine (Fo_{90}) lattice spacings at 1300 °C

Cr-spinel plane	spacing (Å)	Olivine plane	spacing (Å)	mismatch (%)
(110)	5.975	**(001)**	6.080	–1.7
(111)	4.879	**(100)**	4.818	+1.3
(210)	3.779	(101)	3.776	+0.1
3·(211)	10.349	**(010)**	10.405	–0.5
(220)	2.988	(012)	2.918	+2.4
(222)	2.439	(210)	2.347	+3.9

Data on mineral cell parameters and expansivities from Deer et al. (1982); Berman (1987); Smyth and Bish (1988); Saxena and Shen (1992). Observed coincident planes in bold type.

I observed that Cr-spinel dendrites maintain a consistent orientation with respect to their olivine substrates. The measured angles between the crystallographic axes of olivine and the dendritic axes of Cr-spinel crystals show that the relative orientation of the two minerals is $[111]_{sp} \parallel [100]_{ol}$. $[110]_{sp} \parallel [001]_{ol}$, and $[211]_{sp} \parallel [010]_{ol}$ (Fig. **4.13**; Photos

4.9 to 4.11). This is identical to the orientation of Cr-spinel platelets exsolved from certain chondritic olivines (Ashworth, 1979). A listing of the angles between low index zone axes of the two minerals is given in Table 4.6 (see Appendix 8 for a more complete table).

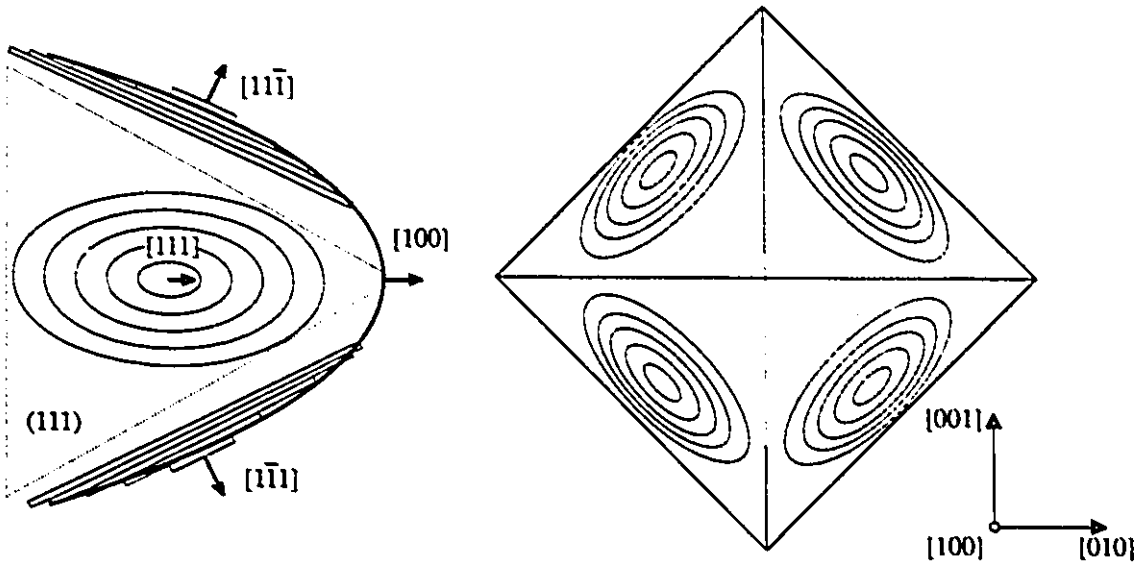

Fig. 4.12 Schematic diagram of {111} growth terraces on paraboloidal tips of isometric crystal dendrites. Side view to left (compare to Photo 4.8); head-on view to right. Modified after Tiller (1991a). Scale is not indicated, but the radius of curvature of Cr-spinel dendrite tips varies from ~2 µm to <200 nm.

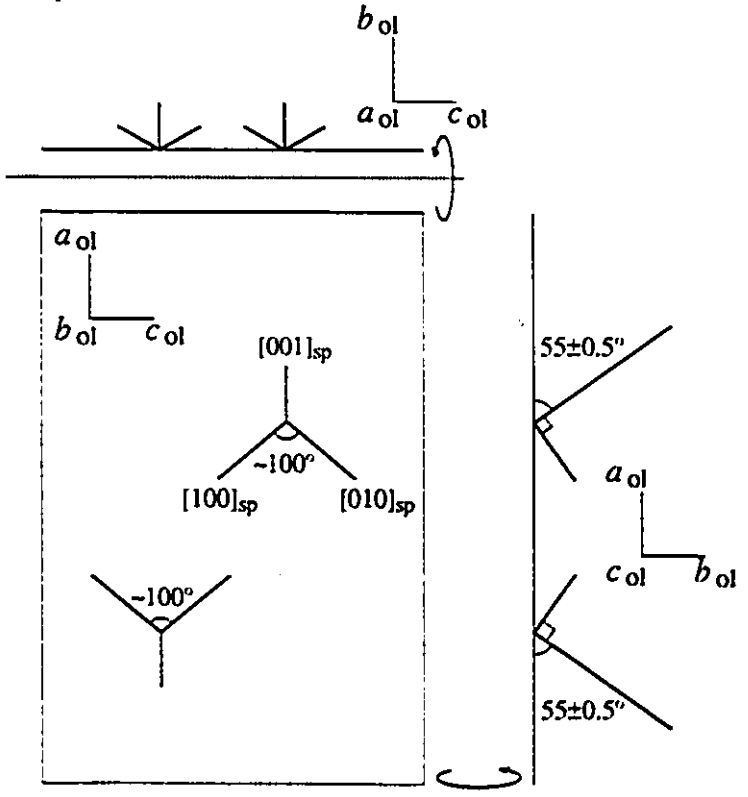

Fig. 4.13 Diagram illustrating the epitaxial relationship between Cr-spinel and its olivine substrate. The figure is based on the study of numerous dendrites in oriented polished sections, and should be compared to the series of oriented photomicrographs shown in Photos 4.9 to 4.11. See text for discussion.

Photo 4.9 View looking down the *b* axis of olivine from the A_3 layer of a thin Pyke hill flow. The *a* axis is oriented parallel to the short edge of the photomicrograph, and *c* is parallel to the long edge. The orientation of the Cr-spinel dendrites is clearly rigidly controlled by the olivine crystal structure. The fact that the dendrites form linear arrays suggests that they may have preferentially nucleated on a ledge or terrace of the growth service. Plane-polarized light; field of view is 500 μm.

Photo 4.10 Section cut from differently oriented section of the same komatiite sample as Photo **4.9**. View looking down the *a* axis of a (serpentinized) chain olivine crystal. The *c* axis is parallel to the long axis of the photo, and the *b* axis to the short edge. Plane-polarized light; field of view is 500 μm.

Photo 4.11 Section cut from differently oriented section of the same komatiite sample as Photo **4.9**. View looking down the *c* axis of a (serpentinized) chain olivine crystal. The *a* axis is parallel to the long axis of the photo, and the *b* axis to the short edge. Plane-polarized light; field of view is 500 μm.

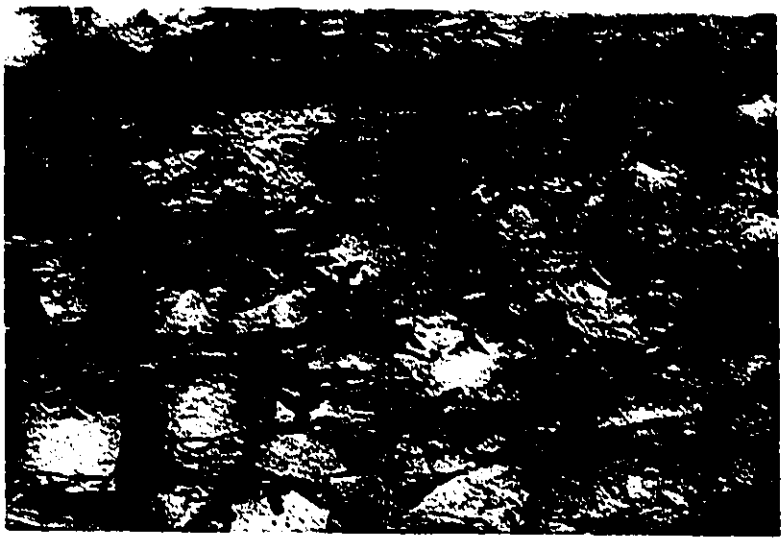

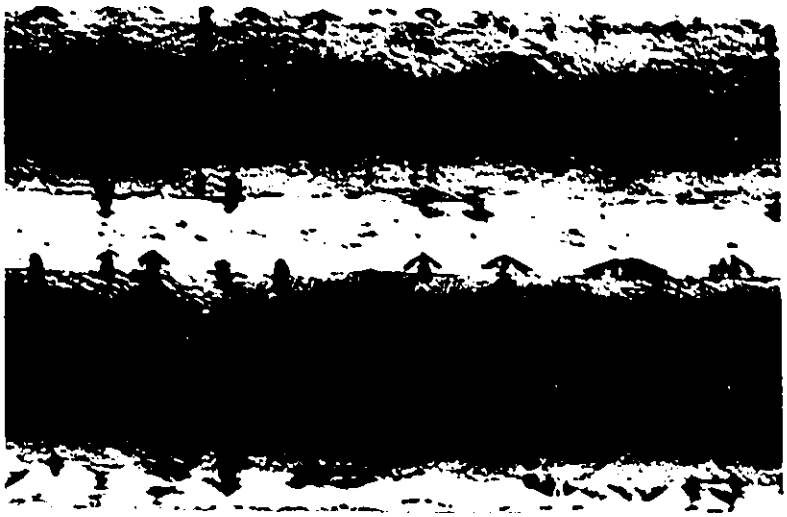

Table 4.6 Calculated and observed angles between spinel and olivine crystallographic axes

Cr-spinel crystal axis (calculated)	axis ∧ $[100]_{ol}$	axis ∧ $[010]_{ol}$	axis ∧ $[001]_{ol}$	Cr-spinel crystal axis (measured)	axis ∧ $[100]_{ol}$	axis ∧ $[010]_{ol}$	axis ∧ $[001]_{ol}$
[100]	54.74°	35.26°	90.00°	[100]	55±0.5°	35±0.5°	90±2°
[010]	125.26	65.91	45.00	[010]	130±5	—[2]	40±5
[001]	125.26	65.91	135.00	[001]	130±5	—[2]	140±5
$[1\bar{1}\bar{1}]$	0.00[1]	90.00	90.00				
[211]	90.00	0.00[1]	90.00				
$[01\bar{1}]$	90.00	90.00	0.00[1]				

[1] Coincident olivine-spinel crystallographic axes.

[2] Dendrite lengths in polished section are <20 μm, precluding accurate angular measurements.

This mutual orientation closely matches three orthogonal lattice planes in each mineral, and is doubtless the reason for the large number (up to 10^6–10^7 crystals mm^{-2}) of Cr-spinel dendrites on the {010} faces of certain olivine crystals in komatiites. The size and spacing of such dendrites indicate that very small Cr-spinel crystals could form stable nuclei for growth into the melt away from the olivine substrates. Careful microscopic examination of distinct brownish-orange patches of very fine-grained groundmass suggests the color arises from microscopic to submicroscopic (i.e., from ~2 μm to <200 nm in size) Cr-spinel crystals.

The shape and orientation of Cr-spinel dendrites on the {010} olivine surface are strikingly similar to those of NH_4I (cubic, NaCl structure) dendrites epitaxially grown on a muscovite {001} cleavage surface (Dunning et al., 1967). Although the composition and structure of the two crystals are completely different, the hexagonally arrayed silica tetrahedra on the mica surface act as a template (with ~1% mismatch) for the hexagonally close-packed {111} surface of the NH_4I crystals.

Other minerals showing similar relationships to olivine

Champness (1970) and Mosely (1984) described identical orientations in TEM studies of magnetite exsolved from olivine; the similar results of Ashworth (1979) have already been noted. Champness suggested that the topotactical relationship was due to the parallel orientation of close-packed oxygen layers in olivine and spinel. Such an

arrangement would minimize both the lattice strain energy and the distance required for oxygen to diffuse during magnetite exsolution.

During post-magmatic cooling or high-grade metamorphism and oxidation of dunites or komatiitic olivine adcumulates, Cr-rich olivine may exsolve platelets of Cr-spinel (Arai, 1978) or magnesioferrite ($MgFe_2O_4$; Khisina et al., 1995). [The latter was interpreted as magnetite by Binns and Champness, 1985; Barnes et al., 1988.] These μm-size Cr-spinel or nm-size magnesioferrite platelets contained within the host olivine crystal are quite distinct from the large (≥ 200 μm long) freely growing dendritic Cr-spinel crystals considered here. In doubly-polished thick sections the cores of most of the studied olivines are water-clear, a sharp contrast to the reddish-brown color of komatiitic olivines containing minute exsolved magnetite platelets (Binns and Champness, 1985). By heating polished sections of komatiite in air at 700 °C for one to two hours I converted colorless olivine to markedly pleochroic reddish-brown olivine. This suggests that relict olivine from Pyke Hill is less altered than the Kambalda olivine examined by Binns and Champness (1985), although the Pyke Hill komatiites are more serpentinized.

Müller et al. (1988) described dendritic wüstite ($Fe_{1-x}O$) crystals intergrown with fayalite in a spinifex-textured slag from a medieval iron foundry. The authors interpreted these dendrites as having formed by exsolution from the fayalite, but it is difficult to see why this would occur. More commonly, Fe-bearing olivine oxidizes to form magnetite or hematite plus enstatite or silica (Champness, 1970; Deer et al., 1982; Mosely, 1984). Quite apart from the reaction itself, diffusion and exsolution are sluggish processes in silicates and it seems unlikely that a slag would have remained hot long enough for the proposed exsolution to occur. A photomicrograph of the dendritic wüstite (Fig. 6 of Müller et al., 1988) shows that it occurs as relatively large, crystallographically continuous dendrites rather than as small platelets or highly flattened dendrites, as would be expected (Mosely, 1984; Binns and Champness, 1985). The wüstite strongly resembles Cr-spinel dendrites oriented so that {111} is subparallel to the plane of the polished section (e.g., see Photo **3.14**). I suggest that an epitaxial relationship similar to that of Cr-spinel and magnesian olivine may exist between wüstite and fayalite. The lattice spacings of the two minerals permits this (Table **4.7**).

Table 4.7 Wüstite and fayalite lattice spacings (at 20 °C)

Wüstite plane	spacing (Å)	Fayalite plane	spacing (Å)	mismatch (%)
2·(110)	6.096	(001)	5.978	+2.0
2·(111)	4.978	(100)	4.753	+4.7
6·(211)	10.559	(010)	10.190	+3.6

Data on mineral cell parameters from Smyth and Bish (1988).

The most important example of a spinel–olivine topotactical relationship may exist between olivine and its high-pressure spinel polymorph. In olivine crystals that have partially transformed to the spinel phase via a martensitic mechanism, {111} of the spinel phase is observed to be parallel to {100} of olivine (e.g., Putnis, 1992). Unfortunately complete crystallographic orientations for these intergrowths do not appear to have been reported. In addition, the olivine-spinel transformation can occur via different mechanisms.

The similar lattice spacings of these different minerals are not coincidental, but reflect the fact that oxygen is in (approximately) hexagonal closest packing in the olivine structure, and in cubic closest packing in the denser spinel and wüstite structures. The hexagonally close-packed plane of oxygen atoms is parallel to {100} in olivine, and to {111} in spinel and wüstite. Fixing one crystallographic plane of the epitaxial phase in relation to the substrate allows one degree of freedom. For example, if the (111) plane of spinel is made parallel to the (100) plane of olivine, different orientations about the [111] zone axis of the spinel are still permitted. Only if a second crystallographic orientation is fixed by the substrate will the epitaxial crystal be in regular crystallographic registry with the substrate.

Metal-silicate epitaxy

Epitaxy is not restricted to closely related substances (e.g., amphiboles on pyroxenes, spinels on olivines) but includes such diverse combinations as Si on Al_2O_3, ZnS on CaF_2, and NH_4I on muscovite. It can also include metal on silicate growth. Crystals of tourmaline and labradorite containing thin plates of native copper have been described (Brandstatter and Niedermayr, 1994; Johnston et al., 1991), and I list possible crystallographic orientations for these minerals in Table 4.8. Such specimens are mineralogical rarities, but may give insight into the behavior of the platinum group elements (PGE) in mafic and ultramafic magmas. It is known that differentiation processes

in thin komatiite flows—almost exclusively olivine crystallization—fractionate Ir and Os from Pt and Pd (Zhou, 1994), and more generally that PGE can be concentrated in chromitite seams in layered mafic intrusions. Proposed explanations for these effects include the substitution of divalent Ir and Os for Mg in olivine (O'Neil et al., 1995), insoluble microscopic particles of Ir-Os alloy attaching to settling olivine or Cr-spinel crystals (Hiemstra, 1979), or trivalent PGE entering spinel crystals (Capobianco and Drake, 1990). Epitaxial growth of native Ir-Os alloys on olivine or Cr-spinel crystals might explain the PGE fractionation as well as rare occurrences of euhedral osmiridium crystal inclusions in chromite. However, the lattice mismatch between Ir-Os alloys and olivine or Cr-spinel is 7–8%, which is close to the maximum permissible for epitaxial growth.

Table 4.8 Lattice parameters of minerals with plate-like copper inclusions

Host mineral plane	spacing (Å)	Cu plane	spacing (Å)	mismatch (%)
elbaite (1000)	15.83	6·{110}	15.34	–3.2
elbaite (0001)	7.103	2·(001)	7.23	+1.8
labradorite (010)	12.87	5·{110}	12.78	–0.7
labradorite (001)	7.096	2·(001)	7.23	+1.9

4.2.4 Evidence for Cr_2O_3 supersaturation in komatiitic liquids

The zoning of olivine crystals in thin spinifex-textured komatiite flows can be closely modeled by perfect fractional crystallization (Section **4.1.1**). This allows the composition and temperature of the melt when Cr-spinel first crystallized to be estimated from whole-rock composition, olivine compositions, and textural criteria. Although the Cr concentration of olivine shows considerable scatter when plotted against Mg/(Mg+Fe), a maximum is found in olivine of composition ~Fo_{86} (mg# ~87). The calculated composition and temperature of the differentiated melt in equilibrium with Fo_{86} (12.5% MgO, 3400 µg/g Cr, 1250 °C) are in good agreement with experiments that show Cr-spinel first crystallizes between 1350 and 1300 °C (Arndt, 1976). In other experiments at 1300 °C and with f_{O_2} between FMQ and FMQ – 2 $\log_{10}$ units, the maximum concentration of Cr in komatiitic liquids in equilibrium with Cr-spinel is between 1400–2100 µg/g, with higher Cr solubility at lower f_{O_2} (Murck and Campbell, 1987; Roeder and Reynolds, 1991). The modeled concentration of Cr in the natural komatiite liquid at the point when Cr-spinel nucleated (~3400 µg/g) represents approximately two-fold supersaturation of Cr in the liquid, equivalent to an undercooling of ~50–100 K (Table **4.9**). The scatter in Cr

concentrations in olivine within a single flow may be due to variable cooling rates, leading to different degrees of Cr supersaturation prior to Cr-spinel growth.

Table 4.9 Cr content of experimental melts in equilibrium with olivine and Cr-spinel

Sample	T (°C)	$\log_{10} f_{O_2}$	MgO wt.%	FeO_T wt.%	Cr (µg/g)
K30	1300	–8.5	14.4	6.5	1100[1]
K30	1300	–9.2	15.0	5.3	1450[1]
K30	1300	–9.9	15.0	4.3	1850[1]
K1300	1300	–7.2	13.0	11.3	1350
K1300	1300	–8.2	13.0	11.3	1700[2]
K1300	1300	–9.2	13.0	11.3	2100[2]
TS1A3	1250 ± 50	–9 ± 1	12.5	11.0	3350[3]

[1] Experimental values of Roeder and Reynolds (1991) reduced by 40% to account for higher FeO of natural komatiite.

[2] Experimental value of Murck and Campbell extrapolated to lower f_{O_2} based on other runs at higher temperature.

[3] Approximate komatiite melt content when Cr-spinel nucleated on A_3 layer olivine; in sample TS1A3 I analyzed olivine adjacent to the nucleation site of Cr-spinel crystals.

4.2.5 Influence of cooling rate on Cr-spinel habit

The habit of Cr-spinel crystals of komatiites appears to be a more sensitive indicator of cooling rates than that of the olivine crystals. Quenched margins of the studied flows contain ~5 vol.% of equant olivine phenocrysts and sparse skeletal crystals with dendritic overgrowths in a 0.8 mm thick glassy layer (now devitrified). There is a sharp transition to ≥100 µm long skeletal olivine crystals within 2 cm of the flow margin, and a very gradual transition to the larger plate-like crystals of the A_3 layer. There is little difference in the size or external morphology of olivine crystals from the cumulate layer and the upper randomly oriented spinifex layer. The major distinction lies in the solid versus somewhat skeletal internal structure of the crystals from the respective layers (Photos **3.9** and **3.10**). Cr-spinel, on the other hand, varies from submicroscopic (≤ 200 nm) crystallites that give an orange-brown color to patches of devitrified glass near quenched margins, to µm-size dendrites several cm below the flowtop, to well developed 100–200 µm-long dendrites between olivine plates in the A_3 layer. At the base

of a typical thin flow, over a vertical distance of ~10 cm, dendritic Cr-spinel crystals change to skeletal grains, to octahedral crystals with inclusions, and to equant octahedra (Photos **4.12** and **4.13**). Even a single dendrite may show a wide range of morphologies over a 150 μm length.

I propose a simple explanation for the various tip shapes: dendrites whose growth was slowed and ultimately halted by depletion of Cr in the nearby liquid developed well-formed {111} facets because sufficient time existed for the process of slow growth (possibly also involving local dissolution and surface diffusion) to form an octahedral habit that minimized the overall surface energy of the crystals. In contrast, dendrites whose growth into Cr-undepleted liquid was halted by decreasing temperature and slower chemical diffusion preserve paraboloidal tips with very sharp (100–200 nm) radii of curvature. A continuum of intermediate shapes lies between these extremes. Such behavior is analogous to that of NH_4Br dendrites grown below the "roughening temperature" (Maurer et al., 1989), but with local Cr concentration rather than temperature being the controlling factor. By measuring the cross-section and length of the first through fourth-order branches of one well-developed dendritic Cr-spinel crystal, I determined that it had ~50–100 times the surface area of an octahedral crystal of equivalent mass. The reduced role of surface area energy minimization in these crystals compared to more typical Cr-spinels in basalts is presumably due to the rapid cooling rate and high concentration of Cr in the komatiite lava.

I also estimated the mass of Cr in a representative Cr-spinel dendrite and compared it to that contained in the equivalent volume of melt at the start of crystallization. Dendritic Cr-spinel crystals in the A_2 layer (and the A_3 layer of thin flows) contain approximately 2–4 times more Cr than would originally have been present in the volume of melt now outlined by the leading dendrite tips. In addition, the spatial distribution of Cr-spinel crystals can be quite inhomogeneous on a mm-scale within the komatiite groundmass. These observations show that transport of Cr from undepleted melt must have occurred during Cr-spinel growth, either through convection or diffusion. Strong convection appears unlikely as it is known to suppress dendritic growth (Donaldson, 1977; Tiller, 1991a), and bending or breakage of the dendrites is quite rare. The closely spaced second and third-order arms and thin central axes of the dendrites would have made them sensitive indicators of even very weak flow within the melt. Transport solely by diffusion would require a significant amount of Cr to travel up to 50–100 μm towards the growing

Cr-spinel dendrite. [Because of the many uncertainties involved, this does not seem to be a promising technique for evaluating cooling rates.]

As noted above, certain Cr-spinel crystals in the A_3, B_1, and B_2 layers have a hybrid crystal shape, consisting of an octahedral core overgrown by dendritic arms. Contrary to the suggestion of Zhou and Kerrich (1992), this does not require that the core grew under drastically different ambient conditions than did the arms. On the basis of computer simulations of crystal growth in a pillow basalt, Kirkpatrick (1978) noted that at a given distance from a cooling surface, undercooling increases continuously as crystallization proceeds. With progressive undercooling, a compact crystal form caused by layer growth mechanisms may break down to hopper, skeletal, and ultimately dendritic forms. In a cooling komatiite magma, the combination of rapidly decreasing solubility of Cr^{3+} and lower chemical diffusivity would all serve to destabilize the layer-by-layer growth of equant Cr-spinel.

According to crystal-field theory, Cr^{3+} ions prefer octahedral sites over those of lower coordination. This means Cr^{3+} is unlikely to remain in the glass phase, and indeed tiny Cr-spinel crystals ($\leq$1 μm in size) are found at the margins of skeletal olivine crystals only 2 cm away from glassy quenched margins. Even smaller submicroscopic crystals ($\lesssim$200 nm) are present throughout flows; these cannot be resolved with the optical microscope but give a distinctive reddish-brown coloration to patches of the groundmass. Such crystals are commonly arrayed in bands that mark the former margins of dendritic olivine crystals that are now completely serpentinized (e.g., Photo 3.8).

4.2.6 Summary of Cr-spinel behavior

Chromian spinel dendrites in komatiite flows typically formed by epitaxial nucleation on olivine crystals, particularly in spinifex-textured rocks. Their habits are characteristic of dendrites in other face-centered cubic crystals, and indicate that rapid growth occurred on {111} planes of paraboloidal branching tips oriented along ⟨100⟩ crystallographic axes. Compositional data indicate that the Cr-spinel crystals began to grow at approximately two-fold Cr_2O_3 supersaturation; on the basis of the Cr solubility vs. temperature data of Murck and Campbell (1988) and Roeder and Reynolds (1991), this corresponded to a peak undercooling of 50–100 K.

Photo 4.12 B_4 sample from ~3 cm above the base of a 1.5 m thick flow from Pyke Hill. Skeletal and equant olivine crystals in a groundmass made up largely of dendritic augite. The number of equant olivine crystals in this photomicrograph is not representative of the polished section, which as a whole contains a lower concentration of such crystals. Note that the lengths of the Cr-spinel dendrites approach 100 μm. Plane-polarized light; field of view is 500 μm.

Photo 4.13 Same polished section of the B_4 sample as shown above, except ~2 cm above the flow base. Note that the Cr-spinel crystals are barely visible (they are the small, somewhat elongate dark crystals at the margins of the skeletal olivine crystals). Textural study of other samples also indicates that Cr-spinel grew rapidly, and with a crystal habit that is sensitive to cooling rates. Plane-polarized light; field of view is 500 μm.

4.3 Other magmatic phases

4.3.1 Augite

Although enstatite and pigeonite are found in other komatiite flows (Arndt, 1986a; Renner et al., 1994), the most abundant clinopyroxene in the Pyke Hill flows is augite, containing between 4–12 wt.% Al_2O_3 (Appendix 5). Dendritic augite crystals from the A-layer are highest in Al_2O_3, and are among the most aluminous pyroxenes reported in any subalkaline rock crystallized at low pressures. This is likely due to the Ca-Tschermak substitution $^{[6]}Al^{[4]}Al \rightleftharpoons {}^{[6]}(Mg,Fe^{2+})^{[4]}Si$, favored by high pressure or rapid cooling and crystallization (Deer et al., 1978). This substitution can lead to the metastable growth of augite with respect to plagioclase and pigeonite because the crystallization of Al-rich augite removes Ca and Al from the melt, elements obviously required for the growth of calcic plagioclase. The earlier nucleation and subsequent rapid growth of augite is a key factor in the suppression of plagioclase crystallization.

4.3.2 Pigeonite, plagioclase, and other minerals

In the 5 to 6 m thick flow studied, the groundmass in the A_3 layer more than ~1–2 m below the flowtop consists of intergrown dendritic plagioclase (An_{50-60}) and iron-rich pigeonite with Mg/(Mg+Fe) as low as ~0.50. [The largest grain size I found for these minerals was ~2 μm by 20 μm, too small to obtain a microprobe analysis of a single phase. However, by assuming that all of the measured Fe and Ti was in pigeonite, and all of the Na and Al in plagioclase, the proportions and compositions of the two minerals could be estimated from analyses of the mixed phases.] These intergrowths have been noted by some previous workers (e.g., Beaty and Taylor, 1982; Arndt, 1986a), but appear to have escaped the notice of many petrologists studying komatiites, perhaps because they examined thinner flows. Micrometer-size subhedral ilmenite is found in certain A_3 layer rocks, and chalcopyrite and Ni-poor pyrrhotite are commonly present in very low concentrations. It is not clear whether pyrrhotite and chalcopyrite are primary magmatic phases or metamorphic minerals.

4.3.3 Glass

The outermost layer of chilled upper and lower margins consisted largely of glass, now altered to an assemblage of metamorphic minerals. Due to the rapid nucleation and

growth of olivine, portions of the flow more than a few mm away from direct contact with water or cold underlying rock contained considerably less glass. Slightly deeper within flows dendritic clinopyroxene also grew rapidly, further reducing the amount of glass present. The amount of glass originally present in the different flow layers (based on petrography) ranged between ~95% in the chilled margins to <<5% in the B-layer of the 5–6 m thick flow that I studied. In komatiites a substantial proportion of incompatible elements (e.g., large-ion lithophile elements) would have been concentrated in residual glass of basaltic compositions, or possibly in the outer margins of fine-grained dendritic plagioclase, if these were zoned. Both phases are susceptible to alteration (Section **4.4.2**).

4.3.4 Summary of Pyke Hill komatiite mineralogy

For convenience, the magmatic and metamorphic mineralogy that I have observed in the Pyke Hill lavas is listed in Table **4.10**. Except for the absence of brucite, my observations are consistent with (if somewhat more detailed than) those of other workers.

Table 4.10 Observed mineralogy of Pyke Hill komatiites

Magmatic minerals in Pyke Hill komatiites	Metamorphic minerals in Pyke Hill komatiites	Common or diagnostic minerals *not* observed in Pyke Hill komatiites
olivine	chrysotile[1]	alkali feldspar
augite	lizardite	apatite
Cr-spinel	antigorite	biotite
pigeonite	talc	brucite[2]
labradorite	tremolite–actinolite	epidote
ilmenite	chlorite–clinochlore	magnesite
	smectite (?)	muscovite
	magnetite	phlogopite
	calcite	prehnite
	andradite	pumpellyite
	chalcopyrite[3]	pyrite
	bornite	quartz
	heazlewoodite	titanite
	pyrrhotite (Ni-bearing)[3]	zircon
	pentlandite (Co-bearing)[3]	

[1] Exact polymorph (clinochrysotile, orthochrysotile, or parachrysotile) not determined.
[2] Beaty and Taylor (1982) reported brucite in Pyke Hill lavas.
[3] Possibly magmatic, although this seems unlikely.

4.4 Metamorphic mineralogy

4.4.1 Introduction

Minerals formed during alteration of the flows include serpentine (chrysotile appears to predominate, but lizardite and antigorite also occur), clinochlore (and possibly amesite), talc, magnetite, Co-bearing pentlandite, heazlewoodite (Ni_3S_2), calcite, andradite, and tremolite. The metamorphic silicates are commonly highly magnesian, with (Mg/(Mg+Fe) as high as 0.97. This is consistent with low-temperature serpentinization of olivine with preferential partitioning of Fe, Ni, and Co into magnetite and sulfides, and the loss of Ca and Mn. The sporadic occurrence of Cr-rich phyllosilicates is indicated by patches and veins of pale (in thin section) emerald-green serpentine or chlorite. I did not analyze such patches, but serpentine that is colorless to very pale yellowish-green contains ~0.2 wt.% Cr_2O_3. Because Cr-spinel shows very few signs of alteration or dissolution the Cr was likely derived from olivine. Although Ni^{2+} and Cr^{3+} will readily enter the octahedral site of magnetite, the low concentration of these metals in secondary magnetite indicates that Ni strongly partitioned into sulfides (heazlewoodite and pentlandite) and Cr into secondary silicates. Calcite is almost entirely confined to veins and interstices between glass globules in the flowtop breccia. Andradite is uncommon, but is found as isolated crystals or small crystal aggregates in the flowtop breccia. Its composition is close to the ideal $Ca_3Fe_2^{3+}Si_3O_{12}$, and indicates oxidizing conditions during its formation. Tremolite, with Mg/(Mg+Fe) from 0.92 to 0.85, forms sheaves of small (20–60 μm in length), weakly oriented crystals that replace olivine and groundmass in the flowtop breccia and adjacent to serpentine or chlorite veins deeper in the flow. The role of hydrothermal solutions circulating through fractures, or contact metamorphic effects due to subsequent flows may have been important in the formation of tremolite.

The very low degree of strain and recrystallization of the flows is indicated by the fact that pseudomorphs of extremely fine (≤ 1 μm thick) olivine dendrites are preserved in quenched "glassy" flow margins (Photo 3.6). [The original glass is now a mixture of submicroscopic tremolite, magnetite, and clay minerals.] Such excellent preservation of microtextures seems inconsistent with greenschist-facies regional metamorphism; growth of neoblastic tremolite or actinolite might instead be expected. The flows appear to be of prehnite-pumpellyite or possibly even lower grade, although few diagnostic minerals are present. According to Jolly (1982, his Table 17.1), chrysotile and lizardite are indicative of prehnite-pumpellyite facies. The Alexo nickel deposit is hosted by a komatiitic sill that is

more serpentinized than the Pyke Hill lavas. The footwall rocks (meta-andesite?) immediately underlying the Alexo deposit contain abundant prehnite (my observations).

It is difficult for the non-expert to distinguish between the five (or more) serpentine polymorphs (Wicks and O'Hanley, 1988). Both length-fast and length-slow, sub-μm diameter, apparently fibrous serpentine forms radial arrays around relict olivine grains in the B-layer. To judge from the relative intensities of 4 strongest X-ray diffraction peaks, chrysotile formed the bulk of a serpentine-rich concentrate from one B-layer sample. Lizardite is present in some veins and replaces olivine in patches. I identified antigorite (tentatively) by the irregular tabular habit of certain 20–50 μm-sized crystals, which also had low 2V (nearly uniaxial, with very low birefringence). Certain of these crystals were colored a non-pleochroic deep yellow in thin section, possibly due to Fe-content or inclusions of ferric hydroxides. Despite extensive microscopic examination, I did not find brucite in the rocks I examined. Microprobe analyses confirmed the presence of highly magnesian serpentine (certain analyses showing excess SiO_2) around partially-altered olivine grains. Talc ($Mg_3Si_2O_5(OH)_2$) and clinochlore ($\sim Mg_5Al_2Si_3O_{10}(OH)_8$) are less common alteration phases. Both minerals are typically associated with fractures, although clinochlore also replaces olivine phenocrysts in the flowtop, and talc fills vesicles in the B-layer and replaces the finest olivine blades in the A-layer. Jolly (1982) attributed the formation of these various hydrous Mg-phyllosilicates to the differing concentrations of Mg, Si, Ca, and Al in the immediate vicinity of the altered olivine or precipitated secondary mineral. I agree, with the qualification that because certain minerals (e.g., Cr-spinel, augite) did not break down during metamorphism (and thus could not supply key elements to reacting phases) the local metamorphic assemblage also depends upon what phase(s) contained those elements (e.g., glass, augite, pigeonite, or plagioclase).

4.4.2 Serpentinization of the flows

The "serpentinization problem" and the inferred reaction

The classic "serpentinization problem" is that isochemical serpentinization (i.e., simple hydration) of olivine must cause a significant expansion that is not always obvious when examining serpentinized rocks. Isovolumetric serpentinization, on the other hand, requires large losses in Mg and Si; generally, little evidence is found of such losses. [There is, conversely, very strong evidence that Mg and Si were immobile in the Pyke Hill lavas

(Section **3.2.4**).] Some proposed serpentinization reactions for forsterite are as follows (from Best, 1982):

I. $3\ Mg_2SiO_4 + 4\ H_2O + SiO_2 \rightarrow 2\ Mg_3Si_2O_5(OH)_4$

forsterite	(introduced)	serpentine	
131 cm^3		215 cm^3	($\Delta V = +64\%$)

II. $2\ Mg_2SiO_4 + 3\ H_2O \rightarrow Mg_3Si_2O_5(OH)_4 + Mg(OH)_2$

forsterite	serpentine	brucite	
87 cm^3	108 cm^3	24 cm^3	($\Delta V = +52\%$)

III. $5\ Mg_2SiO_4 + 4\ H_2O \rightarrow 2\ Mg_3Si_2O_5(OH)_4 + 4\ MgO + SiO_2$

forsterite	serpentine	(removed)	
219 cm^3	215 cm^3		($\Delta V = -2\%$)

By using a combination of methods, including X-ray powder diffraction, optical microscopy, electron microprobe analysis, whole-rock XRF analysis, and density measurements I was able to rule out reactions (II) and (III). Reaction (I), in contrast, is consistent with all of the available observations (detailed below). Of course, reactions (I) through (III) as written are idealized and must be modified for komatiite olivine, which is a multi-element solid solution, not forsterite. Because certain of these constituent elements partition more strongly into magnetite, sulfides, or aqueous solution than into serpentine, they must be accounted for by other reactions (the following examples are schematic):

$Fe_2SiO_4 + H_2O \rightarrow 2/3\ Fe_3O_4 + SiO_2 + H_2$;
$3/2\ Ni_2SiO_4 + 2\ S^{2-}_{aq} \rightarrow Ni_3S_2 + 3/2\ SiO_2 + 3/2\ O_2$;
$Mn_2SiO_4 \rightarrow SiO_2 + 2\ Mn^{2+}_{aq} + O_2$; etc.

An instructive way of looking at serpentinization that can explain certain textural features (differing orientations of radial chrysotile fibers, concentric zones of magnetite and sulfide grains) is to look at the process as a reaction front moving inward on the olivine grain. The mass transfer for this reaction (for simplicity using pure forsterite) is given in Table **4.11**. Because serpentinization must proceed inwards from the outer margins or fracture surfaces of the olivine grains, the reaction consists of dissolution of olivine and *in situ* reprecipitation of much of the Mg and Si as radially oriented fibers of

chrysotile (or antigorite or lizardite). As the process requires net migration of both Si and Mg away from the reaction front, the excess ions (together with other elements contained in the olivine) must migrate along the hollow cores and interstices of the chrysotile fibers. At some point, typically at an interface between chrysotile fibers of differing orientation, the dissolved Fe^{2+}, Fe^{3+}, Ni^{2+}, and Co^{2+} form magnetite and sulfides, and the Mg- and Si-bearing solution form serpentine (Photos **4.14** to **4.16**).

Table 4.11 Mass transfer during isovolumetric serpentinization of forsterite

Mineral	MgO (g cm^{-3})	SiO_2 (g cm^{-3})	H_2O (g cm^{-3})
Mg_2SiO_4	1.845	1.375	0.000
$Mg_3Si_2O_5(OH)_4$	1.113	1.106	0.331
net transfer	–0.732	–0.269	+0.331

The additional Si required by reaction (I) is probably leached from the groundmass at this point by the fluid phase. Whole-rock analyses show that certain elements have been lost from serpentinized B-layer rocks. This is particularly true of Ca; up to ~30% of the original Ca has been leached from the most serpentinized rocks (see Section **3.2.4**). A similar loss occurs on a very local scale. By repeatedly grinding a serpentinized B-layer komatiite in an agate mortar under ethanol and decanting the finest fraction, I was able to separate it into a relatively coarse (but <200 mesh) black powder and a much finer light grey powder. The compositions of the bulk rock and these two fractions are related by the amount and composition of any minerals that were preferentially concentrated into the finer-grained (presumably more altered) fraction. By making the reasonable assumption that the TiO_2 content of the serpentine is negligible, the composition of the mixture of alteration products can be derived via extrapolation (Table **4.12**). The calculated end-member composition is consistent with a mixture of ~94 wt.% serpentine (mg# ~97), ~5 wt.% magnetite, and ~1% minor phases (e.g., chlorite, pentlandite). Perhaps more convincingly, a similar assemblage is observed *in situ*.

Photos 4.14 to 4.16 Photomicrographs of a partially serpentinized equant olivine crystal from the B-layer of a thin flow from Pyke Hill. From top to bottom these are taken with: transmitted light, crossed polars; transmitted plane-polarized light; reflected light. The extremely fine serpentine fibers are oriented more-or-less perpendicular to the surface of the relict olivine grains. Fine to coarse grains of magnetite and minor heazlewoodite are found near the outer margins of the altered grain; another set of finer particles is concentric about the olivine core. Offsets between the fragments of relict olivine indicate differential movement during alteration, presumably due to expansion. The ultrafine fibers of serpentine would be sensitive markers of even very small amounts of strain. Field of view is 500 μm.

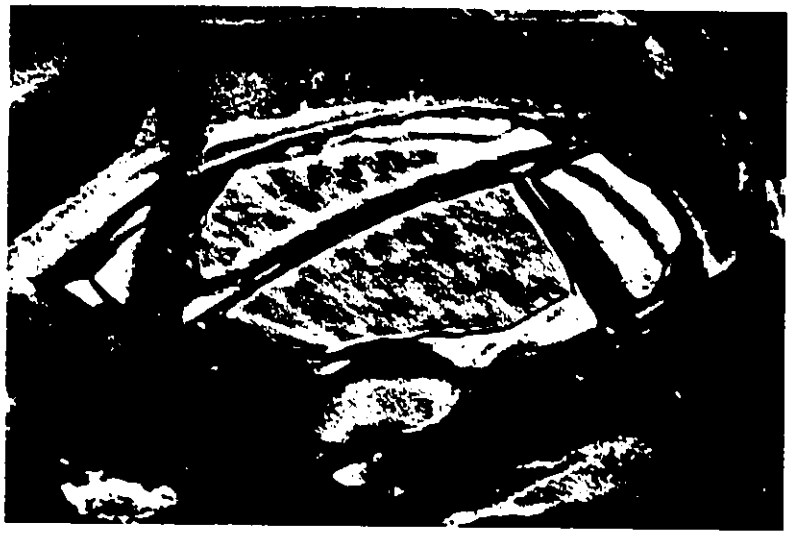

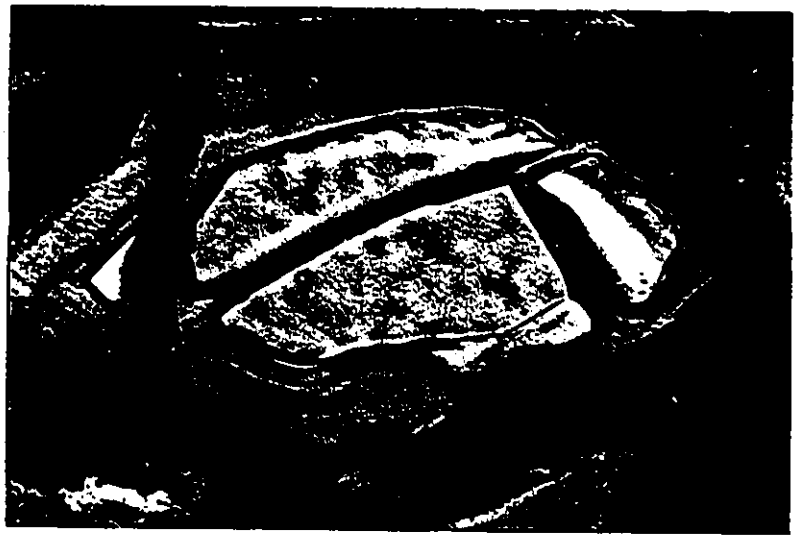

Table 4.12 Coarse and fine fractions of serpentinized B-layer komatiite 92-07

Oxide (wt.%); element (µg/g)	MS93-07(CF) coarse fraction	MS93-07 bulk rock	MS93-07(FF) fine fraction	Extrapolated to $TiO_2 = 0$	r^2 of regression vs. TiO_2
SiO_2	41.29	40.97	40.93	39.95	—*
TiO_2	0.212	0.189	0.155	0.000	—
Al_2O_3	4.51	4.07	3.43	0.49	1.000
Fe_2O_3 (T)	8.84	8.62	8.32	6.91	0.999
MnO	0.120	0.107	0.097	0.035	0.932
MgO	33.90	34.51	35.36	39.33	0.999
CaO	3.38	2.93	2.29	–0.68	1.000
Na_2O	0.357	0.288	0.234	–0.10	0.935
K_2O	0.077	0.066	0.051	–0.020	0.999
P_2O_5	0.0135	0.0106	0.0100	0.0005	—*
V	96	88	70	–1	0.977
Cr	1848	1779	1705	1320	0.984
Co	91	95	102	132	0.996
Ni	1875	1986	2089	2670	0.965
Sr	14.5	11.2	9.3	–5	0.863
Oxide sum	93.11	92.17	91.27	86.38	0.970
LOI	8.6	n.d.	10.3	15.1	—*

* Only MS93-07(CF) and MS93-07(FF) used in the calculation.
LOI determined by gravimetry independently of XRF analysis.

Interestingly, the calculated concentration of CaO in serpentine in Table **4.12** is –0.68 wt.%. The calculated concentrations of Na, K, and Sr are also negative; on a small scale I have produced an effect similar to that seen in the whole-rock data set (see **Fig. 3.18**). Because Ca is low in both serpentine and its precursor olivine, the only explanation is that it has been removed from the groundmass immediately adjacent to the olivine crystals. This can also explain the unexpected immobility of Si and Mg. Reaction (I) requires SiO_2 in excess of the amount contained in olivine, but free silica would not have been present in the komatiite groundmass. An intermediate stage of serpentinization probably involved a reactive Mg-bearing solution; a *schematic* reaction is $Mg^{2+}_{aq} + CaSiO_3 \rightleftharpoons MgSiO_3 + Ca^{2+}_{aq}$. [Similarly, the silicate rock–atmospheric weathering cycle is sometimes written as $CaSiO_3 + CO_2 \rightleftharpoons SiO_2 + CaCO_3$ without implying that continents are made of wollastonite.] Considering the removal of Ca, local mass-transfer

of Si, and the presence of Fe in olivine (but neglecting other minor constituents such as Ni), leads to reaction (IA), a modified version of reaction (I):

IA. $Mg_{1.8}Fe_{0.2}SiO_4 + 0.24\ CaSiO_3 + 1.309\ H_2O \longrightarrow$

$$0.62\ Mg_{2.9}Fe_{0.1}Si_2O_5(OH)_4 + 0.046\ Fe_3O_4 + 0.24\ Ca^{2+}_{aq} + 0.069\ H_2$$

Using the literature values for the molar volumes of the minerals in reaction (IA), the calculated $\Delta V/V = +29\%$. Molar volumes are calculated from unit-cell dimensions (measured by X-ray diffraction), so this estimate is a minimum because it does not account for the hollow cores and interstitial gaps of chrysotile fibers, nor any possible reduction in density of the decalcified and desilicated phase. A better estimate is $\Delta V/V = +30$ to 35%.

Because augite in the Pyke Hill flows appears to be unaltered, the missing Ca must have been leached from the glass or fine-grained plagioclase and pigeonite that formed the bulk of the groundmass. Presumably the desilication reaction involves glass or plagioclase being altered to clay minerals. I suggest that there was enough leachable SiO_2 in the groundmass to act as an internal buffer for the serpentinization reaction. This would explain both the immobility (or at least unchanged concentrations) of Mg and Si and the systematic loss of Ca (+/– Na, K, and Sr) with increasing MgO content of the rock. The excess Mg released by the breakdown of olivine and the Si released by the leaching of the groundmass are both bound up in serpentine, and the Ca and other mobile elements lost in solution.

It is worth noting that calcium mobility is found on a much larger scale in rodingites, which are low-grade hydrothermally altered rocks commonly associated with large serpentine bodies. The essential feature of these rocks—typically former gabbros—is that they contain a high proportion of Ca-rich minerals such as diopside, vesuvianite, epidote, and grossular. A widely held interpretation is that they form by the action of Ca-bearing fluids expelled from ultramafic bodies during serpentinization (e.g., Best, 1982).

Magnetite and other minerals formed during serpentinization

Magnetite is ubiquitous in low-grade altered komatiites, comprising up to ~5 wt.% of serpentinized B-layer rocks. It commonly forms patchy or spongy aggregates of very fine-grained material in serpentine. EDS microprobe analyses (Appendix 5) show that it is

nearly pure Fe_3O_4, suggesting formation at low temperature. Minor constituents include NiO (≤1 wt.%), Cr_2O_3 (≤0.5 wt.%), and MnO (≤0.2 wt.%). In olivine $MnO/FeO_{(total)}$ is 0.014 and in the bulk flow is ~0.017, although the whole-rock data show scatter due to leaching of Mn. In secondary magnetite, $MnO/FeO_{(total)}$ is <0.002. The difference probably arose due to the very low solubility of Fe^{3+} in hydrothermal solutions, which commonly leads to the rapid precipitation of fine-grained iron hydroxides, or in this case magnetite; Mn^{2+} and Mn^{3+} are more soluble and can be removed in solution.

Magnetite commonly forms intergrowths with, overgrows, or is itself overgrown by heazlewoodite (Ni_3S_2). Heazlewoodite is also found alone in serpentine, forming acicular crystals >20 μm long, with triangular cross-sections ~2 μm across. The overgrowths and intergrowths of the two phases suggests another case of heteroepitaxial growth. Magnetite is cubic (a = 8.394 Å), and heazlewoodite is trigonal (a = 5.935 Å, c = 7.139 Å). Potential crystallographic orientations and lattice spacings for the two minerals are listed in Table **4.13**.

Table 4.13 Lattice spacings of coincident(?) magnetite and heazlewoodite planes

Magnetite	spacing (Å)	Heazlewoodite	spacing (Å)	mismatch (%)
3·[111]	14.54	2·(0001)	14.28	−1.8
$[1\bar{1}0]$	5.94	(1000)	5.74	−3.4

The presence of clinochlore (aluminous chlorite) replacing olivine near the flowtop and filling certain veins indicates the serpentinizing fluid could also transport Al (at least locally, at high temperatures, and from glass). Talc fills most of the small spherical vesicles in the B-layer, replaces fine olivine blades and crystal tips, and is also present in and adjacent to some veins.

4.4.3 Mechanics, timing, and kinetics of serpentinization

Extent of serpentinization

The serpentinization reaction did not go to completion in any of the studied flows from Pyke Hill, but the cumulate layers of the two 1–1.5 m thick flows examined are notably less serpentinized than those of the overlying 6 m thick flow and other thick flows studied (Arndt, 1986a; Barnes et al, 1983; Barnes, 1985). There is no ready explanation

for this if the serpentinization occurred during tectonism; olivine would have been a reactive mineral in a deeply buried thick pile of volcanic rocks, and whether a given grain was 50 cm or 3 m from a flow margin would have been inconsequential, especially over the time frame of regional metamorphism. On the other hand, if the serpentinization occurred during the cooling and fracturing of the flow, then thick flows would have experienced longer-lived hydrothermal circulation as a result of their larger heat content and serpentinization could have proceeded further than in thin flows.

Because the solubility of Si in water is typically ≤ 500–1000 mg/L, at least 250–500 mL of water is required to transport the ~0.27 g of Si released from 1 cm^3 of serpentinized olivine. Regardless of the exact details, the dissolution and transport of Si is likely to be the rate-limiting step in serpentinization (Martin and Fyfe, 1970), and a much larger volume of water interacts with the rock than what remains chemically bound in serpentine. Beaty and Taylor (1982) stress this point in their oxygen isotope study of Pyke Hill lavas. They conclude that extensive replacement of oxygen in the original silicates has occurred, at a water-to-rock ratio of at least 2:1 (and possibly much greater). The hydrothermal experiments of Martin and Fyfe (1970) suggest that the serpentinization of these flows could have been accomplished in days or weeks, i.e., on the scale of the cooling time of a thick flow.

Expansion of serpentinized komatiites

According to serpentinization reaction (IA) (Section **4.4.2**), B-layer komatiites would have expanded by up to 25% during serpentinization. Density measurements are less subjective than the textural interpretation of microfractures in altered rocks; in fact, given the demonstrated immobility of most of the major elements, they are unequivocal proof that such expansion occurred. I directly calculated the density of several komatiite samples from the A_2, A_3, and B layers of the 6 m thick flow by using a micrometer to measure the dimensions of unfractured, cut-and-ground blocks of known mass. I also used the Archimedian method to determine the density of several irregular samples. The results (Table **4.14**) show that the B-layer cumulate that would originally have been the densest rock (~3.30 g cm^{-3}) is now the least dense (2.751 g cm^{-3}). Factoring in CaO and Na_2O loss and H_2O gain, this is equivalent to ~25% expansion, which corresponds quite well with the measured 8.5% LOI of the rock (8.5 wt.% H_2O ≈ 65 wt.% serpentine ≈ 22% expansion). The GOR samples are Cretaceous komatiites from Gorgona Island, Colombia, and are courtesy of Dr. N.T. Arndt; GOR-28 and GOR-29 are particularly fresh.

Table 4.14 Measured densities of komatiites

Sample	Textural type	Density (g cm^{-3})	Method
MS93-17	A_2	2.906	direct meas.
MS93-13	A_3	3.027	"
MS93-07	B	2.751	"
GUIB-1	A_3	2.957	"
GOR-28	A_2 (two pieces)	3.082, 3.100	Archimedian
GOR-29	B_1	3.112	"
GOR-30	B (altered)	2.880	"
GOR-07	A_3 (highly altered)	2.930	"
quartz (meas.)	optical quality	2.649	"
quartz (theor.)	—	2.650	XRD

Because of this substantial volume increase, microfractures would have formed continuously and created sufficient permeability to allow water continued access to the rock. It may seem unlikely that petrologists could have overlooked ~25% expansion in these rocks, but careful observation shows that what must originally have been a more or less continuous reticulated groundmass of clinopyroxene and glass has been disrupted on a grain-by-grain scale (Fig. **4.14**). This is not obvious by reflected light microscopy, and even less so in transmitted light. However, fractures and deposition of magnetite and alteration of groundmass is found near stress concentrations, such as sharp interfacial angles of olivine crystal faces (Photos **4.17** and **4.18**). Serpentinization and magnetite formation is visible in small fractures joining olivine grains. Expansion is also evident in offsets across small serpentine-filled fractures in olivine grains (e.g., Photos **4.14** to **4.16**).

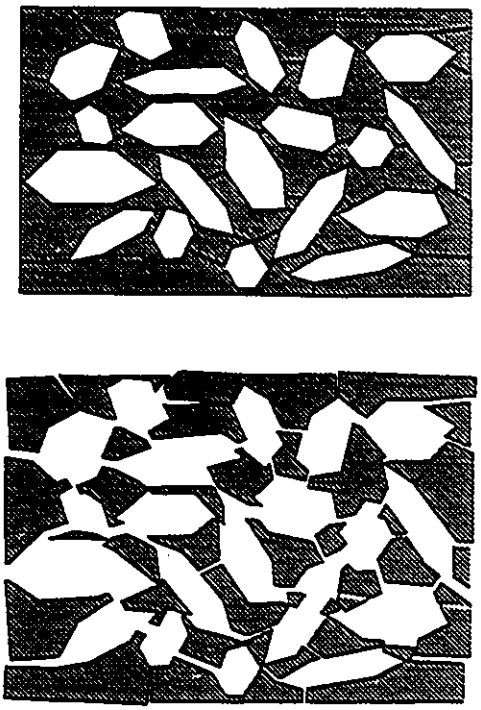

Fig. 4.14 Schematic diagram showing an olivine orthocumulate (touching framework of ~40 vol.% olivine crystals) before and after isochemical serpentinization of olivine. The area (or volume) has increased by ~15% without significantly changing the appearance of the rock. In an actual altered rock, most geologists would recognize the orthocumulus texture without being particularly concerned about the subtle expansion (that would at any rate commonly be masked by metamorphic recrystallization). See Photos **3.10** and **4.14** to **4.18**.

A number of researchers (e.g., Barnes, 1985) who have made mass-balance calculations of the olivine lost from the A-layer and gained by the B-layer have found excess olivine in the latter and concluded that the flow behaved as an open system. Although such excess olivine *is* present in many flows, including the Pyke Hill lavas (Fig. **3.17**), in neglecting the volumetric expansion of the B-layer the amount of cumulus olivine has been overestimated by up to ~25%. Clearly, not every komatiite flow can contain excess olivine. It is possible that the more differentiated lavas have been undersampled because they are dull-looking, massive flows lacking spinifex texture; my own sampling certainly reflected such a bias.

Photos 4.17 and 4.18 These photomicrographs of the B-layer of a thin flow from Pyke Hill (upper one taken with transmitted light, lower one with reflected light) show that deposition of magnetite (white in reflected light, opaque in transmitted light)—and presumably additional alteration of the groundmass—occurred near fractures that originated at the sharp edges formed by olivine crystal faces. Because serpentinization increased the volume of the olivine crystals, stress concentrations occurred at such edges and fractures formed linking one olivine crystal to the next. Such fracturing is a potential method for introducing fluid on a grain-by-grain basis. [High-relief colorless grains surrounded by serpentine are relict olivine. Groundmass consists of unaltered augite in chlorite. About a dozen small yellow grains of heazlewoodite are visible in serpentine.] Field of view is 500 μm.

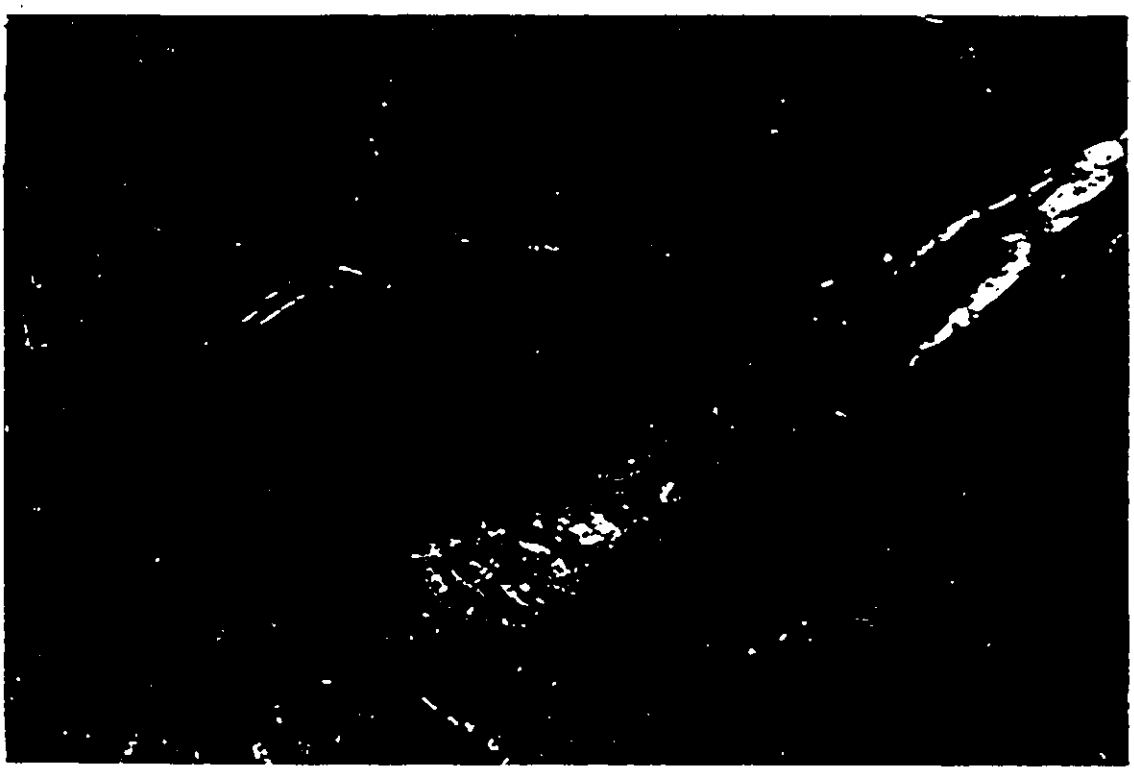

Timing of serpentinization

As I noted in at the beginning of this section, a number of observations suggest that serpentinization did not occur as a result of large-scale metamorphism. However, the enhanced preservation of relict olivine in thinner flows hardly constitute definitive proof of that hypothesis. Stronger evidence comes by observing the manner in which komatiites expanded during serpentinization. Under hydrostatic pressure no particular direction of expansion would be favored, and a rather massive serpentinite would result. I have observed such rocks near Thetford Mines and Asbestos, Quebec. However, in an exposed or shallowly buried flow on the seafloor, expansion would be strongly directed towards the free upper surface (the way bread rises in a pan, for example). Microfractures and planar laminae of magnetite and serpentine are ubiquitous in the B-layers of the Pyke Hill komatiites, and are consistently parallel to the upper and lower flow surfaces (Photo **4.19**). These laminae superficially resemble the shear bands or axial planar schistosity developed in strained rocks. However, microscopic study shows that they are actually caused by uniaxial expansion during serpentinization, presumably parallel to σ_3 (i.e., the least principle stress axis). This indicates that the net 20 to 30% volume increase was mainly accommodated vertically, at low pressures, and *prior* to the ~2700 Ma tectonism that folded (or rotated) the flows into their present near-vertical attitudes. It is possible that the flows were serpentinized at some other point in the 5–10 Ma prior to their deformation during the Kenoran orogen. However, serpentinization immediately following volcanism is appealing for other reasons. The temperature of the solidified lava flow is at a maximum, and there is a lower probability that cooling fractures will be sealed by secondary minerals.

Photo 4.19 Photograph of the cut and ground surface of a typical B-layer komatiite from a thin Pyke Hill flow. The rock is 7.5 cm high, and is oriented upright. The actual light to medium grey color of the rock appears yellowish green through a combination of photography under tungsten light and the photocopy process. It is important to note that the closely spaced laminae are not shear bands, pressure-solution cleavage, or axial planar foliation, nor are they a primary structure such as igneous layering. Rather the laminae occur as a result of expansion during the serpentinization process; the expansion was directed parallel to the least principle stress axis, which would have been perpendicular to the surface of the flow (or thin volcanic pile). This is apparently a novel mechanism for the development of foliation in ultramafic rocks, and will be further investigated. [I thank Dr. K. Benn for a helpful discussion on the subject.]

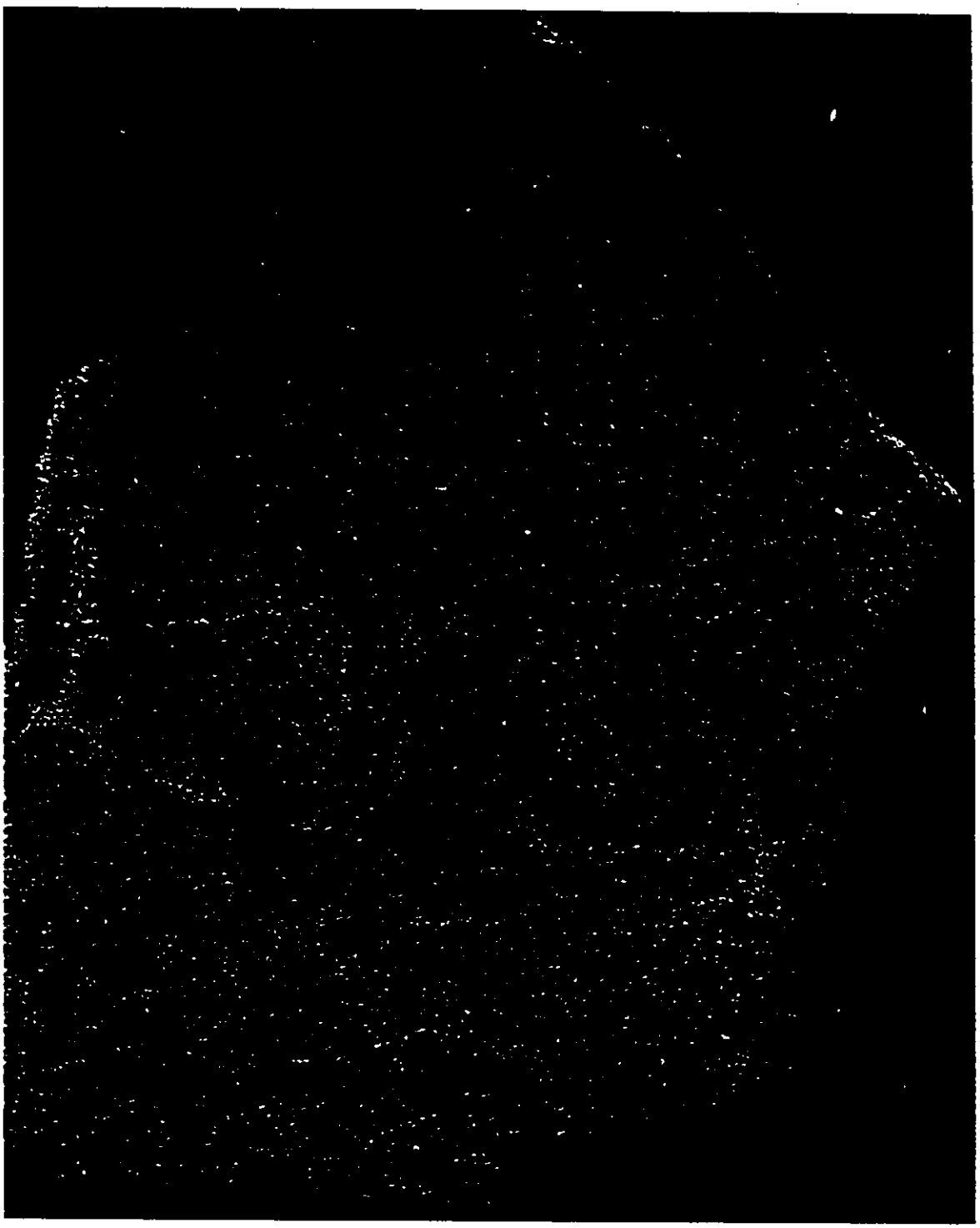

Possible synvolcanic flowtop alteration

The unequal preservation of adjoining upper and lower chilled margins is also consistent with the hypothesis of synvolcanic alteration. The flowtops of the studied lavas are highly oxidized and chloritized, have no relict olivine, and locally contain 5–10% by volume of ragged, 20–50 μm tremolite crystals in weakly oriented sheaves. The basal chills of the overlying flows, which would have been mineralogically and texturally identical to the flowtops, are much better preserved. They contain abundant relict olivine, no tremolite, and oxidation and serpentinization that is largely confined to the margins of small fractures.

I suggest that the highly reactive combination of olivine and a Mg, Ni, and Cr-rich glass rapidly altered on the sea floor, possibly due to hydrothermal fluids circulating through the lower portion of the flow, and then underwent short-lived (hours to days) but intense (600–700 °C) contact metamorphism due to the subsequent overlying flow. The environment around a molten submarine lava flow is an active one, both physically and chemically. Films made of underwater lava flows from Kilauea show that hot basalt is surrounded by clouds of gas bubbles. These must be largely composed of H_2 and O_2 formed by the thermal decomposition of water because H_2O vapor would recondense almost instantly, and other magmatic volatiles have largely been degassed during the ~10 km flow to the sea. High levels of dissolved H_2 have also been directly measured in such waters (e.g., Sansone et al., 1991). Superheated steam is a powerful oxidizing agent, and could easily have formed the magnetite and serpentine adjacent to many fractures.

4.4.4 Mineralogy of geochemically-mobile elements

The question arises, if Ca and Mn were leached by a reactive fluid phase that penetrated entire flows on a grain-by-grain scale, then what of Na, K, Rb, Sr, and Ba? Whole-rock geochemical data in this work (and others) indicates that these elements, unlike Al or Ti, are not controlled by simple olivine fractionation (Section 3.2.4). The amount of these elements originally contained in olivine was negligible, and augite probably contained less than a quarter of the original Na and Sr in the bulk rock, and a very small fraction of the K and Rb. In all probability, the alkalis and alkaline earths Sr and Ba were originally concentrated in residual glass or the margins of μm-size feldspar dendrites. In komatiites the glass has been altered, predominantly to clinochlore or a related mineral with various accessory oxides, sulfides, and silicates. I carried out an XRD

scan of a texturally well-preserved basal chilled margin, which indicated the presence of tremolite, magnetite, minor olivine, and a poorly crystalline clay mineral. Because the clay mineral lacked the ~14 Å diffraction peak of chlorite-group or smectite-group minerals, it was probably a septechlorite, with a composition somewhere between serpentine ($Mg_3Si_2O_5(OH)_4$) and amesite ($Mg_2Al_2SiO_5(OH)_4$). [Accurate determinations of clay mineralogy generally involve glycolation, repeated XRD scans, differential thermal analysis, and other techniques. I did not undertake this, so apart from aluminous chlorite analyzed by microprobe and identified optically, my identification of clay minerals must be considered as tentative.]

Few of the observed secondary minerals contain favorable sites for Na, K, Rb, Sr, and Ba. I suggest that in rocks lacking feldspar these petrogenetically interesting elements may be concentrated in a smectite or illite-group mineral, possibly intergrown or interlayered with chlorite. In any event, neither μm-size clay or dendritic feldspar crystals are resistant minerals; in particular, smectites can easily exchange cations with interstitial solutions. For example, even the very fresh Zvishavane flows have discordant ^{87}Rb–^{87}Sr isotopic ratios due to mobilization of Rb (Nisbet et al., 1987). Walker et al. (1988) determined an apparent ^{87}Rb–^{87}Sr age for Pyke Hill komatiite flows of ~1000 Ma, and suggested that this resulted from a resetting of the isotopic system caused by the Grenville orogeny. This suggestion is not unreasonable. Morton (1985) documented similar resetting of ^{87}Rb–^{87}Sr systematics during the diagenetic crystallization of sub-μm illite under conditions of very mild diagenesis (~60 °C) of Paleozoic shales in Texas. Therefore, even a mild thermal perturbation, possibly associated with groundwater flow, could have caused chemical exchange of the more mobile elements in komatiites. See also Section 3.2, whole-rock geochemistry.

5 Cooling and differentiation

5.1 Cooling at the microscopic level

5.1.1 Crystallization of olivine from silicate liquids

The growth rate and crystal habit of olivine in silicate rocks depends upon the composition of the melt, amount of undercooling, cooling rate, thermal gradients, crystal anisotropy, and melt flow (e.g., Donaldson, 1976). Other parameters, such as melt viscosity (which affects solute transport via diffusion and convection), can also be related to the temperature and composition of the melt. Undercooling and olivine supersaturation are not independent variables; for a given slowly cooled, near-equilibrium system the temperature determines the amount of olivine crystallized. In more-rapidly cooled systems kinetic factors such as nucleation rate, solute diffusion, and interface-controlled crystallization can decrease (if excess Mg remains in glass) or increase (if crystallization of Mg-bearing phases such as pigeonite or augite is suppressed) the amount of olivine that actually crystallizes in a given rock or experimental charge.

Despite the potential importance of thermal gradients and melt flow, these effects have seldom been studied by experimental petrologists (exceptions include Walker et al., 1988, and Donaldson, 1993). This may be due to the fact that experimental parameters such as sample composition, the partial pressure of water, oxygen fugacity, temperature, and cooling rate are readily controlled and of clear significance, whereas the other factors are difficult to control or even to measure. In experiments where the charge is held in a crucible or on a wire loop in a vertical-tube furnace, thermal gradients are likely to be low ($\leq$1 °C mm^{-1}) but not negligible (Walker et al., 1988). Thermal gradients in box furnaces would be considerably lower due to the larger volumes and more uniformly heated walls, but such furnaces are not widely used by petrologists. In high-pressure multi-anvil presses, thermal gradients can be enormous (>100 °C mm^{-1}) because a massive heat sink surrounds the small heated volume, and the efficiency of thermal insulators is reduced at high temperatures and pressures (Zhang and Herzberg, 1994). Experimental petrologists have only recently begun to address the significant effects—zonation of charges due to temperature variation, crystal-liquid separation, Soret diffusion, etc.—caused by such extreme thermal gradients (Zhang and Herzberg, 1994; Herzberg and Zhang, 1995).

The rate of crystallization of different minerals from their stoichiometric melts varies greatly. The crystallization of tectosilicates (silicates with complex structures polymerized or cross-linked in three dimensions) such as albite or cristobalite from the melt is very slow due to sluggish crystallization kinetics, low heats of crystallization, and high melt viscosities; in consequence glasses of such compositions are easily formed. Less polymerized diopside or anorthite melts crystallize more rapidly but still readily quench to glasses. In contrast it is very difficult to quench a forsterite melt to glass because the transformation from the highly depolymerized melt to the orthosilicate structure is extremely fast. The short to medium-range structure of molten olivine may in fact be somewhat similar to that of crystalline olivine, although cations such as Mg^{2+}, Fe^{2+}, and Ni^{2+} may be in 4 or 5-fold coordination with oxygen rather than the 6-fold coordination of olivine (e.g., Jackson et al., 1993; Galoisy and Calas, 1993).

In magmas—which inevitably crystallize incongruently—crystal growth rates are also dependent upon the diffusion of required components towards, and rejected components away from the crystal–melt interface. [From this point on, instead of referring to a congruently-crystallizing stoichiometric liquid, the term "melt" will be used in its broad geological sense of a silicate liquid. A more precise (but clumsy term) would be high-temperature silicate solution.] Chemical diffusion in a very hot, depolymerized melt such as a komatiite will be considerably faster than in a typical molten basalt, and orders of magnitude faster than in a rhyolite. The very low viscosity of molten komatiite also permits physical mixing via bulk flow or thermally or compositionally driven convection to occur much more readily. The controlled cooling-rate experiments of Donaldson (1976) showed that for a given undercooling the growth rate of olivine was roughly proportional to the normative olivine content of a melt, and increased in the order picrite → komatiite → peridotite (~15, ~28, and ~40 wt.% MgO, respectively). As is true of many other minerals, rapid crystallization affects the crystal habit of olivine; however olivine is somewhat unusual in developing a plate-like habit rather than an acicular one when grown at moderately large undercoolings. This is because both the *a* and *c* axes are parallel to directions of rapid growth (e.g., Fleet, 1975a), in contrast to minerals such as feldspars in which rapid growth occurs parallel to only one axis.

When the major element composition of the komatiite melt and olivine is given in terms of molar volumetric concentrations (Table 5.1) it can be seen that, to a first approximation, the crystallization of olivine requires only the counterdiffusion of Mg vs. Ca and Al. Chemical diffusion within multicomponent silicate melts is considerably more

complex than the tracer or self-diffusion of single elements, and only in recent years has it been studied in detail (Trial and Spera, 1994). However, a simplified observation is that chemical diffusion in such melts is strongly controlled by the diffusivities of network-forming elements such as Si and Al (Baronnet, 1984). The net flux of Si at the olivine–komatiite melt interface is quite small, and the self-diffusivity of divalent cations such as Mg and Ca is considerably greater than that of Al. Therefore it is reasonable to assume that mass transfer is limited either by the rate at which Al ions diffuse away from the growing olivine crystal face, or by compositionally driven convection of the depleted boundary layer surrounding the crystal.

Table 5.1 Volumetric concentration of major elements in komatiite melt and olivine

Phase T=1560 °C	SiO_2 mol cm^{-3}	MgO mol cm^{-3}	FeO mol cm^{-3}	CaO mol cm^{-3}	Al_2O_3 mol cm^{-3}
Melt (28% MgO)	0.0208	0.0189	0.0037	0.0035	0.0038
Olivine (Fo_{94})	0.0215	0.0402	0.0025	0.00011	0.00005

The crystallization behavior of komatiites differs significantly from that of felsic lavas and low-Mg basalts. In the latter magmas nucleation rates, surface growth kinetics, and chemical diffusivities have greater influence on crystal growth-rates than they do in komatiites. Because of the simple structure of olivine, its broad structural and chemical similarity to the komatiite liquid, and the enhanced chemical diffusion within the hot, non-viscous melt, the dominant factor controlling olivine growth in thin komatiite flows would have been the rate of heat loss from the lava. In ultramafic liquids olivine can crystallize rapidly enough to be a nuisance in high-pressure experimental petrology. In such experiments enough skeletal olivine (± pyroxene) can grow during 10–30 second quenches to make the composition of the glass in the quenched sample quite different from that of the high-temperature liquid (e.g., Green et al., 1975; Zhang and Herzberg, 1994; many others). Because of the strong role of heat flow in the growth of olivine crystals in komatiites, factors that can be neglected in the growth of olivine in basaltic rocks (thermal gradients, thermal diffusivity, infrared transmissivity of crystals, etc.) must be considered carefully.

Textural evidence indicates that the homogeneous nucleation and growth of olivine occurred readily in komatiites (see Section 3.1.2). Even in chilled basal margins or in the cm-size globules that form the brecciated flowtop, the layer of predominantly glassy material is only about 0.8 mm thick, with an abrupt transition to a groundmass rich in

skeletal olivine. The innermost layer of glass would have cooled from 1550 °C to below 1000 °C in about 2–5 seconds. [This calculation is based on thermal conduction through glass having a thermal diffusivity of 4×10^{-7} m^2 s^{-1} and with a heat flux of 1–2 MW m^{-2} at the glass–water interface, appropriate for nucleate boiling (e.g., Holman, 1990; nucleate boiling involves the formation of many small vapor bubbles, as contrasted to the film boiling that can occur on very clean, smooth surfaces). This subject is further treated below.] The chilled margins of Pyke Hill lavas contain 5–10% of euhedral olivine phenocrysts, and so were not superheated. Presumably olivine nuclei were abundant in the melt, but this cannot be determined from examination of the devitrified glass. Even komatiite melts heated 100–200 °C above the liquidus and quenched by pouring onto cold steel plates crystallize ~10 vol.% olivine (Miller et al., 1991); glasses of olivine composition cannot be quenched from the melt but only made by shock-induced amorphization or the drying and densification of gel precursors. Such observations show that the nucleation of olivine, as well as its subsequent growth, is very rapid in Mg-rich silicate melts.

5.1.2 Thermal conductivity of crystals

The mechanisms of thermal conduction in matter are lattice (phonon) conductivity, radiant (photon) conductivity, electronic conductivity, and convection; the last is restricted to fluids and combines flow with one or more of the other mechanisms. Electronic conduction in olivine is negligible at the temperatures of interest and will not be discussed. Phonons are quantized lattice vibrations (i.e., resonant frequencies) permitted by the symmetry of the crystal unit cell. In highly perfect crystals phonons are transmitted with little scatter, leading to very high thermal conductivities (at low temperatures the thermal conductivity of most crystalline substances increases ~T^3, but reaches a maximum at temperatures that vary widely between different materials). The thermal conductivity of single-crystal NaCl, a representative ionic material, is shown in Fig. **5.1**. At higher temperatures (i.e., $T \geq 100$ K) atomic thermal vibrations lead to increased phonon scattering, which causes the lattice conductivity of many ionic and covalent crystals to vary inversely with temperature (Berman, 1976). The thermal conductivity (or diffusivity) of olivine has been measured several times, generally at high pressures (Kanamori et al., 1968; Fujisawa et al., 1968; Beck et al., 1978; Katsura, 1995). Many of these measurements are highly inconsistent (discussed below). At low to moderately high temperatures olivine exhibits normal behavior; however at high temperatures certain of these measurements show anomalous increases in thermal conductivity (e.g., Kanamori et

al., 1968), and were likely affected by radiant heat transfer, an experimental problem common in measurements of the thermal conductivity of other transparent single crystals, polycrystalline aggregates, and glasses (Touloukian et al., 1970, 1973). Significantly, anomalous increases at high temperatures are minimized in strongly scattering (e.g., polycrystalline ZrO_2 and ThO_2) or strongly absorbing (e.g., Mo-sintered Al_2O_3) compounds (Touloukian et al., 1970).

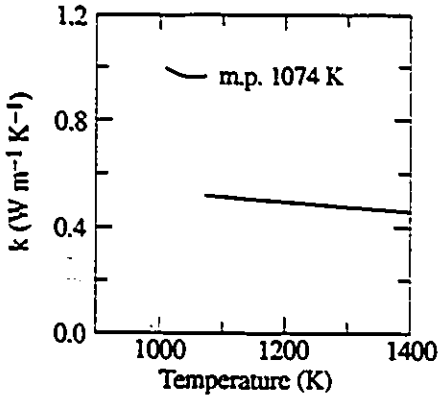

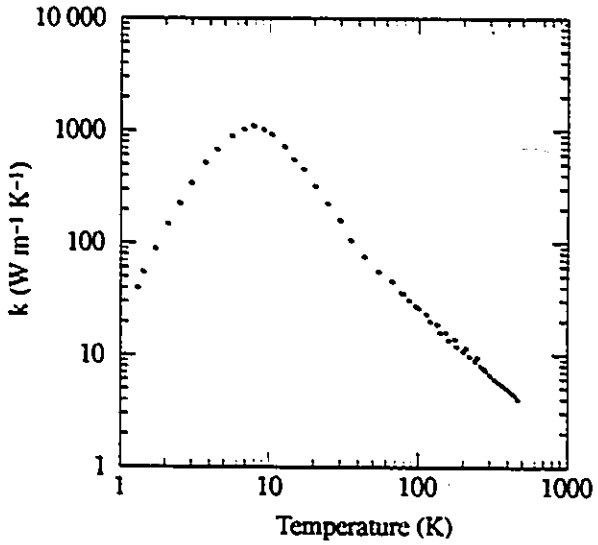

Fig. 5.1 The thermal conductivity (k) of NaCl at low to moderate temperatures (right), and in the vicinity of the melting point (below). The thermal conductivity of olivine shows similar behavior, but the available data are much less accurately known than that of NaCl, a model ionic substance that has been studied in great detail. Data are from Touloukian et al., 1970; Janz, 1991; and Khokhlov et al., 1993.

The thermal transport properties of minerals and melts at high temperatures are much more poorly known than the heat capacities or coefficients of thermal expansion. Substantial technical difficulties are involved in measuring small samples at very high temperatures. In some cases, measurements may have large errors due to uncorrected radiative thermal transfer or other systematic experimental errors (e.g., Kanamori et al., 1968; Beck et al., 1978; Snyder et al., 1994). At best, typical measurements at low to moderate temperatures appear accurate to ±20%, with accuracy decreasing to ±50% at temperatures above 1200 K. Certain reasonably consistent data sets in the literature do not show a rise in thermal conductivity at high temperature, and indicate the lattice thermal conductivity of olivine at low pressures varies from 5.0 W m^{-1} K^{-1} at 300 K to ~2.0 W m^{-1} K^{-1} at 1750 K (e.g., Fujisawa et al., 1968; Beck et al., 1978, when corrected for an apparent systematic experimental overestimate of the conductivity). These values

correspond to thermal diffusivities of ~2×10^{-6} to 0.5×10^{-6} m^2 s^{-1}. Measurements of the thermal diffusivity of synthetic polycrystalline olivine (Fo_{80}) by Katsura (1995) are consistent with these values, and converge to ~$0.6–0.8\times10^{-6}$ m^2 s^{-1} at high temperatures. In addition, recent measurements (at ambient conditions) by Chai et al. (1996) show that the thermal diffusivity of olivine parallel to the *a*, *b*, and *c* crystallographic directions is 2.16(4), 1.25(2), and 1.87(4) $\times10^{-6}$ m^2 s^{-1}, respectively. [The corresponding values of thermal conductivity are 5.9(1), 3.40(6), and 5.1(1) W m^{-1} K^{-1}.] This previously unrecognized strong anisotropy is a possible explanation for inconsistent values of the thermal conductivity of olivine, even at moderate temperatures where the measurements should be quite straightforward.

5.1.3 Thermal conductivity of silicate melts and glasses

Introduction

Although the lattice thermal conductivity is an important transport property of silicate glasses and melts, few reliable measurements of this property above ~600 K exist. Glass manufacturers are satisfied with relatively inaccurate data, in part because commercial glasses are much more transparent than basaltic glasses, making lattice thermal conductivity less important than radiative heat transfer (e.g., Kruszewski, 1961; Condon, 1968). In the physics literature, much of the research into thermal conductivity of glasses has focused on very low temperatures (1–100 K). The geological literature contains a number of measurements of the thermal conductivity of glasses at low to moderate temperatures (0–400 °C), and a handful of measurements of silicate liquids. Because of the limited number of reliable high-temperature data for silicates, I have extrapolated reliable low-temperature data to higher temperatures (see below).

Temperature dependence

The thermal conductivity of glasses has a weaker dependence on temperature than does that of crystals. The variation is also of the opposite sign, with thermal conductivity increasing slowly with temperature up to at least the glass transition temperature (Touloukian et al., 1970). This can be explained by phonon scattering in a medium that is strongly disordered even at low temperatures; at higher temperatures the disorder does not significantly increase (Berman, 1976). Above the glass transition temperature (typically about ~0.8 T_L where T_L is the liquidus temperature) the thermal conductivity is

likely to decrease as the glass changes from an amorphous solid to a supercooled liquid. Certainly, other properties such as the heat capacity, thermal expansivity, viscosity, and mean velocity of sound change across this transition.

Crystalline substances typically show a decrease in thermal conductivity of 30–50% upon melting. Examples include ice and water: 2.2 and 0.59 W m^{-1} K^{-1} at 273 K; $NaCl_{(s)}$ and $NaCl_{(l)}$: 0.97 and 0.52 W m^{-1} K^{-1} at 1074 K; and $Na_{(s)}$ and $Na_{(l)}$: 120 and 88 W m^{-1} K^{-1} at 371 K. One simple reason for the drop in thermal conductivity at the melting point is that phonons with a shear component cannot propagate through a liquid. The change from a crystalline substance to a melt (even one possessing some short-range order) must also be significant.

Murase and McBirney (1973) measured the thermal conductivity of silicate glasses and melts ranging from rhyolite to basalt. Above ~1100 °C, thermal conductivities showed anomalous increases that were likely due to radiant heat transfer in the steady-state measurement technique used. Samples containing more FeO were less affected, presumably because of their greater absorption in the near-infrared region. The values measured for mafic melts at 1500 K (~1 W m^{-1} K^{-1}), are probably fairly close to the true values. Accurate data for molten salts show that the thermal conductivity decreases weakly with increasing temperature (Janz, 1991); the molten silicates show analogous behavior when the data most affected by radiant heat transfer (low FeO melts at high temperatures) are omitted.

Few studies of the thermal conductivity of silicate melts were made subsequent to the work of Murase and McBirney (1973). Recently, Snyder et al. (1994) measured the thermal conductivity of a melt of diopsidic composition at temperatures between 1673 and 1873 K, and obtained extremely low values, particularly at high temperatures (e.g., as low as ~0.02 W m^{-1} K^{-1} at 1873 K). The transient hot-wire method they employed uses a refractory metal filament as a simultaneous line heat-source and resistance thermometer, and is suitable for measuring a wide variety of fluids to an accuracy of 1% or better. However the experiment had significant flaws as carried out (Shore, 1995). In addition Snyder et al. appear to have made many numerical errors in correcting for the thermal radiation emitted by the filament. Given these points, I consider their data unreliable and do not use it. Instead, I assume a value of thermal conductivity of 1.0 W m^{-1} K^{-1} for the komatiite liquid between 1550 and 1200 °C.

Compositional dependence

The thermal conductivity of silicate glasses depends weakly upon composition. Broadly speaking, glasses with heavy elements of large ionic radii (e.g., Sr, Ba, Pb) have lower thermal conductivities than those rich in light elements (e.g., Li, B) or cations with small effective ionic radii (e.g., $^{[4]}Zn^{2+}$). However the variation between the lowest and highest conductivities is only a factor of ~2. At 300 K the thermal conductivity of a typical mafic glass is ~1.2 W m^{-1} K^{-1}, quite similar to that of fused silica, Pyrex, or soda-lime glass (1.4, 1.2, and 1.2 W m^{-1} K^{-1}, respectively).

5.1.4 Radiant heat transfer

Radiant heat transfer has similarities with other modes of heat transport. Energy is transmitted down a temperature—or emissive power—gradient by the emission and absorption of photons (Siegel and Howell, 1981). The measurement of this property is not always straightforward. Whereas lattice conductivity is independent of sample thickness and shape, radiative conductivity also depends on geometric factors and the far-field temperature distribution. The radiative thermal conductivity (k_R) within a large body at thermal equilibrium with temperature varying in one direction only is described by the expression:

$$k_R = \frac{20\sigma T^3}{\pi^4}\int_0^{\infty} l_x \frac{e^x x^4 n_x^2}{\left(e^x - 1\right)^2}\,dx\,, \quad \text{with } x = \frac{h\nu}{kT}\,,$$

with l_x and n_x equal to the photon mean free path and refractive index at frequency ν and mean temperature T (Shankland et al., 1979); h is Plank's constant (6.626×10^{-34} J s), k is Boltzmann's constant (1.38×10^{-23} J K^{-1}), and σ is the Stefan-Boltzmann constant (5.67×10^{-8} W m^{-2} K^{-4}). Where scattering is minimal, as in a homogeneous liquid, glass, or single crystal, the mean free path equals the reciprocal of the absorption coefficient, i.e., $l_x = \alpha^{-1}$. In a grey medium (i.e., absorption is wavelength-independent) of low dispersion with average refractive index $\bar{n}$, $k_R = (16/3)\sigma \bar{n}^2 T^3 \alpha^{-1}$ (Condon, 1968). According to this formula radiant thermal conductivity would dominate heat transport in highly transparent (low α) substances, even at room temperature, and the radiant thermal conductivity of a vacuum would approach infinity. However this simplified analysis does not consider temperature discontinuities or photon mean free paths larger than the size of an object. In solid matter, absorption edges in the near to mid-IR (e.g., ~3.5, 5, 8, and 16

μm for fused silica, Al_2O_3, CaF_2, and NaCl, respectively) also block a significant proportion of the low-temperature thermal emission.

Effective radiant thermal conductivity of olivine

Precise knowledge of the optical properties $n(\lambda,T)$ and $\alpha(\lambda,T)$ at wavelength λ is sufficient to allow the numerical calculation of the radiative thermal conductivity, even in a substance with optical properties that are highly wavelength- or temperature-dependent. An uncertainty of ~10% in the value of k_R determined by Shankland et al. (1979) arises from the poorly known values of $\partial n/\partial\lambda$ and $\partial n/\partial T$ because these parameters affect the experimental measurement of the absorption. Measuring the transmitted intensity of a reference beam with no sample and with parallel-sided samples of different thickness allows a sensitive determination of $\alpha(\lambda,T)$, but not of $n(\lambda,T)$. [A 1% measurement error of $\alpha(\lambda)$ leads to a 3% error in $n(\lambda)$: Gryvnak and Burch, 1965).

Olivine is not a grey medium and the broadening and intensification of optical absorption bands in the near-IR with increasing temperature reduces its effective radiant conductivity from the theoretical T^3 dependence. At temperatures from ~1200–1550 °C, the effective radiant thermal conductivity of a large single crystal or weakly scattering polycrystalline body of olivine (Fo_{90}) is ~2–3 W m^{-1} K^{-1} (Shankland et al., 1979; Burns, 1993). In Fe–Mg olivines Fe is disordered over the M1 and M2 sites, so the Fe^{2+} absorption coefficient obeys the Beer-Lambert law; i.e., its molar absorptivity is constant for a given temperature and crystallographic orientation. [Iron-bearing olivine is strongly pleochroic in the near-IR (Burns, 1993) with a maximum absorption occurring for light polarized parallel (i.e., with the electric field vector parallel) to the γ optical axis (equivalent to the *a* crystallographic axis); the lowest absorption of unpolarized near-IR radiation occurs for propagation parallel to the *a* axis.] In the critical 0.9–1.5 μm band, the absorption coefficient of the most magnesian komatiitic olivine ($Fo_{93.7}$) will be about half that of the Fo_{90} measured by Shankland et al., and about one-third that of the least magnesian komatiitic olivine (Fo_{83}). Considering the proportion of the heat flow contributed within the 1 μm band, this would imply a radiant thermal conductivity 20–30% larger in $Fo_{93.7}$ and about 30–40% smaller in Fo_{83} than in Fo_{90}. Shankland et al. (1979) did not specify the exact composition of the olivine crystals used, only that they were $(Mg_{0.9}Fe_{0.1})_2SiO_4$ from San Carlos, New Mexico. Olivine from that location can vary from Fo_{88} to Fo_{92}, so a more detailed compositional correction is not justified here.

Radiant heat transfer in glasses and melts

The near-IR transmissivity of a komatiitic or basaltic melt will be lower than that of a coexisting olivine because of the higher concentration and less-regular coordination of Fe^{2+} in the melt, which cause broader and more intense absorption bands. For example, at 300 K the molar absorption coefficient of Fe^{2+} ($\lambda = 1\mu m$) is approximately ten times larger in a Na_2O-Fe_2O_3-FeO-SiO_2 glass (20 cm^{-1} for 0.9 wt.% FeO) than in Fo_{90} (20 ± 10 cm^{-1} for ~10 wt.% FeO) (Shankland et al., 1979; Burns, 1993; Susa et al. 1993). The contrast will decrease at higher temperatures because the absorption coefficient of a disordered material such as glass will have a weaker temperature dependence than that of olivine. Other species in the melt, such as Fe^{3+}, Ni^{2+}, Cr^{3+}, and Co^{2+} will give rise to additional absorption bands, further lowering the near-infrared transmissivity. However the much lower concentration of these ions makes these considerably less important than Fe^{2+}.

Underwater basalts have been observed to cool from bright yellowish-orange incandescence (T ~1150 °C) to black (T <550 °C) in about 0.6 second (Moore, 1975). The assumption that the glassy margins of such lavas cool predominantly by conduction is reasonable; basaltic glasses strongly absorb visible and near-IR radiation, and are essentially opaque to red light for thicknesses >0.5 mm (my observations), and to near-IR radiation for thicknesses >0.1 mm (Susa et al., 1993). Thus, incandescent basalt is invisible beneath even a very thin layer of cooled glass, and *direct* radiant heat transfer from molten lava through a solidified crust to the environment will not occur. [In subaerial basalts the heat transfer from the outermost crust to the environment involves a substantial radiative component that will exceed the convective heat transfer to air over much of the cooling period. However, this involves a temperature/material discontinuity and does not concern us here.] In molten silicates with low concentrations of transition metals (e.g., rhyolite, soda-lime glass) the mean free path of infrared radiation is several cm, and radiant thermal conductivity may be the dominant mechanism of heat transfer (e.g., Condon, 1968; Gable and Shankland, 1984).

Much of the above theory is predicated on one-dimensional diffusion of heat in a body of dimensions much greater than the photon mean free path. This does not hold for plate-like olivine crystals in spinifex-textured rock, where the mean free path of near-IR radiation is comparable to or larger than the crystal thickness. To evaluate this effect, I calculated the radiant heat transfer through a perfectly transmissive crystal using simplified but reasonable assumptions (e.g., similar refractive index for olivine and melt, melt

emissivity = 1, triangular olivine crystal cross-section). In an olivine crystal 10 cm high, infinitely long (not a critical assumption), varying from 0 to 0.6 mm thick, and with a basal temperature of 1200 °C and tip temperature of 1560 °C, the calculated heat flow through the crystal base due to lattice conductivity is ~7 kW m^{-2}. Depending upon the particular assumptions made about the thermal gradient, the heat flow due to radiation will be 6–9 kW m^{-2}. The radiative heat flux, even for the extreme case of a perfectly transparent crystal, is similar whether calculated directly or via the simplified method of using an effective thermal conductivity—i.e., adding an approximate radiative thermal conductivity of 2–3 W m^{-1} K^{-1} to the lattice conductivity of ~2 W m^{-1} K^{-1}. This is sufficiently accurate for the order-of-magnitude calculations considered here.

5.1.5 Constrained crystallization of olivine

A large number of measurements, coupled with the basic principles of thermal transport and optical absorption, indicate that both the lattice and radiant thermal conductivity of the komatiite melt will be significantly lower than those of olivine. The available (rather imprecise) data show that the overall thermal conductivity (radiative plus lattice) of the olivine crystals would have been about 3–5 times greater than that of the komatiitic melt in which they formed. Therefore, because the olivine crystals in spinifex-textured layers grew downwards into hotter melt, heat must have flowed from the melt through olivine. Considering heat flowing in parallel through elongated olivine crystals and the adjacent groundmass, the relatively high total thermal conductivity of the olivine (Fo_{90}) would have increased the thermal conductivity of the bulk rock by 30–50% over a typical dense basalt.

However, the most significant effect of the difference of thermal conductivity between liquid and olivine would have occurred at the tip of a growing crystal. The leading tip of an olivine crystal (assumed here to be the {120} form) will subtend an internal angle of 94.0°. The ability of the tip–melt interface, the hottest part of the crystal, to radiate and conduct heat into this ~π solid angle of cooler olivine must have had a significant effect on local undercooling and growth (Fig. 5.2). Such an effect was convincingly demonstrated by experiments in which yttrium aluminum garnets ($Y_3Al_5O_{12}$), containing varying amounts of Dy were grown under identical conditions. Garnets that contained a higher concentration of Dy^{3+}, a strong absorber in the near-infrared (2.4–3.5 μm), grew with a much flatter crystal–melt interface than did the more transmissive Dy-poor garnets (Cockayne et al., 1969; Fig. 5.3).

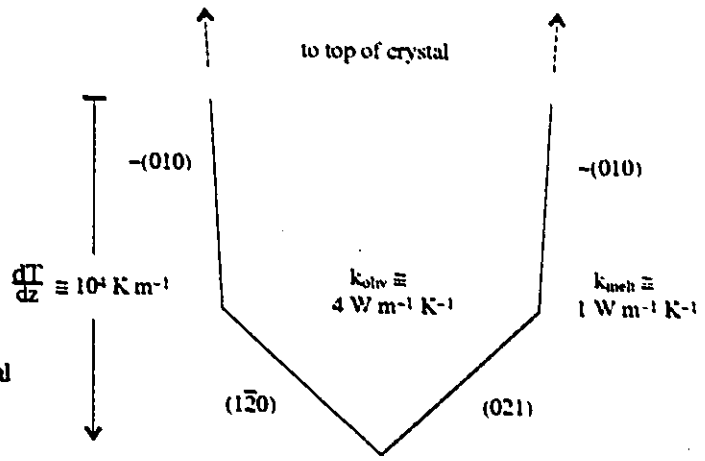

Fig. 5.2 Schematic diagram of the tip of a near-vertical plate-like olivine crystal that is growing in an extreme vertical thermal gradient. Such gradients are reasonable in a hydrothermally cooled flowtop. The thermal conductivities shown include the effects of radiant heat transfer, which is much more significant in the olivine than in the melt. The latent heat of crystallization produced at the growing {120} and {010} faces is removed more quickly than would be the case for an equant crystal suspended in a nearly isothermal melt, leading to correspondingly greater undercooling and faster growth rates.

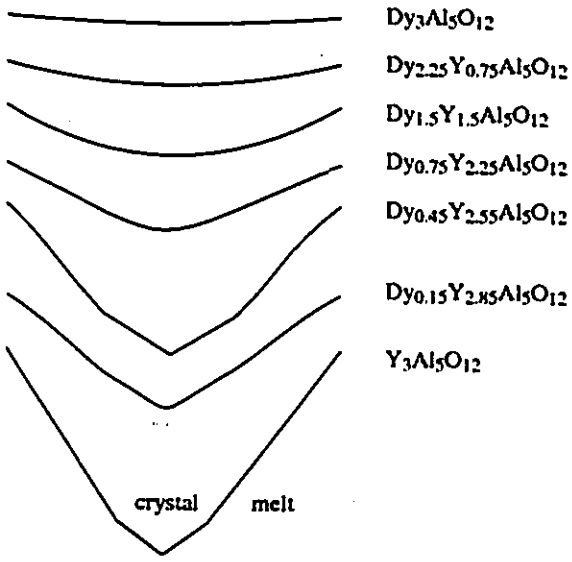

Fig. 5.3 Profiles of Czochralski-grown dysprosium/yttrium aluminum garnet crystals grown under identical conditions (redrawn from Cockayne et al., 1969). The diameters of the crystals were ~1 cm. The only relevant difference between Dy^{3+} and Y^{3+} is that the former possesses strong near and mid-IR absorption bands that sharply reduce radiant heat transfer within the crystal and lower the thermal gradient near the crystal-melt interface. The profiles of $Dy_{0.45}Y_{2.55}$ and $Dy_{0.15}Y_{2.85}$ are reproduced as shown in the original reference, where they appear to have been transposed.

The growth of a crystal from a hotter melt is termed *constrained crystallization*, and forms the basis for commercial techniques for growing large, highly perfect single crystals, such as the Czochralski method. Constrained crystallization is typical of crystal growth from congruent melts. It is less typical of growth from solution, and is quite unlikely to occur in free-standing equant crystals in a large magma body. The special circumstances of a high thermal gradient, elevated temperatures, and large differences in the thermal transport properties of melt and olivine (including anisotropy) make it likely to have occurred in komatiites, possibly playing a key role in the formation of spinifex texture. Donaldson (1977, 1982) noted the potential role of constrained crystallization in spinifex texture (as well as in the formation of comb layering of olivine, pyroxene, and plagioclase in other rocks), but did not appear to have investigated further.

Many crystals, ranging from refractory oxides and silicates grown from high-temperature melts to salts growing from ambient solutions, commonly grow from the margins of their containers inwards. This is often attributed to heterogeneous nucleation on pre-existing crystal surfaces or scratches. However, undercooling of the melt or solution in the immediate vicinity of the crystal tip due to the greater thermal conductivity of the crystal may act to stabilize tip growth parallel to the local thermal gradient (i.e., perpendicular to the crucible wall). This is seen clearly in a number of photomicrographs of quenched high-temperature silicate melts where skeletal olivine crystals grew at high angles to the melt surface or capsule walls (e.g., Zhang and Herzberg, 1994). In some cases the increased undercooling may be only a few mK, but due to the μm-scale distances involved thermal gradients can be substantial (Tiller, 1991a). Of course, this phenomenon can be coupled with compositional gradients caused by crystallization, and in many cases the chemical gradient will play a more important role than the thermal one.

Magmatic minerals more typically grow by unconstrained crystallization where thermal gradients are low and the latent heat of crystallization is dissipated in the slightly cooler (≤ 1 K in volcanic rocks, $<<1$ K in intrusive rocks) melt surrounding the crystal. The excess free energy associated with increased crystal surface area is the main factor stabilizing the planar crystal–melt interface in such growth. It is probable that olivine crystals in the cumulate layer of komatiite flows grew by unconstrained crystallization. It is possible that the dendritic and spherulitic clinopyroxene found in komatiites would not have had these habits had they grown by constrained crystallization as the first liquidus phase. Possible evidence for this is the "string-beef" texture commonly found in komatiitic basalts which is somewhat similar to spinifex texture, but formed by coarsely acicular

clinopyroxene rather than plate-like olivine. Despite cooling rates that must have been broadly similar to those of komatiite flows, clinopyroxene crystals in spinifex-textured komatiitic basalts commonly grew with well-formed planar facets, suggesting that they too grew by constrained crystallization.

Constrained crystallization exerts a stabilizing influence on the planar crystal–melt interfaces; the increased temperature away from the crystal surface suppresses the growth of protrusions and side-branches (Brice, 1986; Tiller, 1991b). Heat flow would be focused through the tip of the growing olivine because of its greater thermal conductivity. In effect, despite the release of latent heat of crystallization, the olivine tip would act as a heat sink and not a heat source. Although the difference in temperature is probably small, there is a significant qualitative distinction between a crystal tip which acts as a local heat sink and one which acts as a heat source. The ultimate habit and size of individual olivine crystals (whether small, equant crystals or large blades in spinifex-textured rocks) depends upon tip or layer growth processes that operated on small scales.

For example, in olivine the higher thermal conductivity and near-IR transparency parallel to the *a* axis (~20% greater than those parallel to the *c* axis) would confer a growth advantage to crystals oriented with the *a* axis parallel to the maximum thermal gradient, because such crystals could dissipate their latent heat of crystallization more efficiently. Over the time required (several hours) to cool and crystallize a meter-thick spinifex-textured layer, this slight advantage could become a significant factor, as shown by the very strongly preferred orientation of olivine crystals within A_3 layers (Section 3.1.2). To use a biological analogy, olivine crystals compete with differently oriented (non-related) olivine crystals for nutrients (Mg) in order to grow and reproduce (by branching of sub-parallel crystals in sheaves). In this inorganic Darwinian race for survival, natural selection of the fastest-growing crystals enables them to eliminate their rivals. [The role of Cr-spinel epitaxy, augite growth, and serpentinization could correspond to parasitism, ecological successor communities, and decay, respectively, but I've already stretched the analogy far enough.]

It would be remarkable if meter-scale sheaves of sub-parallel olivine crystals had their origin in a small temperature difference at the μm-scale of a growing crystal tip. However, many physical parameters are involved in this problem, e.g.:

(1) latent heat of crystallization of olivine from komatiitic melt;
(2) the heat capacity of olivine and melt;
(3) the thermal diffusivity of melt and olivine (anisotropic in the latter);
(4) thermal gradients within the partially-crystallized layer;
(5) the shape, orientation and growth-rate of olivine crystals;
(6) the near-IR absorption bands of olivine at high temperature;
(7) possible continuous flow of melt in the interior of the lava flow, etc.

Some of these parameters (2, 6) are reasonably well known, or can be calculated from thermodynamic data bases (1). Others are poorly measured (3) or unknown (7). The remaining parameters (4, 5) are those of most importance to modeling the formation of spinifex texture. Unfortunately, if other crystal–melt systems are any guide, the textures formed during crystallization would have been very sensitive to coupled transfer of heat and mass, as well as to the surface energy and growth kinetics of crystals (e.g., Tait and Jaupart, 1993; Glicksman et al., 1986; Hill, 1990; many others). The numerical solution to such a problem would be difficult in a simple aqueous system, and is probably intractable in komatiites, particularly given the poorly constrained parameters. The observation that many different growth habits of olivine occur together on a cm-scale in komatiites (Section 3.1.2) is another indication that multiple or complex growth mechanisms are involved (for example, examine Photo 3.12). Thus it is probably premature to attempt numerical modeling of the constrained growth of olivine, but perhaps the above considerations can guide the design of experimental investigations of the phenomenon.

5.2 Cooling at the macroscopic level

5.2.1 Modeling the cooling of a sheet flow

In the simplest possible conceptual model of a cooling submarine lava flow, constant thermal diffusivity is assumed, latent heat and volume change of crystallization are neglected, convection within the flow neglected, and the temperature of the upper surface is fixed (generally at 0 °C). The temperature at the lower contact is determined by the far-field temperature of the substrate (also generally at 0 °C). The temperature variation with time and depth in the flow can be solved analytically (Jaeger, 1968) as:

$$\phi(x,\tau)=\frac{T}{T-T_\infty}(\varphi(x,\tau)-\varphi(2-x,\tau)),\ \text{where}\ \varphi(x,\tau)=\frac{1}{2}\text{erf}\left(\frac{x+1}{2\sqrt{\tau}}-\frac{x-1}{2\sqrt{\tau}}\right)$$

where ϕ is the reduced temperature T/T_∞, T_∞ the far-field temperature, x the dimensionless depth z/z_{max}, z_{max} the thickness of the flow, and τ the dimensionless time $4\kappa t(z_{max})^{-2}$, where κ is the thermal diffusivity and t is time. Temperature vs. depth for different cooling times are plotted in Fig. 5.4. Clearly this model is a gross oversimplification, because the effects of latent heat of crystallization, volume change upon crystallization, variable thermal diffusivity, and thermal convection have been neglected. These corrections have been made in various cooling models of greater sophistication and detail (e.g., Irvine, 1970; Peck, 1978; Marsh, 1989; Worster et al., 1993). Whereas there are significant quantitative differences between the various models, on a fundamental level they are quite similar. The presence of solid upper and lower boundaries that transmit heat largely by conduction is common to all these models, and leads to cooling times $\propto L^2$ and thermal gradients $\propto L^{-1}$, where L is a characteristic dimension of the magma body such as thickness or diameter. The detailed thermophysical behavior of magmatic bodies is unknown, and open disagreement exists between researchers over whether magma bodies are stagnant, convect sluggishly, or convect vigorously. Although a number of practical methods for directly determining whether thermal convection occurs in lava lakes come to mind, none of these appears to have been carried out. For example, long-term (e.g., weeks or months) precision (±1 K) monitoring of temperatures at fixed depths in lava lakes could potentially be carried out with robust probes such as heavy-gauge thermocouples in thick-walled alumina tubes. Alternately, sensitive non-contact electromagnetic methods could be used to detect periodic temperature-related variations in the electrical properties of the subcrustal magma layer. [Note: Davaille and Jaupart (1993a) interpreted temperature fluctuations of ~10 K that

were measured in Makaopuhi lava lake between 1965-67 as arising from thermal convection. However, the data consists of only 30–40 readings obtained from three separate probes over a three-month period.]

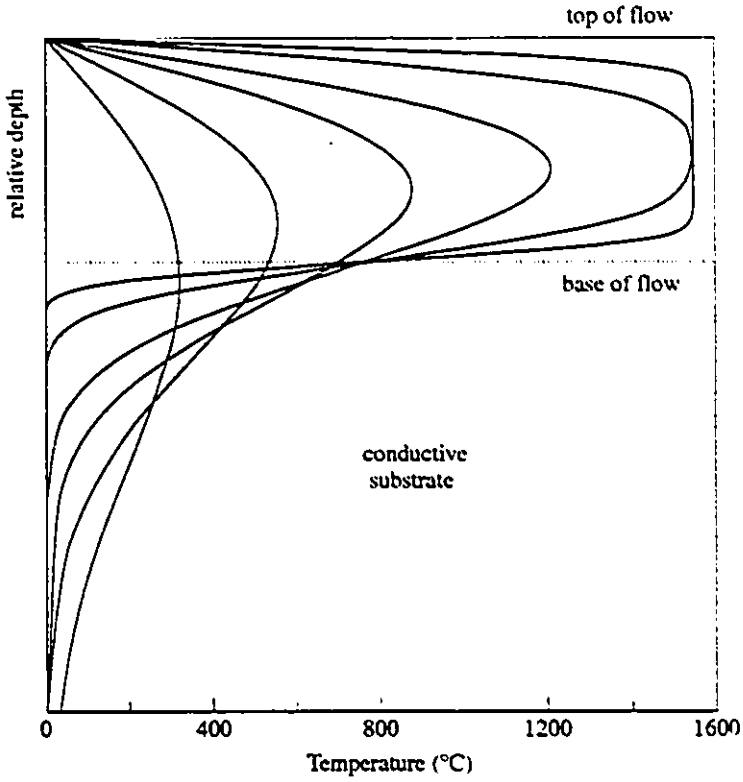

Fig. 5.4 Calculated temperatures vs. depth for a solid slab emplaced at 1550 °C, with the upper boundary held at 0 °C and conductive cooling through the base into an infinite half-space having the same thermal diffusivity of the slab. This cannot be taken to be anything more than a crude and inaccurate model of a komatiite flow because the latent heat of crystallization, effects of within-flow convection, and most importantly the effects of hydrothermal convection within the top of the flow are neglected. For a flow 1 meter thick with a thermal diffusivity of 7×10^{-7} m^2 s^{-1}, the curves represent the temperature at 1 hour, 5 hours, 1, 2, 4, and 8 days after emplacement.

5.2.2 Hydrothermal cooling

Thermal convection in the interior of a komatiite flow may have had a significant effect on rock textures, but a relatively minor effect on the overall cooling of the flow. As Marsh (1988) showed, vigorous thermal convection within a cooling closed-system body can double the initial heat flux, but the flux eventually drops below that of a stagnant body. More significantly, a purely conductive upper boundary condition is inappropriate for a submarine lava flow because convective cooling by seawater within the flow *must* be an important heat transfer mechanism. Numerous studies and semi-quantitative observations show that the heat transfer from hot rock to water can be orders of magnitude greater than that due to thermal conductivity through solid rock. I present some quantitative or semi-quantitative examples:

•a transient hydrothermal plume containing ~10^{16}–10^{17} J excess heat (calculated with respect to ambient ocean water) was associated with the eruption of a <5 m-thick, 3.5 km^2 basalt flow on the East Pacific Rise (EPR)(Baker, 1994); recently (March, 1996) a similar plume containing ~10^{16} J excess heat and estimated to be only 2–3 days old has been detected over the Gorda Ridge, associated with the eruption of a 3.5 km long, 100–200 m wide flow (NOAA unpublished data);

•voluminous warm (<100 °C) and hot (~400 °C) water was observed venting from fractures, fissures, and rubble in an extremely fresh (days old) submarine lava flow on the EPR, a phenomenon the authors termed syn-eruption venting (Haymon et al., 1993);

•diffuse low-temperature hydrothermal venting from the fissure area of a 1987 submarine lava flow on the EPR was measured at 60 °C in 1988, 25 °C in 1990, and was extinct in 1991 (Embley and Chadwick, 1994);

•a thermal output of ~90 MW was measured from a single 10 cm diameter black smoker in a hydrothermal field on the EPR (Ginster et al., 1994);

•the average rate of heat transfer over a 40-year period from one Icelandic volcano into a crater lake was estimated to be 4000 MW (Ágústsdóttir and Brantley, 1994);

•a steady-state heat flux of ~100 kW m^{-2} (with a transient flux approaching 1.0 MW m^{-2}) was obtained by injecting water into molten basalt in a Hawaiian lava lake (Hardee et al., 1981);

•a heat flux of ~40 kW m^{-2} was obtained when an advancing lava flow was deliberately sprayed with seawater at Heimaey, Iceland; thermal probes indicated lava temperature gradients >>1000 K m^{-1} (Björnsson et al., 1982);

•the existence of maars, subaerial volcanic craters typically ~20–100 m deep and 200–4000 m in diameter that form when rising basaltic lava explosively interacts with groundwater (e.g., Cas and Wright, 1987).

Of the preceding examples perhaps the most useful are the direct, quantitative measurements of Hardee et al. (1981) and Björnsson et al. (1982). To apply similar figures to komatiites, a flux of 0.5 kg s^{-1} m^{-2} of water circulating through the thick, fractured upper crust of a flow and emerging heated by 30 °C would remove ~60 kW m^{-2}, heat flow equivalent to pure conduction through unfractured crust only 10 cm thick. [I have suggested a rather high mass flux but a low temperature difference to account for mixing of hot and cold water within fractures.] Lowell and Germanovich (1995) consider that dikes on the order of ~1 m thick emplaced below the seafloor can drive short-lived megaplumes (e.g., 250 MW for 10 days over 10^4 m^2 surface area) provided the wallrock permeability exceed ~10^{-6} m^2. The rock permeability is the most important parameter

controlling fluid flow but is difficult to measure in crystalline rocks, even in modern ones. However, even the freshest komatiites in Munro Township are pervasively fractured and veined. In fact, fracturing is an inevitable consequence of the cooling and thermal contraction of *any* extensive shallow magmatic body.

The cooling of hot rock by pressurized seawater is a complex process that cannot be reliably calculated from basic theory (Sleep, 1983; Lister, 1983). The heat flux from recently active volcanic fields has been measured with reasonable accuracy, but up to now no submarine basalt flow has been observed in the process of eruption (although Haymon et al. (1993) came very close). There are a number of simplified methods to estimate the heat flux from a hydrothermally cooled lava flow. One way is to consider the downward migration of a fracture/cooling front. Because both the thickness of the unfractured layer and the temperature difference across it are controlled by intrinsic properties of water and rock (e.g., the thermal conductivity, thermal expansivity, and fracture toughness of rock; the thermal conductivity, viscosity, and equation of state of seawater) the rate of advance of the front will reach a steady state provided hydrothermal circulation can efficiently remove the heat conducted through the solid layer. Thus, this scenario involves a constant heat flux out of the flow, and a cooling front which propagates downwards with a constant velocity (i.e., $\propto L^0$, where L is the thickness of a flow). A "crude" (their word) calculation by Lowell and Germanovich (1994) showed that such a front could migrate (race!) downwards at 1 mm s^{-1}. More realistically, as the length, tortuosity, and sealing of fractures become more significant in thicker flows, the heat transfer through the cooled upper portion of the flow would approach the conductive limit, and the cooling front would propagate downward with a velocity $\propto L^{-1}$. Mixed-mode convection would presumably lie between these extreme cases.

The key factor is the fracture-controlled permeability of the komatiite flowtop, but this cannot be directly measured due to serpentinization of the rock and sealing of the fractures. I mapped one massive lava tube in close detail, using a photomontage (scale ~1:1) of a well-cleaned outcrop with visible fractures carefully marked in chalk (Fig. **2.1**). The fractures (now serpentine and chlorite-filled veins) visible in outcrop varied in thickness from ~3 cm to less than 0.5 mm; optical microscopy shows that microfractures have thicknesses ranging down to 10 μm or less. The total length of the macroscopic fractures in the lava tube (area ~1.45 m^2) was 40 ± 5 m. The permeability of a parallel-fractured medium is given (Nehlig, 1994) as $d^3/12\varphi$, where d is the fracture width and φ the fracture spacing. Given d = 0.5 mm and φ = 0.036 m (= 1.45 m^2/40 m), the calculated

permeability is 3×10^{-10} m^2 (or equivalently 300 darcy). This is a very rough estimate: the fractures are clearly neither planar nor parallel, many small fractures must have been overlooked, the weighted mean thickness of the fractures is difficult to measure, and not all fractures would have been open simultaneously. Realistically, the original permeability is only bounded within the broad range 10^{-9} to 10^{-12} m^2. [For comparison, a well-sorted coarse sand would also have a permeability of 10^{-9} to 10^{-12} m^2, increasing with grain size. In this case permeability arises from interconnected or continuous pore spaces rather than fractures.] This estimated permeability of the fractured komatiite flow is quite high, but similar values have been measured in situ in fractured crystalline rocks. In certain gas and oil reservoirs in fine-grained sedimentary rocks significant permeability (~10^{-12} m^2) is caused by fractures with in-situ widths of 0.1 mm to 0.01 mm (Nelson, 1985).

Ingebritsen and Hayba (1994) used finite-difference modeling to study heat flow near the critical point of water in a saturated porous medium. Their results showed that conduction dominated heat transport for permeability $\leq10^{-18}$ m^2, but that highly efficient convection occurred for permeabilities $\geq10^{-13}$ m^2. The maximum Nusselt number (the convective heat-transfer rate divided by the theoretical conductive heat-transfer rate that would occur given the same temperature difference) in such convection was typically ~100–1000. The authors suggested that such "superconvection" would be rare in natural environments. However, they considered only relatively deep intrusive magmatic systems with much lower permeabilities ($\leq10^{-15}$ m^2) than appropriate for a komatiite lava. There is some question whether seawater cooling a komatiite lava would have exceeded the critical point ($T \geq 380$ °C and $P \geq 23$ MPa). The temperature is not in doubt—cracks in a cooling komatiite would begin to open at ~800–900 °C—but the pressure is (the minimum required is equivalent to a water depth of 2.3 km). However, Ingebritsen and Hayba found that two-phase (liquid-steam) convection also removed heat very efficiently.

Although the fracture density is greatest at the surface of spinifex-textured flows, those fractures which continue deeper into the flow branch and lengthen. In a fractured flow, the surface area exposed to hydrothermal cooling is considerably larger than the external surface area, and whereas the latter is fixed, the internal surface area would have increased as water entered the flow and thermally fractured the adjoining rock. The leading edges of fractures would have been vulnerable to cracking under the stress caused by thermal contraction, and this process could be further aided by the hydrolytic action of hot steam. The self-propagating nature of such a hydrothermal fracture front is discussed by Lowell and Germanovich (1994). This issue took on practical importance at Heimaey,

Iceland, where a plan to blast a submarine lava flow that was blocking the town harbor was reportedly canceled when the possibility of a runaway explosive water-lava interaction could not be satisfactorily discounted. The fact that intact submarine sheet and pillowed lava flows are common in the geological record, and that more recent observations show active submarine flows can be safely approached by divers indicates that the water-rock interaction is usually moderated, possibly by a thin film of steam. However the energy released during the formation of maars (noted above) suggests that canceling the Heimaey blast was a prudent decision.

The detailed physical and textural study of hydrothermal fracturing processes is not well advanced. Exceptions include the study of textural variations across episodically flooded subaerial basalt flows (Björnsson et al., 1982; Long and Wood, 1986). Such rocks are typically brecciated to a greater extent than spinifex-textured komatiites. I suggest this may be due to the much greater expansion of steam trapped in fractures at low pressure compared to its expansion at high pressures (i.e., under great depths of water).

Other processes that could have influenced crystallization and textural development of komatiites include the inflation of lava flows beneath a thin solidified skin (e.g., Hon et al., 1994). It is possible that a solidified lava flow tens of meters thick may not have contained more than a small thickness of melt at any one time. Conversely, the drainage of thick flows leaving much thinner crusts or hollow shells behind has been observed in both subaerial and subaqueous flows. Estimates of the syn-eruption thickness, flow velocity, and Reynolds number of molten lava made on the basis of the thickness of a solidified flow involve assumptions that are difficult or impossible to verify. Where extensive, continuous, and clean outcrops of komatiitic basalts are available for mapping, the flow morphology can readily be interpreted in terms of mechanisms operating in modern basalts. For example, sub-crustal lava flow and vertical inflation may explain thick, areally extensive, flat-topped komatiitic basalt flows (Arndt, 1982; Baragar, 1984), or the (apparently) common excess cumulus olivine in spinifex-textured komatiite flows.

5.3 Physical processes during cooling of komatiites

5.3.1 Thermal and compositional convection

Large scale thermal convection

I will not attempt a detailed discussion of the controversy over the style and vigor of convection within komatiite flows. I am not an expert in fluid mechanics, but I will summarize the debate. Turner et al. (1986) have calculated that due to their very low viscosity, moderate to large thicknesses, and the presence of high thermal gradients, komatiite lava flows would have experienced within-flow turbulent convection strong enough to keep olivine crystals in suspension and significantly increase the cooling rates of the flows. Marsh (1988, 1989), largely in the context of magma chambers cooled from above, has raised strong objections to this picture. He notes that by assuming a small but arbitrarily fixed temperature gradient one can increase the Rayleigh number of a flow without bound simply by increasing the depth or thickness of the magma layer, and that one could equally well assume an arbitrary Rayleigh number and calculate ever-smaller temperature gradients. However, the cooled uppermost layer of fluid (the boundary layer) has no way of "knowing" how deep the underlying liquid is, but simply acts according to the buoyancy and shear forces acting upon it, largely controlled by heat loss through the overlying rocks. Additionally Marsh notes that the strongly nonlinear temperature dependence of magma viscosities can suppress or eliminate convection. In my simplified view, the fundamental disagreement arises over what characteristic length-scale of a magma body to use: its overall thickness or the much smaller thickness of the thermal boundary layer. [This point does not seem to be settled yet: Worster et al. (1993) use the overall thickness in their Equation (3).]

Liquid flow, crystal settling, and sedimentary structures

Marsh (1988) has also pointed out that due to the laminar boundary layer that must be present near a no-slip boundary (such as near the top of a cumulus layer), some crystals may permanently settle out from descending plumes of cooled magma even if the mean velocity of the return flow (which is generally diffuse) exceeds that required to keep the crystals in suspension. Here we enter into the field of magmatic layering, an exotic hybrid of igneous and sedimentary petrology.

As a geologist I have always observed the rich variety of flow-induced structures (cross-bedding, graded bedding, ripple marks, and so on) present in clastic and volcanoclastic rocks with great interest, if not always equal understanding. I have not observed any structures in komatiite B-layers that unequivocally correlate with such sedimentary features. Arndt et al. (1977) and Renner et al. (1994) document the reverse grading of olivine (i.e., the grain sizes increase upward) in the B-layer of several flows, but this could be caused by other mechanisms. I have visited the well-exposed but highly altered flows at Spinifex Ridge in Quebec, where Lajoie and Gélinas (1978) described cross-bedding and multiple graded bedding within B-layers; in my opinion those authors misinterpreted metamorphic and tectonic structures as primary magmatic ones. Significantly, similar features have never been described from any other locality.

Several features are consistent with flow and crystal sorting within komatiites. The first, noted in Section 3.2.3 and by other researchers, is the presence of excess olivine within lava flows and is unequivocal: magma flowed through certain parts of such lava bodies and left behind olivine, either in the form of pre-existing crystals held in suspension or as constituent elements supplied from a less-differentiated liquid. Another is the presence of the B_1 layer, which will be discussed below.

Density and komatiite differentiation

Olivine is the first phase to crystallize as molten komatiite cools. The composition of the olivine is readily calculated for a given melt temperature (Appendix 2). Given the temperature and composition, the density of both olivine and melt may be calculated. Except possibly at very high pressures (Agee and Walker, 1988), olivine is denser than primary and differentiated komatiite liquids, so olivine crystals are never buoyant. Spinifex texture is formed by the subparallel growth of large, flat olivine crystals that have branched from other crystals higher in the flow. Because of their tightly intergrown nature few if any would have sunk from the top crust under their own weight. Significant compositional or thermal convection within the spinifex-textured layers would have been minimized by the close spacing of subparallel olivine plates in the A_3 layer and the strongly temperature-dependent viscosity of the melt (see Fig. 2.3). In addition the ~10% volume decrease of solid olivine and clinopyroxene compared to their molten constituents could have created a negative pressure gradient and drawn melt up between the olivine plates.

Despite the above arguments, geochemical evidence clearly indicates that as much as ~20 wt.% olivine has been lost from parts of the A_3 layer of the studied 6 meter thick flow, and that the B-layer in that flow (and other flows) contains excess olivine, at least some presumably derived from above. I suggest that a likely mechanism for this fractionation would be convection of the cooled boundary layer that would exist below the downward growing spinifex-textured upper crust. With progressive heat loss the cooled melt layer (possibly including small, free olivine crystals) would increase in thickness and density and sink to the base of the flow. Experiments dynamically scaled to resemble cooling (but non-crystallizing) basaltic liquids in magma chambers show that small-scale, intermittent, sluggishly sinking diapirs or fingers of sinking cooler liquid occur in such cases (Brandeis and Jaupart, 1986; Davaille and Jaupart, 1993b).

A key prediction based upon detailed modeling of olivine fractional crystallization and the thermal and compositional variation of the density of liquid silicates (Lange and Carmichael, 1990) is that the density of komatiitic melts is at a maximum at ~20 wt.% MgO (Fig. 5.5). This contradicts an assumption made by Huppert et al. (1984) and Huppert and Sparks (1985a) concerning the role of convection in the formation of spinifex texture. This means that the growing tips of plate-like olivines in the A_3 layers would *not* have remained surrounded by a stagnant layer of light depleted melt until after a significant amount of cooling and crystallization had occurred (c.f. Huppert and Sparks, 1985a; Turner et al., 1986). Only when the partition coefficient of iron exceeds unity does the melt become less dense with differentiation. My calculations (starting composition of Appendix 2) indicate that this occurs after the crystallization of 25 ± 5 mol.% of olivine—only about half the ultimate total, but probably enough to determine the final texture of the rock.

On a much larger scale, a liquid density maximum at ~20 wt.% MgO could explain the commonly observed compositional gap that exists between non-cumulate komatiites and basaltic komatiites. It is generally accepted that magma chambers act as highly efficient filters of dense xenoliths or unfractionated melts. One need only consider mantle xenoliths and highly primitive xenocryst-rich alkaline basalts and kimberlites; a large proportion of these are found in small, short-lived volcanic systems that were not active long enough to develop a steady-state magma chamber. A similar explanation has been offered to explain the fact that high MgO liquids are never observed to erupt subaerially from Hawaiian volcanoes although such glasses are found in the submarine environment (Clague et al., 1995). Given the existence of a partially molten komatiite magma reservoir,

melts containing ~20 wt.% MgO would have considerable difficulty in erupting, being denser than both less and more-fractionated liquids. Such a melt would presumably have ponded at the base of a reservoir (not necessarily deeply buried) pending further differentiation or mixing with more primitive melt.

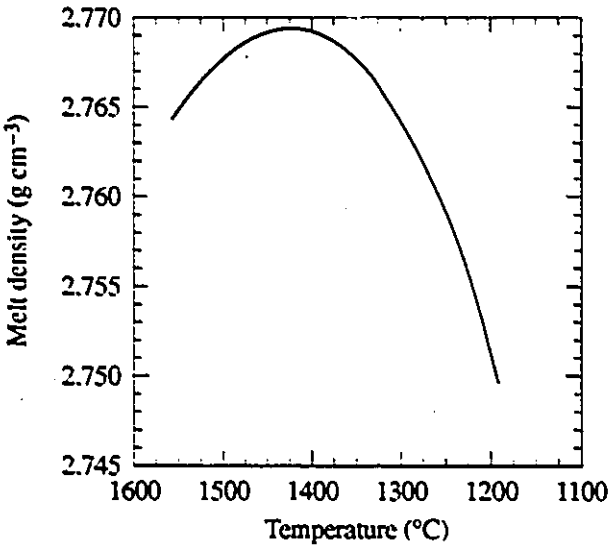

Fig. 5.5 Calculated density of a komatiite liquid with progressive fractional crystallization of olivine. I used an iterative method to calculate the equilibrium olivine and liquid composition and temperature using steps of 0.5 mol% olivine. I then calculated the density from the partial molar volumes of the constituent oxides (see Appendix 2 for details). A density maximum occurs between 1450 and 1400 °C, corresponding to a melt containing ~21 wt.% MgO that is in equilibrium with olivine of 100Mg/(Mg+Fe) = 92.1 ± 0.5 (or $Fo_{91.2}$). The density inversion has significant consequences for within-flow differentiation (see text).

This density inversion of the liquid could also become significant during the cooling of the B-layer olivine orthocumulate. Settled olivine crystals would have formed a loosely packed framework with a porosity of about 50%. Eventually, as the cumulate cooled and more olivine crystallized, the liquid would have become less dense than the hotter overlying melt and compositional convection would have occurred. When the net decrease in volume with crystallization is also considered, the rise of cool (but light) olivine-depleted melt and the sinking of hot (but dense) less-differentiated melt would have enabled adcumulus growth of olivine to occur in slowly cooled thick flows (e.g., Morse, 1986). There is no clear textural evidence of adcumulus growth of olivine in any of the flows I studied. However, thick komatiite-related dunite units composed of more than 95 vol.% olivine are known in the Abitibi and in Western Australia (e.g., Barnes et al., 1988), and compositionally driven melt percolation may have occurred in these larger bodies.

The B_1 and B_3 layers

The B_1 layer, with its horizontally layered plate-like olivines, makes a dramatic contrast to the vertically oriented olivine sheaves of the A_3 layer directly above (Photos 3.2 and 3.3). The change is so abrupt that certain lava flows at Pyke Hill have split along the A–B contact (Photos 5.1 and 5.2). Despite numerous attempts, no-one has fully explained all the features of this layer (nor will I do it here). In those layered komatiite flows in which it occurs, it formed late in the crystallization sequence, more or less contemporaneously with the A_3 layer. However, it can contain highly magnesian olivines, suggesting physical mixing of early and late-formed crystals (Arndt, 1986a; Thomson, 1989b; Renner et al., 1994).

The B_3 layer is very similar to its neighbouring B_2 and B_4 layers, with the exception of cm-size rounded patches that are slightly more resistant to weathering (hence the term "knobby layer"). This layer is rarely reported from Australian and southern African localities. Petrographic examination shows it to consist of clumps of olivine and rather equant augite crystals. In the boreal climate of the Abitibi, the unaltered clinopyroxene resists weathering better than the partially serpentinized olivine. Similarly, the A-layer of komatiite flows tends to be more resistant than the B-layers in Canada (e.g., Arndt, 1982). In South Africa, with its very different climate, the situation is reversed and it is the B-layers that stand out in relief (Viljoen and Viljoen, 1969). In the Kambalda area of Western Australia, tens of millions of years of glacier-free weathering has left few and generally deeply weathered outcrops. However, Thomson (1989a) described blotchy clinopyroxene-rich patches ('obscure' open packed cumulates) in drill core samples from Kambalda that could correspond to the B_3 knobs.

Assuming, as I have, that equant olivine crystals would generally settle to the base of a layered komatiite flow, a framework of touching grains with substantial porosity would have formed. Dense, somewhat depleted melt at ~1400 °C could have percolated downward and remained more-or-less stagnant in the pores until further crystallization of olivine reduced its density and it rose upwards or mixed with other melt. This differentiated melt is enriched in Ca, Al, and Si, all necessary constituents of aluminous augite; presumably there is some interplay between cooling rates, trapping of melt, and growth of well-formed augite crystals. In my interpretation, the B_4 layer lost heat via conduction to the underlying rock too rapidly to form large clinopyroxene crystals. The B_2 layer either cooled slowly enough to allow its buoyant differentiated melt to percolate

upwards (and either crystallize in the A_3 layer or be mixed with through-flowing lava), or a cooling front swept downwards rapidly enough to solidify the interstitial melt with a fine grain size (in cumulates, the texture and grain size of the groundmass may have little relation to that of the cumulus phase). Because the B_3 layer tends to occur at a similar distance above the base of flows of differing thicknesses, I do not favor the latter hypothesis. The cooling rate of the B_3 layer would have struck a balance, slow enough to have allowed the growth of large clinopyroxene crystals but not so slow that the differentiated melt is mixed with dense melt, delaying the onset of pyroxene crystallization and reducing the size of the pore spaces between olivine grains.

5.3.2 Thermal assimilation of underlying rocks

Assimilation of sulfur in komatiite-hosted nickel deposits

The association of sulfide mineralization (i.e., ≥0.5 wt.% Ni-Fe-Cu sulfides) with komatiites that directly overlie non-komatiitic rocks has long been used as a nickel prospecting guide in Western Australia, and occasionally so in Canada. A widely accepted theory is that komatiites may have flowed turbulently due to their low viscosity and high liquidus temperature, and thus efficiently transferred heat to, melted, and assimilated underlying rocks (e.g., Huppert et al., 1984). Because of dilution, the associated chemical contamination might have few physically observable effects, with the potential exception of sulfide supersaturation and precipitation (e.g., Groves et al., 1986).

Sulfur (as S^{2-}) has a limited solubility in komatiite magmas and silicate magmas in general (Naldrett, 1989). Typically, elements that have very low solubilities in silicate liquids tend to form small accessory minerals when oversaturation occurs (e.g., chromite, zircon, apatite). Due to the high temperature of ultramafic and mafic magmas and the relatively low melting points of sulfides, magmas oversaturated in S tend instead to unmix into silicate and sulfide liquids, with chalcophile elements (e.g., Cu, Ni, Co, PGE) preferentially partitioning into the sulfide phase. The density of the sulfide liquid is considerably higher than the silicate magma, and gravitational settling of sulfide droplets can occur (e.g., Naldrett, 1989). As noted in Section **3.2.4**, the low S content of unmineralized komatiites is consistent with the highly depleted nature of komatiites. Thus it is the high S content of mineralized komatiites and not the sulfide accumulation itself that requires explanation; in any mafic or ultramafic magma with a sufficiently high S

content (i.e., ~0.5–1 wt.%), a sulfide liquid will unmix, scavenge chalcophile elements from the silicate liquid, and settle out.

Largely on the basis of studies of mineralized komatiite flows in Kambalda, Western Australia, it has been suggested that komatiites assimilated S from underlying sulfide-rich pelitic rocks (Groves et al., 1986); the sediments themselves are described in detail by Bavinton (1981). Many geochemical studies of the sulfides associated with mineralized komatiites have been inconclusive regarding whether the S is mantle- or footwall-derived, and Cowden (1988) reinterpreted the Kambalda troughs (considered to be thermal erosion channels) as being caused by post-magmatic folding. However, recent study of several komatiite-related mineral deposits have found $\delta^{34}S$ values that differ strongly from the mantle-expected 0‰, but that correlate well with the $\delta^{34}S$ of underlying sedimentary rocks (C.M. Lesher, unpublished data, 1994).

The Pyke Hill komatiite lavas are poorly suited for the study of substrate assimilation. They are not interlayered with other types of rock, and the sequence is in faulted contact with tholeiitic gabbro to the south (Pyke et al., 1973). Komatiites in Dundonald Township studied by Arndt (1986a), Barnes (1985), and Barnes et al. (1983) are in faulted contact with felsic lavas, as is the Alexo nickel deposit itself (Baker, 1917; Barnes et al., 1983; my observations). The nearby occurrence of cm to dm-size rounded xenoliths of felsic rocks in komatiite or komatiitic basalt flows suggests the original contact was depositional (or erosional) and subsequently tectonized (Baker, 1917; my observations). [Unfortunately the somewhat massive, altered "komatiite" immediately overlying sedimentary rocks that I collected at a nearby site was actually a high-Mg tholeiite or a low-Mg komatiitic basalt. The Ti, V, Co, Ni, and Pb content of the basalt was not consistent with an origin via simple mixing of a komatiite and the sediment.] Falconbridge geologists showed me other possible thermal erosional structures in Dundonald and south-central Munro townships, but I found these to be equivocal at best.

Photo 5.1 View looking east along the northern edge of Pyke Hill (picket in foreground is 1.5 meters high). Several flows have split at or near the A–B contact rather than at the contact with the overlying or underlying flow, as might be expected.

Photo 5.2 Close-up photograph of one of these fractures. In this case the splitting occurred near the B_1–B_2 contact and the A_3–B_1 contact remained joined, although intact blocks could be split off from it (e.g., note the missing piece of rock, currently residing in Ottawa). The gap between the sides is about 5 cm wide.

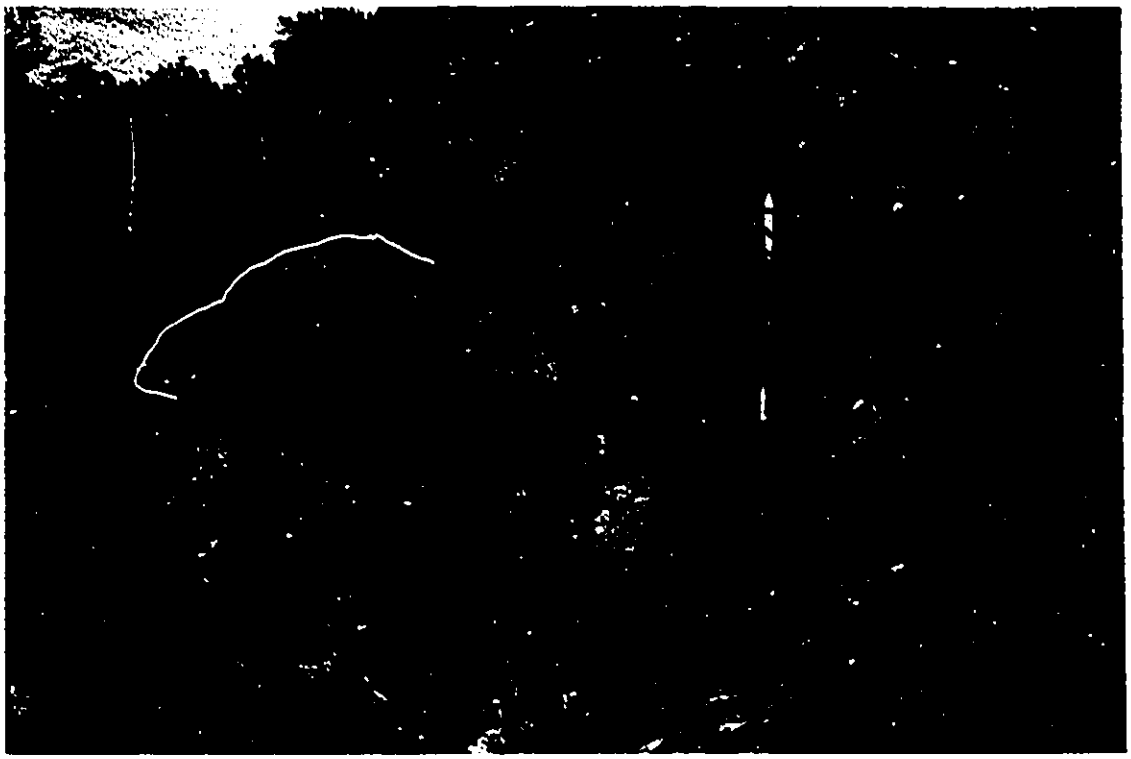

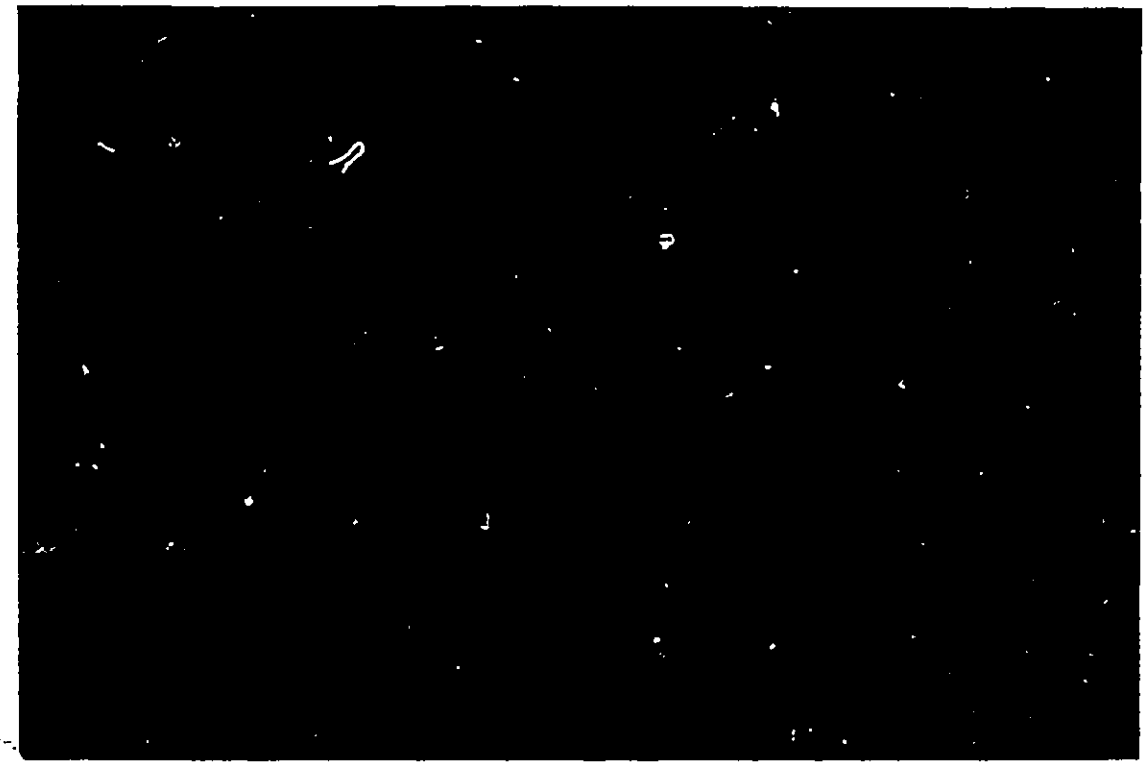

Assimilation of other elements

Studies have reported apparent trace-element contamination of komatiite flows, but some of the data is equivocal (e.g., Arndt and Jenner, 1986; Cattell et al., 1984), and certain anomalies, such as minor gain of light REE could have been caused by hydrothermal alteration. Direct evidence of contamination is rare, but has been found in certain Archean lavas: e.g., zircon xenocrysts in basalts overlying komatiite flows at Kambalda (Compston et al, 1986). Many komatiite flows show little evidence of crustal or substrate contamination, even when incompatible trace elements are analyzed at the ng/g level (Jochum et al., 1991; Shirey and Barnes, 1994). However, McNaughton et al. (1988) described "xenomelts" apparently derived from underlying sedimentary material in some ocellar komatiites at Kambalda. Certain recent analyses of komatiites from Kambalda show clear geochemical anomalies that are consistent with assimilation of crustal material (Lesher and Arndt, 1995); it is worth noting that it has taken more than a decade for such evidence to be discovered since substrate assimilation was proposed (e.g., Arndt, 1986b).

As noted earlier, Pyke Hill flows commonly exhibit a glassy lower chilled margin (now devitrified). Komatiite and komatiitic basalt flows in the Dundonald are intercalated with graphitic sediment and contain undigested graphite inclusions (Muir and Comba, 1979; my observations). Komatiite flows in South Africa formed molds of underlying stromatolites (Byerly et al., 1986), which are analogous to the tree molds commonly formed by Hawaiian lava flows. These features hardly seem compatible with a turbulently flowing lava that erodes its own chilled margins and efficiently assimilates rocks of lower melting temperature as postulated by Huppert and Sparks (1985a, 1989).

In theory, the remelting of a chilled layer is quite possible (Huppert and Sparks, 1989), and in practice such effects are observed in industrial processes such as the dipping of a cold metal object into molten glass or other refractory coating. However the particular conditions that existed during the flow and cooling of komatiite lavas are not known. My observations show that in thin flows at Pyke Hill, glassy chilled basal margins are still present, a strong argument against remelting of either the chill or its substrate. I suggest that the answer could lie in the formation of a chilled layer of glass followed by the rapid solidification of a viscous olivine–melt boundary layer, and settling of cumulus olivine that was not re-suspended by flowing lava. In other words, in typical flows a refractory base may have formed that greatly reduced the heat transfer to the underlying rocks. Circumstances that would favor melting would be the contact of large volumes of

komatiite melt with less refractory rock under conditions of slow heat loss. Thick subvolcanic sills, or possibly very thick long-lived flows, would meet the requisite conditions.

5.3.3 Crystallization in aqueous systems used as analogs to komatiites

There are reasons why the above sections contain many hypotheses but few proofs. First, komatiites do not presently erupt and thus active flows cannot be observed. This is a serious hindrance, but one we can do nothing about. Secondly, komatiites have very high melting points and are difficult to study experimentally, particularly because many phenomena cannot easily be duplicated (e.g., hydrothermal cooling), or occur on inconveniently large scales (e.g., the A_3 layer, within-flow convection), or both (e.g., the B_1 layer). Thirdly, it is difficult (or even impossible) to derive realistic models for the behavior of komatiites through theoretical considerations alone; too many of the required physical parameters and processes are poorly known, or even completely unknown.

A practical approach to some of the above difficulties is to use a more tractable analog system or material in place of the natural one. For example, Davaille and Jaupart (1993b) used golden syrup (presumably sugar-based) to model the convection of magma cooled from above, and Griffiths and Fink (1992) used molten wax to study the solidification of submarine basalts. The analog must be chosen carefully, however. Huppert and Sparks (1985a) used a stream of hot water flowing over a sheet of solid polyethylene glycol (which is soluble in water) to model the melting and assimilation of substrate rocks by a komatiite flow. Because this system was incapable of crystallization (its ultimate state under those conditions would have been a hot aqueous solution of polyethylene glycol) I argue that it was a very poor analog to komatiites.

Hypereutectic aqueous solutions of various salts (e.g., $Na_2CO_3 \cdot 10H_2O$, $Na_2SO_4 \cdot 10H_2O$, KNO_3, NH_4Cl) have been used with some success as analogs to crystallizing komatiites and metallic alloys (Huppert et al., 1984; Turner et al., 1986). These systems succeed in reproducing the basic features of spinifex texture, i.e., bladed crystals of increasing size growing downwards from a cooled roof, with a layer of equant or granular crystals at the base. However, one may question the extent to which a ~0 °C aqueous solution can be fundamentally similar to a ~1550 °C silicate lava. Significant and possibly insurmountable differences exist between the aqueous systems and komatiites, such as:

(1) the difference in magnitude and even sign of the density variation of the solution with temperature and composition;

(2) the strongly nonlinear variation of the viscosity of the molten komatiite with temperature;

(3) the large, though difficult to quantify, effect of hydrothermal fracturing and cooling of the lavas;

(4) the role of radiative thermal transfer, important in komatiites but negligible in the aqueous solutions.

Each of the above points is important, but perhaps the key point is (1). I quote from Turner et al. (1986, p. 399): "...residual fluid which is less dense, though cooler than the original fluid...is the critical property required to model the decrease in density that occurs in komatiite melts during the crystallization of olivine." A glance at Fig. 5.5 will show that this statement is incorrect over the temperature interval that is of greatest importance during the formation of spinifex texture.

Finally, in certain analog experiments organic polymer additives were used to increase solution viscosities in order to evaluate the influence of viscosity on cumulate textures and solute advection (e.g., Tait and Jaupart, 1993). Concentrations as low as 1–10 μg/mL of inorganic salts or dissolved organic compounds can have drastic effects on the habits of some crystals (e.g., Tiller, 1991a; Putnis, 1992). This effect, though probably not important, does not seem to have been independently evaluated in such experiments.

6 Summary and final discussion

6.1 Summary of major conclusions

The komatiite flows that outcrop on Pyke Hill are among the best-preserved in the world. Strain and metamorphic recrystallization are minimal, and primary structures and textures are generally preserved extremely well, excepting the effects of serpentinization that occurred early in the history of the flows. My detailed observations and mapping of several typical flows are in general agreement with other observations of komatiite flow morphology (e.g., Arndt et al., 1977; Arndt, 1982). However, other hypotheses or generalizations regarding the requisite conditions of spinifex texture formation (e.g., damming of lava behind levees; Thomson, 1989a) must be questioned in the light of the structures and textures observed.

The metamorphic grade of the Pyke Hill lavas is prehnite-pumpellyite facies or lower. Serpentinization caused chemical alteration of the komatiites, predominantly addition of water, loss of Ca and Mn, and mobilization of Sr and the alkali elements. The relative concentrations of Mg and Si, as well as more typically immobile elements (e.g., Al, Ti, Zr) are essentially unchanged from their magmatic values. Silica consumed in the serpentinization reaction was probably supplied by plagioclase and glass in the komatiite groundmass. The reaction leached Ca (+/– other large ion lithophile elements) from the rock, and caused a volume increase of ~30–35 %. This expansion is directly shown by density measurements, and indirectly by microstructures in the rock. It is extremely likely that the serpentinization predated regional metamorphism.

The immobility of most of the constituent elements of olivine, coupled with Pearce element ratio analysis, permitted a highly precise determination of the composition of the olivine that was the sole fractionating phase within the flows. The within-flow differentiation of a moderately thick flow that was studied can be closely modeled by olivine fractionation from a bulk melt of similar composition to that of the A_1 or A_2 layers of the flows, plus a substantial excess component of highly magnesian olivine. A sampling section through a 5.3 meter thick flow showed that it acted as an open system and accumulated excess olivine, presumably by the lateral flow of lava through the core of the flow during the crystallization of the upper and lower surfaces.

The composition and zoning of olivine is modeled to a high degree of accuracy by fractional crystallization from the bulk melt. The interesting problem of accommodating high concentrations of Cr in olivine is dealt with at length, and two substitutional mechanisms, $^{[6]}Cr^{3+} + {}^{[4]}Al^{3+} \rightleftharpoons {}^{[6]}Mg^{2+} + {}^{[4]}Si^{4+}$ and $2\ {}^{[6]}Cr^{3+} + {}^{[6]}\square \rightleftharpoons 3\ {}^{[6]}Mg^{2+}$ are shown to be responsible.

The crystal habit of Cr-spinel is examined in detail, and shown to be caused by typical mechanisms of dendritic growth. Chromian spinel nucleated heteroepitaxially on olivine surfaces and maintained a consistent crystallographic orientation with that mineral. The Cr-spinel dendrites likely grew at undercoolings of 50–100 K.

Strong evidence is offered that hydrothermal cooling of the lava flows caused heat losses that could have been an order of magnitude higher than those calculated by models based only on conductive heat transfer within the solidified portions of the flow. The effect of such cooling on the thermal history of a flow would be far greater than the potential effects of sluggish convection within the molten core of a flow. A cooling/cracking front would have migrated downwards into the flow; thermal gradients in the unfractured rock ahead of the front could easily have exceeded 10^4 K m^{-1}.

An evaluation of published data, including the effects of radiant heat transfer, shows that the thermal conductivity of olivine would have been 3–5 times greater than the komatiitic liquid from which it grew. Given the high thermal gradients implied by the hydrothermal cooling, olivine would have grown by constrained cooling; i.e., it would have been cooler than the surrounding liquid. In most cases of magmatic crystallization, the opposite is true. The rate of heat removal, not chemical diffusivity, would have been the rate-limiting factor of olivine growth (at least in the *a* and *c* crystallographic directions). The crystallographic anisotropy of near-infrared absorptivity and of thermal diffusivity is likely responsible for the preferred orientation of olivine (with the *a* axis normal to the upper flow surface) in A_3 layer komatiite.

Although the komatiites studied were not ideal for that purpose, the problem of wallrock assimilation was considered. Based on the textures and structures observed (and also those that were *not* observed) in the Pyke Hill and other lavas, together with a review of the literature, it is concluded that the melting and assimilation of substrate rocks is likely to require special circumstances. Many flows show no evidence of such behavior.

6.2 Suggestions for further research

6.2.1 Study of natural komatiites and basalts

The study of the behavior of mobile elements would be significantly advanced if a greater understanding was obtained of the very fine-grained magmatic and metamorphic minerals hosting the bulk of those elements. Such research could use transmission electron microscopy (TEM) and analytical electron microscopy to study the minerals in the groundmass of both well-preserved and moderately well-preserved komatiites.

The direct imaging of cross-hatch dislocations could be attempted using TEM or acid etching of polished sections of unserpentinized plate-like olivine.

Water-rock interactions must be studied in more detail. The rate of heat-transfer from erupted ocean-floor basalts, which is difficult to derive from theory, is of particular interest. [The detection, observation, and measurement of very recent abyssal eruptions is technically challenging, but much work has been accomplished by oceanographers over the last decade. This is currently a very active field of research.]

6.2.2 Experimental work

Although a significant amount of experimental work has been carried out on komatiites, the following avenues could be fruitful.

The growth of olivine in a thermal gradient could be attempted under controlled (or semi-controlled) conditions. Possible methods would be to use a glassworks-type apparatus with cooled molds and a large volume of melt, or else smaller-scale laboratory equipment such as a high-temperature microscope heating stage or a furnace adapted for Bridgeman growth of crystals.

The growth of olivine in a sheared liquid could be studied using a rotated crucible. This would simulate the inferred growth conditions of olivine in massive komatiite lavas.

Certain recent experimental results (Miller et al., 1991; Parman et al., 1995; Ginibre 1995) are discordant with the $T_L = 1000 + 20 \times MgO$ thermometer. More accurate measurements of the olivine liquidus at low pressure would be useful. This could

involve the *in situ* observation of olivine growth and resorption, using for example, a high-temperature microscope heating stage.

The growth of dendritic Cr-spinel in normal or Fe-free (to facilitate optical observations) komatiitic melts would permit a more refined study of the growth mechanisms than is possible given the altered, microcrystalline groundmass of natural samples. The sole published report of synthetic Cr-spinel dendrites is that of Lofgren et al. (1974, noted as an entry in a table). [In an unpublished work, Ginibre (1995) also reported such textures.] Given the fascinating and intricate crystal habits of the dendrites, this seems an interesting project.

Accurate measurements of the thermal conductivity of olivine and silicate melt (not necessarily komatiitic) at high temperatures are clearly required (e.g., Snyder et al., 1994; Shore, 1995).

Finally, it would be relatively simple to evaluate the hypothesized buffering effect of plagioclase in the serpentinization reaction by mixing powdered olivine, labradorite, and water (possibly including HCl to simulate acidic conditions or speed reaction-rates) in a sealed pressure vessel at moderate temperatures and pressures (i.e., <400 °C and <300 bars). Both the leachate and the solid reaction products could easily be studied.

Appendices

Appendix 1. Calculation of cation molar fractions

Most instrumental analytical methods do not differentiate between cation valence states, and very few analyze oxygen content, although it is the most abundant element in most rocks. In addition, many analyses omit such anions as F^-, Cl^-, S^{2-}, OH^-, CO_3^{2-}, NO_3^-, and SO_4^{2-}. Regardless, it is common practice to report the major and minor constituents of silicate rocks and minerals as oxide weight percentages, assuming O^{2-} as the only anion. In addition, particularly in certain felsic rocks, substantial concentrations of such elements as Li, Be, and B may be present but undetectable by XRF techniques. Apart from OH^- (measured indirectly by loss on ignition), relatively low concentrations of S^{2-} and Cl^- (measured by XRF with unfused samples), and minor CO_3^{2-} (small amounts of calcite in flowtop breccias), the concentration of these elements are likely to be very low in komatiites.

The molar fraction of an element is often a more useful measure than its oxide weight percentage. The cation molar fraction may be calculated by dividing the weight percentage of an oxide by its molar weight (e.g., 71.844 g/mole for FeO and 79.844 g/mole for $FeO_{3/2}$) to obtain the moles per 100 g. This ratio is then divided by the sum of all cations per 100 g. This calculation allows different valences of an element to be treated as separate species, which is useful if a crystallizing system is closed to oxygen. A sample komatiite analysis is given in oxide wt.% and the equivalent cation fraction in Table A2.2.

Appendix 2. Calculation of equilibrium olivine composition

The melt composition (in oxide wt.%) is first converted to cation molar fraction. Olivine stoichiometry—in general, very closely adhered to—requires 2 moles of divalent cations per mole of silica. Magnesium and iron are the most abundant cations, constituting between 98.9 and 99.3% (average: 99.0%) of the M1+M2 cations in all (n=144) of my multi-element microprobe analyses. Therefore, the fraction of (Mg,Fe) among all cations in olivine averages 0.660 (i.e., 2/3 × 0.990). The calculated average exchange partition coefficient $K_{D\,Fe/Mg}^{ol/L}\left(=\frac{FeO_{ol}\times MgO_{L}}{MgO_{ol}\times FeO_{L}}\right)$ for the range of melt compositions relevant to komatiites is 0.308 (calculated from Beattie et al., 1991, 1993b). This allows the Mg/(Mg+Fe) of olivine in equilibrium with a melt of a given Mg/Fe^{2+} to be estimated, and from this the olivine–melt partition coefficient for Mg. The molar partition coefficients for other divalent cations may then be calculated via the following empirical relationship (Beattie et al., 1991): $D_{M_i}^{ol/L}=a_i\times D_{Mg}^{ol/L}+b_i$ for M_i = Fe, Mn, Cr, Ni, and Ca, using the coefficients listed in Table **A2.1**.

Table A2.1 Distribution coefficients for olivine–melt pairs

Cation	a[1]	b[1]	a[2]	b[2]
Ca	0.0056	0.0135	0.0015	0.025
Cr	—	—	0.11	0.18
Mn	0.259	–0.049	0.23	0.11
Fe	0.299	0.027	0.299	0.027
Ni	3.346	–3.665	1.7	–0.9

[1] From Beattie et al., 1991, 1993b.

[2] Modified coefficients that provide a better fit to observed range of olivine compositions in Pyke Hill komatiites. (See Section **4.1.1**).

For calculations of olivine-melt equilibrium during continuous fractional crystallization the following iterative procedure was used. The molar fraction of M1+M2 cations is calculated by multiplying each cation molar fraction in the liquid by its partition coefficient. An amount equal to half this sum is allotted for Si, then the total is multiplied by a step size and subtracted from the bulk liquid. Steps of 0.5 mol.% (~0.45 wt.%) were

small enough for the purpose of modeling the liquid line of descent; about 100 steps covered the full range of observed olivine compositions. Given the cation molar fractions in the M1 and M2 sites, the oxide wt.% composition of the olivine and residual melt are easily calculated. The initial liquid composition was estimated from XRF analyses of the least-altered undifferentiated rocks, assuming an initial MgO content of 27.5 wt.% and with $FeO/(FeO+Fe_2O_3)$ equal to 0.93 (calculated using wt.% oxides). The latter ratio was estimated from the composition of the most magnesian olivine phenocrysts in chilled margins, and is also consistent with f_{O_2} values similar to those of modern mid-ocean ridge basalts. For a komatiitic melt with the composition listed in Table **A2.2** the following $FeO/(FeO+Fe_2O_3)$ ratios were calculated using the empirical composition-temperature-oxygen fugacity relation of Kress and Carmichael (1991):

FQM:	0.858;	FQM – 1 $\log_{10}$ unit:	0.907;
FQM – 2 $\log_{10}$ units:	0.940;	FQM – 3 $\log_{10}$ units:	0.961.

[The FQM (fayalite-quartz magnetite) buffer maintains $f_{O_2} = 1.74 \times 10^{-5}$ bars at 1560 °C.]

At each step the physical properties of the liquid (temperature, density, and viscosity) and olivine (density) are calculated. The temperature is calculated from the empirical relation T (°C) = 1000 + 20×MgO wt.% (Nisbet et al, 1993), the density by partial molar volumes (Lange and Carmichael, 1990) and the viscosity by the method of Shaw (1972). A sample calculation of the initial olivine crystallizing from the melt is shown in Table **A2.2**.

Table A2.2 Olivine composition calculated from melt composition and exchange coefficients

Oxide	Melt composition (wt.%)	Melt cation fraction	Molar partition coefficients	Cations per olivine formula unit	Olivine composition wt.%
SiO_2	45.3	0.4021	0.829	1.0000	41.49
TiO_2	0.33	0.0022	(0.008)	(0.00005)	(0.0030)[1]
Al_2O_3	7.0	0.0732	(0.010)	(0.0023)	(0.082)[2]
Fe_2O_3	0.70[3]	0.0047	–	–	–
FeO	8.54[3]	0.0708	0.539	0.1144	5.68
MnO	0.175	0.0013	0.504	0.0020	0.097
MgO	27.5	0.3639	1.711	1.8680	51.99
CaO	7.00	0.0666	0.028	0.0055	0.213
Na_2O	0.60	0.0103	–	–	–
K_2O	0.10	0.0011	–	–	–
Cr_2O_3	0.358	0.0025	0.359	0.0027	0.142
NiO	0.178	0.0013	2.009	0.0077	0.395
Total	98.78[4]	1.0000		3.00	100.00

[1] McDonough and Ireland (1993).

[2] My work.

[3] Estimated values.

[4] Total is less than 100% because all Fe was originally calculated as Fe_2O_3, and certain minor elements are omitted.

The molar and exchange partition coefficients are calculated as follows:

$D^{ol/L}_{Mg^*} = C^{ol}_{MgO^*} / C^{L}_{MgO^*} \equiv 0.660/(C^{L}_{MgO^*} + 0.308 \times C^{L}_{FeO^*})$, and thus

$D^{ol/L}_{Mg} = 0.660/(0.3639 + 0.0708 \times 0.308) = 1.711$ $\quad C^{ol}_{MgO^*} = 0.3639 \times 1.711 = 0.6226,$

$D^{ol/L}_{FeO^*} = 0.299 \times 1.711 + 0.027 = 0.539$ $\quad C^{ol}_{FeO^*} = 0.0708 \times 0.539 = 0.0381,$

and so on. Note that there are three cations (M1, M2, and T) per formula unit of olivine.

Appendix 3. Electron microprobe procedures

The electron microprobe analyses used in this thesis were obtained over several sessions on different instruments. Wavelength-dispersive spectrometer (WDS) microprobe data were obtained at McGill University, the first set of data using a Cameca Camebax microprobe, and the second set with a JEOL Superprobe 8600-L. All compositional data for olivine used in this thesis are from these sessions. Other minerals were measured using energy-dispersive spectrometers (Li-drifted silicon detectors) on a JEOL SEM at Carleton University or on the JEOL Superprobe at McGill. Such analyses are of lower precision than the WDS data, but adequate for general purposes. For some minerals the smaller beam diameter and lower current used in EDS measurement was advantageous.

EDS measurements were accumulated over 100 seconds of livetime, with beam current adjusted to give 20–30% deadtime. Data reduction was performed by software provided by the manufacturers. I do not have details of the methods used. The McGill EDS program automatically summed all detected specified elements (+/– oxygen) to 100%; the Carleton data were calibrated against previously measured standards in order to obtain oxide totals similar to those of WDS analyses. Realistic lower limits of detection for EDS analyses are 0.1–0.2 wt.% for elements K through Cu.

WDS microprobes have considerably better energy resolution than EDS ones and allow much more control over measuring parameters (e.g., beam current, counting time, element selection). The first set of olivine measurements were made using standard operating conditions for silicate analyses: probe current 20 nA, accelerating voltage 20 kV, maximum of 30 seconds counting time on the Kα peak of an element and 15 seconds each on two flanking background points, and various oxide and silicate standards provided by McGill. The results, while acceptable for most purposes, lacked the precision needed to distinguish between various substitutional mechanisms for Cr in olivine. For example, both Na and Ti were analysed in certain olivine grains in the first microprobe sessions, but were below routine microprobe detection limits. After acquiring experience in XRF analysis, including methods of reducing count-rate statistical error, I modified the analytical techniques as described below.

Improved statistical accuracy: The major change was to use a higher beam current (80 nA) and longer counting times (up to 150 seconds on peaks and 75 seconds on each background point). Extended microprobe measurements with high currents cannot be used

for all minerals and glasses, because certain of these (particularly water-, halide-, or alkali-bearing ones) tend to break down under the heat and current of the electron beam. The often-cited "volatilization" of sodium does not occur, however. Instead, Na^+ ions diffuse away from the heated spot, probably counterbalanced to a small extent by Na^+ migration towards implanted electrons. Refractory minerals such as garnet and olivine do not suffer from either problem. However, a layer of carbon does accumulate over the probed spot due to the electrostatic attraction and thermal breakdown of minute amounts of oil from the vacuum pump, and X-ray absorption by the carbon coat causes diminished count rates for light elements. For this reason, Na was always one of the first elements analyzed.

More accurate standards: A second change was to provide my own standards. These consisted of olivine (for Mg, Si, Mn, Fe, and Ni) from a lherzolite xenolith from the Grand Canyon, Arizona, and clinopyroxene (for Na, Al, Ca, and Cr) from a lherzolite xenolith from Hawaii. The hand-picked mineral concentrates (>99.5 % pure) were analyzed by routine XRF techniques (1.3000 g of material in a fused borate disk). The minerals were optically homogeneous and free of inclusions apart from Cr-spinel which was removed by hand from the crushed material using a magnetized needle. I made very small corrections to the analyses of Cr by visually estimating the residual fraction of Cr-spinel in both olivine and clinopyroxene. Two different aliquots of olivine, for example, contained 60 and 80 µg/g Cr, about half of which was from included Cr-spinel.

Interestingly, the Grand Canyon olivine was not consistent with a synthetic olivine routinely used as a Ni standard at McGill University's microprobe lab. The Ni in the synthetic olivine was only ~87% of its nominal value when analyzed as an unknown with the Grand Canyon olivine as a standard. Given that Fe-bearing olivine can be difficult to synthesize, that the nominal composition was provided by a commercial supplier who gave few details of the analytical procedures, and that olivine analyses standardized using the Grand Canyon olivine agreed within ~4% with analyses standardized using NiO, the error most likely lies in the synthetic olivine. The consequence is that over the last 10–15 years analyses of Ni in silicates obtained at McGill may have been systematically ~15% high.

Reduced surface contamination: I also took special measures to avoid the possibility of surface contamination during the preparation of polished samples for analysis. To minimize potential Al contamination, I made several polished sections using only diamond abrasives, and then ultrasonically cleaned and thoroughly rinsed them with methanol and deionized water to reduce the possibility of Na contamination.

Results of high-precision microprobe analyses

I obtained excellent results using the modified analytical technique. By counting 4 times longer with a 4 times larger current, a 16-fold increase in total counts was obtained, leading to a 4-fold increase in precision (and comparable lowering of detection limits). With slight exceptions (i.e., one early session in which the spectrometer measuring Ni drifted erratically), the high-precision data are fully consistent with the earlier measurements. On average, the olivine stoichiometry and oxide totals were somewhat better in the high-precision analyses: Σ Si+Al = 0.997 (0.0024) vs. 1.011 (0.008); total wt.% = 99.80 (0.31) vs. 100.51 (0.44). There was a weak correlation between the oxide totals and the olivine composition, with Fo_{93} averaging ~99.6 wt.% and Fo_{84} averaging ~100.2 wt.%. This was probably caused by flaws in the ZAF data reduction algorithm; Glenn Poirier, McGill University's microprobe analyst, informed me that he preferred using olivine standards close to the composition of the unknown samples to avoid such divergent behavior.

For a given counting time and peak-to-background ratio, it is easy to calculate the statistical precision of an X-ray count-rate. It is desirable to see whether this is the major source of analytical error. In the course of olivine crystallization, Mn^{2+} and Fe^{2+} should behave in a similar manner, and a linear or near-linear relationship should exist between the concentrations of MnO and FeO in komatiite olivine, with scatter about this line primarily due to analytical error. Consistent with this hypothesis, the residual errors from both sets of analyses have Gaussian distributions with a full-width, half-maximum equal to the counting statistical error (standard deviation of 0.014 wt.% MnO for routine precision data and 0.0037 wt.% MnO for high precision data). Thus, the counting statistical error for a given peak and background is used to determine the precision of the microprobe analyses for that element.

Possible effects of secondary fluorescence

An additional problem that is well-known but rarely addressed are X-rays from neighboring minerals excited by stray electrons or secondary X-ray fluorescence. Elements most likely to be effected would be those in which the concentration in adjacent minerals is much greater than in olivine, e.g., Cr in Cr-spinel, Ca in augite, Al in the groundmass, and Ni in pentlandite. In a well-designed microprobe, stray electrons are negligible provided care is taken focusing on a properly grounded and carbon-coated sample.

Because primary electrons penetrate less than 5 μm into a sample, a poorly focused beam will excite a relatively small volume of the mineral(s) around the nominal focal point, so that the effect can be minimized by careful selection of the points to be analyzed. Wherever possible, analyses were made at least 20 μm away from other minerals. No analyses were made within 50 μm of Cr-spinel exposed at the surface of a polished section.

Secondary fluorescence, the basis of XRF analysis, occurs when primary X-rays emitted following electron–atom interactions are absorbed by other atoms in the sample, stimulating the emission of lower energy X-rays. In a typical mineral, X-rays in the 4–10 keV range are scattered or absorbed much less than electrons of comparable energies. Therefore, secondary fluorescence can act over considerably greater distances than can scattered electrons. Tests by Capobianco and Amelin (1994) on adjoining silica glass and stainless steel slabs showed that secondary fluorescence of Cr, Fe, and Ni was insignificant (>0.10%) at spot distances >30 μm from the metal. Their experiment is not entirely relevant for our purposes because the Si and O Kα X-ray energies (1.740 and 0.525 keV) are below the K absorption edges of Cr, Fe, and Ni (5.989, 7.111, and 8.332 keV) and thus cannot excite secondary X-ray emission; any secondary fluorescence that did occur was caused by bremsstrahlung radiation from the primary beam. Iron (6.400 keV) and Ni (7.468 keV) Kα X-rays emitted from olivine are above the K absorption edges of Cr, Ca, and Al (5.989, 4.038, and 1.560 keV) and can excite secondary X-ray fluorescence in augite or Cr-spinel crystals.

A factor that should minimize the potential for secondary fluorescence of Cr is the solid-angle geometry involved, i.e., the small size of most Cr-spinel crystals coupled with their distance from the beam focus. The Cr content of olivine determined by closely spaced analyses across single grains does not show variations consistent with secondary fluorescence effects. In addition, as many data points fall below the general trend of Cr vs. Mg/(Mg+Fe) as fall above it. Perhaps more importantly, analyzed points at the margins of olivine grains did not show anomalously high Ca or Al, even though close to augite crystals containing ~20 wt.% CaO and >5 wt.% Al_2O_3, or groundmass containing more than 10 wt.% of each.

For these reasons, I am confident that the irregular variations of the Cr_2O_3 content of olivine are real and not an artifact of the analytical process.

Appendix 4. Whole-rock X-ray fluorescence procedures

All analytical work was performed at the University of Ottawa by myself, following procedures developed by Mr. Ron Hartree, the XRF analyst of the Department of Geology. Samples were analyzed on an Philips PW2400 automated sequential X-ray spectrometer equipped with a Rh end-window tube. On-line data reduction was carried out on a PC using a modified Lachance-Traill iterative algorithm. The XRF spectrometer was calibrated by least-squares linear regression using approximately 30 international reference standards.

Sample preparation

I removed weathered material from all samples with a diamond saw. Where sample size permitted, the least altered rock was chosen for analysis, avoiding veined or anomalously light or dark material (as seen on cut surfaces). Typically 10–30 g of rock was crushed per sample; with this sample size replicate analyses were quite similar for both fine-grained rocks as well as coarse-grained rocks from A_3 layers. Certain analyses were made of thin slabs cut from rock chips used to make polished sections; some of these slabs weighed only 2–4 g. Analytical results from these small samples are indistinguishable from those of other larger samples, even from A_3 layers. Such homogeneity is surprising, but the thin plate-like habit of the olivine crystals, their fairly uniform distribution, and the fact that no other phenocryst phase is present may account for the low compositional variation observed.

Most samples were analyzed as low-dilution glass disks using the following procedure. The trimmed rock was crushed to 2–10 mm size with a hammer or a steel jaw crusher, and then coarsely ground in a tungsten carbide shatterbox (this stage was omitted in about half of the samples). A 3–5 g aliquot was prepared by mixing and quartering on a clean sheet of paper, finely ground under reagent-grade methanol in an agate mortar, and dried at ~120 °C for at least 30 minutes. 1.3000 (±0.0002) g of dried rock powder was mixed with 4.0750 (±0.0002) g of a flux consisting of an equimolar mixture of $LiBO_2$ + $Li_2B_4O_7$ (Claisse Inc., "Pure grade"). The mixture was fused and continuously swirled for about 12 minutes in $Pt_{95}Au_5$ crucibles over a propane flame at ~1000 °C. The melt was then poured into a polished 30 mm diameter $Pt_{95}Au_5$ mold that had been preheated to ~800 °C. The liquid-filled mold was allowed to cool in air for a few seconds, then placed on a smooth granite slab for cooling to ambient temperature. The resultant glass disks are

smooth, flat, and free of undissolved material such as chromite grains. The glass is homogeneous except for a few sub-mm bubbles (having no effect on XRF analysis) and swirls of lighter-colored glass near the center of the disk. The latter form at the edges of polygonal cells during Bénard-style convection in the mold. They are commonly present in fused disks of basalts or other iron-rich rocks, and appear to have little effect on analytical results.

In an additional step—developed midway through my apprenticeship, so not applied to all samples—the glass disk, crucible, and any loose glass beads are weighed (the sample and crucible having been weighed before fusion) to obtain the loss on ignition (LOI). Volatiles such as CO_2 and H_2O are almost completely lost from the sample. The nominally anhydrous flux contains ~0.2 wt.% H_2O; after correcting for the 1.5–2 mg of water retained in the glass disk, the LOI can be determined to ± 0.1 wt.%. Samples low in volatiles and high in ferrous iron may show a gain on ignition as oxygen is gained during partial oxidation of Fe^{2+} to Fe^{3+}. (Metamorphism has changed the Fe^{2+}:Fe^{3+} ratios of the komatiites from the original magmatic values; I did not feel it worthwhile to determine ferrous iron by titration). The total of all determined constituents, including LOI, was generally ~100.3–100.9 wt.%. Totals generally exceed 100% because any FeO present is reported as Fe_2O_3. Samples rich in F or Cl may lose mass as BF_3 or BCl_3 evaporates from the melt, but this effect is negligible in komatiites.

Spectrometer operating conditions and background corrections

Analyses were performed using a new Philips PW2400 automated sequential X-ray spectrometer equipped with a 3 kW Rh end-window tube. Each element was analyzed using optimized tube voltage, current, primary X-ray filters (various thicknesses of Al sheets), collimators, and diffracting crystals. A scintillation counter measured X-rays with energies greater than 7 keV (i.e., Co and heavier elements) and an gas flow proportional counter (90% Ar, 10% CH_4) measured those with energies less than 7 keV. The low-energy shoulder of the Rh Compton peak, covering the spectral region from Zr to Rb was fitted using a second-order exponential fit; elsewhere linear background fits were adequate. Spectral interferences, such as the Sr Kβ peak (15.83 keV) on the Zr Kα (15.75 keV) peak, were corrected through the use of the appropriate stripping ratios. The PW2400 spectrometer also includes band-pass energy filters to remove higher order reflections that could interfere with the determination of certain elements. For example, previous-generation spectrometers were unable to detect low levels of P in samples having

moderate to high concentrations of Ca because the angular position of the second-order reflection of the Ca Kβ peak (4.012 keV) is very close to that of the first-order P Kα peak (2.013 keV). This is now corrected to the extent that P can be analyzed in calcite (56 wt.% CaO) down to a few tens of μg/g.

Each analysis required approximately 30 minutes of instrument time. Net X-ray counts on elemental peaks were reduced to oxide or elemental concentrations using a modified Lachance-Traill alpha-correction scheme (Philips on-line software; coefficients from Rousseau, 1989, 1992) calibrated against ~30 international standard reference materials (Govindaraju, 1994).

Analytical results

The obtained analytical results were both highly precise and accurate. This statement may seem gratuitous, but until quite recently many laboratories analyzed only major elements on glass disks, with trace elements analyzed on pressed pellets of unfused rock powder. Pressed powders have the advantage of being undiluted, and in having lower backgrounds on the shoulder of the Compton peak—for example, the peak-to-background ratio for Sr is improved by a factor of four in a pressed pellet. However, for all but the least abundant elements analyzed (Rb, Sr, Y, Zr) or for elements which are problematic in fused samples due to volatilization (Cl, F, S, As) or reduction and alloying with the crucible (S, As, Bi, Cu) the convenience and reliability of the fused disk method outweighs the more-or-less doubled precision—but not necessarily accuracy—of the pressed pellet technique.

In comparison to glass disks, pressed pellets exhibit decreased linearity between elemental concentrations and characteristic X-ray count rates. Corrections for matrix effects such as absorption and enhancement are considerably larger, and problems arise with the stable, rapidly-convergent algorithm we use for fused samples. The effects of sample grain-size can become significant for the lighter elements, which is clearly not a problem in glass disks. Finally, something as seemingly straightforward as forming a homogeneous, durable pellet can be difficult. It is necessary to have an evenly-distributed binder that is free of elements being analyzed (largely restricting the choice to organic polymers such as waxes or acrylics), does not significantly increase Compton scattering or secondary X-ray absorption, is stable under vacuum to ~60 °C, and minimizes any contamination of the spectrometer interior. The pressed pellets used in this study were

bonded with methyl methacrylate dissolved in acetone, but subsequent tests using "micronized wax" (Hoechst Inc.) showed that the latter was a superior binder.

Representative total errors (machine reproducibility, counting statistics, sample variance, and fusion process) were evaluated by analyzing 12 disks made from a 25 g batch of a relatively coarse-grained, randomly oriented spinifex-textured komatiite from Alexo (AX-96-01). Similarly, 10 analyses of a single komatiite sample disk give an indication of machine and statistical reproducibility (Table **A4.1**). In my judgment, imperfectly corrected matrix effects are the largest source of inaccuracy in the analysis of major and minor elements; matrix absorption effects, peak interferences, imperfect background corrections, and statistical counting error are all significant sources of analytical uncertainty for trace elements.

Analytical accuracy

As is generally the case in geochemical analyses, accuracy is more difficult to evaluate than precision. This is particularly true for geological standard reference materials, in which recommended values are arrived at through statistical treatment of analytical results from many (~100) different laboratories. Trace elements are rarely known to an accuracy much greater than ~5%, and determinations of SiO_2, the most abundant component of most rocks, often vary by ± 1% between labs. The recommended concentrations of SiO_2 in the two most recent SRMs, the diabase WS-E and fine-grained gabbro PM-S, are 50.70 and 47.00 wt.%, respectively (Govindaraju et al., 1994). Nearly 100 laboratories took part in these analyses, presumably using their best procedures, and yet the standard deviations of SiO_2 were 0.58 and 0.65 wt.% respectively. In part this may be due to the widespread technique of mixed-acid dissolution of silicate rocks. In this method, finely-ground rock is digested by a mixture of concentrated HF, HNO_3, and perchloric acid, evaporated to dryness, and then redissolved in dilute HNO_3 or HCl. During the drying step, volatile SiF_4 is largely or completely lost from the sample. This is desirable for certain analytical techniques as it reduces precipitation of gelatinous silica and clogging of aspirated solutions, but presumably means that fewer labs perform accurate analyses of SiO_2. Because matrix corrections are an integral part of XRF analysis, inaccurate SiO_2 values in reference standards propagate errors in other elements. A nominal SiO_2 content that is 1.0 wt.% too high will lead to a 0.3 wt.% error in Fe_2O_3 in a fused disk, and a similar or larger error in a pressed pellet. By calibrating the XRF spectrometer using many standards of widely varying composition in a weighted least-

squares regression, we have been able to minimize such errors. Our analyses of SRMs rarely differ by more than 0.1 wt.% (0.2 wt.% for SiO_2) from the recommended value for any major element.

Sample contamination during grinding

Contamination from a poorly ventilated sample preparation room (now closed) and certain hard-to-clean crushing machines was a problem with several early samples. In addition, mechanized grinding with a tungsten carbide swing mill (Spex "Shatterbox") was rapid but often led to excessive grain-size variations wherein a significant proportion of a sample would be reduced to an overly fine powder while coarse material was still abundant. Commercial tungsten carbide consists of fine-grained WC particles (~85–95 wt.%) sintered by Co metal (~15–5 wt.%). Contamination of polycrystalline vein quartz crushed in tungsten carbide amounted to ~100 µg/g Co (and presumably ~1000 µg/g W). By comparison to similar samples of komatiites that were hand-ground in agate the amount of Co contamination could be determined. About 10–20 µg/g Co was added to komatiites ground to a fine powder (i.e., <200 mesh) in the shatterbox; Co contamination was halved in samples that were only ground to a coarse powder. This rather small amount of contamination was due to the weakly abrasive nature of partially serpentinized komatiite, and also to careful washing of the swing-mill between samples. Hand grinding in agate under reagent-grade methanol was a superior preparation method, but quite time-consuming.

Several different batches of $LiBO_2$ and $Li_2B_4O_7$ fluxes were used in the XRF lab over a three-year period. While busy learning the potential of the new instrument, lowering detection levels, improving matrix corrections, simplifying sample preparation, etc., we omitted the basic precaution of analyzing each batch of flux as it arrived. One particular batch contained ~0.04 wt.% Na_2O (corresponding to ~0.15 wt.% in the sample). This level of Na in the flux was not detectable using the older Philips PW1400 XRF spectrometer. Certain of my samples were fused with this mixture, and I have subtracted 0.15 wt.% of Na_2O from samples made over that period. Regardless of the batch of flux, the variation of Na is high within the studied komatiite flows.

Table A4.1 Representative precision of XRF analyses

Oxides (wt.%) or elements (µg/g)	AX-96-01 (12 disks analyzed 1×) wt.% or µg/g (standard deviation in parentheses)	MS-93-17A (1 disk analyzed 10×) wt.% or µg/g (standard deviation in parentheses)
SiO_2	41.97(4)	42.70(4)
TiO_2	0.276(1)	0.310(<1)
Al_2O_3	5.70(2)	6.54(1)
Fe_2O_3 (total)	10.17(1)	10.73(1)
MnO	0.151(1)	0.165(<1)
MgO	28.53(4)	26.57(3)
CaO	5.29(2)	6.307(5)
Na_2O	0.23(1)	0.577(3)
K_2O	0.0577(6)	0.097(<1)
P_2O_5	0.0178(9)	0.026(1)
LOI	7.69(6)	———
V	111(3)	139(2)
Cr	2287(25)	2267(4)
Co	94(2)	102(2)
Ni	1554(6)	1393(3)
Zn	59(1)	61(1)
Rb	2.5(15)	3.8(4)
Sr	19.0(3)	29.6(2)
Y	7.6(5)	8.8(2)
Zr	16.3(13)	17.2(4)
Ba	25(6)	30(8)
Total	92.96(6)	94.57(8)
Total (incl. LOI)	100.66(9)	———

Appendix 5. EMP mineral analyses.

A5.1 Olivine high-precision WDS analyses

Sample	SiO_2	Al_2O_3	FeO	MnO	MgO	CaO	Na_2O	Cr_2O_3	NiO	Total	mg#
92-01a	40.98	0.092	5.52	0.091	51.96	0.218	b.d.l.	0.146	0.403	99.40	94.38
92-01b	41.19	0.075	5.62	0.083	51.87	0.211	b.d.l.	0.138	0.400	99.58	94.27
92-01c	41.28	0.082	5.40	0.094	52.25	0.212	b.d.l.	0.134	0.401	99.85	94.52
92-01d	41.01	0.078	5.45	0.095	52.07	0.215	b.d.l.	0.130	0.406	99.46	94.45
92-12a	40.69	0.133	7.44	0.114	50.46	0.226	b.d.l.	0.212	0.404	99.68	92.36
92-12b	40.54	0.077	7.83	0.123	50.14	0.233	0.008	0.170	0.390	99.52	91.94
93-12d	40.45	0.126	10.67	0.159	47.77	0.243	b.d.l.	0.295	0.327	100.05	88.86
92-12d2	40.21	0.085	11.12	0.169	47.74	0.247	b.d.l.	0.212	0.313	100.09	88.44
92-12e	39.89	0.090	12.53	0.185	46.44	0.252	b.d.l.	0.214	0.262	99.86	86.85
92-12f	40.70	0.082	8.37	0.130	49.50	0.235	b.d.l.	0.185	0.390	99.60	91.34
92-12g	40.69	0.089	8.77	0.135	49.41	0.237	b.d.l.	0.191	0.376	99.91	90.94
92-12h	40.37	0.088	9.47	0.144	48.92	0.241	b.d.l.	0.218	0.350	99.80	90.21
abc(b)1	39.80	0.113	12.27	0.188	46.61	0.246	b.d.l.	0.268	0.286	99.78	87.13
abc(b)2	40.10	0.117	11.87	0.181	46.92	0.246	b.d.l.	0.266	0.290	99.99	87.57
abc(b)3	39.93	0.133	11.63	0.174	47.11	0.234	b.d.l.	0.271	0.288	99.77	87.81
abc(b)4	40.07	0.097	9.20	0.139	49.23	0.236	b.d.l.	0.206	0.373	99.56	90.51
abc(b)5	40.19	0.093	9.35	0.150	48.84	0.234	0.017	0.209	0.367	99.46	90.30
abc(b)6	40.13	0.093	8.74	0.136	49.40	0.234	0.008	0.194	0.378	99.31	90.97
abc(b)7	40.54	0.102	9.64	0.155	48.95	0.236	b.d.l.	0.217	0.354	100.19	90.05
abc(a)1	40.93	0.103	7.07	0.110	50.86	0.226	b.d.l.	0.169	0.414	99.88	92.76
abc(a)2	40.90	0.092	7.95	0.126	50.26	0.231	b.d.l.	0.186	0.409	100.15	91.85
abc(a)3	40.83	0.099	8.47	0.133	49.86	0.237	b.d.l.	0.194	0.387	100.22	91.29
abc(a)4	40.65	0.099	9.04	0.140	49.35	0.233	b.d.l.	0.210	0.366	100.09	90.68
abc(a)5	40.09	0.124	12.04	0.188	47.10	0.227	b.d.l.	0.252	0.287	100.31	87.46
abc(a)6	40.01	0.136	13.51	0.203	45.79	0.232	b.d.l.	0.267	0.252	100.39	85.80
m5a	41.17	0.082	5.86	0.097	51.58	0.219	b.d.l.	0.146	0.404	99.56	94.01
m5b	40.80	0.129	7.15	0.115	50.30	0.232	b.d.l.	0.186	0.388	99.30	92.62
m5c	40.43	0.076	9.24	0.148	48.95	0.250	0.008	0.183	0.346	99.62	90.43

b.d.l.: Below 3 σ lower limit of detection for Na_2O (= 0.008 wt.%).

A5.2 Olivine routine precision WDS analyses

Session I (because of a drifting spectrometer NiO analyses are of low quality)

Sample	SiO_2	Al_2O_3	FeO	MnO	MgO	CaO	Cr_2O_3	NiO	Total	mg#
ms25(1)	41.73	0.109	5.48	0.078	52.71	0.229	0.167	0.356	100.86	94.49
ms25(2)	41.64	0.091	5.51	0.075	52.60	0.212	0.171	0.349	100.65	94.45
ms25(3)	41.83	0.099	5.61	0.098	52.45	0.231	0.185	0.328	100.82	94.30
ms25(4)	42.14	0.094	5.51	0.075	52.85	0.223	0.165	0.341	101.40	94.48
ms25(5)	42.04	0.093	5.39	0.090	52.78	0.226	0.179	0.321	101.12	94.58
ms25(6)	41.92	0.095	5.43	0.086	52.37	0.214	0.171	0.331	100.61	94.50
ms25(7)	41.97	0.093	5.47	0.112	52.62	0.232	0.186	0.322	101.01	94.49
ms25(8)	42.36	0.097	5.58	0.101	52.49	0.229	0.174	0.327	101.36	94.37
ms25(9)	42.26	0.101	6.29	0.091	51.96	0.219	0.156	0.306	101.38	93.65
msxx(1)	41.76	0.087	5.78	0.094	52.01	0.228	0.178	0.325	100.46	94.13
msxx(2)	41.96	0.113	5.58	0.074	52.83	0.217	0.151	0.311	101.23	94.41
msxx(3)	41.75	0.092	5.50	0.069	52.34	0.229	0.155	0.278	100.41	94.44
msxx(4)	42.30	0.098	5.66	0.077	52.62	0.235	0.146	0.290	101.43	94.31
msxx(5)	41.91	0.108	5.61	0.068	52.64	0.228	0.203	0.315	101.08	94.36
msxx(6)	42.09	0.103	5.64	0.098	52.18	0.233	0.179	0.290	100.80	94.29
msxx(7)	41.26	0.090	9.20	0.155	49.64	0.233	0.160	0.264	100.99	90.59
msxx(8)	43.19	0.239	11.91	0.194	43.19	0.213	0.173	0.208	98.53	86.60
ms47-1(1)	41.68	0.100	7.13	0.143	50.66	0.242	0.196	0.261	100.41	92.68
ms47-1(2)	41.52	0.083	7.04	0.089	50.93	0.242	0.178	0.258	100.35	92.80
ms47-1(3)	41.45	0.091	6.77	0.095	51.12	0.229	0.177	0.290	100.23	93.08
ms47-1(4)	41.70	0.078	6.68	0.113	51.47	0.224	0.179	0.301	100.75	93.21
ms47-1(5)	41.71	0.085	6.73	0.119	51.42	0.235	0.193	0.287	100.78	93.16
ms47-1(6)	42.00	0.093	6.60	0.098	51.67	0.223	0.186	0.273	101.15	93.31
ms47-1(7)	41.87	0.098	6.59	0.097	51.43	0.241	0.211	0.297	100.84	93.30
ms47-1(8)	41.54	0.086	6.79	0.114	51.25	0.240	0.223	0.275	100.52	93.08
ms47-1(9)	41.59	0.097	7.22	0.134	50.93	0.239	0.203	0.301	100.71	92.63
ms47-1(10)	41.60	0.075	7.43	0.080	50.99	0.232	0.197	0.259	100.87	92.45
ms47-2(1)	41.62	0.084	8.20	0.124	49.44	0.247	0.194	0.245	100.15	91.49
ms47-2(2)	41.43	0.096	8.02	0.121	49.78	0.255	0.201	0.266	100.17	91.71
ms47-2(3)	41.61	0.085	7.65	0.118	50.38	0.247	0.219	0.255	100.56	92.15
ms47-2(4)	41.71	0.091	7.44	0.105	50.42	0.242	0.218	0.266	100.49	92.35
ms47-2(5)	41.62	0.094	7.19	0.106	50.94	0.248	0.209	0.272	100.69	92.66
ms47-2(6)	41.91	0.077	7.12	0.093	51.16	0.236	0.199	0.260	101.06	92.76
ms47-2(7)	41.93	0.105	7.20	0.141	51.32	0.237	0.186	0.278	101.39	92.71
ms47-2(8)	41.53	0.084	7.19	0.106	51.15	0.249	0.176	0.251	100.74	92.69
ms47-2(9)	41.83	0.093	7.39	0.115	50.80	0.236	0.187	0.240	100.89	92.45
ms47-2(10)	41.63	0.094	7.66	0.099	50.20	0.242	0.189	0.262	100.38	92.11

Session I (cont.)

Sample	SiO_2	Al_2O_3	FeO	MnO	MgO	CaO	Cr_2O_3	NiO	Total	mg#
ms47-2(11)	41.65	0.088	8.65	0.123	49.24	0.245	0.213	0.247	100.47	91.03
ms47-2(12)	41.28	0.088	9.18	0.136	48.85	0.261	0.208	0.230	100.23	90.47
ms47-2(13)	40.92	0.094	11.14	0.186	46.76	0.281	0.184	0.231	99.84	88.17
ms15-1(1)	41.93	0.091	6.85	0.117	51.41	0.226	0.193	0.243	101.05	93.05
ms15-1(2)	42.13	0.095	7.07	0.102	51.59	0.234	0.170	0.243	101.64	92.86
ms15-1(3)	41.85	0.091	6.94	0.099	51.40	0.237	0.183	0.273	101.09	92.96
ms15-1(4)	42.02	0.089	6.91	0.120	51.34	0.235	0.190	0.260	101.16	92.98
ms15-1(5)	41.76	0.088	7.61	0.138	50.64	0.233	0.198	0.245	100.91	92.23
ms15-1(6)	41.91	0.101	8.02	0.127	49.46	0.250	0.229	0.219	100.32	91.66
ms15-1(7)	41.43	0.116	9.06	0.129	49.31	0.249	0.245	0.221	100.77	90.65
ms15-1(8)	40.98	0.135	10.65	0.139	48.08	0.247	0.333	0.191	100.75	88.95
ms15-1(9)	40.41	0.157	12.93	0.166	46.52	0.250	0.391	0.174	101.00	86.51
ms15-2(1)	41.96	0.090	6.48	0.092	51.18	0.240	0.189	0.237	100.47	93.37
ms15-2(2)	42.02	0.102	6.59	0.093	51.01	0.248	0.197	0.252	100.51	93.24
ms15-2(3)	42.00	0.101	6.61	0.104	50.60	0.251	0.202	0.243	100.11	93.17
ms15-2(4)	41.77	0.091	6.70	0.085	50.70	0.242	0.189	0.216	99.99	93.09
ms15-2(5)	42.02	0.102	7.05	0.132	50.91	0.239	0.218	0.222	100.89	92.79
ms15-2(6)	41.82	0.099	7.23	0.095	50.34	0.255	0.204	0.223	100.26	92.54
ms15-2(7)	41.84	0.097	7.61	0.113	49.76	0.248	0.224	0.215	100.09	92.10
ms15-2(8)	41.51	0.082	8.72	0.119	49.08	0.253	0.237	0.220	100.21	90.94
ms15-2(9)	41.07	0.100	11.13	0.149	47.48	0.273	0.307	0.159	100.67	88.38
ms15-2(10)	40.30	0.110	15.10	0.240	44.57	0.286	0.293	0.140	101.04	84.03
ms18-1(1)	41.41	0.108	8.64	0.137	49.64	0.235	0.272	0.196	100.64	91.11
ms18-1(2)	41.31	0.114	9.00	0.150	49.06	0.245	0.259	0.213	100.34	90.67
ms18-1(3)	41.44	0.105	9.37	0.109	48.68	0.236	0.274	0.168	100.38	90.26
ms18-1(4)	41.11	0.094	10.32	0.142	48.17	0.264	0.291	0.173	100.55	89.27
ms18-1(5)	40.73	0.115	11.17	0.157	46.96	0.263	0.299	0.157	99.85	88.23
ms18-1(6)	40.52	0.152	12.73	0.183	45.96	0.248	0.357	0.125	100.28	86.56
ms18-1(7)	41.15	0.134	12.22	0.200	41.61	0.216	0.287	0.098	95.91	85.86
ms18-1(8)	40.09	0.120	14.38	0.198	43.85	0.277	0.303	0.108	99.32	84.46

Session II (no problems with spectrometers)

Sample	SiO_2	Al_2O_3	FeO	MnO	MgO	CaO	Cr_2O_3	NiO	Total	mg#
ms18-2(1)	41.50	0.095	6.74	0.104	51.20	0.226	0.243	0.405	100.39	93.12
ms18-2(2)	41.45	0.090	7.02	0.096	51.02	0.202	0.256	0.441	100.45	92.83
ms18-2(3)	41.58	0.091	7.44	0.124	50.51	0.201	0.228	0.417	100.47	92.37
ms18-3(1)	41.51	0.099	7.09	0.097	50.88	0.216	0.143	0.409	100.32	92.75
ms18-3(2)	41.26	0.097	8.17	0.137	50.16	0.227	0.248	0.387	100.58	91.63
ms18-3(3)	40.41	0.105	11.92	0.159	46.57	0.236	0.314	0.283	99.91	87.45
ms18-4(1)	41.04	0.072	9.23	0.155	49.28	0.204	0.204	0.393	100.46	90.49
ms18-4(2)	42.18	0.148	9.00	0.137	47.52	0.198	0.193	0.377	99.75	90.40
ms18-5(1)	40.79	0.088	9.32	0.150	48.86	0.218	0.266	0.428	99.99	90.34
ms18-5(2)	40.10	0.107	12.94	0.212	45.24	0.253	0.341	0.249	99.36	86.17
ms18-6(1)	41.14	0.093	9.10	0.147	48.90	0.202	0.225	0.366	100.07	90.55
ms18-6(2)	41.21	0.094	8.26	0.121	49.53	0.226	0.217	0.409	99.94	91.45
ms18-6(3)	40.75	0.131	11.39	0.159	47.37	0.222	0.287	0.316	100.52	88.12
ms18-7(1)	41.13	0.093	8.55	0.110	49.72	0.206	0.282	0.417	100.39	91.20
ms18-7(2)	41.04	0.141	9.17	0.147	49.17	0.210	0.296	0.350	100.41	90.53
ms18-7(3)	40.33	0.097	12.02	0.154	47.07	0.212	0.256	0.331	100.38	87.47
ms18-8(1)	40.67	0.077	10.85	0.193	47.37	0.215	0.226	0.365	99.86	88.61
ms18-8(2)	41.04	0.115	9.48	0.144	49.22	0.222	0.286	0.347	100.76	90.25
ms18-8(3)	40.83	0.127	9.39	0.138	49.02	0.214	0.295	0.383	100.29	90.29
ms18-9(1)	39.92	0.051	14.30	0.238	44.90	0.228	0.247	0.247	100.06	84.84
nn(1)	41.35	0.082	6.66	0.102	51.45	0.200	0.191	0.413	100.39	93.23
nn(2)	41.09	0.106	7.49	0.105	50.28	0.211	0.203	0.389	99.76	92.29
nn(3)	41.61	0.081	6.51	0.095	51.44	0.2121	0.183	0.412	100.42	93.37
nn(4)	41.69	0.097	6.61	0.097	51.38	0.2111	0.177	0.410	100.55	93.27
nn(5)	41.40	0.094	7.10	0.112	51.14	0.216	0.227	0.389	100.56	92.77
nn(6)	41.44	0.086	8.03	0.121	50.40	0.223	0.197	0.422	100.79	91.80
nn(7)	40.66	0.080	10.56	0.167	48.29	0.226	0.171	0.331	100.38	89.08
nn(8)	41.41	0.081	6.83	0.112	51.39	0.203	0.188	0.402	100.50	93.06
nn(9)	41.33	0.089	7.49	0.112	50.66	0.212	0.181	0.416	100.36	92.34
nn(10)	40.53	0.665	12.70	0.216	45.33	0.214	0.244	0.371	100.29	86.42
nn(11)	41.46	0.082	7.08	0.123	51.13	0.192	0.203	0.444	100.58	92.79
nn(12)	41.36	0.085	7.18	0.11	51.01	0.1892	0.208	0.418	100.43	92.68
nn(13)	41.49	0.079	7.43	0.097	50.71	0.1982	0.222	0.411	100.58	92.42
nn(14)	41.63	0.156	6.71	0.104	51.15	0.185	0.250	0.415	100.48	93.14
nn(15)	41.35	0.090	9.61	0.154	48.76	0.226	0.197	0.373	100.64	90.05
nn(16)	41.33	0.088	8.41	0.134	50.04	0.209	0.222	0.419	100.72	91.39
nn(17)	41.18	0.094	8.51	0.147	49.70	0.213	0.206	0.423	100.35	91.24
nn(18)	41.15	0.074	9.19	0.144	49.24	0.234	0.206	0.366	100.49	90.52

Session II (cont.)

Sample	SiO_2	Al_2O_3	FeO	MnO	MgO	CaO	Cr_2O_3	NiO	Total	mg#
ms25-2(1)	41.71	0.102	5.42	0.083	52.22	0.196	0.158	0.429	100.20	94.50
ms25-2(2)	41.90	0.107	5.32	0.122	52.33	0.185	0.185	0.412	100.44	94.60
ms25-2(3)	41.67	0.099	5.39	0.104	52.58	0.196	0.173	0.411	100.50	94.57
ms25-2(4)	41.90	0.103	5.45	0.094	52.58	0.193	0.161	0.406	100.77	94.51
ms25-2(5)	41.62	0.088	5.41	0.089	52.26	0.188	0.196	0.425	100.15	94.51
ms25-2(6)	41.76	0.095	5.50	0.083	52.60	0.191	0.148	0.385	100.65	94.46
ms25-3(1)	41.76	0.097	5.50	0.072	52.19	0.204	0.168	0.425	100.29	94.42
ms25-3(2)	41.69	0.082	5.57	0.084	52.15	0.190	0.181	0.396	100.22	94.35
ms25-3(3)	41.48	0.100	5.63	0.100	52.09	0.202	0.194	0.406	100.08	94.29
ms25-3(4)	41.46	0.101	5.70	0.101	52.01	0.200	0.176	0.419	100.05	94.21
ms25-3(5)	40.98	0.104	8.49	0.136	48.74	0.209	0.193	0.435	99.15	91.10
ms25-4(1)	41.68	0.095	5.45	0.084	52.37	0.193	0.154	0.404	100.31	94.49
ms25-4(2)	41.79	0.089	5.46	0.098	52.46	0.191	0.180	0.421	100.56	94.48
ms25-4(3)	41.64	0.084	5.58	0.104	52.08	0.202	0.167	0.411	100.14	94.33
ms25-4(4)	41.60	0.074	5.50	0.092	51.94	0.205	0.168	0.439	99.89	94.39
ms25-4(5)	41.59	0.085	5.44	0.081	52.15	0.194	0.168	0.417	100.00	94.48

A5.3 Augite EDS analyses

Sample	SiO_2	TiO_2	Al_2O_3	FeOT	MnO	MgO	CaO	Na_2O	Cr_2O_3	mg#
ms44	47.7	0.98	8.9	8.0	0.47	13.4	20.6	—[1]	—	74.9
ms44	49.6	0.69	6.4	6.4	0.25	14.8	21.8	—	0.18	80.5
ms44	50.5	0.70	5.5	5.9	0.53	14.3	22.2	—	0.41	81.2
ms44	49.6	0.61	6.6	6.7	—	14.9	20.9	—	0.58	79.7
ms44	49.3	0.69	5.9	7.3	0.35	16.5	19.8	—	0.27	80.1
ms44	47.4	0.86	8.0	12.5	0.44	15.0	15.9	—	—	68.3
ms44	48.1	1.00	8.3	8.2	0.52	13.6	20.2	—	—	74.7
ms44	49.1	0.43	8.0	6.7	0.40	13.8	21.0	0.45	0.19	78.6
ms44	48.7	1.00	7.1	6.4	0.25	14.2	21.7	0.27	0.37	79.8
ms44	47.8	1.26	9.4	9.4	—	13.2	18.9	—	0.12	71.5
ms44	49.0	0.58	8.2	6.6	0.11	14.0	20.9	0.37	0.30	79.2
ms44	47.9	0.83	8.2	8.3	—	13.2	20.8	0.64	0.20	74.0
ms44	47.9	0.74	8.5	7.2	0.35	14.2	20.4	0.49	0.24	77.9
ms44	48.7	1.17	7.6	7.0	—	13.8	21.5	—	0.24	77.7
ms44	48.1	0.78	8.2	7.0	0.50	14.3	20.7	0.29	0.22	78.5
ms44	49.7	0.83	6.7	6.9	0.15	14.3	20.9	—	0.45	78.8
SD3	47.8	0.70	9.0	8.9	0.15	11.8	21.3	—	0.34	70.2
SD3	49.4	0.66	8.0	9.3	0.18	16.1	15.9	—	0.43	75.6
ms15	48.1	0.89	9.3	8.4	0.19	13.2	19.8	—	0.22	73.6
ms69	45.4	0.89	11.5	11.6	0.28	10.3	19.6	—	0.27	61.2
MS93-12	49.6	0.48	6.7	9.1	0.31	14.8	18.6	—	0.48	74.5
MS93-12	49.4	0.52	7.1	10.1	0.14	15.7	16.9	—	0.14	73.4
MS93-12	48.5	0.68	7.9	11.4	0.18	14.3	16.7	—	0.12	69.1
MS93-12	51.5	1.27	6.9	8.4	0.12	14.3	16.7	—	0.67	75.1
MS93-12	51.2	0.58	6.4	9.5	0.17	15.8	15.6	0.20	0.44	74.7
MS93-01	51.7	0.61	3.3	11.2	0.20	17.6	15.3	—	0.18	73.6
MS93-01	49.5	0.52	7.2	6.7	—	15.9	19.7	—	0.22	80.9
MS93-01	49.9	0.50	7.6	6.8	—	15.8	19.2	—	0.16	80.6

[1] In this and subsequent tables, — means below EDS detection limit (~0.1–0.2 wt.% for many elements)

A5.3 Augite EDS analyses (cont.)

Sample	SiO_2	TiO_2	Al_2O_3	FeOT	MnO	MgO	CaO	Na_2O	Cr_2O_3	mg#
MS93-17	47.7	0.79	10.0	8.6	0.30	11.9	20.6	—	0.17	71.2
MS93-17	47.5	0.75	9.7	8.6	0.13	12.2	21.0	—	0.13	71.5
MS93-17	46.8	0.92	9.5	11.4	0.13	10.4	20.8	—	0.15	62.0
MS93-03	48.7	0.46	6.2	7.0	0.12	16.1	20.6	0.26	0.17	80.5
MS93-03	50.8	0.38	4.0	6.0	0.33	15.4	22.8	—	0.24	82.1
MS93-03	50.6	0.50	4.4	6.1	0.41	14.6	22.5	—	0.34	81.1
MS93-03	50.1	0.96	6.3	5.6	0.20	15.1	21.0	0.42	0.41	82.7
MS93-03	50.5	0.51	4.6	5.9	0.17	15.7	21.8	—	0.42	82.6
MS93-03	51.1	0.48	4.3	5.7	—	15.5	22.4	—	0.30	82.9
MS93-03	50.9	0.58	4.8	5.7	0.20	15.2	22.3	—	0.31	82.6
MS93-03	49.7	0.56	5.5	5.9	0.41	15.5	21.2	0.19	0.41	82.4
MS93-03	50.2	1.02	5.0	6.2	0.33	15.7	21.0	—	0.43	81.8
MS93-03	50.1	0.53	5.2	6.6	0.45	16.3	20.8	—	—	81.4

A5.4 Pigeonite–plagioclase intergrowth EDS analyses

Sample	SiO_2	TiO_2	Al_2O_3	FeOT	MnO	MgO	CaO	Na_2O	mg#[1]
MS93-12(1)	59.1	0.2	22.2	3.0	0.1	1.0	11.6	2.6	36
MS93-12(2)	59.3	0.3	21.5	3.0	0.3	1.1	10.7	3.6	66
MS93-12(3)	51.9	0.1	22.5	7.3	—	3.1	11.3	4.2	43
MS93-12(4)	52.7	0.2	21.1	7.3	—	2.5	13.2	3.6	42
MS93-12(5)	49.0	0.4	13.0	14.4	0.4	11.0	9.7	2.1	58
MS93-12(6)	48.8	0.3	13.3	15.6	0.4	7.9	10.8	2.5	47
MS93-12(7)	49.9	0.4	12.5	15.6	0.3	10.1	9.4	1.8	54
MS93-12(8)	51.4	0.4	7.9	18.8	0.3	8.5	11.5	1.0	45
MS93-12(9)	51.9	0.4	1.6	22.5	1.0	15.5	6.8	—	55
MS93-12(10)	51.2	0.3	1.4	23.8	0.9	15.7	6.2	—	54

[1] Mg# is highly imprecise.

A5.5 Cr-spinel EDS analyses

Sample	SiO_2	TiO_2	Al_2O_3	FeOT	MnO	MgO	CaO	Cr_2O_3
ms12	—	0.3	15.6	16.3	—	15.9	—	51.8
ms12	0.4	0.4	17.1	19.7	0.5	14.0	—	47.8
ms12	0.4	0.5	16.7	19.9	0.4	14.0	0.1	47.9
ms15	5.6	0.8	19.5	39.7	0.8	2.1	1.4	28.9
ms37	0.3	0.3	13.5	14.6	0.6	15.6	0.1	55.1
ms37	0.0	0.2	14.4	16.6	—	15.5	—	53.1
ms37	0.2	0.4	14.3	16.8	—	15.3	—	53.0
ms37	0.3	0.4	15.6	16.8	0.3	15.1	—	50.9
ms44	—	0.2	14.4	18.6	—	14.4	0.1	53.7
SD3	0.3	0.4	13.9	19.9	—	12.5	—	53.1
SD3	0.3	0.4	13.3	22.1	—	11.7	0.1	52.0
MS93-01	0.3	0.2	14.1	24.1	0.3	9.2	—	51.6
MS93-03	0.2	0.3	14.7	22.4	0.4	11.2	0.2	50.1
MS93-03	0.5	0.3	14.1	21.3	0.7	11.0	—	51.5
MS93-12	0.3	0.3	14.6	21.9	—	10.6	—	52.3
MS93-12	0.3	0.3	13.3	21.3	—	10.8	—	53.6
MS93-12	0.2	0.4	15.3	29.5	—	7.7	—	46.6
MS93-12	0.6	0.6	20.6	29.0	—	7.8	—	40.4
MS93-12	1.0	0.6	19.5	33.1	—	6.4	0.1	39.1
MS93-12	2.5	0.7	19.2	33.2	—	5.2	0.2	38.5
MS93-17	1.3	0.6	17.5	31.5	0.3	6.5	0.3	41.8
MS93-17	0.9	0.4	15.8	28.0	—	9.3	0.2	45.3
msNN	0.7	0.0	12.2	17.5	0.5	16.2	0.2	52.9
msNN	0.2	0.3	15.0	15.8	—	15.8	0.1	52.8
msNN	0.3	0.4	16.3	19.8	—	13.9	0.1	49.3
msNN	—	0.4	15.4	15.9	0.7	15.6	—	52.0
msNN	—	0.6	14.6	15.9	0.6	15.2	—	52.9
msNN	0.3	0.5	14.1	17.8	0.3	14.1	0.1	52.8
msNN	0.5	0.2	13.5	25.9	—	10.7	0.1	48.8
msNN	0.2	0.2	13.8	16.7	—	15.5	—	53.5
msNN	0.3	0.4	14.7	14.7	—	15.9	—	54.1
msNN	0.2	0.1	14.4	15.2	0.4	16.2	—	53.1
msNN	0.2	0.3	15.1	17.1	—	14.9	—	52.6

A5.6 Representative silicate and oxide EDS analyses

Sample	SiO_2	TiO_2	Al_2O_3	FeOT	MnO	MgO	CaO	Na_2O	Cr_2O_3	mg#
ilmenite[1] MS93-12	19.3	28.3	4.4	23.3	5.5	17.8	1.3	—	—	n.d.
magnetite[2] ms37	0.6	—	0.1	97.8	0.2	0.6	0.2	—	0.2	n.d.
talc ms03	57.5	0.2	1.6	4.6	—	35.8	—	0.4	—	93.3
serpentine ms05	39.0	0.2	—	2.1	—	41.9	0.1	—	0.3	97.3
serpentine MS93-17B	43.9	—	0.5	3.5	—	37.5	0.2	—	0.2	95.1
serpentine ms36	41.4	—	—	4.4	—	38.6	0.1	—	0.1	94.0
serpentine ms36	43.0	—	1.2	7.2	0.1	35.7	0.1	—	—	89.8
chlorite ms15	38.8	—	9.7	5.6	—	31.7	—	—	0.4	90.9
chlorite ms36	33.0	—	15.0	7.6	—	30.3	0.5	—	0.7	87.7
tremolite 93-01	58.6	0.1	1.0	3.9	—	24.0	11.9	—	—	91.6
actinolite sd3	54.5	0.1	2.9	6.3	0.2	22.0	11.5	1.2	0.3	86.1
andradite ms110	36.2	—	2.3	26.3	—	0.46	34.8	—	—	n.d.

[1] Ilmenite is very fine-grained (<10 μm in maximum dimension) and a "clean" analysis (i.e., without significant X-rays from neighbouring minerals) could not be obtained.
[2] Magnetite is very fine-grained, spongy, and intergrown with other fine-grained minerals, in particular serpentine. It appears to be >98% pure Fe_3O_4, with the chief impurities being Cr_2O_3, MnO, and NiO (each generally <0.5 wt.%).

A5.7 Sulfide EDS analyses (in molar%)

Sample	Mn	Fe	Co	Ni	Cu	S
pentlandite MS93-12	0.4	17.9	2.3	30.4	0.6	48.5
pentlandite MS93-12	0.2	14.3	6.6	30.7	0.7	47.5
pentlandite ms15	—	12.2	14.3	26.2	—	47.3
pyrrhotite MS93-12	0.4	45.2	—	1.4	0.1	52.9
heazlewoodite MS93-01	—	3.3	—	56.9	—	39.6
chalcopyrite ms69	—	25.0	—	0.2	24.5	50.2
bornite ms110	—	11.7	—	—	49.6	38.7

Heazlewoodite (Ni_3S_2) and bornite (Cu_5FeS_4) are very fine-grained and it is generally difficult to get a "clean" analysis (i.e., without significant X-rays from neighbouring minerals). These minerals appear to be close to end-member compositions.

Appendix 6. Whole rock XRF analyses

Oxides, LOI, and Sum in wt.%; elements in µg/g; certain elements measured in pressed powder pellets are indicated by an asterisk (Cl*, S*, Rb*, Sr*, Y*, and Zr*).

Sample #	MS93 -00	MS93 -01[1]	MS93 -01(A)[1]	MS93 -02	MS92 -03	MS93 -03(A)	MS93 -04	MS93 -05	MS93 -06
SiO_2	43.81	43.73	43.86	40.87	41.41	40.79	42.41	41.00	40.87
TiO_2	0.289	0.366	0.409	0.235	0.207	0.204	0.210	0.198	0.180
Al_2O_3	6.32	5.58	5.50	4.98	4.47	4.35	4.49	4.25	3.90
Fe_2O_3T	10.61	10.36	10.70	9.36	9.06	8.95	8.47	9.11	8.55
MnO	0.159	0.160	0.169	0.143	0.120	0.118	0.128	0.104	0.100
MgO	28.69	30.74	30.11	30.79	33.42	32.87	34.41	33.75	35.11
CaO	5.87	5.56	6.09	4.54	3.91	3.86	3.97	3.39	2.66
Na_2O	0.60	0.38	0.33	0.32	0.29	0.24	0.28	0.34	0.24
K_2O	0.095	0.123	0.132	0.082	0.048	0.043	0.036	0.050	0.036
P_2O_5	0.0171	0.0266	0.0287	0.0123	0.0122	0.0121	0.0115	0.0119	0.0108
Cl*	140	160	—	162	218	—	279	289	310
S*	288	303	—	205	185	—	163	135	168
V	129	122	125	102	94	95	97	84	81
Cr	2216	1988	1912	1975	1975	1944	2024	1847	1789
Co	103	105	95	97	102	101	99	102	99
Ni	1466	1718	1631	1710	1875	1827	1938	1918	2025
Zn	59	65	71	50	50	47	43	47	36
Rb	1.9	0.1	4.5	0.8	0.3	2.1	2.6	3.5	1.9
Rb*	2.3	2.7	—	2.4	1.4	—	1.7	1.8	1.8
Sr	10.0	17.6	23.5	7.5	9.4	9.0	7.9	11.4	10.8
Sr*	9.9	16.8	—	7.3	8.9	—	7.9	11.8	10.8
Y	7.1	7.6	7.2	6.7	6.1	5.2	5.0	5.2	4.9
Y*	7.3	7.1	—	6.0	5.4	—	5.3	5.2	4.9
Zr	13.6	22.2	21.3	12.4	10.6	8.3	8.0	7.2	8.5
Zr*	12.0	18.0	—	9.9	8.5	—	8.8	8.0	7.5
Ba	16	38	48	10	11	17	10	22	16
Sum	96.86	97.44	97.74	91.73	93.36	91.83	94.84	92.61	92.07
LOI	—	—	—	—	—	9.2	—	—	—

[1] Sample contaminated with K, Ti, P, Zr (and possibly other elements) from dust in crushing room.

[2] — not measured.

Sample #	MS93 -06(A)	MS93 -07(ag)	MS93 -07(A)	MS93 -07(B)	MS93- 07 (CF)	MS93- 07(FF)	MS93- 07(sv)	MS93 -08	MS93 -09
SiO_2	39.23	41.28	41.73	40.97	41.29	40.93	40.36	41.72	41.80
TiO_2	0.175	0.193	0.193	0.189	0.212	0.155	0.191	0.215	0.220
Al_2O_3	3.72	4.19	4.23	4.07	4.51	3.43	4.14	4.70	4.81
Fe_2O_3T	8.43	8.49	8.57	8.62	8.84	8.32	9.06	9.35	9.49
MnO	0.097	0.116	0.112	0.107	0.120	0.097	0.129	0.126	0.131
MgO	34.06	34.47	34.71	34.51	33.90	35.36	33.22	32.88	31.29
CaO	2.56	2.96	2.97	2.93	3.38	2.29	2.67	3.91	4.24
Na_2O	0.29	0.28	0.30	0.29	0.36	0.23	0.17	0.45	0.39
K_2O	0.039	0.064	0.068	0.066	0.077	0.051	0.047	0.063	0.059
P_2O_5	0.0100	0.0116	0.0117	0.0106	0.0134	0.0100	0.0113	0.0123	0.0133
Cl*	—	—	292	—	—	—	233	338	220
S*	—	—	193	—	—	—	177	203	183
V	79	88	81	88	96	70	91	95	96
Cr	1745	1825	1809	1779	1848	1705	1791	1941	1943
Co	93	95	96	95	91	102	107	107	97
Ni	1995	1947	1986	1986	1875	2089	1952	1841	1794
Zn	35	49	46	42	47	43	54	46	43
Rb	3.4	1.6	2.2	3.5	1.3	1.4	0.6	3.7	5.2
Rb*	—	—	1.8	1.8	—	—	2.3	—	—
Sr	10.8	12.4	11.8	11.2	14.5	9.3	7.8	16.6	12.8
Sr*	—	—	9.0	11.7	—	—	8.7	—	—
Y	5.1	5.4	5.0	5.4	5.4	4.3	5.6	5.9	4.4
Y*	—	—	5.2	4.9	—	—	5.1	—	—
Zr	6.5	9.5	7.6	6.7	10.6	7.6	10.4	8.0	5.8
Zr*	—	—	8.3	7.8	—	—	7.9	—	—
Ba	8	17	11	13	7	14	7	18	19
Sum	89.00	92.45	93.32	92.17	93.11	91.28	90.41	93.83	92.84
LOI	—	10.1	—	—	8.8	10.6	—	—	—

Sample #	MS93-09(ag)	MS93-10	MS93-11	MS93-12	MS93-13(A)	MS93-13(B)	MS93-13(ag)	MS93-14(A)	MS93-14(B)
SiO_2	41.39	43.69	43.78	45.06	44.97	45.81	45.36	43.38	43.38
TiO_2	0.226	0.324	0.373	0.368	0.360	0.391	0.379	0.321	0.326
Al_2O_3	4.88	6.95	7.81	7.92	7.84	8.51	8.17	6.94	7.06
Fe_2O_3T	9.93	11.22	9.71	11.87	12.02	12.19	12.34	11.36	11.46
MnO	0.133	0.181	0.166	0.180	0.178	0.184	0.183	0.162	0.168
MgO	31.55	25.43	23.81	23.37	23.52	21.90	22.42	25.32	24.89
CaO	4.19	7.12	8.30	7.63	7.63	8.14	8.20	6.59	6.81
Na_2O	0.38	0.72	0.35	0.93	1.10	1.23	1.20	0.78	0.78
K_2O	0.059	0.108	0.035	0.099	0.133	0.168	0.125	0.105	0.103
P_2O_5	0.0130	0.0183	0.0183	0.0208	0.0210	0.0240	0.0219	0.0180	0.0196
Cl*	—	261	289	349	441	—	—	278	—
S*	—	316	258	324	383	—	—	328	—
V	98	143	157	158	151	172	167	139	136
Cr	1977	2434	2712	2498	2589	2606	2636	2448	2420
Co	93	98	77	99	101	93	92	100	91
Ni	1859	1227	1016	1036	1051	916	933	1227	1200
Zn	57	71	63	71	66	70	71	64	64
Rb	1.5	5.4	1.5	0.0	6.1	5.8	4.6	4.2	3.2
Rb*	—	—	—	—	—	—	—	—	—
Sr	25.4	30.5	19.0	44.4	54.2	63.1	58.2	38.4	39.8
Sr*	—	—	—	—	—	—	—	—	—
Y	6.2	8.2	11.0	9.7	9.1	9.5	9.1	7.7	7.9
Y*	—	—	—	—	—	—	—	—	—
Zr	10.3	11.4	18.4	21.2	14.1	17.3	15.1	13.4	14.5
Zr*	—	—	—	—	—	—	—	—	—
Ba	19	31	9	17	47	62	36	30	38
Sum	93.16	96.17	94.77	97.87	98.20	98.96	98.78	95.41	95.40
LOI	7.2	—	—	—	—	—	—	—	—

Sample #	MS93 -15	MS93 -16	MS93- 17A(A)	MS93- 17A(B)	MS93- 17B	MS93- 18(A)	MS93- 18(B)	MS93- LT(ag)	MS91 -01
SiO_2	44.09	43.07	43.16	43.08	43.98	44.40	42.65	42.08	43.75
TiO_2	0.328	0.285	0.301	0.300	0.315	0.276	0.331	0.269	0.312
Al_2O_3	7.17	6.21	6.56	6.51	6.87	6.10	7.12	5.76	6.72
Fe_2O_3T	11.53	10.51	10.82	10.84	10.97	9.64	10.85	10.90	10.59
MnO	0.169	0.163	0.165	0.162	0.165	0.136	0.158	0.161	0.159
MgO	25.30	28.29	26.73	27.12	26.28	26.11	24.50	29.51	26.72
CaO	6.82	6.00	6.32	6.20	6.54	6.94	7.64	4.57	6.28
Na_2O	0.77	0.63	0.67	0.69	0.71	0.28	0.35	0.31	0.55
K_2O	0.143	0.085	0.100	0.106	0.152	0.023	0.041	0.033	0.113
P_2O_5	0.0194	0.182	0.0177	0.0181	0.0190	0.0178	0.0196	0.0133	0.0178
Cl*	327	326	365	—	449	—	190	—	—
S*	341	292	370	—	363	—	365	—	—
V	145	124	126	129	140	118	150	120	138
Cr	2460	2187	2308	2304	2352	2322	2497	2467	2431
Co	97	97	104	98	102	109	104	98	97
Ni	1209	1493	1404	1361	1399	1281	1380	1501	1329
Zn	66	59	62	61	65	54	72	52	70
Rb	3.5	6.0	4.5	3.4	5.3	1.6	2.9	1.9	2.9
Rb*	—	—	—	—	—	—	3.2	—	—
Sr	30.0	29.9	28.6	29.4	35.0	8.3	6.7	7.9	22.0
Sr*	—	—	—	—	—	—	6.7	—	—
Y	8.5	6.7	8.0	7.3	8.0	7.3	8.3	7.8	8.4
Y*	—	—	—	—	—	—	8.8	—	—
Zr	15.3	9.2	12.6	14.7	13.4	11.8	15.3	12.8	15.1
Zr*	—	—	—	—	—	—	14.1	—	—
Ba	41	40	41	36	27	8	10	21	12
Sum	96.74	95.69	95.26	95.43	96.42	94.34	94.25	94.04	95.61
LOI	—	—	—	—	—	5.6	—	6.7	—

Sample #	MS91 -02	MS91 -03	MS91 -04	MS91 -05	MS91 -06	MS91 -09	MS91 -10	MS91 -11	MS91 -12
SiO_2	41.9	42.22	43.34	42.29	43.06	44.27	43.95	44.44	42.33
TiO_2	0.245	0.248	0.291	0.264	0.281	0.325	0.325	0.335	0.260
Al_2O_3	5.28	5.38	6.29	5.62	6.05	7.05	6.98	7.24	5.55
Fe_2O_3T	10.48	10.86	10.93	11.00	10.88	11.51	11.43	11.60	10.19
MnO	0.160	0.151	0.156	0.152	0.160	0.174	0.173	0.177	0.143
MgO	29.88	30.46	27.71	29.57	28.28	26.06	25.98	25.48	29.92
CaO	4.56	4.85	5.86	4.87	5.27	6.69	6.69	7.11	4.76
Na_2O	0.46	0.56	0.58	0.51	0.58	0.85	0.78	0.95	0.51
K_2O	0.063	0.067	0.110	0.074	0.087	0.110	0.107	0.117	0.068
P_2O_5	0.0146	0.0153	0.0182	0.0155	0.0177	0.0184	0.0194	0.0195	0.0160
Cl*	—	—	—	—	—	—	—	—	—
S*	—	—	—	—	—	—	—	—	—
V	110	115	123	112	119	141	138	147	114
Cr	2131	2102	2314	2174	2280	2425	2431	2471	2340
Co	101	99	100	101	102	106	106	103	97
Ni	1719	1642	1415	1561	1492	1265	1269	1225	1608
Zn	62	61	63	61	62	69	69	71	55
Rb	0.3	1.3	5.7	4.8	4.1	3.8	3.3	4.2	0.2
Rb*	—	—	—	—	—	—	—	—	2.1
Sr	22.5	27.7	20.2	18.4	20.4	32.6	31.8	43.4	16.3
Sr*	—	—	—	—	—	—	—	—	16.2
Y	7.2	6.7	7.5	6.2	7.1	8.4	7.4	8.5	7.3
Y*	—	—	—	—	—	—	—	—	6.9
Zr	14.3	12.4	9.6	9.2	11.4	13.8	14.6	13.2	14.0
Zr*	—	—	—	—	—	—	—	—	11.0
Ba	28	31	26	26	36	31	40	31	26
Sum	93.47	95.24	95.68	94.77	95.08	94.47	96.84	97.88	94.34
LOI	—	—	—	—	—	—	3.4	2.3	—

Sample #	MS91-13	MS91-14	MS91-15	ms-08(ag)	ms-15A(ag)	ms-15B(ag)	ms-16(ag)	ms-20(ag)	ms-23(ag)
SiO_2	40.59	42.00	41.21	41.63	43.82	43.00	42.89	43.61	43.44
TiO_2	0.190	0.216	0.200	0.228	0.355	0.313	0.357	0.326	0.344
Al_2O_3	4.04	4.63	4.30	4.88	7.60	6.69	7.66	6.99	7.40
Fe_2O_3T	9.29	9.64	9.52	10.06	11.52	10.97	11.69	11.60	11.64
MnO	0.100	0.144	0.136	0.148	0.182	0.190	0.197	0.181	0.168
MgO	34.00	33.23	34.07	32.15	23.36	25.74	23.21	25.59	23.99
CaO	2.83	4.07	3.42	4.49	7.77	6.65	8.02	6.59	7.13
Na_2O	0.32	0.41	0.34	0.37	0.65	0.57	0.41	0.51	0.49
K_2O	0.046	0.081	0.063	0.077	0.140	0.089	0.070	0.205	0.094
P_2O_5	0.0145	0.0135	0.0131	0.0132	0.0204	0.0187	0.0204	0.0182	0.0197
Cl*	—	—	—	—	—	—	—	—	—
S*	—	—	—	—	—	—	—	—	—
V	83	96	88	93	154	138	150	150	151
Cr	1870	1958	1904	1984	2527	2359	2529	2418	2484
Co	101	102	103	96	90	91	89	95	91
Ni	1963	1875	1946	1800	1095	1391	1051	1269	1145
Zn	36	53	51	54	89	91	97	75	73
Rb	1.0	1.4	1.9	5.7	2.7	2.0	4.2	2.1	4.1
Rb*	1.7	—	—	—	—	—	—	—	—
Sr	10.1	10.8	9.5	16.8	41.7	38.6	18.9	22.7	25.9
Sr*	10.2	—	—	—	—	—	—	—	—
Y	5.4	5.6	5.9	5.5	8.9	8.5	8.7	8.9	9.2
Y*	5.2	—	—	—	—	—	—	—	—
Zr	8.9	10.3	9.2	6.1	17.7	15.0	15.6	18.0	16.6
Zr*	8.1	—	—	—	—	—	—	—	—
Ba	17	13	27	34	35	36	26	22	32
Sum	92.00	95.00	93.83	94.46	95.83	94.65	94.92	96.05	95.12
LOI	—	—	—	5.7	4.5	5.5	5.4	4.2	5.2

Sample #	ms-44(ag)	ms-60(ag)	ms-69(ag)	AX-10	AX-11(A)	AX-11(B)	AX-13	AX96-01	PONT-01
SiO_2	43.17	42.97	43.02	43.06	41.67	43.44	43.17	41.97	42.68
TiO_2	0.276	0.305	0.340	0.278	0.297	0.304	0.300	0.276	0.291
Al_2O_3	5.99	6.55	7.30	6.01	6.33	6.66	6.19	5.70	6.45
Fe_2O_3T	10.93	11.44	10.03	10.60	10.74	10.93	10.19	10.17	10.51
MnO	0.165	0.159	0.169	0.165	0.140	0.142	0.168	0.151	0.154
MgO	29.37	26.52	24.55	28.57	27.89	29.47	27.51	28.53	27.42
CaO	5.56	5.75	7.27	5.59	3.93	4.01	6.58	5.29	5.44
Na_2O	0.47	0.40	0.28	0.35	0.05	0.06	0.31	0.23	0.26
K_2O	0.114	0.058	0.235	0.077	0.036	0.038	0.056	0.058	0.012
P_2O_5	0.0157	0.0170	0.0198	0.0161	0.0155	0.0173	0.0183	0.0178	0.0014
Cl*	—	—	—	—	—	—	—	—	—
S*	—	—	—	—	—	—	—	—	—
V	123	134	140	122	128	133	119	111	108
Cr	2177	2391	2533	2371	2531	2581	2335	2287	2273
Co	97	94	85	102	102	99	95	94	104
Ni	1548	1336	960	1523	1433	1454	1485	1554	1599
Zn	58	62	45	62	60	61	55	59	63
Rb	2.9	0.6	13.7	6.7	4.7	4.8	4.0	2.5	1.1
Rb*	—	—	—	—	—	—	—	—	—
Sr	17.7	22.9	22.4	23.3	12.1	12.4	14.8	19.0	47.1
Sr*	—	—	—	—	—	—	—	—	—
Y	7.3	6.0	8.5	6.8	6.8	7.2	7.9	7.6	5.2
Y*	—	—	—	—	—	—	—	—	—
Zr	12.1	15.9	12.4	11.7	13.9	14.0	17.4	16.3	15.4
Zr*	—	—	—	—	—	—	—	—	—
Ba	22	20	33	38	22	19	19	25	21
Sum	96.47	94.57	93.60	95.15	91.54	95.51	94.92	92.96	93.65
LOI	3.9	5.8	7.0		9.0			7.7	7.9

Appendix 7. Sample locations

Sample	location	texture	sample	location	texture
MS93-00	Pyke H. area A	massive sill(?)	MS91-01	flow B (0.30 m)	A3
MS93-01	flow C (0.07 m)[1]	B4	MS91-02	flow B (0.25 m)	B1
MS93-02	flow C (0.23 m)	B3	MS91-03	flow B (0.25 m)	B1
MS93-03	flow C (0.45 m)	B2	MS91-04	flow B (0.45 m)	A3
MS93-04	flow C (0.70 m)	B2	MS91-05	flow B (0.30 m)	B1
MS93-05	flow C (1.00 m)	B2	MS91-06	flow B (0.25 m)	B1
MS93-06	flow C (1.60 m)	B2	MS91-09	flow B (0.20 m)	B1
MS93-07	flow C (1.86 m)	B2	MS91-10	flow B (0.20 m)	B1
MS93-08	flow C (2.15 m)	B2	MS91-11	flow B (0.50 m)	A3
MS93-09	flow C (2.40 m)	B2	MS91-12	flow B (0.25 m)	B2
MS93-10	flow C (2.92 m)	A3	MS91-13	flow B (0.20 m)	B2
MS93-11	flow C (2.58 m)	B1	MS91-14	flow A (0.48 m)	B2
MS93-12	flow C (3.37 m)	A3	MS91-15	flow A (0.40 m)	B2
MS93-13	flow C (3.66 m)	A3	ms08	flow A (0.32 m)	B2
MS93-14	flow C (3.96 m)	A3	ms15A	flow A (0.72 m)	A3
MS93-15	flow C (4.26 m)	A3	ms15B	flow A (0.68 m)	B1
MS93-16	flow C (4.55 m)	A3	ms16	flow A (0.84 m)	A3
MS93-17A	flow C (4.97 m)	A2	ms20	flow A (1.38 m)	A1
MS93-17B	flow C (5.17 m)	A2	ms23	flow A (0.13 m)	A2
MS93-18	flow C (5.39 m)	flowtop bx	ms44	flow A (0.12 m)	B3
MS93-LT	Pyke H. area B	lava tube	ms60	flow A (0.35 m)	B1
AX-11	Alexo	flowtop bx	ms69	flow B (0.02 m)	B4
AX-10	Alexo	A2			
AX-13	Alexo	A3			
AX-96-01	Alexo	coarse A2			
PONT-1	L. Opasatica	polyhed. flow			

[1] (height above base of flow)

Appendix 8. Interzonal angles between olivine and Cr-spinel

The angles in Table **A8.1** were calculated by assuming parallelism of three orthogonal crystallographic zone axes in olivine and Cr-spinel (see Section **4.2.3** for observations and theoretical considerations that justify this assumption). These zone axes are $[100]_{oliv} \parallel [1\bar{1}\bar{1}]_{spin}$, $[010]_{oliv} \parallel [211]_{spin}$, and $[010]_{oliv} \parallel [11\bar{1}]_{spin}$. The interzonal angles were calculated from the cosine products of the zonal vectors in reciprocal space. Note that the zone axis [*hkl*] is generally perpendicular to the plane (*hkl*) only in the cubic system; fortunately the zone axes [100], [010], and [001] are perpendicular to the planes (100), (010), and (001) in olivine (orthorhombic system) and it was not necessary to deal with more complex zones or planes.

Table A8.1 Full table of calculated angles between axes consistent with measured angles between Cr-spinel and olivine crystallographic axes

Cr-spinel crystal axis	axis ∧ $[100]_{ol}$	axis ∧ $[010]_{ol}$	axis ∧ $[001]_{ol}$	Cr-spinel crystal axis	axis ∧ $[100]_{ol}$	axis ∧ $[010]_{ol}$	axis ∧ $[001]_{ol}$
[100]	54.74°	35.26°	90.00°	[112]	118.13°	33.56°	106.78°
[010]	125.26	65.91	45.00	$[\bar{1}12]$	160.53	80.41	106.78
[001]	125.26	65.91	135.00	$[1\bar{1}2]$	90.00	60.00	150.00
				$[11\bar{2}]$	61.87	80.41	30.00
[111]	109.47	19.47	90.00	[121]	118.13	33.56	73.22
$[\bar{1}11]$	**180.00 †**	**90.00**	**90.00**	$[\bar{1}21]$	160.53	80.41	73.22
$[1\bar{1}1]$	70.53	61.87	144.74	$[1\bar{2}1]$	61.87	80.41	150.00
$[11\bar{1}]$	70.53	61.87	35.26	$[12\bar{1}]$	90.00	60.00	30.00
				[211]	**90.00**	**0.00 †**	**90.00**
[110]	90.00	30.00	60.00	$[\bar{2}11]$	160.53	109.47	90.00
$[1\bar{1}0]$	35.26	73.22	120.00	$[2\bar{1}1]$	61.87	48.19	125.26
[101]	90.00	30.00	120.00	$[21\bar{1}]$	61.87	48.19	54.74
$[10\bar{1}]$	35.26	73.22	60.00				
[011]	144.74	54.74	90.00	[221]	101.10	17.72	76.37
$[01\bar{1}]$	**90.00**	**90.00**	**0.00 †**	$[\bar{2}21]$	164.21	97.82	76.37
				$[2\bar{2}1]$	54.74	65.91	135.00
[210]	75.04	24.09	71.57	$[22\bar{1}]$	78.90	47.12	45.00
$[2\bar{1}0]$	39.23	56.79	108.43	[212]	101.10	17.72	103.63
[201]	75.04	24.09	108.43	$[\bar{2}12]$	164.21	97.82	103.63
$[20\bar{1}]$	39.23	56.79	71.57	$[2\bar{1}2]$	78.90	47.12	135.00
[120]	104.96	43.09	50.77	$[21\bar{2}]$	54.74	65.91	45.00
$[1\bar{2}0]$	39.23	90.00	129.23	[122]	125.26	35.26	90.00
[102]	104.96	43.09	129.23	$[\bar{1}22]$	164.21	74.21	90.00
$[10\bar{2}]$	39.23	90.00	50.77	$[1\bar{2}2]$	78.90	74.21	160.53
[012]	140.77	56.79	108.43	$[12\bar{2}]$	78.90	74.21	19.47
$[01\bar{2}]$	75.04	100.52	18.43				
[021]	140.77	56.79	71.57				
$[02\bar{1}]$	104.96	79.48	18.43				

†Coincident olivine and spinel crystallographic axes.

References

Journals referenced only a few times are spelled out in full or with obvious abbreviations. Commonly used or less-obvious abbreviations are as follows:

Am. Min.: American Mineralogist.
Can. Min.: Canadian Mineralogist.
CJES: Canadian Journal of Earth Sciences.
CMP: Contributions to Mineralogy and Petrology.
Econ. Geol.: Economic Geology and the Bulletin of the Society of Economic Geologists.
EPSL: Earth and Planetary Science Letters.
GCA: Geochimica and Cosmochimica Acta.
GRL: Geophysical Research Letters.
GSA Bull.: Bulletin of the Geological Society of America.
GSC: Geological Survey of Canada.
JGR: Journal of Geophysical Research.
J. Pet.: Journal of Petrology.
Min. Mag.: Mineralogical Magazine.
ODM: Ontario Department of Mines, predecessor of the OGS.
OGS: Ontario Geological Survey, successor to the ODM.
Phys. Chem. Min.: Physics and Chemistry of Minerals.
Rev. in Min.: Reviews in Mineralogy (published by Mineralogical Society of America).

Abraham, E.M. (1953) Geology of Sothman Township. ODM Ann. Rep. **52**(6), 1-36.

Agee, C.B., and Walker, D. (1988) Static compression and olivine flotation in ultrabasic silicate liquid. JGR **93**, 3437-3449.

_____ and _____ (1990) Aluminum partitioning between olivine and ultrabasic silicate liquid to 6 GPa. CMP **105**, 243-254.

Ágústsdóttir, A.M., and Brantley, S.L. (1994) Volatile fluxes integrated over 4 decades at Grimsvotn volcano, Iceland. JGR **99**, 9595-9522.

Akella, J., Williams, R.J., and Mullins, O. (1976) Solubility of Cr, Ti, and Al in co-existing olivine, spinel, and liquid at 1 atm. Proc. Seventh Lun. Sci. Conf., Vol. 2, 1179-1194.

Arai, S. (1978) Chromian spinel lamellae in olivine from the Iwanai-dake peridotite mass, Hokkaido, Japan. EPSL **39**, 267-273.

Arndt, N.T. (1975) Ultramafic rocks of Munro Township and their tectonic setting. Ph.D. thesis, U. of Toronto.

_____ (1976) Melting relations of ultramafic lavas (komatiites) at 1 atm and high pressure. Carnegie Institut. Washington Yearbook **75**, 555-562.

_____ (1977) Partitioning of nickel between olivine and ultrabasic and basic komatiite liquids. Carnegie Institut. Washington Yearbook **76**, 553-557.

_____ (1982) Proterozoic spinifex-textured basalts of Gilmour Island, Hudson Bay. GSC Curr. Res. **83-1A**, 137-142.

_____ (1986a) Differentiation of komatiite flows. J. Pet. **27**, 279-301.

_____ (1986b) Komatiites: A dirty window to the Archean mantle. Terra cognita **6**, 59-66.

_____ (1994) Archean komatiites. In *Archean Crustal Evolution*, K.C. Condie, Ed. Elsevier, Amsterdam.

Arndt, N.T., and Nisbet, E.G. (1982) What is a komatiite? In *Komatiites*, N.T. Arndt and E.G. Nisbet, Eds. Allen and Unwin, London.

_____ and Jenner, G.A. (1986) Crustally-contaminated komatiites and basalts from Kambalda, Western Australia. Chem. Geol. **56**, 229-255.

_____, Naldrett A.J., and Pyke, D.R. (1977) Komatiitic and iron-rich tholeiitic lavas of Munro Township, northeast Ontario. J. Pet. **18**, 319-369.

_____, Francis, D., and Hynes, A.J. (1979) The field characteristics and petrology of Archean and Proterozoic komatiites. Can. Min. **17**, 147-163.

Ashworth, J.R. (1979) Two kinds of exsolution in chondritic olivine. Min. Mag. **43**, 535-538.

Aubele, J.C., Crumpler, L.S., and Elston, W.E. (1988) Vesicle zonation and vertical structure of basalt flows. J. Volc. Geoth. Res. **35**, 349-374.

Baker, E.T. (1994) A 6-year time series of hydrothermal plumes over the Cleft segment of the Juan de Fuca Ridge. JGR **99**, 4889-4904.

Baker, M.B. (1917) Alexo nickel mine, Timiskaming district. Ont. Bur. Mines, Ann. Rept. **26**, 258-274.

Baragar, W.R.A. (1984) Pillow formation and layered flows in the Circum-Superior Belt of eastern Hudson Bay. CJES **21**, 781-792.

Barnes, S.-J. (1985) The petrology and geochemistry of komatiite flows from the Abitibi greenstone belt, Canada, and a model for their formation. Lithos **18**, 241-270.

_____ and Often, M. (1990) Ti-rich komatiites from northern Norway. CMP **105**, 42-54.

_____, Gorton, M.P., and Naldrett, A.J. (1983) A comparative study of olivine and clinopyroxene spinifex flows from Alexo, Abitibi greenstone belt, Ontario, Canada. CMP **83**, 293-308.

Barnes, S.J., Hill, R.E.T., and Gole, M.J. (1988) The Perseverance ultramafic complex, Western Australia: The product of a komatiite lava river. J. Pet. **29**, 305-331.

Baronnet, A. (1984) Growth kinetics of the silicates. Fortschritte der Mineralogie **62**, 187-232.

Bavinton, O.A. (1981) The nature of sulfidic metasediments at Kambalda and their broad relationships with associated ultramafic rocks and nickel ores. Econ. Geol. **76**, 1606-1628.

Beaty, D.W., and Taylor, H.P. (1982) The oxygen isotope geochemistry of komatiites: evidence for water-rock interaction. In *Komatiites*, N.T. Arndt and E.G. Nisbet, Eds. Allen and Unwin, London.

Beattie, P. (1994) Systematics and energetics of trace-element partitioning between olivine and silicate melts: Implications for the nature of mineral/melt partitioning. Chem. Geol. **117**, 57-71.

_____, Ford, C., and Russell, D. (1991) Partition coefficients for olivine-melt and orthopyroxene-melt systems. CMP **109**, 212-224.

_____, _____, and _____ (1993a) Erratum: Partition coefficients for olivine-melt and orthopyroxene-melt systems. CMP **114**, 288.

_____, Drake, M., Jones, J., Leeman, W., Longhi, J., McKay, G., Neilsen, R., Palme, H., Shaw, D., Takahashi, E., and Watson, B. (1993b) Terminology for trace-element partitioning. GCA **57**, 1605-1606.

Beck, A.E., Darbha, D.M., and Schoessin, H.H. (1978) Lattice conductivities of single-crystal and polycrystalline materials at mantle pressures and temperatures. Physics of the Earth and Planetary Interiors **17**, 35-53.

Berman, R. (1976) *Thermal Conduction in Solids*. Clarendon Press, Oxford.

Berman, R.G. (1988) Internally-consistent thermodynamic data for minerals in the system Na_2O-K_2O-CaO-MgO-FeO-Fe_2O_3-Al_2O_3-SiO_2-TiO_2-H_2O-CO_2. J. Pet. **29**, 445-522.

Berry, L.G. (1940) Geology of the Langmuir-Sheraton area. ODM Ann. Rep. **49**(4), 1-21.

Bershov, L.V., Gaite, J.-M., Hafner, S.S., and Rager, H. (1983) Electron paramagnetic resonance and ENDOR studies of Cr^{3+}– Al^{3+} pairs in forsterite. Phys. Chem. Min. **9**, 95-101.

Besson, M. (1988) Zonage des olivines dans deux échantillons de komatiites. Comptes Rendus Acad. Sci. Paris **307** (Ser. II), 45-48.

_____ and Vannier, M. (1994) Spinelles chromifères témoins d'un minéral précurseur dans un échantillion de komatiite. Comptes Rendus Acad. Sci. Paris **319** (Ser. II), 443-446.

Best, M.G. (1982) *Igneous and Metamorphic Petrology*. W. H. Freeman, New York.

Bickle, M.J., Nisbet, E.G., and Martin, A. (1994) Archean greenstone belts are not oceanic crust. J. Geol. **102**, 121-137.

Binns, R.A., and Champness, P.E. (1985) Analytical electron microscopy of red-brown olivines in ultramafic rocks from the Yilgarn Block. W.A. CSIRO Research Review, Div. of Mineral. and Geochem., pp. 32-33.

_____, Hallberg, J.A., and Taplin, J.H. (1982) Komatiites in the Yilgarn Block, Western Australia. In *Komatiites*, pp. 117-130, N.T. Arndt and E.G. Nisbet, Eds. Allen and Unwin, London.

Björsson, H., Björnsson, S., and Sigurgeirsson, T. (1982) Penetration of water into hot rock boundaries of magma at Grímsvötn. Nature **295**, 580-581.

Bowen N.L. (1922) The Evolution of the Igneous Rocks. Princeton University Press.

Brandeis, G., and Jaupart, C: (1986) On the interaction between convection and crystallization in cooling magma chambers. EPSL **77**, 345-361.

Brandstatter, F., and Niedermayr, G. (1994) Copper and tenorite inclusions in cuprian elbaite tourmaline from Paráiba, Brazil. Gems and Gemology **30**, 178-183.

Brice, J.C. (1987) *Crystal Growth Processes*. Blackie, Glasgow.

Brown, G.E. (1982) Olivines and silicate spinels. In *Orthosilicates*, Second Edition, P.H. Ribbe, Ed. Rev. in Min. **5**, 275-381.

Bruce, E.L. (1926) Geology of McArthur, Bartlett, Douglas and Geikie Townships (Redstone River area), District of Timiskamong. ODM Ann. Rep. **35**(6), 37-56.

Burns, R.G. (1993) *Mineralogical Applications of Crystal Field Theory*, Second Edition. Cambridge University Press.

Byerly, G.R., Lower, D.M., and Walsh, M.M. (1986) Stromatolites from the 3300–3500-Myr Swaziland Supergroup, Barberton Mountain Land, South Africa. Nature **319**, 489-491.

Capobianco, C.J., and Drake, M.J. (1990) Partitioning of ruthenium, rhodium, and palladium between spinel and silicate melt and implications for platinum group element fractionation trends. GCA **54**, 869-874.

_____ and Amelin, A.A. (1994) Metal-silicate partitioning of nickel and cobalt: The influence of temperature and oxygen fugacity. GCA **58**, 124-140.

Cas, R.A.F., and Wright, J.V. (1987) *Volcanic Successions: Modern and Ancient*. Allen and Unwin, London.

Cattell, A., Krogh, T.E., and Arndt, N.T. (1984) Conflicting Sm-Nd whole rock and U-Pb zircon ages for Archean lavas from Newton Township, Abitibi belt, Ontario. EPSL **70**, 280-290.

Chadwick, W.W., and Embley, R.W. (1994) Lava flows from a mid-1980s submarine eruption on the Cleft segment, Juan de Fuca Ridge. JGR **99**, 4761-4776.

Chai, M., Brown, J.M., and Slutsky, L.J. (1996) Thermal diffusivity of mantle minerals. Phys. Chem. Min., in press.

Chakraborty, S., and Meissner, E. (1995) Fe-Mg interdiffusion in olivine: New experimental results. Eos **76**(17), Spring Meeting Suppl., S299.

Champness, P.E. (1970) Nucleation and growth of iron oxides in olivines. Min. Mag. **37**, 790-800.

Clague, D.A., Moore, J.G., Dixon, J.E., and Friesen, W.B. (1995) Petrology of submarine lavas from Kilauea's Puna Ridge, Hawaii. J. Pet. **36**, 299-349.

Cockayne, B., Chesswas, M., and Gasson, D.B. (1969) Facetting and optical perfection in Czochralski grown garnets and ruby. J. Materials Sci. **4**, 450-456.

Colson, R.O., McKay, G.A., and Taylor, L.A. (1989) Charge balancing of trivalent trace elements in olivine and low-Ca pyroxene: A test using experimental partitioning data. GCA **53**, 643-648.

Compston, W., Williams, I.S., Campbell, I.H., and Gresham, J.J (1986) Zircon xenocrysts from the Kambalda volcanics: Age constraints and direct evidence for older continental crust below the Kambalda-Norseman greenstones. EPSL **76**, 299-311.

Condon, E.U. (1968) Radiative transport in hot glass. J. Quantitative Spectroscopy and Radiation Transfer **8**, 369-385.

Cowden, A. (1988) Emplacement of komatiite lava flows and associated nickel sulfides at Kambalda, Western Australia. Econ. Geol. **83**, 436-442.

Cox, K.G., Smith, M.R., and Beswetherick, S. (1987) Textural studies of garnet lherzolites: evidence of exsolution origin from high temperature harzburgites. In *Mantle Xenoliths*, P.H. Nixon, Ed. John Wiley and Sons, Chichester.

Crockett, J.H., and MacRae, W.E. (1986) Platinum-group element distribution in komatiitic and tholeiitic volcanic rocks from Munro Township, Ontario. Econ. Geol. **81**, 1242-1251.

Davaille, A., and Jaupart, C. (1993a) Thermal convection in lava lakes. GRL **20**, 1827-1830.

_____ and _____ (1993b) Transient high-Rayleigh-number convection with large viscosity variations. J. Fluid Mech. **253**, 141-166.

Deer, W.A., Howie, R.A., and Zussman, J. (1978) *Rock-Forming Minerals, Vol. 2A: Single-Chain Silicates*, Second Edition. Longman, London.

_____, _____, and _____ (1982) *Rock-Forming Minerals, Vol. 1A: Orthosilicates*, Second Edition. Longman, London.

Dingwell, D.B., O'Neil, H.S.C., Ertel, W., and Spettel, B. (1994) The solubility and oxidation state of nickel in silicate melt at low oxygen fugacities: Results using a mechanically assisted equilibration technique. GCA **58**, 1967-1974.

Dixon, J.E., Clague, D.A., and Stolper, E.M. (1991) Degassing history of water, sulfur, and carbon in submarine lavas from Kilauea volcano, Hawaii. J. Geol. **99**, 371-394.

Dollase, W.A., Seifert, F., and O'Neil, H.S.C. (1994) Structure of Cr_2SiO_4 and possible metal-metal interactions in crystal and melt. Phys. Chem. Min. **21**, 104-109.

Donaldson, C.H. (1974) Olivine crystal types in harrisitic rocks of the Rhum pluton and Archean spinifex rocks. GSA Bull. **85**, 1721-1726.

_____ (1976) An experimental investigation of olivine morphology. CMP **57**, 187-213.

_____ (1977) Laboratory duplication of comb layering in the Rhum pluton. Min. Mag. **41**, 323-336.

_____ (1979) An experimental investigation of the delay in nucleation of olivine in mafic magmas. CMP **69**, 21-32.

_____ (1982) Spinifex-textured komatiites: A review of textures, compositions and layering. In *Komatiites*, N.T. Arndt and E.G. Nisbet, Eds. Allen and Unwin, London.

_____ (1993) Convective fractionation during magnetite and hematite dissolution in silicate melts. Min. Mag. **57**, 469-488.

_____ and Henderson, C.M.B. (1988) A new interpretation of round embayments in quartz crystals. Min. Mag. **52**, 27-33.

Drever, H.I., and Johnston, R. (1957) Crystal growth of forsteritic olivine in magmas and melts. Trans. R. Soc. (Edin.) **63**, 289-315.

Dunning, W.J., Fox, P.G., and Parker, D.W. (1967) Observations on the epitaxial growth of ammonium iodide on mica crystals. In *Crystal Growth: Proceedings of an Internation Conference on Crystal Growth, Boston 20-24 June 1966*, H. Steffan Peiser, Ed. Pergamon, New York.

Eaglesham, D.J., and Hull, R. (1995) Island formation in Ge/Si epitaxy. Materials Science and Engineering B **30**, 197-200.

Echeverria, L.M., and Aitken, B.G. (1986) Pyroclastic rocks: another manifestation of ultramafic volcanism on Gorgona Island, Colombia. CMP **92**, 428-436.

Embley, R.W., and Chadwick, W.W. (1994) Volcanic and hydrothermal processes associated with a recent phase of seafloor spreading at the northern Cleft segment, Juan de Fuca Ridge. JGR **99**, 4741-4760.

Ernst, R.E., Fowler, A.D., and Pearce, T.H. (1988) Modelling of igneous fractionation and other processes using Pearce diagrams. CMP **100**, 12-18.

Fleet, M.E. (1975a) The growth habits of olivine — a structural interpretation. Can. Min. **13**, 293-297.

_____ (1975b) Growth habits of clinopyroxene. Can. Min. **13**, 336-341.

_____ and MacRae, N.D. (1975) A spinifex rock from Munro Township, Ontario. CJES **12**, 928-939.

Fujisawa, H., Fujii, N., Mizutani, H., Kanamori, H., and Akimoto, S. (1968) Thermal diffusivity of Mg_2SiO_4, Fe_2SiO_4, and NaCl at high pressures and temperatures. JGR **73**, 4727-4733.

Gable, C.W., and Shankland, T.J. (1984) Radiative heat transfer in molten and glassy obsidian. JGR **89**, 7107-7110.

Galoisy, L., and Calas, G. (1993) Structural environment of nickel in silicate glass melt systems 2. Geochemical implications. GCA **57**, 3627-3633.

Gelinas, L., Lajoie, J., and Brooks, C. (1977) The origin and significance of Archean ultramafic volcaniclastics from Spinifex Ridge, Lamotte Township, Quebec. GAC Spec. Pub. **16**, 8-20.

Ginibre, C. (1995) Etude expérimentale des textures des komatiites de Gorgona, Colombie. Unpublished thesis (degré d'études avancées), Université de Rennes.

Ginster, U., Mottl, M.J., and Von Herzen, R.P. (1994) Heat flux from black smokers on the Endeavor and Cleft segments, Juan de Fuca Ridge. JGR **99**, 4937-4950.

Glicksman, M.E., Coriell, S.R., and McFadden, G.B. (1986) Interaction of flows with the crystal-melt interface. Ann. Rev. Fluid Mech. **18**, 307-335.

Govindaraju, K. (1994) 1994 compilation of working values and sample description for 383 geostandards. Geostandards Newsletter **18**, 1-158.

_____, Potts, P.J., Webb, P.C., and Watson, J.S. (1994) 1994 Report on Whin Sill Dolerite WS-E from England and Pitscurrie Microgabbro PM-S from Scotland: Assessment by one hundred and four international laboratories. Geostandards Newsletter **18**, 211-300.

Green, D.H., Nicholls, I.A., Viljoen, M., and Viljoen, R. (1975) Experimental demonstration of the existence of peridotitic liquids in earliest Archean magmatism. Geology **3**, 11-14.

Greenwood, N.N (1968) *Ionic Crystals, Lattice Defects and Nonstoichiometry.* Butterworth, London.

Griffiths, R.W., and Fink, J.H. (1992) Solidification and morphology of submarine lavas: A dependence on flow rate. JGR **97**, 19 729-19 737.

Groves, D.I., Korkiakoski, E.A., McNaughton, N.J., Lesher, C.M., and Cowden, A. (1986) Thermal erosion by komatiites at Kambalda, Western Australia and the genesis of nickel ores. Nature **319**, 136-139.

Gryvnak, D.A., and Burch, D.E. (1965) Optical and infrared properties of Al_2O_3 at elevated temperatures. J. Optical Soc. Am. **55**, 625-629.

Haggerty, S.E. (1991) Oxide minerals—A mini-atlas. In *Oxide Minerals: Petrologic and Magnetic Significance*, D.H. Lindsay, Ed. Rev. in Min. **25**, 129-219.

Hardee, H.C., Dunn, J.C., and Hills, R.G. (1981) Probing the melt zone of Kilauea Iki lava lake, Kilauea volcano, Hawaii. GRL **8**, 1211-1214.

Haymon, R.M., and 14 others (1993) Volcanic eruption of the mid-ocean ridge along the East Pacific Rise crest at 9°45-52' N: Direct submersible observations of seafloor phenomena associated with an eruption event in April, 1991. EPSL **119**, 85-101.

Herzberg, C.T. (1992) Depth and degree of melting of komatiites. JGR **97**, 4521-4540.

_____ (1993) Lithospheric peridotites of the Kaapvaal craton. EPSL **120**, 13-29.

_____ and Zhang, J. (1995) Melting experiments on peridotite to 22.5 GPa: Phase chemistry. Eos **76**(17), Spring Meet. Suppl., S297.

Hiemstra, S.A. (1979) The role of collectors in the formation of platinum deposits in the Bushveld Complex. Can. Min. **17**, 469-482.

Hill, A. (1990) Entropy production as the selection rule between different growth morphologies. Nature **348**, 426-228.

Hill, R.E.T., Barnes, S.J., Gole, M.J., and Dowling, S.E. (1995) The volcanology of komatiites as deduced from field relationships in the Norseman-Wiluna greenstone belt, Western Australia. Lithos **34**, 159-188.

Hirsch, L.M., and Shankland, T.J. (1993) Quantitative olivine-defect chemical model: insights on electrical conduction, diffusion, and the role of Fe content. Geophysical J. International **114**, 21-35.

Hirschmann, M.M., and Ghiorso, M.S. (1994) Activities of nickel, cobalt, and manganese silicates in magmatic liquids and applications to olivine-liquid and silicate-metal partitioning. GCA **58**, 4109-4126.

Holloway, H. (1994) Curvature in boron-doped silicon and other compositionally graded single crystals. J. Appl. Phys. **75**, 2297-2299.

Holman, J.P. (1990) *Heat Transfer*, Seventh Edition. McGraw-Hill, New York.

Hon, K., Kauahikaua, J., Denlinger, R., and Mackay, K. (1994) Emplacement and inflation of pahoehoe sheet flows: Observations and measurements of active lava flows on Kilauea Volcano, Hawaii. GSA Bull. **106**, 351-370.

Huebner, J.S., Lipin, B.R., and Wiggins, L.B. (1976) Partitioning of chromium between silicate crystals and melt. Proc. Seventh Lun. Sci. Conf., Vol. 2, 1195-1220.

Huppert, H.E., and Sparks, R.S.J. (1985a) Komatiites I: Eruption and flow. J. Pet. **26**, 694-725.

_____ and _____ (1985b) Cooling and contamination of mafic and ultramafic magmas during ascent through continental crust. EPSL **74**, 371-386.

_____ and _____ (1989) Chilled margins in igneous rocks. EPSL **92**, 397-405.

_____, _____, Turner, J.S., and Arndt, N.T. (1984) Emplacement and cooling of komatiite lavas. Nature **309**, 19-22.

Hynes, A., and Francis D. (1982) Komatiitic basalts of the Cape Smith foldbelt, New Quebec, Canada. In *Komatiites*, N.T. Arndt and E.G. Nisbet, Eds. Allen and Unwin, London.

Ingebritsen, S.E., and Hayba, D.O. (1994) Fluid flow and heat transport near the critical point of H_2O. GRL **21**, 2199-2202

Irvine, T.N. (1970) Heat transfer during solidification of layered intrusions. I. Sheets and sills. CJES 7, 1031-1061.

Isaak, D.G., Anderson, O.L., and Goto, T. (1989) Elasticity of single-crystal forsterite measured to 1700 K. JGR 94, 5895-5906.

Ito, J. (1977) Crystal synthesis of a new olivine. Am. Min. 62, 365-361.

Jackson, S.J., and Fyon, J.A. (1991) The western Abitibi subprovince in Ontario. In *Geology of Ontario*, P.C. Thurston, H.R. Williams, R.H. Sutcliffe, and G.M. Stott, Eds. OGS Spec. Vol. 4(1), 405-482.

Jackson, W.E., Mustre de Leon, J., Brown, G. E., Waychunas, G.A., Conradson, S.D., and Combes, J.-M. (1993) High-temperature XAS study of Fe_2SiO_4 liquid: Reduced coordination of ferrous iron. Science 262, 229-233.

Jaeger, J.C. (1968) Cooling and solidification of igneous rocks. In *Basalts: The Poldervaart Treastise on Rocks of Basaltic Composition*, Vol. 2, H.H. Hess and A. Poldervaart, Eds. Interscience Publisher (John Wiley and Sons).

Janz, G.J. (1991) High temperature calibration quality data: Molten salts and metals. Materials Sci. Forum 73–75, 707-714.

Jensen, L.S., and Pyke, D.R. (1982) Komatiites in the Ontario portion of the Abitibi belt. In *Komatiites*, N.T. Arndt and E.G. Nisbet, Eds. Allen and Unwin, London.

_____ and Langford, F.F. (1985) Geology and petrogenesis of the Archean Abitibi belt in the Kirkland Lake area, Ontario. OGS Misc. Paper 123.

Jochum, K.P., Arndt, N.T., and Hofmann, A.W. (1991) Nb-Th-La in komatiites and basalts: constraints on komatiite petrogenesis and mantle evolution. EPSL 107, 272-289.

Johnson, M.E., Anderson, A.T., and Rutherford, M.J. (1994) Pre-eruptive volatile contents of magmas. In *Volatiles in Magmas*, M.R. Carroll and J.R. Holloway, Eds. Rev. in Min. 30, 281-330.

Johnston, C.J., Gunter, M.E., and Knowles, C.R. (1991) Sunstone labradorite from the Ponderosa mine, Oregon. Gems and Gemology 27, 220-233.

Jolly, W.T. (1982) Progressive metamorphism of komatiites and related Archean lavas of the Abitibi area, Canada. In *Komatiites*, N.T. Arndt and E.G. Nisbet, Eds. Allen and Unwin, London.

Kanamori, H., Fujii, N., and Mizitami, H. (1968) Thermal diffusivity of rock-forming minerals from 400° to 1100 °K. JGR 73, 595-605.

Katsura, T. (1995) Thermal diffusivity of olivine under upper mantle conditions. Geophysical J. International 122, 63-69.

Kern, R. (1989) Fundamentals of epitaxy. In *Crystal Growth in Science and Technology*, H. Arend and J. Hulliger, Eds. Plenum Press, New York.

Khisina, N.R., Khramov, D.A., Kolosov, M.V., Kleschev, A.A., and Taylor, L.A. (1995) Formation of ferriolivine and meagnesioferrite from Mg–Fe-olivine: Reactions and kinetics of oxidation. Phys. Chem. Min. 22, 241-250.

Khokhlov, V.A., Kodintseva, A.O., and Filatov, E.S. (1993) "Anomalous" thermal conductivity of crystalline alkali halides close to their melting point. Zeitschrift fur Naturforschung A: Physical Sciences 48a, 595-598.

Kinzler, R.J., and Grove, T.L. (1985) Crystallization and differentiation of Archean komatiitic lavas from northeast Ontario: phase equilibrium and kinetic studies. Am. Min. 70, 40-51.

Kirkpatrick, R.J. (1978) Processes of crystallization in pillow basalts, Hole 396B, DSDP Leg 46. Init. Rep. Deep Sea Drilling Prog. 46, 271-282.

_____, Kuo, L.C., and Melchior, J. (1981) Crystal growth in incongruently-melting compositions: programmed cooling experiments with diopside. Am. Min. 66, 223-241.

Kress, V.C., and Carmichael, I.S.E. (1991) The compressibility of silicate liquids containing Fe_2O_3 and the effect of composition, temperature, oxygen fugacity and pressure on their redox states. CMP **108**, 82-92.

Kruszewski, S. (1961) Total heat-transmission coefficients of amber and green glasses in temperatures of melting range. J. Am. Ceramic Soc. **44**, 333-339.

Kusky, T.M., and Kidd, W.S.F. (1992) Remnants of an Archean oceanic plateau, Belingwe greenstone belt, Zimbabwe. Geology **20**, 43-46.

Kusky, T.M., and Winsky, P.A. (1995) Structural relationships along a greenstone/shallow water shelf contact, Belingwe greenstone belt, Zimbabwe. Tectonics **14**, 448-471.

Lajoie, J., and Gélinas, L. (1978) Emplacement of Archean peridotitic komatiites in La Motte Township, Quebec. CJES **15**, 672-677.

Lange, R.L., and Carmichael, I.S.E. (1990) Thermodynamic properties of silicate liquids with emphasis on density, thermal expansion and compressibility. In *Modern Methods of Igneous Petrology: Understanding Magmatic Processes*, J. Nicholls, and J.K. Russell, Eds. Rev. in Min. **24**, 25-64.

Lesher, C.M., and Arndt, N.T. (1995) REE and Nd isotope geochemistry, petrogenesis, and volcanic evolution of contaminated komatiites at Kambalda, Western Australia. Lithos **34**, 127-157.

Li, J.-P., O'Neil, H.S.C., and Seifert, F. (1995) Subsolidus phase relations in the system MgO–SiO_2–Cr–O in equilibrium with metallic Cr, and their significance for the petrochemistry of chromium. J. Pet. **36**, 107-132.

Lister, C.R.B. (1983) The basic physics of water penetration into hot rock. In *Hydrothermal Processes at Seafloor Spreading Centers*, P.A. Rona, K. Boström, L. Laubier, and K.L. Smith, Eds. Plenum Press, New York.

Lofgren, G.E. (1983) Effect of heterogeneous nucleation on basaltic textures: A dynamic crystallization study. J. Pet. **24**, 229-255.

_____, Donaldson, C.H., Williams, R.J., Mullins, O., and Usselman, T.M. (1974) Experimentally reproduced textures and mineral chemistry of Apollo 15 quartz normative basalts. Proc. Fifth Lunar Sci. Conf., Vol. 1, 549-567.

Long, P.E., and Wood, B.J. (1986) Structures, textures, and cooling histories of Columbia River basalt flows. GSA Bull. **97**, 1144-1155.

Lowell, R.P., and Germanovich, L.N. (1994) On the temporal evolution of high-temperature hydrothermal systems at ocean ridge crests. JGR **99**, 565-575.

_____ and _____ (1995) Dike injection and the formation of megaplumes at ocean ridges. Science **267**, 1804-1807.

Mandernack, K.W., and Tebo, B.M. (1993) Manganese scavenging and oxidation at hydrothermal vents and in vent plumes. GCA **57**, 3907-3923.

Marsh, B.D. (1988) Crystal capture, sorting, and retention in convecting lava. GSA Bull. **100**, 1720-1737.

_____ (1989) On convective style and vigor in sheet-like magma chambers. J. Pet. **30**, 479-530.

Martin, B., and Fyfe, W.S. (1970) Some experimental and theoretical observations on the kinetics of hydration reaction with particular reference to serpentinization. Chem. Geol. **6**, 185-202.

Mathez, E.A. (1976) Sulfur solubility and magmatic sulfides in submarine basalt glasses. JGR **81**, 4269-4276.

Maurer, J., Bouissou, P., Perrin, B., and Tabeling, P. (1989) Faceted dendrites in the growth of NH_4Br crystals. Europhysics Letters **8**, 67-72.

McBirney, A.R., and Murase, T. (1984) Rheological properties of magmas. Ann. Rev. Earth Plan. Sci. **12**, 337-357.

McDonough, W.F., and Danyushevsky, L.V. (1995) Water and sulfur contents of melt inclusions from Archean komatiites. Eos **76**(17), Spring Meet. Suppl., S266.

_____ and Ireland, T.R. (1993) Intraplate origin of komatiites inferred from trace elements in glass inclusions. Nature **365**, 432-434.

McNaughton, N.J., Frost, K.M., and Groves, D.I. (1988) Ground melting and ocellar komatiites: a lead isotopic study at Kambalda, Western Australia. Geol. Mag. **125**, 285-295.

MERQ-OGS (1983) Lithostratigraphic map of the Abitibi Subprovince: Ontario Geological Survey/Ministère de l'Énergie et Ressources, Quebec; 1: 500 000; "Map 2484" in Ontario and "DV 83-16" in Quebec.

Miller, G.H., Stolper, E.M., and Ahrens, T.J (1991) The equation of state of a molten komatiite 1. Shock wave compression to 36 GPa. JGR **96**, 11 831-11 848.

Moore, J.G. (1975) Mechanism of formation of pillow lava. American Scientist **63**, 269-277.

Morioka, M., and Nagasawa, H. (1991) Ionic diffusion in olivine. In *Diffusion, Atomic Ordering, and Mass Transport*, J. Ganguly, Ed. Springer Verlag, New York.

Morse, S.A. (1986) Convection in aid of adcumulus growth. J. Pet. **27**, 1183-1214.

Morton, J.P. (1985) Rb-Sr dating of diagenesis and source age of clays in Upper Devonian black shales of Texas. GSA Bull. **96**, 1043-1049.

Mosely, D. (1984) Symplectic exsolution in olivine. Am. Min. **69**, 139-153.

Muir, J.E., and Comba, C.D.A. (1979) The Dundonald deposit: An example of volcanic-type nickel-sulfide mineralization. Can. Min. **17**, 351-359.

Müller, G., Schuster, A.K., and Zippert, Y. (1988) Spinifex textures and texture zoning in fayalite-rich slags of medieval iron-works near Schieder Village, NW-Germany. Neues Jahrbuch für Mineralogie, Monatschefte 1977, pp. 111-120.

Murase, T., and McBirney, A.R. (1973) Properties of some common igneous rocks and their melts at high temperature. GSA Bull. **84**, 3563-3592.

Murck, B.W., and Campbell, I.H. (1988) The effects of temperature, oxygen fugacity and melt composition on the behavior of chromium in basic and ultrabasic melts. GCA **50**, 1871-1887.

Nakamura, A. and Schmalzried, H. (1983) On the nonstoichiometry and point defects of olivine. Phys. Chem. Min. **10**, 27-37.

Naldrett, A.J. (1989) *Magmatic Sulphide Deposits*. Clarendon Press, New York.

_____ and Mason, G.D. (1967) Contrasting Archean ultramafic igneous bodies in Dundonald and Clergue Townships, Ontario. CJES **5**, 111-143.

Natland, J.H. (1980) Crystal morphologies in basalts dredged and drilled from the East Pacific Rise near 9N and the Siqueiros fracture zone. Init. Rep. Deep Sea Drilling Prog. **54**, 605-633.

Nehlig, P. (1994) Fracture and permeability analysis in magma-hydrothermal transition zones in the Samail ophiolite (Oman). JGR **99**, 589-601

Nelson, R.A. (1985) *Geologic Analysis of Naturally Fractured Reservoirs*. Gulf Publishing Co., Houston.

Nesbitt, R.W. (1986) Are komatiitic lavas voracious? Nature **319**, 97-98.

_____, Sun, S.S., and Purvis, A.C. (1979) Komatiites: Geochemistry and genesis. Can. Min. **17**, 165-186.

Nisbet, E.G., and Chinner, G.A. (1981) Controls of the eruption of mafic and ultramafic lavas, Ruth Well Ni-Cu prospect, West Pilbara. Econ. Geol. **76**, 1729-1735.

Nisbet, E.G., Bickle, M.J., and Martin, A. (1977) The mafic and ultramafic lavas of the Belingwe greenstone belt, Rhodesia. J. Pet. **18**, 521-566.

_____, _____, _____, Orpen, J.L., and Wilson, J.F. (1982) Komatiites in Zimbabwe. In *Komatiites*, pp. 97-104, N.T. Arndt and E.G. Nisbet, Eds. Allen and Unwin, London.

_____ and ten others. (1987) Uniquely fresh 2.7 Ga komatiites from the Belingwe greenstone belt, Zimbabwe. Geology **15**, 1147-1150.

_____, Cheadle, M.J., Arndt, N.T., and Bickle, M.J. (1993) Constraining the potential temperature of the Archean mantle: A review of the evidence from komatiites. Lithos **30**, 291-307.

O'Neil, H.S.C., Dingwell, D.B., Borisov, A., Spettle, B. and Palme, H. (1995) Experimental petrochemistry of some highly siderophile elements at high temperatures, and some implications for core formation and the mantle's early history. Chem. Geol. **120**, 255-273.

Onorato, P.I.K., Uhlmann, D.R., Taylor, L.A., Coish, R.A., and Gamble, R.P. (1978) Olivine cooling speedometers. Proc. Ninth Lun. Sci. Conf., Vol. 1, 613-628.

Osten, H.J. (1994) Modification of growth modes in lattice-mismatched epitaxial systems: Si/Ge. Physica Status Solidi (A) **145**, 235-245.

Parman, S.W., Grove, T.L., Dann, J., and deWit, M. (1995) Quantitative estimates of the chemical composition and liquidus temperatures of komatiite magmas from the Barberton Mountainland, South Africa. Eos **76**(17), Spring Meeting Suppl., S297.

_____, _____, _____, and _____ (1996) Pyroxene compositions in 3.49 Ga Barberton komatiite: Evidence of variable H_2O contents. Eos **77**(17), Spring Meeting Suppl., S281.

Pearce, T.H. (1987) The identification and assessment of spurious trends in Pearce-type ratio variation diagrams: a discussion of some statistical arguments. CMP **97**, 529-534.

Peck, D.L. (1978) Cooling and Vesiculation of Alae Lava Lake, Hawaii. USGS Prof. Pap. 935-B.

Prest, V.K. (1950) Geology of the Keith-Muskego Townships area. ODM Ann. Rep. **49**(7), 1-44.

Putnis, A. (1992) *Introduction to Mineral Sciences*. Cambridge University Press.

Pyke, D.R., Naldrett, A.J., and Eckstrand, O.R. (1973) Archean ultramafic flows in Munro Township, Ontario. GSA Bull. **84**, 955-978.

Rager, H., Taran, M., and Khomenko, V. (1991) Polarized absorption spectra of synthetic chromium doped Mg_2SiO_4 (forsterite). Phys. Chem. Min. **18**, 37-39.

Renner, R., Nisbet, E.G., Cheadle, M.J., Arndt, N.T., Bickle, M.J., and Cameron, W.E. (1994) Komatiite flows from the Reliance Formation, Belingwe belt, Zimbabwe: I. Petrography and mineralogy. J. Pet. **35**, 361-400.

Richard, D., Marty, B., Chaussidon, M, and Arndt, N.T. (1996) Helium isotopic evidence for a lower mantle component in depleted Archean komatiite. Science, in press.

Rivalenti, G., Girardi, V.A.V., Coltorti, M., Correia, C.T., and Mazzucchelli, M. (1989) Geochemical models for the petrogenesis of komatiites from the Hidrolina greenstone belt, central Goias, Brazil. J. Pet. **30**, 175-197.

Roeder, P.L., and Reynolds, I. (1991) Crystallization of chromite and chromium solubility in basaltic melts. J. Pet. **32**, 909-934.

Rousseau, R.M. (1989) Concepts of influence coefficients in XRF analysis and calibration. In *X-Ray Fluorescence Analysis in the Geological Sciences: Advances in Methodology*, S.T. Ahmedali, Editor. GAC-MAC Short Course Vol. 7.

_____ (1992) CiLT (ver. 4.1) Software for chemical compositional calculations using the Lachance-Traill algorithm in X-ray fluorescence spectrometric analysis. Les logiciels R. Rousseau, Inc.

Sansone, F.J., Resing, J.A., Tribble, G.W., Sedwick, P.N., Kelly, K.M., and Hon, K. (1991) Lava-seawater interactions at shallow-water submarine lava flows. GRL **18**, 1731-1734.

Satterly, J. (1951) Geology of Munro Township. ODM Ann. Rep. 60(8), 1-60.
Saxena, S.K., and Shen, G. (1992) Assessed data on heat capacity, thermal expansion, and compressibility for some oxides and silicates. JGR 97, 19813-19825.
Scheetz, B.E., and White, W.B. (1972) Synthesis and optical absorption spectra of Cr^{2+}-containing orthosilicates. CMP 37, 221-227.
Schreiber, H.D., and Haskin, L.A. (1976) Chromium in basalts: Experimental determination of redox states and partitioning among synthetic silicate phases. Proc. Seventh Lun. Sci. Conf., Vol. 2, 1221-1259.
Schwab, R.G., and Küstner, D. (1977) Precise determination of lattice constants to establish X-ray determinative curves for synthetic olivines of the solid solution series forsterite–fayalite. (In German.) Neues Jahrbuch für Mineralogie, Monatshefte 1977, pp. 205-215.
Seigel, R., and Howell, J.R. (1981) *Thermal Radiation Heat Transfer*, Second Edition. Hemisphere Publishing, New York.
Shankland, T.J., Nitsan, U., and Duba, A.G. (1979) Optical absorption and radiative heat transfer in olivine at high temperature. JGR 84, 1603-1610.
Shannon, R.D. (1976) Revised effective ionic radii and systematic studies of interatomic distances in halides and chalcogenides. Acta Crystallographica A32, 751-767.
Shaw, H.R. (1972) Viscosities of magmatic silicate liquids: An empirical method of prediction. Am. J. Sci. 272, 870-893.
Shirey, S.B., and Barnes, S.-J. (1994) Re-Os and Sm-Nd isotopic constraints on basaltic komatiitic volcanism and magmatic sulphide formation in the Cape Smith Foldbelt, Quebec. Min. Mag. 85A, 835-836.
Shore, M. (1995) Comment on "Experimental determination of the thermal conductivity of molten $CaMgSi_2O_6$ and the transport of heat through magmas", by Don Snyder, Elizabeth Gier, and Ian Carmichael. JGR 100, 22401-22402.
Sleep, N.H. (1983) Hydrothermal convection at ridge axes. In *Hydrothermal Processes at Seafloor Spreading Centers*, P.A. Rona, K. Bostrŏm, L. Laubier, and K.L. Smith, Eds. Plenum Press, New York.
Smyth, J.R., and Bish, D.L. (1988) *Crystal Structures and Cation Sites of the Rock-Forming Minerals*. Allen and Unwin, Boston.
Snyder, D., Gier, E., and Carmichael, I. (1994) Experimental determination of the thermal conductivity of molten $CaMgSi_2O_6$ and the transport of heat through magmas. JGR 99, 15503-15506.
Storey, M., Mahoney, J.J., Kroenke, L.W., and Saunders, A.D. (1991) Are oceanic plateaus sites of komatiite formation? Geology 19, 376-379.
Susa, M., Nagata, K., and Mills, K.C. (1993) Absorption coefficients and refractive indices of synthetic glassy slags containing transition metal oxides. Ironmaking and Steelmaking 20, 372-378.
Sutton, S.R., Jones, K.W., Gordon, B., Rivers, M.L., Bajt, S., and Smith, J.V. (1993) Reduced chromium in olivine grains from lunar basalt 15555: X-ray absorption near edge structure (XANES). GCA 57, 461-468.
Tait, S., and Jaupart, C. (1993) Compositional convection in a reactive crystalline mush and melt differentiation. JGR 97, 6735-6756.
Takahashi, E. (1978) Partitioning of Ni^{2+}, Co^{2+}, Fe^{2+}, Mn^{2+}, and Mg^{2+} between olivine and silicate melts: Compositional dependence of partition coefficient. GCA 42, 1829-1844.
Taran, M.N., Langer, K., Platonov, A.M., and Indutny, V.V. (1994) Optical absorption investigation of Cr^{3+} ion-bearing minerals in the temperature range 77-797 K. Phys. Chem. Min. 21, 360-372.

Thompson, G. (1991) Metamorphic and hydrothermal processes: Basalt-seawater interactions. In *Oceanic Basalts*, P.A. Floyd, Ed. Blackie, Glasgow.

Thomson, B. (1989a) Petrology and stratigraphy of some texturally well preserved thin komatiites from Kambalda, Western Australia. Geol. Mag. **126**, 249-261.

_____ (1989b) B_1 subdivisions in thin komatiites at Kambalda, Western Australia. Geol. Mag. **126**, 263-270.

Tiller, W.A. (1991a) *The Science of Crystallization: Microscopic Interfacial Phenomena*. Cambridge University Press.

_____ (1991b) *The Science of Crystallization: Macroscopic Phenomena and Defect Generation*. Cambridge University Press.

Touloukian, Y.S., Powell, R.W., Ho, C.Y., and Klemens, P.G. (1970) *Thermal Conductivity: Nonmetallic Solids*. Thermophysical Properties of Matter, Volume 2. Plenum Publishing.

Touloukian, Y.S., Powell, R.W., Ho, C.Y., and Nicolaou, M.C. (1973) *Thermal Diffusivity*. Thermophysical Properties of Matter, Volume 10. Plenum Publishing.

Trial, A.F., and Spera, F.J. (1994) Measuring the multicomponent diffusion matrix: Experimental design and data analysis for silicate melts. GCA **58**, 3769-3783.

Tribble, G.W. (1991) Underwater observations of active lava flows from Kilauea volcano, Hawaii. Geology **19**, 633-636.

Turner, J.S., Huppert, H.E., and Sparks, R.S.J. (1986) Komatiites II: Experimental and theoretical investigations of post-emplacement cooling and crystallization. J. Pet. **27**, 397-437.

Urbain, G., Bottinga, Y., and Richet, P. (1982) Viscosity of liquid silica, silicates and alumino-silicates. GCA **46**, 1061-1072.

Viljoen, M.J., and Viljoen, R.P. (1969) Evidence for the existence of a mobile extrusive peridotitic magma from the Komati Formation of the Onverwacht Group. Spec. Pub. Geol. Soc. South Afr. **2**, 87-112.

Vines, K.J. (1987) Comments on "Ratio correlations and major element mobility in altered basalts and komatiites" by H.R. Rollinson and C.R. Roberts. CMP **97**, 525-526.

Wagner, G., Gottschalch, V., Rhan, H., and Paufler, P. (1989) Pseudomorphic growth and nucleation of misfit dislocations in the epitaxial system (001) $InP/In_{1-x}Ga_xAs$. I. Pseudomorphic growth, tetragonal distortion, and lattice relaxation by dislocation nucleation. Physica Status Solidi (A) **112**, 519-531.

Walker, D., Jurewicz, S., and Watson, E.B. (1988) Adcumulus dunite growth in a laboratory thermal gradient. CMP **99**, 306-319.

Walker, G.P. (1992) Morphometric study of pillow-size spectrum among pillow lavas. Bull. Volcanology **54**, 459-474

Walker, R.J., Shirey, S.B., and Stecher, O. (1988) Comparative Re-Os, Sm-Nd, and Rb-Sr isotope and trace element systematics for Archean komatiite flows from Munro Township, Abitibi belt, Ontario. EPSL **87**, 1-12.

Wicks, F.J., and O'Hanley, D.S. (1988) Serpentine Minerals: Structure And Petrology. In *Hydrous Phyllosilicates*, S.W. Bailey, Ed. Rev. in Min. **19**, 91-167.

Wilks, M.E., and Nisbet, E.G. (1988) Stratigraphy of the Steep Rock Group, northwest Ontario: a major Archaean unconformity and Archaean stromatolites. CJES **25**, 370-391.

Worster, M.G., Huppert, H.S., and Sparks, R.J.S. (1993) The crystallization of lava lakes. JGR **98**, 15 891-15 901.

Wright, K., and Catlow, C.R.A. (1994) A computer simulation study of (OH) defects in olivine. Phys. Chem. Min. **20**, 515-518.

Xie, Q. and Kerrich, R. (1994) Silicate perovskite and majorite signature komatiite from the Archean Abitibi Greenstone belt: Implications for early mantle differentiation and stratification. JGR **99**, 15 799-15 812.

Zhang, J., and Herzberg, C. (1994) Melting experiments on anhydrous peridotite KLB-1 from 5.0 to 22.5 GPa. JGR **99**, 17 726-17 742.

Zhou, M.-F. (1994) PGE distribution in 2.7-Ga layered komatiite flows from the Belingwe greenstone belt, Zimbabwe. Chem. Geol. **118**, 155-172.

_____ and Kerrich, R. (1992) Morphology and composition of chromite in komatiites from the Belingwe greenstone belt, Zimbabwe. Can. Min. **30**, 303-317.